IntechOpen

# Simulation and Modelling of Electrical Insulation Weaknesses in Electrical Equipment

*Edited by Ricardo Albarracín Sánchez*

# SIMULATION AND MODELLING OF ELECTRICAL INSULATION WEAKNESSES IN ELECTRICAL EQUIPMENT

Edited by **Ricardo Albarracín Sánchez**

**Simulation and Modelling of Electrical Insulation Weaknesses in Electrical Equipment**
http://dx.doi.org/10.5772/intechopen.72459
Edited by Ricardo Albarracín Sánchez

**Contributors**

Dengming Xiao, Mona Ghassemi, Peter Kung, Joao Batista Batista Rosolem, Sender Rocha dos Santos, Rodrigo Peres, Wagner Francisco Rezende Cano, Pablo Gomez, Fermin P. Espino-Cortes, Mohammed Khalil Hussain, Fuping Zeng, Ju Tang, Siyuan Zhou, Cheng Pan, Xiaoxing Zhang, Cristina Fernández-Diego, Carlos Javier Renedo, Inmaculada Fernández, Isidro Alfonso Carrascal, Felix Ortiz, Fernando Delgado, Agustín Santisteban, Alfredo Ortiz, Carlos J Renedo, Félix Ortiz



**Notice**



First published in London, United Kingdom, 2018 by IntechOpen
eBook (PDF) Published by IntechOpen, 2019
IntechOpen is the global imprint of INTECHOPEN LIMITED, registered in England and Wales, registration number: 11086078, The Shard, 25th floor, 32 London Bridge Street
London, SE19SG – United Kingdom
Printed in Croatia

British Library Cataloguing-in-Publication Data
A catalogue record for this book is available from the British Library

Additional hard and PDF copies can be obtained from orders@intechopen.com

Simulation and Modelling of Electrical Insulation Weaknesses in Electrical Equipment
Edited by Ricardo Albarracín Sánchez

p. cm.

Print ISBN 978-1-78923-768-9

Online ISBN 978-1-78923-769-6

eBook (PDF) ISBN 978-1-83881-685-8

# Meet the editor

Ricardo Albarracín Sánchez received his BSc, MSc and PhD degrees in Electrical Engineering, respectively, in 2008, 2010 and 2014 from the Universidad Carlos III de Madrid (UC3M), Spain. Currently, he is an assistant professor at the Senior Technical School of Engineering and Industrial Design (ETSIDI) at the Universidad Politécnica de Madrid (UPM). He is a member of the research group Networks and Installations at Low Voltage and High Voltage (RIBAT) and an assistant to the Director for International Mobility (Erasmus+ School coordinator). His main research interest areas are electrical insulation, partial discharges, condition monitoring, UHF sensors, nanodielectrics, power transformers and renewable energy.

# Contents

# Preface

The reliability of power grids and their electrical assets is crucial to avoid discontinuity of the electrical supply and breakdowns. To prevent those non-desirable scenarios, it is necessary to carry out a proper maintenance of electrical insulation systems. The advances in computing are allowing the implementation of models that behave as real systems. This book provides the reader with models for electrical insulation evaluation of power transformers, power electronics, voltage sensors and power generators and proposes environmentally friendly insulation gases as alternatives to sulphur hexafluoride gas.

The editor would like to acknowledge the authors for their contributions. In addition, the editor would like to thank the Spanish Ministry of Economy and Competitiveness (project DPI2015-71219-C2-2-R).

**Prof. Ricardo Albarracín Sánchez**
Dept. of Electrical, Electronic and Automation Engineering and Applied Physics
E.T.S. Ingeniería y Diseño Industrial (ETSIDI)
Universidad Politécnica de Madrid (UPM)
Madrid, Spain

Section 1

# Insulation Systems Modelling for Power Transformers

Chapter 1

# Assessment of Dielectric Paper Degradation through Mechanical Characterisation

Cristina Fernández-Diego, Inmaculada Fernández, Felix Ortiz, Isidro Carrascal, Carlos Renedo and Fernando Delgado

Additional information is available at the end of the chapter

http://dx.doi.org/10.5772/intechopen.77972

**Abstract**

Power transformers life is limited fundamentally by the insulation paper state, which can be analysed through different techniques such as furanic compound concentration, dissolved gases, methanol concentration, Fourier transform infrared spectroscopy, X-ray diffraction, scanning electron microscope, refractive index of cellulose fibres, degree of polymerisation or tensile strength. The two last techniques provide the best way to evaluate mechanical resistance of insulation paper. This chapter describes briefly the most remarkable studies about post-mortem assessment and thermal ageing tests in which mechanical properties are some of the characteristics evaluated to determine paper degradation. This work also gathers the main relationships developed until now to relate different by-products generated during transformer operation with loss of paper mechanical properties. Finally, this chapter defines the future approaches, which could be used to study paper degradation.

**Keywords:** dielectric paper, insulation oil, tensile strength, post-mortem, thermal ageing test

## 1. Introduction

Since the nineteenth century, the use of alternating current (AC) against direct current (DC) was imposed. The machine used for increasing or reducing of AC voltage is the transformer, which has allowed the development of the power market, making possible the electricity transport over long distances thanks the reduction of Joule losses during high-voltage (HV)

transport. Electrical insulation and cooling systems are critical parts of electric power transformers during their operation [1].

Transformer losses generate heat, which produces an increase in temperature and an efficiency decrease. Once a power transformer starts its operation, heat begins to be produced, which origins a progressive increase of the temperature. This increase continues until permanent regime conditions are reached. The temperature rise above the service conditions results in an accelerated degradation of the insulating materials. Additionally, insulation systems of oil-filled transformers are subjected to repeated lightning impulses, which brings potential risk to the insulation system, being the liquid/solid interface the weak link. Assessment of insulation condition can be obtained by partial discharge (PD) monitoring [2]. For instance, some authors [3–8] have analysed the effect of oil and pressboard ageing (electrical and/or thermal) on the characteristic of PD from inception to flashover, surface discharge inception voltage (SDIV) variation, creepage discharge inception voltage (CDIV) or creepage discharge flashover voltage (CDFV) of oil/solid insulation specimens with different ageing degrees. Other authors have studied the effect of polarity on the accumulation of charges at the oil-solid interface [9], the accumulative effect of repeated lightning impulses and its damage mechanism [10], the electrical deterioration caused by PD under long-term AC voltage [11] or the performance of alternative liquids in comparison with mineral oil [12].

On the other hand, thermal ageing of insulation system in power transformers can favour the initiation of short-circuit forces, which can end up in a permanent deformation or failure [13].

The type of cooling system in power transformers depends on different factors, mainly associated with the machine power. The two main groups in which this kind of systems can be divided are: dry and liquid cooling. For small transformers (100–50,000 kVA) [14], the external surface of the transformer is sufficient to evacuate by convection and/or radiation the generated heat to the environment. In such cases, the transformer is air-cooled, being called dry transformer. These transformers depend on air to enter at the bottom, flow upward over the core and coil surfaces and exit through the openings near to the top. In medium-large powers, the cooling system is generally of liquid type, so that the core and the windings are immersed in oil and contained in a steel tank. This kind of transformers is named oil-filled and in them, the oil absorbs the heat generated, transports it and dissipates it to the environment through an exchange boundary. In some cases, this boundary is the outer surface of the tank, often flapped, which evacuates heat by natural convection and radiation. As the power of the transformer increases, external radiators are added to increase the exchange surface as well as fans to force the convection. In high-power transformers, the cooling of the oil can be also carried out by means of an oil–water exchanger.

In power systems, most of power transformers are oil-filled [15], and their insulation system is mainly composed of cellulose [16]. The oil provides electrical insulation together with cellulosic materials, as well as cooling. Once a transformer starts its operation, the insulation system degrades over time through different physical–chemical mechanisms. In the case of oil, it is quite simple to maintain it in suitable conditions, and it is even feasible to replace if it would be required. However, this is not possible with solid insulation because this cover wires which constitute the windings of the transformer. Under a practical point of view, replacing the solid

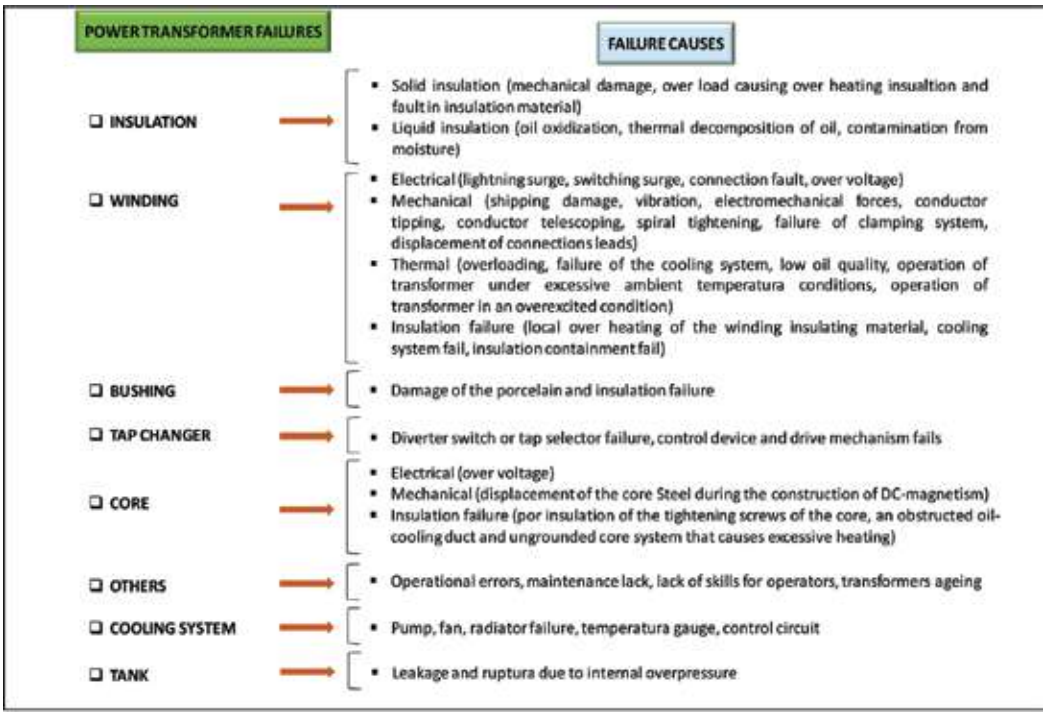


**Figure 1.** Transformer failures and their causes.

insulation would imply re-manufacturing the transformer almost completely, which is not practical. Consequently, it can be concluded that the life of a power transformer is limited fundamentally by the insulation paper state, which highlights the enormous importance of knowing its behaviour and its degradation rate over time.

Not only solid insulation components suffer continuous ageing, but also the dielectric oil. During transformers operation, the insulation system degrades generating a wide range of by-products such as furanic compounds, water, $CO_2$, CO, low and high molecular weight acids, and so on [16].

These by-products can influence the normal operation of the transformers causing a raise of failure probability. Therefore, it is important to determine the ageing state of the transformers through the monitoring of the condition of their electrical insulation. The state of degradation of the oil can be determined through various parameters such as interfacial tension, oxidation stability, acidity, dissolved gases analysis (DGA), breakdown voltage, dissipation factor, and so on [16, 17]. In the case of insulation paper, the study of its degradation can be done through the determination of the degree of polymerisation (DP) or through the tensile index. The purpose of these two procedures is to determine the mechanical strength of the paper. While the first method does a representative strength measure, the second one determines the true measurement [18]. However, both tests can only be carried out through scrapping transformers, since in both cases it is necessary to take a sample of the solid component, which requires drain the oil.

The knowledge of the oil and paper ageing processes through the measure of the real state of degradation of the machine is essential to predict the failure of a transformer in service [19, 20], which can be due to different causes as was gathered by Murugan and Ramasamy [21], **Figure 1**.

The main aim of this chapter is to describe the opportunities offered by the variables obtained through stress–strain curve in post-mortem studies as well as accelerated thermal ageing tests carried out in laboratory, describing some of its advantages and challenges. This chapter is structured as follows: Section 2 explains some of the most used methods to evaluate paper ageing. Section 3 exposes the main post-mortem studies carried out until now, as well as the methods and a mathematical model based on DP and tensile index used to analyse paper degradation. The following section describes accelerated thermal ageing tests in which mechanical properties have been used to determine paper degradation. Additionally, this section describes a mathematical model defined by the authors of this chapter, which can be used to determine the paper ageing through mechanical properties, obtained from tensile test. Finally, the conclusions are presented.

## 2. Paper degradation assessment

The study of paper ageing in power transformers is critical to maximise the operation period, and it can be carried out through different methods, some of the most used are:

### 2.1. Furanic compounds concentration

This is a non-intrusive technique, which can be used to estimate the ageing of the dielectric paper. It has been concluded by different authors [22–32] that there is a relation between furanic compounds and degree of polymerisation. This relation has been defined through mathematical models such as gathered in **Table 1**.

These models are empirical, obtained through experimental data, so when they are applied to a 2-FAL concentration of for example 0.25 ppm, the value of DP ranges from 764.45 to 535.45 Therefore, there is a huge difference between the results.

These compounds can be determined through high performance liquid chromatography (HPLC) or extraction with methanol [32, 33]. The first step of the furanic compounds measure is to extract them from the oil, which can be done through solid–liquid extraction or liquid–liquid extraction. After that, it is analysed by the HPLC in which it is eluted in the specified column and detected through an ultra violet (UV) detector [18].

A varied range of factors could affect the analysis of furanic compounds: high moisture (furfuryl alcohol, FA), overheating or normal ageing (2-furfuraldehyde, 2FAL), high temperature (5metyl-2furfural, 5MEF).

| Mathematical model | | Reference |
|---|---|---|
| $DP = 325 \cdot \left(\frac{19}{13} - \log_{10}(2FAL)\right); 100 \leq DP \leq 900$ | (1) | [22] |
| $DP = \frac{1}{0.0035} \cdot \left(1.51 - \log_{10}(2FAL)\right); 150 \leq DP \leq 1000$ | (2) | [23] |
| $DP = \frac{1850}{2.3+2FAL}; 150 \leq DP \leq 600$ | (3) | [24] |
| $DP = \frac{1}{-0.0035} \cdot \left(\log_{10}(2FAL \cdot 0.88) - 4.51\right)$ | (4) | [25, 26] |
| $DP = \frac{800}{[0.186 \cdot 2FAL]+1}$ | (5) | [27] |
| $DP = 356.1 - 343.8 \cdot \log_{10}[TotalFurans]$ | (6) | [28] |
| $DP = \frac{1.4-\log_{10}(2FAL)}{0.003}; 200 \leq DP_{av} \leq 800$ | (7) | [29] |
| $DP = \frac{2.6-\log_{10}(2FAL)}{0.0049};$ | (8) | [30] |
| $DP = 402.47 - 220.87 \cdot \log_{10}(C_{fur})$ | (9) | [30] |
| $DP = -121 \cdot \ln(C_{fur}) + 458$ | (10) | [31] |
| $DP = 405.25 - 347.22 \cdot \log_{10}(2FAL)$ | (11) | [32] |

DP: degree of polymerisation of the cellulosic paper in the windings of a transformer.
2FAL: mg of furfural/kg of oil.
DPav: average degree of polymerisation of the cellulosic paper in the windings of a scrapped transformer.
Total furans: mg of total concentration of furans/kg of oil.
Cfur: mg of total concentration of furans/kg of oil.

**Table 1.** Furans and DP correlations.

### 2.2. Dissolved gas analysis

It is a technique used to identify faults during transformer operation. This analysis can be also utilised to describe the paper ageing through CO and $CO_2$ dissolved in the oil. Different works have showed that there is a relationship between the concentration of these gases and the DP ($CO_2/CO \leq 7.4$, DP > 600; $7.4 < CO_2/CO < 8.0$, 400 < DP < 600; $8 \leq CO_2/CO < 8.7$, 250 < DP < 400; $CO_2/CO \geq 8.7$, DP < 250) [34, 35]. The gases, which can be extracted from the oil using different methods [18], are detected using the gas chromatography technique whose operating principle is like HPLC.

### 2.3. Methanol concentration

The determination of the amount of this alcohol can be used to monitor the depolymerisation of the paper under normal operating conditions of the transformer. Methanol offers a faster indication of the early stages of paper degradation than furans [18]. This volatile product can be measured through a gas chromatograph equipped with a mass selective detector in the electron impact mode [36].

### 2.4. Fourier transform infrared spectroscopy

Infrared spectroscopy is a technique used for materials analysis, which uses the infrared region of the electromagnetic (EM) spectrum [37]. It is based on the specific vibration frequencies, which have the chemical bonds of the substances. These frequencies correspond to the energy levels of the molecule and depend on the shape of the potential energy surface of the molecule, the molecular geometry, the atomic mass and the vibrational coupling. If a sample receives light with the same energy from that vibration and the molecules suffer a change in their bipolar moment during vibration, then this will appear in the infrared spectrum. To make measurements on a sample, a monochrome ray of infrared light is passed through the sample, and some of this radiation is absorbed by the sample and some of it is transmitted. By repeating this operation in a range of wavelengths, an infrared spectrum can be obtained. This spectrum represents the molecular absorption and transmission, generating a fingerprint of a sample with absorption peaks, which correspond to the frequencies of vibrations between the bonds of the atoms that constitute the material. The size of the peaks in the spectrum is a direct indication of the amount of material [37, 38]. This technique provides precise information about functional groups (O-H, CH, C=O, C-O) changes [37, 38].

### 2.5. X-ray diffraction

This is a rapid analytical technique based on the dispersion of the X-ray beam by matter and on the constructive interference of waves that are in phase and that are dispersed in certain directions of space. X-rays are generated in a cathode ray tube by heating a filament to produce electrons, which are accelerated toward the sample applying a voltage. When the electrons have sufficient energy to dislodge inner shell electrons of the target material, characteristic X-ray spectrum is obtained which allows the identification of crystalline phases qualitatively and quantitatively. The crystal structure and crystallinity are the key properties of the crystalline polymer material for deciding its electrical performance. By analysing the length, width, height and diffraction angle, crystal structure identification and chemical phase analysis could be implemented. Therefore, X-RD analysis is very helpful in the investigation of the crystal structure of the cellulose fibres in the transformer paper [39].

### 2.6. Scanning electron microscope

Scanning electron microscope (SEM) can obtain the electronic image of sample's surface to show its microstructure [40]. The SEM is capable of producing high-resolution images of a sample surface (**Figure 2**). A heated electron emission produces an electron beam, which is focused by one or two condenser lenses to a fine focal spot. The beam passes through a pair of scanning coils in the objective lens, which deflect the beam both horizontally and vertically. Consequently, the beam scans in a raster fashion over a rectangular area of the sample surface [39]. It allows knowing in detail the state of the surface of a material, which can provide important information about the microstructure, impurities, degree and origin of alteration of the material.

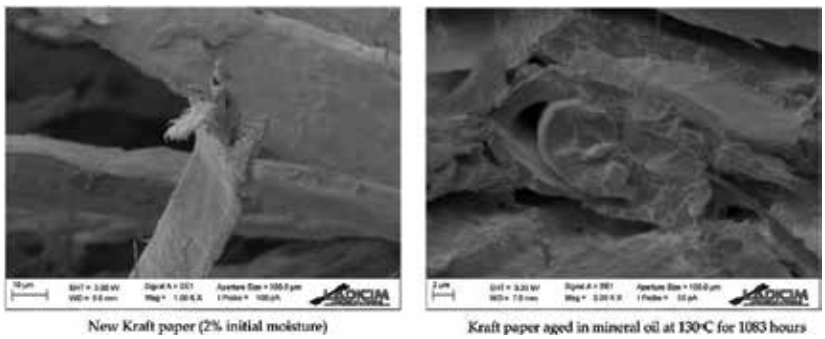


**Figure 2.** SEM result of Kraft paper.

### 2.7. Refractive index of cellulose fibres

The refractive index (RI) of cellulose fibres can be determined using the dispersion staining method (DSM) whose principle is as follows: when cellulose fibres are immersed in liquid, white light will be dispersed at the boundary of the two substances. At this point, there is a spectrum that does not refract (it passes straight through). This particular spectrum has the condition: "RI of cellulose fibre = RI of immersion-liquid." When this particular spectrum is intercepted by an optical mask and condenses the spectra that are not intercepted, the cellulose fibre appears to be coloured. It is possible to know the RI of cellulose fibres at a particular spectrum by observing dispersion colour through DSM [41].

### 2.8. Degree of polymerisation

The degree of polymerisation can be defined as the average number of glucose rings in each cellulose chain and it is dimensionless [19]. These chains of cellulose break up during transformer operation by exposure to oxygen, moisture and heat, which produce a decrease of mechanical strength of paper. This weakening end up in transformer fail and it is commonly accepted that this failure occurs when DP = 150 to 200 [34].

The DP of dielectric paper can be measured using an Ubbelohde viscometer tube [42]. The first step of the procedure is to measure the viscosity of paper, deionised water and cupriethylenediamine (Cuen) mixture and the next step is to calculate the specific viscosity. Once the specific viscosity has been obtained the DP can be estimated.

### 2.9. Stress: strain curve

The paper strength is due to fibre strength and inter-fibre bonding strength [18]. Tensile strength (TS) can be described by stress and strain curve (**Figure 3**), which is obtained through tensile test.

This test is used to determine the behaviour of a material when a specimen is clamped in an axial loading frame (**Figure 4**). The data obtained from this test (load and displacement) are used to determine stress and strain using the original specimen cross-sectional area $A_0$ (m2) and length $L_0$ (mm).

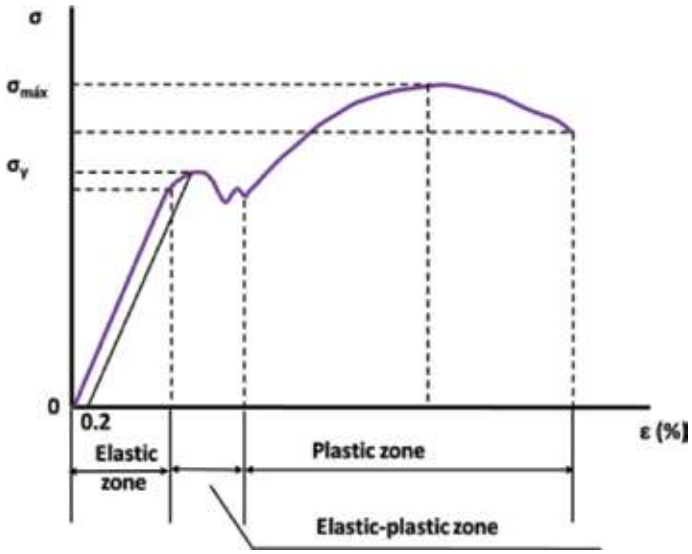


**Figure 3.** Stress–strain curve.


**Figure 4.** An universal servo hydraulic test machine (model ME-405-1, SERVOSIS) with an axial load cell of ±1 kN capacity, an actuator of ±50 mm of dynamic stroke and equipped with pneumatic flat grips.

Stress (σ) is the internal load applied to a specific surface; it is usually expressed in Pa or MPa when the value is high.

$$\sigma = \frac{F}{A_0} = \frac{F}{b \cdot a} \tag{1}$$

where σ is the stress (Pa); F is the load (N); $A_0$ is the original specimen cross-sectional area ($m^2$); a is the original width of the specimen (m) and b is de original thickness of the specimen (m).

Strain (ε) is the change in the size or shape of a specimen due to internal stress produced by one or more loads applied to it or by thermal expansion.

$$\varepsilon = \frac{l - l_0}{l_0} \tag{2}$$

At the beginning of stress–strain curve (**Figure 3**), many materials follow Hooke's law, so that stress is proportional to strain being the modulus of elasticity or Young's modulus (Y, Pa) the constant of proportionality. As strain increases, many materials end up deviating from this linear proportionality, the point in which this happens is named the proportional limit. This behaviour is associated with plastic strain. This plasticity requires molecular mobility and not all materials have it. The microstructural rearrangements associated with plastic strain are usually not reversed when the load is removed, so the proportional limit is often the same as or close to the materials' elastic limit, which is the stress needed to produce a permanent residual strain on a specimen once this is unloaded. A parameter related with this behaviour is the yield stress ($\sigma_y$, Pa), which is the stress required to generate plastic strain in a specimen and it is often considered to be the stress needed to generate a permanent strain of 0.2%. In the stress–strain curve appears a point of Maximum Tensile Strength ($\sigma_{max}$, Pa), beyond this point the material appears to strain soften. The area under the stress–strain curve up to a given value of strain is the total mechanical energy per unit volume consumed by the material to get that strain [43]. An additional parameter, which can be obtained through stress–strain curve, is the tensile index.

$$TI = \frac{F/a}{G} \tag{3}$$

where TI is the tensile index (kN $m^{-1}$ $kg^{-1}$); F is the load (kN); a is the original width of the specimen (m) and G is the grammage (kg $m^{-2}$).

Dielectric papers used in the isolation system of oil-filled transformers have different values of the mechanical properties (**Table 2**).

As dielectric paper ages, the risk of transformer failure will rise. According to the study carried out by Murugan and Ramasamy [21], approximately 41% of the faults produced in a fleet of transformers (196 transformers ranging from 33 to 400 kV and from 5 to 315 MVA) were due to failures in the insulation system. Thus, it is critical to monitor the condition of the insulating

| Property | | Grade K presspaper | Grade 3 presspaper | Grade K diamond dotted presspaper | Grade 3 diamond dotted presspaper | PSP 3050 |
|---|---|---|---|---|---|---|
| Typical thickness (mm) | | > 0.2 | > 0.2 | > 0.2 | > 0.2 | 0.7 |
| $\sigma_{max}$ (MPa) | MD | 110 | 91 | 110 | 91 | ≥ 70 |
| | XD | 50 | 40 | 39 | 40 | ≥ 50 |
| ε (%) | MD | 2.4 | 2.8 | 2.4 | 2.8 | ≥ 6 |
| | XD | 7.6 | 7.8 | 7.5 | 7.8 | ≥ 8 |

MD: machine direction of paper; and XD: cross direction of paper.

**Table 2.** Typical mechanical properties of dielectric papers.

solid, which can be carried out through techniques based on paper ageing by-products (furanic compounds, methanol, dissolved gases…), DP or stress–strain curve. The last technique is the best way to analyse paper degradation [18]. However, the implementation of the two last techniques is only possible through post-mortem studies (scrapping transformers). Another possibility to paper assessment is through correlations based on thermal ageing tests carried out in laboratory. The following sections describe the possibilities that stress–strain offer in order to obtain useful information not only in post-mortem studies, but also in accelerated thermal ageing tests.

However, the implementation of the two last techniques is impossible during transformer operation because it is not possible obtain paper samples from in-service transformers and the only opportunity is through post-mortem studies (scrapping transformers). Another possibility to paper assessment is through correlations based on thermal ageing tests carried out in laboratory. The following sections describe the possibilities that stress–strain offer in order to obtain useful information not only in post-mortem studies, but also in accelerated thermal ageing tests.

## 3. Post-mortem studies

Although power transformers are tested machines whose life-span pass 20 years even in many cases 40 years [44, 45], their failure diagnostics are becoming increasingly important due to the high cost of these devices.

The aim of power transformers post-mortem studies is to understand the failure mechanisms, so it is essential to collect information about the fault, sequence of events previous the fault, protective operation and protective devices performance. This information requires to be collected immediately after the failure occurs, to reproduce it accurately. Therefore, if there is no an efficient diagnostic methodology included in maintenance program, test results will not be useful to prevent future failures. There are cases in which failures do not manifest in a protective device operation, so routine monitoring can help to detect abnormal operation conditions. Though end-of-life assessments can provide useful information, they are not always conclusive enough to make the decision about the appropriate time to remove a transformer from service. This is the reason why the availability of the history of test results from a power transformer may help to have a better evaluation about the most suitable moment to replace this kind of machines [46].

There are some examples of post-mortem studies that have used the DP as technique to determine the paper ageing. For instance, Koch et al. [17] through a research project in which worked together the IEH Karlsruhe, power stations, utilities and a manufacturer. One of its aims was the definition of a correlation between DP and furanes in the oil, the other aim was to obtain data about the ageing process of transformers populations. This project carried out the post-mortem analysis of two generator transformers. The result tests showed that the lowest DP value occurs at about 75% of the winding length and not at the top in the LV and the HV windings. This allowed to conclude that the hot spot temperature does not occur at the top of

the winding. Additionally, these authors obtained that there is a good correlation between DP and the content of furanes in the oil and that the $CO_2$/CO ratio can be used to detect the degree of carbonisation of the insulation paper. Martins et al. [47] also evaluated the condition of a single power transformer, specifically a 63-MVA, 150/63/10-kV, shell-type unit to make a decision regarding its transfer to a new substation. They measured the DP from selected points in the transformer connections insulation to get a paper-ageing diagnostic and compare it with the predicted diagnostic based on the previous oil analysis [dissolved gas analysis (DGA), colour, appearance, breakdown voltage, water content, acidity, dielectric dissipation factor, sediment and sludge, interfacial tension, flash point and furanic compounds]. Their evaluation showed that the calculation of DP using correlations based on 2-FAL require care because DP values depend on variables such as temperature, oxygen, water content, oil type and degradation oil. These authors also estimated DP values using the calculated thermal profiles. However, their results concluded that loading data included the daily peaks are insufficient to obtain an accurate temperature distribution. Finally, they concluded that more post-mortem studies with detailed operational data would improve the knowledge of the correlation between 2-FAL in oil and the DP of insulating paper. DP was also used to estimate paper ageing in the post-mortem assessment carried out by other authors [28, 48]. Leibfried et al. [28] proposed a systematical method for taking paper samples from scrapped power transformers and a methodology for the evaluation of DP values suggesting a grouping into different types of transformers, at least in Germany, which the operation mode and consequently the ageing rate inside transformers is substantially different. Using the data obtained in their study, Leibried et al. derived a formula to estimate average DP through the 2-FAL concentration, although they obtained that this equation does not provide 100% reliable evaluation of transformer condition. In the case of Jalbert and Lessard [48], insulating paper from six power transformers (open-breathing core-type power transformers built in 1958, initially cooled with OFWF systems and since 1990s modified to OFAF cooling systems) as well as representative oil samples needed to evaluate the oil quality and its content of chemical markers (furans and alcohols) were tested. These authors concluded that it is critical to obtain a complete DP profile of the transformer in order to apply any model. They also focused on the need to establish concentration thresholds to define more accurately the insulation paper condition. The experimental results of these post-mortem assessments give a variation of DP values ranged from less than 5% to more than 40%, which indicates the results variability of this technique.

It was not until 2014, that post-mortem studies were carried out considering not only DP, but also tensile index, despite the fact that some authors like Emsley et al. [49] have developed an expression, which correlated DP and tensile strength with temperature and time. The approach applied by Carcedo et al. [50] showed a case study, which used, the model proposed by Emsley et al. to predict the values of tensile index and degree of polymerisation [49], in an alternative way for post-mortem assessment. These authors estimated temperature distributions considering the machine life-span and the DP and TI values of new and aged Kraft paper. Carcedo et al. [50] took paper samples from a failed distribution transformer (three-phase transformer with a rated power of 800 kVA at 50 Hz and manufactured in 1986 with an ONAN cooling system) to measure DP and TI. Later, the temperature distributions were obtained based on DP and TI test results and Emsley et al. model [49]:

$$DP_t = \frac{k_2 \cdot DP_0 \cdot e^{k_2 t}}{e^{k_2 t} \cdot (DP_0 \cdot k_{1_0} + k_2) - DP_0 \cdot k_{1_0}} \tag{4}$$

$$TI_t - TI_0 = K_1 \cdot e^{-k_2 t} + K_2 \cdot \ln\left(e^{k_2 t} - K_3\right) - K_4 \tag{5}$$

$$k_{1_0} = A_{1_0} \cdot e^{\frac{-E_{a10}}{R^* T}} \tag{6}$$

$$k_2 = A_2 \cdot e^{\frac{-E_{a2}}{R^* T}} \tag{7}$$

$$K_1 = \frac{k_2 \cdot k_{1_0}}{k_2} \tag{8}$$

$$K_2 = k_4 \cdot K^{'} \tag{9}$$

$$K_3 = k_{1_0} \cdot K^{'} \tag{10}$$

$$K_4 = K_2 \cdot (\ln(1 - K_3)) + K_1 \tag{11}$$

$$K^{'} = \frac{DP_0}{DP_0 \cdot k_{1_0} + k_2} \tag{12}$$

where $DP_t$ is the insulation DP value at time t; $DP_0$ is the initial insulation DP value; t is the time (s); $k_{10}$ is the initial rate at which bonds break; $k_2$ is the rate at which $k_{10}$ changes; $TI_t$ is the insulation tensile strength index value at time t; $TI_0$ is the initial insulation tensile strength index value; $k_{10}$, $k_2$, $k_3$ and $k_4$ constants can be obtained assuming that Arrhenius equation is valid from normal temperature of power transformers up to the temperatures used in ageing experiments:

$$k = A \cdot e^{\frac{-E_a}{RT}} \tag{13}$$

where k is a rate constant; A is the pre-exponential factor ($s^{-}1$); $E_a$ is the activation energy (J $mol^{-}1$); R is the molar gas constant (8.314 $JK^{-}1$ $mol^{-}1$) and T is the temperature (K).

Finally, these temperature distributions obtained by Carcedo et al. [50] and represented by authors of this chapter (**Figure 5**) were compared in order to show the suitability of tensile analysis for post-mortem studies. These authors concluded that the maximum difference for the same point was less than 3.3 K; therefore, both methods were suitable for post-mortem evaluations, being the TI more reliable and repeatable indicator.

Azis et al. also used stress–strain curve to investigate the mechanical strength of paper from 10 scrapped power transformers [51]. These authors not only used TI to carried out the transformers assessment, but also the low molecular weight acid (LMA). They concluded that there is a relationship between LMA in oil and TI of paper, which tends to be generic for both laboratory tests and in-service ageing data.

In the paper written by Müllerová et al. [52], was described the methodology followed to create and utilise as a making decision tool a database which gathers data about the condition of the insulation system of a group of 24 transformers (1 transformer of 330 MVA, 400/121 kV;

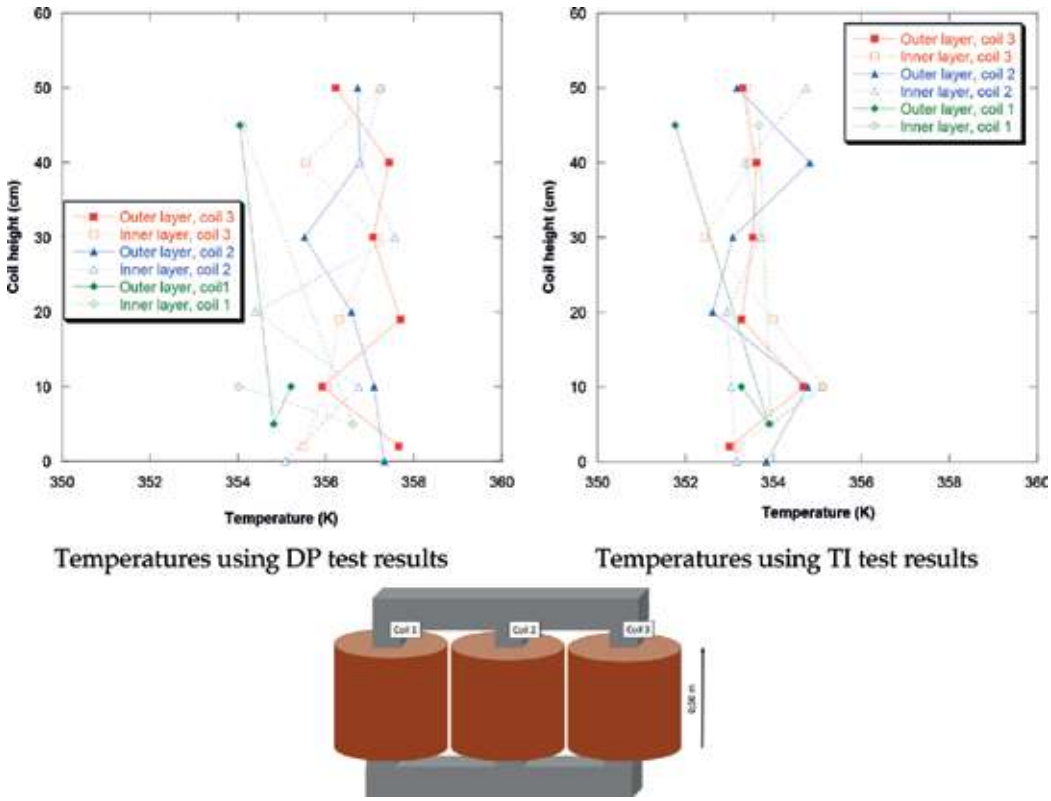


**Figure 5.** Temperature distribution using different test results.

3 transformers of 254 MVA, 420/13.8 kV; 3 transformers of 250 MVA, 400/121 kV; 15 transformers of 250 MVA, 420/15.75 kV; 1 transformer of 200 MVA, 231/121 kV; 1 transformer of 200 MVA, 230/121 kV). These machines were studied through post-mortem analysis carried out for several years. The study of these devices analysed the values of DP, tensile strength, as well as, information from running history of the transformers (DGA and 2-FAL). They observed that transformers with similar level of ageing are defined rather by manufacturer and construction than by the loading regime, which has less influence. Moreover, they found that the correlation of DP and tensile strength corresponds with specific transformers groups. Nevertheless, there are some transformers whose DP values range far less in comparison with tensile strength, which might indicate a higher accuracy of this variable to distinguish paper degradation. On the other hand, the DGA tests showed that they are essential for ageing evaluation because they can provide information about running problems (ineffective cooling, leaking, higher gases development).

Even though the number of post-mortem studies has increased during the last years, there is not enough data to develop an accurate end-of-life failure model [53]. For this reason, it is essential to go on with the study of scrapped transformers to obtain more information about the most representative variables of the transformer ageing. Initially, the state of insulating

solid was measured through DP; however, later assessments have demonstrated that in some cases the tensile or index strength can be more sensitive to differentiate the level of paper ageing.

## 4. Accelerated thermal ageing in laboratory

Currently, most of oil-filled power transformers use as dielectric liquid, mineral oil, which is obtained from the middle range of petroleum-derived distillates. This fluid has shown suitable thermal and dielectric properties to carry out its functions as cooling and insulation. Nevertheless, it possess two important drawbacks, the first one is its low flash point and the second one is its low biodegradability, which can represent a high risk if spills or leaks would take place. This situation has led to the development of alternative transformer oils such as silicones, synthetic and natural esters. In particular, vegetal oils have drawn most attention and research [54].

During last two decades, the study of transformer oil-based nanofluids has become of great interest due to their prospective properties as cooling and dielectric liquids [55]. For example, Li et al. [56] prepared a nanofluid dispersing $Fe_3O_4$ nanoparticles in a vegetal oil and using oleic acid as surfactant. These authors compared the behaviour of this nanofluid with the pure oil measuring power frequency breakdown voltage and relative permittivity. The breakdown voltage of nanofluids has also been measured by Thabet et al. [57], nevertheless, in that work the insulation liquid was based on mineral oil and different nanoparticles (ZnO, MgO, $Al_2O_3$, $TiO_2$, $SiO_2$, $LiTaO_3$, $Fe_3O_4$, graphite), as well as multi-nanoparticles collections, which were combination of two of the nanoparticles studied previously. These dielectric properties and other such as dissipation factor, dielectric constant or electrical resistivity have been studied by many authors [58, 59], analysing the effect of different nanoparticles ($CaCu_3Ti_4O_{12}$, $TiO_2$, $Al_2O_3$). The streamers in transformer oils under lightning impulse voltage have been observed, too by authors such as et al. [60, 61], Cavallini et al. [62], Sima et al. [63] and Liu et al. [64] or simulated as Velasco et al. [65]. The last ones not only evaluated dielectric properties, but also thermal conductivity of nanofluids obtained through the dispersion of AlN nanoparticles. The effect of nanoparticles on heat transfer characteristics was also studied by Guan et al. [64] and Morega et al. [66]. The last ones additionally evaluated the specific magnetisation of other nanofluid to open new venues in optimising conventional electrotechnic constructions or to design novel devices [67]. Creeping discharge and flashover characteristics of the oil/pressboard interface under AC and impulse voltages was studied by Lv et al. for a nanofluid based on $TiO_2$ nanoparticles [68], obtaining an increase of the shallow trap density and a lower shallow trap energy level of oil-impregnated pressboard which can improve the creeping flashover strength of oil/pressboard interface.

When it is desired, the replacement of one usual component of the insulation system, as in the case of alternative dielectric oils, it is important to study the stability of the new system and compare it with the system widely used in power transformers (mineral oil/Kraft paper). For this reason, many accelerated thermal ageing studies have been carried out in the laboratory.

The first laboratory tests of accelerated thermal ageing focused on the behaviour of paper in mineral oil. For instance, Shroff and Stannett [69] aged Kraft paper and thermal upgraded

paper in mineral oil at four temperatures. The results of their study showed that there is a direct relationship between the DP and the moisture in paper and the concentration of furanic compounds. These authors also proposed as paper end-of-life criteria a DP = 200 and a tensile strength equal to 50% of its original value. Other authors such as Yoshida et al. [70] also implemented ageing tests using mineral oil as dielectric liquid at different temperatures (120, 140 and 160°C). In this case, they analysed the behaviour of Kraft and pressboard paper, obtaining as main conclusions the existence of a relationship between the concentration of $CO/CO_2$ and the evolution of the DP and the tensile strength. On the other hand, Hill et al. [71] studied the tensile strength of the paper, the DP and the concentration of furans in ageing tests of Kraft paper in mineral oil at different temperatures, obtaining as a result the existence of a relationship between furans, DP and tensile strength. In addition, these authors proposed a paper degradation model based on the tensile strength. Emsley et al. [49, 72, 73] also proposed a degradation model, although this was based on the relationship between tensile strength and DP for Kraft paper and cotton paper aged in mineral oil. Since last decade, ageing studies have begun to take into account alternative oils. For example, Mcshane et al. [74–77] evaluated DP, tensile strength, moisture in oil and paper, as well as furan content when Kraft and thermal upgraded paper were aged in a mineral oil and in a natural ester. The results of their tests showed that the degradation rate experienced by the paper during thermal ageing at different temperatures was lower in the natural ester. These authors proposed the protective mechanisms developed by the ester that might explain the minor degradation suffered by the paper in the alternative oil. Other authors such as Shim et al. [78] also obtained greater thermal stability in the natural ester compared to mineral oil by the measure of the tensile strength for Kraft and diamond dotted paper. Similar results were presented by Azis [18], who analysed paper degradation using tensile strength, breakdown voltage, dynamic viscosity, acidity and concentration of low and high molecular weight acids in the oil. The measure of the concentration of low molecular weight acids (LMA) allowed observing that these tend to remain in the natural ester, which might explain the best behaviour of the Kraft paper during the ageing, in addition to the hydrolytic protection made by the oil. The behaviour of thermal upgraded and Kraft paper in mineral oil and in natural ester was also evaluated by Abdelmalik et al. [79], who studied the tensile and dielectric strength of the paper. Their results also showed that oils based on natural esters protect better against the degradation than mineral oil. Saruhashi et al. [80] studied for aramid paper tensile index, as well as breakdown voltage, acidity, colour and kinematic viscosity of the oil. In their study, they carry out ageing tests at two temperatures in three different oils (silicone, natural ester and synthetic ester). They found a slight variation of the tensile index in the three oils. The degradation of Kraft paper aged in a natural ester was also evaluated through the tensile strength by Widyanugraha et al. [35], who also measured the gases generated during ageing at two different temperatures. The tensile strength suffered initially a decrease and subsequently an increase during thermal ageing. It was assumed that this behaviour was due to the transesterification process. The tensile strength of the paper, besides other characteristic properties of the oil degradation, was analysed by Madavan and Balaraman [81], who obtained that the paper aged in oils based on natural esters had a lower degradation compared to Kraft paper immersed in mineral oil. In recent years, different authors have tried to find additional methods to study paper degradation when this is aged thermally in laboratory. For example, Arroyo et al. [16, 82, 83] related the paper's tensile index

with an indirect measure of its degradation, such as the concentration of methanol and ethanol in the oil. They also proposed three degradation models for Kraft and thermal upgraded paper. Each model was based on a different property (tensile index, DP, methanol and ethanol concentration in oil). The proposed models were obtained from the ageing data of the paper in mineral oil at three temperatures. Finally, they evaluated the influence that the concentration of stabilisation additives can have on the thermal stability of thermal upgraded paper. The results showed that the higher this concentration is, the better the paper stability, although it changes whereas the degradation of the paper takes place. Another alternative model based on a damage parameter D to predict the remaining life of Kraft paper has been defined by the authors of this chapter. This parameter can be based on any mechanical property (strength, Young's modulus, yield stress, energy consumed, strain under ultimate strength, etc.) obtained of the tensile test (Annex). This damage parameter can be used to evaluate additional mechanical properties which have not been used previously in a new proposed mathematical model based on temperature and time. The damage parameter D is defined as:

$$D = 1 - \frac{\mathrm{Pr}operty_i}{\mathrm{Pr}operty_0} \tag{14}$$

where $\mathrm{Property_i}$ is the value of a macroscopic property (strength, yield stress…) in any situation of time (t) and temperature (T) and $\mathrm{Property_0}$ is the value of the same property of the original paper not subject to ageing. It can be observed that the damage parameter D can only take values between 1 and 0. The value 1 represents an insulation paper which has lost all its mechanical resistance whereas the value 0 corresponds to new insulation solid.

The evolution of D with t for different ageing conditions can be obtained through the mathematical model:

$$D = D_{\max} \cdot \left(1 - \exp(-a \cdot t)\right) \tag{15}$$

where the parameter $a$ is a rate constant that indicates the effect of oil temperature in which the paper is aged, on the increase of the damage, D, suffered by paper along the time; $\mathrm{D_{max}}$ is the maximum value reached experimentally by the damage; t is the time (h). The parameter $a$ can be expressed by means of Arrhenius equation as a function of the ageing temperature.

Finally, the analysed Property can be expressed as a function of the time and the temperature:

$$\mathrm{Pr}operty_i = \mathrm{Pr}operty_0 \cdot \left(1 - D_{\max}\left(1 - \exp(-a \cdot t)\right)\right) \tag{16}$$

This mathematical model, which determines the damage suffered by paper aged in an oil, is a simplified macroscopic model that takes into account the general damage experienced by the paper.

On the other hand, Pei et al. [40] tried to relate the degradation suffered by pressboard aged at 130°C in mineral oil, through the tensile strength, with the microscopic appearance of its surface, using for this analysis the scanning electron microscope (SEM). The results of his study showed that the pressboard degradation is accompanied by changes in the superficial structure.

All these works have found that the thermal degradation of the paper can be evaluated using mechanical parameters such as tensile strength or TI. However, until now, other parameters obtained from the tensile test have not been considered, such as Young's modulus, strain, elastic limit, and so on, which might offer a more accurate view of the loss of mechanical strength by the paper. On the other hand, the use of SEM for materials aged in mineral oil seems to provide additional information on the relationship between the shape of cellulose fibres and their mechanical strength. Regarding the behaviour of cellulosic material in alternative oils, although several ageing studies have been carried out, degradation models based on mechanical properties have not been proposed. These mathematical models will allow to estimate the remaining life of dielectric papers as a function of temperature and time. The development of these degradation models requires analyse which mechanical properties can offer a better description of the loss of mechanical resistance. Additionally, the utilisation of SEM can help to detect when the behaviour of the solid insulation becomes fragile increasing the failure probability.

## 5. Conclusions

There are several techniques that can be used to evaluate insulation paper degradation; however, the two most used in post-mortem analysis have been the degree of polymerisation (DP) and tensile strength. One of these post-mortem studies obtained as conclusions that the experimental results give a variation of DP values ranged from less than 5% to more than 40%, which indicates the results variability of this technique. On the other hand, all these end-of-life studies have shown the necessity of complement DP profile of the transformer with chemical markers such as furans, methanol, dissolved gases, and so on. Because of these by-products derived from paper and oil degradation can detect running problems (ineffective cooling, leaking, higher gases development), which might be useful to prevent future failures.

Data obtained from post-mortem analysis should be complemented with tests carried out in the laboratory. These tests have provided useful correlations between oil markers and paper degradation in a short period of time and make possible establish comparisons between mineral and alternative oils in accelerated thermal ageing tests. The measure of paper mechanical strength has been limited until now at the estimation of tensile strength and tensile index, in spite of the fact that additional parameters (Young's modulus, yield stress, energy consumed, etc.) obtained in the tensile test can provide more accurate analysis of the loss of mechanical properties. For instance, the energy consumed might be more convenient to follow the changes of mechanical properties of insulation paper since in its definition the other two parameters (strength and strain) are used. Data obtained from stress–strain curve should be complemented with the information provided by techniques as SEM, which could detect behaviour changes in the paper related with type of failure. This could be carried out using texture analysis, which might provide information about thermal degradation of paper using the information provided by the statistical variation of pixels grey level intensities in an image.

The results obtained from PD measurements have shown that solid ageing has little influence; nonetheless, oil ageing has great influence on PD characteristics over liquid/solid interface.

Additionally, it has been observed by different authors that thermal ageing has significant impacts on surface morphology of insulation solid, which influences the developing process of PD. Therefore, it is necessary to analyse the effect of increasing the ageing time on the reduction in partial discharge magnitude for application in on-field practical tests. This analysis needs to take into account not only mineral oil, but also new insulating oils (natural and synthetic esters) which have proved to be a viable substitute. Moreover, there is an incomplete understanding of the oil/solid interface yet, as well as a lack of standardisation in PD measurements for diagnostic purposes of the HV components in which insulating liquids are employed.

Finally, the use of nanoparticles in power transformers has opened new ways in optimising their design because different studies have obtained an enhancement in dielectric properties (breakdown strength, partial discharge inception voltage, creeping flashover strength of oil-impregnated papers…) and thermal conductivity without significant change in the viscosity.

## Acknowledgements

The authors are grateful for the funding received to carry out this work from the State Scientific and Technical Research and Innovation Plan under the DPI2013-43897-P grant agreement, financed by the Government of Spain.

## A. Annex

Having the data of Force (kN) and Displacement (mm), the following sequence of MATLAB, allows to obtain the different mechanical parameters of the material, which will be used in the mathematical model based on damage parameter defined by the authors of this chapter.

1-Define the constants: Initial length, Gramage, $A_0$, a…

2-Load from a file with the results of Force (kN), Position (mm).

3-Matlab performs the calculations, represents the stress–strain graph and shows a summary table with the mechanical parameters.

```
clc

clear.

% Define constants.

a0 = 3;g = 0.15783222;a = 0.015;l = 180;

nm = 4;

% Open files Data.

fileID = fopen('data.txt');
```

```
D = textscan(fileID,'%f %f');
fclose(fileID);
% Preparate Data.
F_data = D{1};
pos_data = D{2};
F = zeros((length(F_data)-1)/nm,1);
pos = zeros((length(F_data)-1)/nm,1);
for i = 1:((length(F_data)-1)/nm).
F(i) = 0.25*(F_data(nm*(i-1) + 2) + F_data(nm*(i-1) + 3) + F_data(nm*(i-1) + 4) + F_data(nm*(i-1) + 5));
pos(i) = 0.25*(pos_data(nm*(i-1) + 2) + pos_data(nm*(i-1) + 3) + pos_data(nm*(i-1) + 4) + pos_data(nm*(i-1) + 5));
end
pos0 = pos_data(1);
eps = (pos-pos0)./l;
sigma = F./a0;
% Calculate.
n = 0;
while true.
n = n + 1;
pdte1 = (sigma(n + 1)-sigma(n))/(eps(n + 1)-eps(n));
pdte2 = (sigma(n + 2)-sigma(n + 1))/(eps(n + 2)-eps(n + 1));
pdte3 = (sigma(n + 3)-sigma(n + 2))/(eps(n + 3)-eps(n + 2));
if (abs((pdte1-pdte2)/pdte1) < 3e-2) && (abs((pdte2-pdte3)/pdte1) < 3e-2).
pdte = pdte1;
break.
end
if n + 3==length(sigma).
break.
end
```

```
end
rect1 = pdte.*eps;
sigmar = sigma(length(sigma));
epsd = eps(length(sigma));
rect2 = pdte.*(eps-0.002);
sigmay = 0;
for i = 1:length(sigma).
if abs((sigma(i)-rect2(i))/sigma(i)) < 1e-2.
sigmay = sigma(i);
i_corte = i;
break.
end
end
Am = 0;
tem = zeros(length(sigma)-1,1);
for i = 1:length(sigma)-1.
tem(i) = (sigma(i + 1) + sigma(i))*0.5*(eps(i + 1)-eps(i));
Am = Am+tem(i);
end
ts = max(F)/a/g/1000;
% Screen size.
ss = get(0,'screensize');
width = ss(3);
height = ss(4);
% Graphic.
f = figure;
vert = ss(4)/1.5;
horz = ss(3)/1.5;
set(f,'Position',[(width/2)-horz/2, (height/2)-vert/2, horz, vert]);
plot(eps,sigma,'b').
```

```
hold on.

axis([0 epsd 0 max(sigma)]).

plot(eps,rect1,'–r').

plot(eps,rect2,'–m').

plot([eps(1) eps(i_corte)],[sigmay sigmay],':k').

plot([eps(i_corte) eps(i_corte)],[0 sigmay],':k').

% Resumen Data.

dat = {pdte,sigmay,sigmar,epsd,Am,ts};

t = uitable(f);

t.ColumnName = {'Elasticity Modulus','Elastic limit','Maximun Tension','Deformation under maximum tension','Absorbed Energy','Tensile Index'};

t.Data = dat;

t.Position = [vert/2 vert-50 t.Extent(3) t.Extent(4)];
```

## Author details

Cristina Fernández-Diego[1]*, Inmaculada Fernández[1], Felix Ortiz[1], Isidro Carrascal[2], Carlos Renedo[1] and Fernando Delgado[1]

*Address all correspondence to: fdezdiegoc@unican.es

1 Electrical and Energy Engineering Department, School of Industrial and Telecomunications Engineering, University of Cantabria, Santander, Cantabria, Spain

2 LADICIM (Laboratory of Materials Science and Engineering), School of Civil Engineering, University of Cantabria, Santander, Cantabria, Spain

## References

[1] Karsai K, Kerényi D, Kiss LL. Large Power Transformers. Amsterdam; New York: Elsevier; New York, NY, U.S.A.: Distribution for the U.S.A. and Canada, Elsevier Science Pub. Co., 1987. Studies in electrical and electronic engineering, 25. 614 p. ISBN: 0444995110 9780444995117 0444417133 9780444417138

[2] Siada AA. Power Transformer Condition Monitoring and Diagnosis. Chapter 2: Power Transformer Condition Monitoring and Diagnosis: concepts and Challeges. Albarracin R, Robles G, Ardila-Rey JA, Cavallini A, Passaglia Pagination R: c. 300pp. 2018. ISBN: 978-1-78561-254-1

[3] Li J, Si W, Yao X, Li Y. Partial discharge characteristics over differently aged oil/pressboard interfaces. IEEE Transactions on Dielectrics and Electrical Insulation. 2009;**16**(6):1640-1647. DOI: 10.1109/TDEI.2009.5361584

[4] Dai J, Wang ZD, Jarman P. Creepage discharge on insulation barriers in aged power transformers. IEEE Transactions on Dielectrics and Electrical Insulation. 2010;**17**:1327-1335. DOI: 10.1109/TDEI.2010.5539705

[5] Xu J, Wang W, Li C, Wang X, Zhou B, Li Y, Wang T, Experimental research on the evolution of creepage discharge in aged pressboard. Annual Report Conference on Electrical Insulation and Dielectric Phenomena (CEIDP). 2011;484-488. DOI: 10.1109/CEIDP.2011.6232700

[6] Sarathi R, Yadav KS, Swarna M. Understanding the surface discharge characteristics of thermally aged copper sulphide diffused oil impregnated pressboard material. IEEE Transactions on Dielectrics and Electrical Insulation. 2015;**22**:2513-2521. DOI: 10.1109/TDEI.2015.004905

[7] Niasar MG, Taylor N, Janus P, Wang X, Edin H, Kiiza RC. Partial discharges in a cavity embedded in oil-impregnated paper: Effect of electrical and thermal aging. IEEE Transactions on Dielectrics and Electrical Insulation. 2015;**22**:1071-1079. DOI: 10.1109/TDEI.2015.7076808

[8] Yadav KS, Sarathi R. Understanding the dielectric properties of pressboard material thermally aged in dibenzyl disulphide (DBDS) included transformer oil. IEEE Transactions on Dielectrics and Electrical Insulation. 2017;**24**:647-655. DOI: 10.1109/TDEI.2016.006083

[9] Qi B, Zhao X, Li C, Wu H,Transient electric field characteristics in oil-pressboard composite insulation under voltage polarity reversal. IEEE Transactions on Dielectrics and Electrical Insulation. 2015;**22**(4):2148-2155. DOI: 10.1109/TDEI.2015.004347

[10] Sima W, Sun P, Yang Q, Yuan T, Lu C, Yang M. Study on the accumulative effect of repeated lightning impulses on insulation characteristics of transformer oil impregnated paper. IEEE Transactions on Dielectrics and Electrical Insulation. 2014;**21**:1933-1941. DOI: 10.1109/TDEI.2014.004298

[11] Cui Y, Zhu L, Ji S, Cao P, Zhang F. Partial discharge development in needle-plane configuration of oil-paper insulation under AC voltage. IEEE Transactions on Dielectrics and Electrical Insulation. 2017;**24**:2469-2476. DOI: 10.1109/TDEI.2017.006270

[12] Azcarraga CG, Cavallini A, Piovan U, A comparison of the voltage withstand properties of ester and mineral oils. IEEE Electrical Insulation Magazine. 2014;**30**(5):6-14. DOI: 10.1109/MEI.2014.6882595

[13] Geißler DH, Short-Circuit Withstand Capability of Power Transformers

[14] Siemens, Power Engineering Guide Edition 7.0

[15] VITO, LOT 2: Distribution and power transformers Tasks 1–7. 2011

[16] Arroyo OH, Fofana I, Jalbert J, Ryadi M. Relationships between methanol marker and mechanical performance of electrical insulation papers for power transformers under

accelerated thermal aging. IEEE Transactions on Dielectrics and Electrical Insulation. 2015;**22**(6):3625-3632. DOI: 10.1109/TDEI.2015.005386

[17] Koch M, Tenbohlen S, Giselbrecht D, Homagk C, Leibfried T. Onsite, online and post mortem insulation diagnostics at power transformers. CIGRE 2007. Brugge, Belgium, 2007

[18] Azis N. Ageing assessment of insulation paper with consideration of in service ageing and natural ester application [Thesis] UK: The University of Manchester; 2012

[19] Zhang GJ, Wei JL, Dong M, Mu HB, Li HJ, Zhang YB, Li YM, Yan Z. Lifetime monitoring and estimation strategy for large power transformer. In: International Conference on Condition Monitoring and Diagnosis; 21–24 April 2008; Beijing, China. p. 1-6

[20] Morais DR, Bencz E, Rolim JG Condition assessment of power transformers through the integration of historical and on-line data in a multi-agent system. Journal of Control, Automation and Electrical Systems. 2014;**25**:93-102. DOI: 10.1007/s40313-013-0069-3

[21] Murugan R, Ramasamy R. Failure analysis of power transformer for effective maintenance planning in electric utilities. Engineering Failure Analysis. 2015;**55**:182-192. DOI: 10.1016/j.engfailanal.2015.06.002

[22] Heisler A, Banzer A. Zustandsbeurteilung von Transformatoren mit Furfurol-Bestimmung. Das Magazin für die Energiewirtschaft. 2003:58-59

[23] Chendong X. Monitoring paper insulation ageing by measuring furfural contents in oil. In: EPRI, 7th Int. Symp. High Voltage Eng.; 26–30 August; Dresden, Germany; 1991:139-142

[24] De Pablo A. Interpretation of Furanic Compounds Analysis—Degradation Models. In: CIGRE WG D1.01.03. 1997; Paris. France

[25] Stebbins RD, Myers DS, Shkolnik AB. Furanic compounds in dielectric liquid samples: Review and update of diagnostic interpretation and estimation of insualtion ageing. In: Proceedings of the 7th International Conference on Properties and Applications of Dielectric Materials; 1–5 June 2003. p. 921-926

[26] Shkolnik AB, Rasor RT, Myers SD. Statistical insights into furan interpretation using a large dielectric fluid testing database. In: Transmission and Distribution Conference and Exposition (T&D) IEEE PES; 7–10; Orlando. 2012. p. 1-8

[27] Mtetwa NS. Accuracy of furan analysis in estimating the degree of polymerization in power transformers [thesis]. M. Sc. (Eng.) University of the Witwatersrand; 2008

[28] Leibfried T, Jaya M, Majer N, Schafer M, Stach M, Voss S. Postmortem investigation of power transformers—profile of degree of polymerization and correlation with furan concentration in the oil. IEEE Transactions on Power Delivery. 2013;**28**(2):886-893. DOI: 10.1109/TPWRD.2013.2245152

[29] Lütke H, Höhleim I, Kachler AJ. Transformer aging research on furanic compounds dissolved in insulating oil. In: CIGRE; París, Francia; 2002. p. 15-302

[30] Dong M, Yan Z, Zhang GJ. Comprehensive diagnostic and aging assessment method of solid insulation in transformer. In: Annual report conference on electrical insulation and dielectric phenomena, Albuquerque USA; 2003. 19-22 p. 137-140

[31] Li E, Song B. Transformer health status evaluation model based on multi-feature factors. In: International Conference on Power System Technology (POWERCON 2014); 20–22 October 2014; Chengdu, China. p. 1417-1422

[32] Lin C, Bide Z, Yuchun Y. The aging diagnosis of solid insulation for oil-immersed power transformers and its remaining life prediction. In: Power and Energy Engineering Conference (APPEEC), 2010 Asia-Pacific; 28-31 march 2010; Chengdu; China. 2010. p. 1-3

[33] Levchik S, Scheirs J, Camino G, Tumiatti W, Avidano M. Depolymerization processes in the thermal degradation of cellulosic paper insulation in electrical transformers. Polymer Degradation and Stability. 1998;**61**:507-511. DOI: 10.1016/S0141-3910(97)00249-8

[34] Teymouri A, Vahidi B. $CO_2$/CO concentration ratio: A complementary method for determining the degree of polymerization of power transformer paper insulation. IEEE Electrical Insulation Magazine. 2017;**33**(1):24-30. DOI: 10.1109/MEI.2017.7804313

[35] Widyanugraha T, Rachmad R. Wendhy, Suwarno. DGA and tensile strength test on accelerated thermal aging of ester oil and Kraft paper. In: 5th International Conference on Electrical Engineering and Informatics; August. Vol. 2015. Indonesia: Bali; 2015. pp. 177-180

[36] Schaut A, Autru S, Eeckhoudt S. Applicability of methanol as new marker for paper degradation in power transformers. IEEE Transactions on Dielectrics and Electrical Insulation. 2011;**18**(2):533-540. DOI: 10.1109/TDEI.2011.5739459

[37] Thermo Nicolet Corporation. Introduction to Fourier Transform Infrared Spectrometry, [Internet]. 2001. Available from: https://www.niu.edu/analyticallab/_pdf/ftir/FTIRintro.pdf

[38] Abi Munajad A, Subroto C, Suwarno. Fourier transform infrared spectroscopy (FTIR) analysis of transformer insulation paper in natural ester. In: International Conference on High Voltage Engineering and Power Systems (ICHVEPS); 2-5 October 2017; Sanur, Indonesia. p. 446-450

[39] Liao R, Tang C, Yang L. Stanislaw G. Thermal aging micro-scale analysis of power transformer pressboard. IEEE Transactions on Dielectrics and Electrical Insulation. 2008; **15**(5):1281-1287. DOI: 10.1109/TDEI.2008.4656235

[40] Pei C, Shengchang J, Lingyu Z, Yanjie C, Shihua Z, Yun L, Huisheng Y, Ping P. The effect of thermal aging on surface structure and mechanical strength of oil-impregnated pressboard. International Conference on Condition Monitoring and Diagnosis (CMD); 25–28 September 2016; Xi'an; China. 2016:1000-1003

[41] Yoshida M, Uchida K, Kato M, Konishi Y. New diagnosis method of aging degradation for insulating paper in power transformers by measuring the refractive index of cellulose fibers. In: 2012 IEEE International Conference on Condition Monitoring and Diagnosis (CMD) International Conference; 23–27 September 2012; Bali, Indonesia; p. 56-59

[42] IEC 60450:2004 Measurement of the average viscometric degree of polymerization of new and aged electrical papers

[43] Roylance D. Stress-strain curves. Department of Materials Science and Engineering, Massachusetts Institute of Technology, Cambridge, MA 02139. 2001. Available froom: https://ocw.mit.edu/courses/materials-science-and-engineering/3-11-mechanics-of-materials-fall-1999/modules/MIT3_11F99_ss.pdf

[44] Martin D, Marks J, Saha T. Survey of Australian power transformer failures and retirements. IEEE Electrical Insulation Magazine. 2017;**33**(5):16-22. DOI: 10.1109/MEI.2017.8014387

[45] Sanchez J, Banovic M. A general overview of power transformer diagnosis. Transformers Magazine. 2013:22-26

[46] Binder W. Trends in power transformer failure analysis. Transformers Magazine. 2014;**1**(1): 30-33

[47] Martins MA, Fialho M, Martins J, Soares M, Castro MC, Lopes R, Campelo H. Power transformer end-of-life assessment—Pracana case study. IEEE Electrical Insulation Magazine. 2011; **27**(6):15-26. DOI: 10.1109/MEI.2011.6059980

[48] Jalbert J, Lessard MC. Cellulose chemical markers relationship with insulating paper post-mortem investigations. IEEE Transactions on Dielectrics and Electrical Insulation. 2015; **22**(6):3350-3354. DOI: 10.1109/TDEI.2015.005295

[49] Emsley M, Heywood RJ, Ali M, Xiao X. Degradation of cellulosic insulation in power transformers. Part4: Effects of ageing on the tensile strength of paper. IEEE Proceedings - Science Measurement and Technology. 2000;**147**(6):285-290. DOI: 10.1049/ip-smt:20000644

[50] Carcedo J, Fernández I, Ortiz A, Carrascal IA, Delgado F, Ortiz F, Arroyo A. Post-mortem estimation of temperature distribution on a power transformer: Physicochemical and mechanical approaches. Applied Thermal Engineering. 2014;**70**(1):935-943. DOI: 10.1016/j.applthermaleng.2014.06.003

[51] Azis N, Liu Q, Wang ZD. Ageing assessment of transformer paper insulation through post mortem analysis. IEEE Transactions on Dielectrics and Electrical Insulation. 2014;**21**(2): 845-853. DOI: 10.1109/TDEI.2013.004118

[52] Müllerová E, Hrůza J, Velek J, Ullman I, Stříska F. Life cycle management of power transformers: Results and discussion of case studies. IEEE Transactions on Dielectrics and Electrical Insulation. 2015;**22**(4):2379-2389. DOI: 10.1109/TDEI.2015.005025

[53] Awadallah SKE, Milanović JV, Jarman PN. Quantification of uncertainty in end-of-life failure models of power transformers for transmission systems reliability studies. IEEE Transactions on Power Systems. 2016;**31**(5):4047-4056. DOI: 10.1109/TPWRS.2015.2497969

[54] Mahanta DK, Laskar S. Electrical insulating liquid: A review. Journal of Advanced Dielectrics. 2017;**7**(4):1-9. DOI: 10.1142/S2010135X17300018

[55] Primo VA, García B, Albarracín R. Improvement of transformer liquid insulation using nanodielectric fluids; a review. Electrical Insulation Magazine. 2018 in press

[56] Li J, Zhang Z, Zou P, Grzybowski S, Zahn M. Preparation of a vegetable oil-based nanofluid and investigation of its breakdown and dielectric properties. IEEE Electrical Insulation Magazine. 2012;**28**(5):43-50. DOI: 10.1109/MEI.2012.6268441

[57] Thabet A, Allam M, Shaaban SA. Investigation on enhancing breakdown voltages of transformer oil nanofluids using multi-nanoparticles technique. IET Generation, Transmission & Distribution. 2018;**12**(5):1171-1176. DOI: 10.1049/iet-gtd.2017.1183

[58] Arun Ram Prasath RT, Roy NK, Mahato SN, Thomas P. Mineral oil based high permittivity CaCu3Ti4O12 (CCTO) nanofluids for power transformer application. IEEE Transactions on Dielectrics and Electrical Insulation. 2017;**24**(4):2344-2353. DOI: 10.1109/TDEI.2017.006096

[59] Emara MM, Mansour DA, Azmy AM. Mitigating the impact of aging byproducts in transformer oil using TiO2 nanofillers. IEEE Transactions on Dielectrics and Electrical Insulation. 2017;**24**(6):3471-3480. DOI: 10.1109/TDEI.2017.006586

[60] Lv Y, Ge Y, Du Q, Sun Q, Shan B, Huang M, Li C, Qi B, Yuan J. Fractal analysis of positive streamer patterns in transformer oil-based TiO2 nanofluid. IEEE Transactions on Plasma Science. 2017;**45**(7):1704-1709. DOI: 10.1109/TPS.2017.2705167

[61] Lv Y, Ge Y, Li C, Wang Q, Zhou Y, Qi B, Yi K, Chen X, Yuan J. Effect of TiO2 nanoparticles on streamer propagation in transformer oil under lightning impulse voltage. IEEE Transactions on Dielectrics and Electrical Insulation. 2016;**23**(4):2110-2115. DOI: 10.1109/TDEI.2016.005730

[62] Cavallini A, Karthik R, Negri F. The effect of magnetite, graphene oxide and silicone oxide nanoparticles on dielectric withstand characteristics of mineral oil. IEEE Transactions on Dielectrics and Electrical Insulation. 2015;**22**(5):2592-2600. DOI: 10.1109/TDEI.2015.005016

[63] Sima W, Shi J, Yang Q, Huang S, Cao X. Effects of conductivity and permittivity of nanoparticle on transformer oil insulation performance: Experiment and theory. IEEE Transactions on Dielectrics and Electrical Insulation. 2015;**22**(1):380-390. DOI: 10.1109/TDEI.2014.004277

[64] Liu D, Zhou Y, Yang Y, Zhang L, Jin F. Characterization of high performance AIN nanoparticle-based transformer oil nanofluids. IEEE Transactions on Dielectrics and Electrical Insulation. 2016;**23**(5):2757-2767. DOI: 10.1109/TDEI.2016.7736835

[65] Velasco J, Frascella R, Albarracín R, Burgos JC, Dong M, Ren M, Yang L. Comparison of positive streamers in liquid dielectrics with and without nanoparticles simulated with finite-element software. Energies. 2018;**11**(2):361. DOI: 10.3390/en11020361

[66] Pîslaru–Dănescu L, Morega AM, Morega M, Stoica V, Marinică OM, Nouraş F, Păduraru N, Borbáth I, Borbáth T. Prototyping a ferrofluid-cooled transformer. IEEE Transactions on Industry Applications. 2013;**49**(3):1289-1298. DOI: 10.1109/TIA.2013.2252872

[67] Pîslaru-Dănescu L, Morega AM, Telipan G, Morega M, Dumitru JB, Marinescu V. Magnetic nanofluid applications in electrical engineering. IEEE Transactions on Magnetics. 2013;**49**(11):5489-5497. DOI: 10.1109/TMAG.2013.2271607

[68] Lv YZ, Zhou Y, Li CR, Ma KB, Wang Q, Wang W, Zhang SN, Jin ZY. Nanoparticle effects on creeping flashover characteristics of oil/pressboard interface. IEEE Transactions on Dielectrics and Electrical Insulation. 2014;**21**(2):556-562. DOI: 10.1109/TDEI.2013.004151

[69] Shroff DH, Stannett AW. A review of paper aging in power transformers. IEEE Proceedings on Generation, Transmission and Distribution. 1985;**132**(6):312-319. DOI: 10.1049/ip-c:19850052

[70] Yoshida H, Ishioka Y, Suzuki T, Yanari T, Teranishi T. Degradation of insulating materials of transformers. IEEE Transactions on Electrical Insulation. 1987;**22**(6):795-800. DOI: 10.1109/TEI.1987.298942

[71] Hill DJT, Le TT, Darveniza M, Saha T. A study of degradation of cellulosic insulation materials in a power transformer part 2: Tensile strength of cellulose insulation paper. Polymer Degradation and Stability. 1995;**49**(3):429-435. DOI: 10.1016/0141-3910(95)00100-Z

[72] Emsley AM, Heywood RJ, Ali M, Eley CM. On the kinetics of degradation of cellulose. Cellulose. 1997;**4**(1):1-5. DOI: 10.1023/A:1018408515574

[73] Gasser HP, Huser J, Krause C, Dahinden EAM. Determining the ageing parameters of cellulosic insulation in a transformer. In: High Voltage Engineering, 1999. Eleventh International Symposium on (Conf. Publ. No. 467). Vol. 23-27. August; London, UK: IEEE; 2002. pp. 1-5

[74] Mcshane CP, Rapp KJ, Corkran JL, Gauger GA, Luksich J. Aging of paper insulation in natural ester dielectric fluid. In: Transmission and Distribution Conference and Exposition, 2001 IEEE/PES; 2–2 November. Vol. 2001. Atlanta GA, USA: IEEE; 2002. pp. 675-679

[75] Rapp KJ, Luksich J. Reaction rates of paper aged in natural ester dielectric fluid. In: Conference on Electrical Insulation and Dielectric Phenomena, 2001 Annual Report. Vol. 14-17. Canada: October;.Kitchener, Ontario; 2001. pp. 209-212

[76] Mcshane CP, Rapp KJ, Corkran JL, Gauger GA, Luksich J. Aging of Kraft paper in natural ester dielectric fluid. In: IEEE 14th International Conference on Dielectric Liquids, 2002. ICDL 2002. Proceedings of 2002. Vol. 12-21. Austria: July; Graz; 2002. pp. 173-177

[77] Mcshane CP, Corkran JL, Rapp KJ, Luksich J. Aging of paper insulation retrofilled with natural ester dielectric fluid. In: Conference on Electrical Insulation and Dielectric Phenomena, 2003 Annual Report. Vol. 19-22. USA: October; Albuquerque; 2004. pp. 124-127

[78] Shim MS, Jung JI, An JS, Choi SH, Seo YJ, Huh CS. Tensile strength of electrical insulating paper in natural ester and mineral oil. In: 4th International Conference of Power Engineering and Optimization (peoco2010). Vol. 23-26. Malaysia: June; Shah Alam; 2010. pp. 563-565

[79] Abdelmalik AA, Fothergill JC, Dodd SJ. Aging of Kraft paper insulation in natural ester dielectric fluid. In: IEEE International Conference on Solid Dielectrics (ICSD 2013); 30 June – 4 July; Bologna, Italy: IEEE 2013. p. 541-544

[80] Saruhashi D, Bin X, Zhiyuan I, Yanabu S. Thermal degradation phenomena of flame resistance insulating paper and oils. IEEE Transactions on Dielectrics and Electrical Insulation. 2013;**20**(1):122-127. DOI: 10.1109/TDEI.2013.6451349

[81] Madavan R, Balaraman S. Failure analysis of transformer liquid - solid insulation system under selective environmental conditions using weibull statistics method. Engineering Failure Analysis. 2016;**65**:26-38. DOI: 10.1016/j.engfailanal.2016.03.017

[82] Arroyo OH, Jalbert J, Fofana I, Ryadi M. Temperature dependence of methanol and the tensile strength of insulation paper: Kinetics of the changes of mechanical properties during ageing. Cellulose. 2017;**24**(2):1031-1039. DOI: 10.1007/s10570-016-1123-7

[83] Arroyo OH, Fofana I, Jalbert J, Rodriguez E, Rodriguez IB, Ryadi M. Assessing changes in thermally upgraded papers with different nitrogen contents under accelerated aging. IEEE Transactions on Dielectrics and Electrical Insulation. 2017;**24**(3):1829-1839. DOI: 10.1109/TDEI.2017.006449

Chapter 2

# Thermal Modelling of Electrical Insulation System in Power Transformers

Agustín Santisteban, Fernando Delgado,
Alfredo Ortiz, Carlos J. Renedo and Felix Ortiz

Additional information is available at the end of the chapter

http://dx.doi.org/10.5772/intechopen.78070

**Abstract**

Temperature is one of the limiting factors in the application of power transformers. According to IEC 60076-7 standard, a temperature increase of 6°C doubles the insulation ageing rate, reducing the expected lifetime of the device. Power losses of the transformer behave as a heating source, and the insulating liquids act as a coolant circulating through the windings and dissipating heat. For these reasons, thermal modelling becomes an important fact of transformer design, and both manufacturers and utilities consider it. Different techniques for thermal modelling have been developed and used for determining the hot-spot temperature, which is the highest temperature in the winding, and it is related with the degradation rate of the solid insulation. First models were developed as a first estimation for modelling the hot-spot temperature and the top-oil temperature. These models were based on thermal-electric analogy and are known as dynamic models. Other two different kinds of models are widely used for thermal modelling, known as Computational Fluid Dynamics (CFD) and Thermal Hydraulic Network Models (THNMs). These two techniques determine the temperature and velocity fields in the winding and in the insulating fluid. In this chapter, the different techniques for transformer thermal modelling will be introduced and described.

**Keywords:** thermal modelling, power transformer, electrical insulation system, CFD, THNM

## 1. Introduction

Power transformers are key devices in the electrical grids, and this is a main reason for utilities and manufacturers to improve its performance and lifetime expectancy. Although its performance

| $\theta_h$ (°C) | Normal paper | Thermally upgraded paper |
|---|---|---|
| 80 | 0.125 | 0.036 |
| 86 | 0.25 | 0.073 |
| 92 | 0.5 | 0.145 |
| 98 | 1.0 | 0.282 |
| 104 | 2.0 | 0.536 |
| 110 | 4.0 | 1.0 |
| 116 | 8.0 | 1.83 |
| 122 | 16.0 | 3.29 |
| 128 | 32.0 | 5.8 |
| 134 | 64.0 | 10.1 |
| 140 | 128.0 | 17.2 |

**Table 1.** Relative ageing rate for different hot-spot temperatures [1].

is over 99%, heat generation becomes a key factor for power limitation and expected lifetime. Transformer insulation ageing is sensible to temperature, doubling the ageing rate with a 6°C increase over the designed temperature according to IEC Standard 60076-7 [1]. High temperatures are caused by losses in the device, mainly due to Joule losses and eddy losses in the windings. The transformer insulation system that consists of a dielectric fluid and a solid insulation is the most critical part, and its degradation is related with the expected lifetime of the device [1]. The standard previously cited proposes a formulation to determine the ageing acceleration with the temperature

$$U = 2^{((\theta_h - 98)/6)} \tag{1}$$

$$U = e^{\left(\frac{15000}{110+273} - \frac{15000}{\theta_h + 273}\right)} \tag{2}$$

where V is the relative ageing rate of the insulation, which is calculated by Eq. (1) for normal insulation paper and by Eq. (2) for thermally upgraded insulation paper, and $\theta_h$ refers to the hot-spot temperature (°C). Both equations indicate that the relative ageing rate is sensible to hot-spot temperature variations as shown in **Table 1**.

For this reason, the estimation of the hot-spot temperature becomes an important task for manufacturers and utilities. Different models have been developed for the study of hot-spot temperature in oil-immersed power transformers that will be introduced in the following sections.

## 2. Dynamic models

The first thermal modelling technique described is the dynamic thermal model. These models are based on the thermoelectric analogy to design a circuit based on the thermal resistance and

thermal capacitance of the transformer [2]. The circuit is modelled by a partial differential equation whose solution gives the evolution of the hot-spot temperature over time. Normally, to simplify the solution, an intermediate circuit often comes with the hot-spot temperature model to obtain the top-oil temperature, **Figure 1**.

These models are associated with the differential equations, Eqs. (3) and (4) [2].

$$\frac{1+R\cdot K^2}{1+R}\cdot \mu_{pu}^{n}\cdot \Delta\theta_{oil,\,rated}=\mu_{pu}^{n}\cdot \tau_{oil,\,rated}\cdot \frac{\partial\theta_{oil}}{\partial t}+\frac{\left(\theta_{oil}-\theta_{amb}\right)^{1+n}}{\Delta\theta_{oil,\,rated}^{n}} \tag{3}$$

$$\left\{K\cdot P_{cu,\,pu}(\theta_{hs})\right\}\mu_{pu}^{n}\cdot \Delta\theta_{\mathrm{hs},\,rated}=\mu_{pu}^{n}\cdot \tau_{\mathrm{wdg},\,rated}\cdot \frac{\partial\theta_{hs}}{\partial t}+\frac{\left(\theta_{hs}-\theta_{oil}\right)^{n+1}}{\Delta\theta_{\mathrm{hs},\,rated}^{n}} \tag{4}$$

where the terms are as follows: R, ratio of rated load losses to no-load losses; K, the load factor; $\mu_{pu,}$ oil viscosity (per-unit value); $\theta_{amb,}$ ambient temperature (°C); $\theta_{hs,}$ hot-spot temperature (°C); $\theta_{oil,}$ top-oil temperature (°C); $\Delta\theta_{oil,rated,}$ rated top-oil temperature rise over ambient (°C); $\Delta\theta_{hs,rated,}$ rated hot-spot temperature rise over top-oil temperature (°C); $\tau_{oil,rated,}$ rated oil time constant (s); $\tau_{wdg,rated,}$ rated winding time constant (s); n is a constant obtained from tables; and $P_{cu,pu}(\theta hs)$ load loss's dependence on temperature (per-unit value).

In addition, the IEC 60076-7 standard proposes their own method with Eqs. (5) and (6):

$$\theta_h(t)=\theta_a+\Delta\theta_{oi}+\left\{\Delta\theta_{or}\cdot\left[\frac{1+R\cdot K^2}{1+R}\right]^{x}-\Delta\theta_{oi}\right\}\cdot f_1(t)+\Delta\theta_{hi}+\left(H\cdot g_r\cdot K^{y}-\Delta\theta_{hi}\right) \tag{5}$$

$$\theta_h(t)=\theta_a+\Delta\theta_{or}\cdot\left[\frac{1+R\cdot K^2}{1+R}\right]^{x}+\left\{\Delta\theta_{oi}-\Delta\theta_{or}\cdot\left[\frac{1+R\cdot K^2}{1+R}\right]^{x}\right\}\cdot f_3(t)+H\cdot g_r\cdot K^{y} \tag{6}$$

where Eq. (5) is applied for increasing the load factor and Eq. (6) is applied for decreasing the load factor. The functions $f_1$, $f_2$ and $f_3$ can be calculated as explained in [1]. With these two models, the hot-spot temperature of a power transformer can be predicted over time, under different load conditions. In [2], both methods are tested with different transformers of different power rates and contrasted its accuracy with experimental measurements.

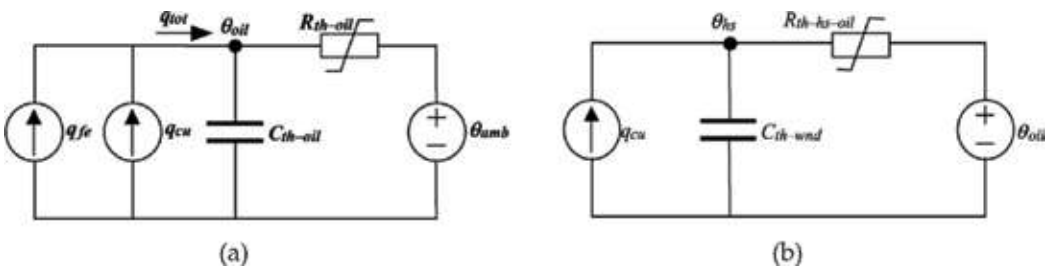


**Figure 1.** Dynamic models presented in [2]. (a) Top-oil model and (b) hot-spot model.

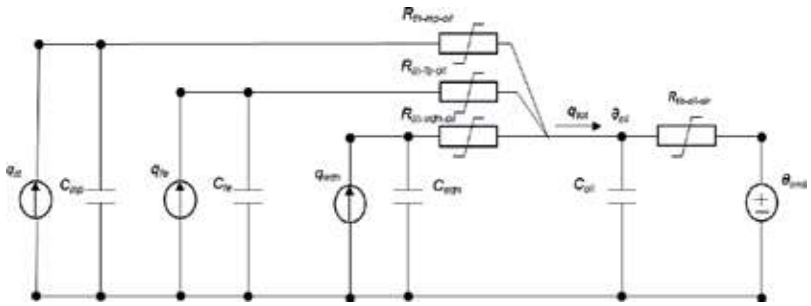

**Figure 2.** Complex top-oil thermal circuit [3].

For both models, a large number of parameters obtained from heat-run tests are necessary for calculations. However, the model proposed in [2] requires less input data than the model proposed by the standards.

Other complex models have been developed for top-oil and hot-spot temperature prediction. These models take into account the different thermal resistances that appear from the different heating sources in power transformer as shown in **Figure 2** [3]. In addition, models for bottom-oil temperature and bottom-winding temperature have been developed in [4].

In conclusion, dynamic thermal models are useful and can be implemented in computer software without hardly computational cost, requiring less than 5 min in a normal PC. However, the input data necessary to run the model come from the results of heat-run tests, which made this method dependent on the knowledge of these results.

## 3. Steady-state models

An alternative to dynamic models is steady-state model. Steady-state models attempt to predict the temperature field in the transformer winding, determining the hot-spot temperature and its location. In these modelling techniques, the geometrical parameters of the transformer winding gain importance. Among the former, the one that is based on heat-run test is shown in the next section. Then, between the second ones, models based on Computational Fluid Dynamics (CFD) and those based on Thermal-Hydraulic Network Modelling (THNM) are developed.

### 3.1. Hot-spot temperature rise from normal heat-run test data

The fundamental objective of a transformer thermal modelling is to be able to accurately predict winding and component temperature rises above ambient temperature. For the industry and transformer users, the determination of the location of the hot-spot and the hot-spot temperature rise is especially interesting. In [1], the limit temperature for top oil and hot spot is established at 105 and 120°C for normal operation.

These temperature rises are caused by the combination of voltage-related losses (no-load losses) and current-related losses (load losses). The loss distribution is a scalar function P(r,φ, z) [W/m$^3$] over the volume of these transformer metal parts. The determination of electromagnetic (EM) losses is usually made using the Finite Element Method (FEM). Windings are divided into many rectangular sections with a uniform ampere-turn distribution. The eddy losses are calculated for each conductor using Eq. (7)

$$P = \frac{\omega^2 \cdot B^2 \cdot T^2}{24 \cdot \rho} \tag{7}$$

where B is the peak leakage flux density (T), $\omega = 2\pi f$, where f is the frequency (Hz), T is the conductor dimension perpendicular to the direction of the leakage flux density (m) and $\rho$ is the resistivity ($\Omega \cdot m/mm^2$).

The axial and radial flux densities are assumed to be constant over a single conductor and equal to the value at its centre. The total eddy losses for each winding are calculated by integrating the losses of all its conductors.

The boundary conditions can influence the results. A transformer is a 3D construction, in which the windings usually are symmetric, but the surrounding steel parts (core and tank) are not, **Figure 3**.

The temperature rise over ambient temperature has to be calculated based on this loss distribution taken into account thermal conductivity of the metal, the thermal conductivity of the electrical insulation and convective cooling due to oil flow (viscosity of oil is important, which makes the oil temperature also an important parameter).

The temperature rise of a transformer winding above the ambient temperature is built up from three component temperature rises: (1) the temperature rise of the inlet oil, (2) the temperature rise of the cooling oil as it passes through the transformer and (3) the temperature rise of the

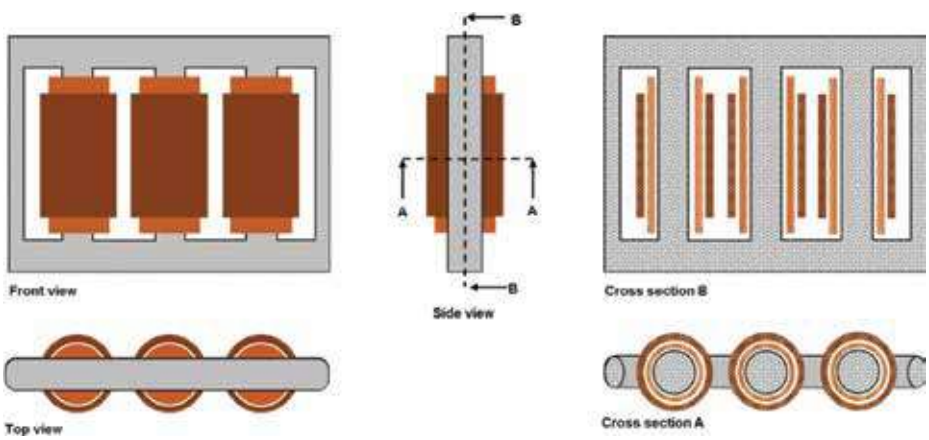


**Figure 3.** Three-phase transformer with five-legged core and LV winding with a large pitch (front, top and side views, and cross sections).

winding above the cooling oil. These temperatures can be measured in the surrounding of the transformer and in three points of it: inlet and outlet oil temperatures and mean winding temperature.

The temperature increase of the oil on passing through the transformer is the difference between the inlet and the outlet oil temperatures, but in a transformer, usually there are more than one parallel oil paths, and each one could have their own temperature rise. It is accepted that this increase is approximately the difference between the top-oil temperature and the cooled oil inlet temperature [1].

The temperature rise of the winding above the oil is referred to as the "gradient," g. A mean value for this is obtained from the difference between the mean winding temperature, usually determined by resistance measurements, and the mean oil temperature. The gradient can vary with position because of local variations in winding losses and cooling effectiveness.

The temperature rise at the hot spot, $\Delta\theta_h$ (°C), top-oil temperature, $\Delta\theta_o$ (°C), is expected to be greater than the mean winding gradient, g, as expressed by a hot-spot factor, H, Eq. (8):

$$\Delta\theta_h = \Delta\theta_0 + (H \cdot g) \tag{8}$$

where H could be expressed as the product of two dimensionless factors, $Q_{fac}$, related to additional loss, and $S_{fac}$, related to the efficiency of cooling, Eq. (9):

$$H = Q_{fac} \cdot S_{fac} \tag{9}$$

The H factor can be derived from **Figure 4** and can be expressed according to Eq. (10):

$$H = \frac{\theta_h - \theta_0}{\theta_w - \frac{\theta_0 - \theta_b}{2}} \tag{10}$$

where $\theta_w$ and $\theta_b$ are, respectively, the average winding and bottom-oil temperatures (°C).

The Q-factor is a dimensionless factor as a ratio of two losses, and in cylindrical coordinates is defined according to Eq. (11)

$$Q_{fac} = \frac{q(r, z, \varphi, \mathrm{T})}{q_{ave}} \tag{11}$$

where q (r, z, φ, T) is the local loss density at a location (W/m$^3$), r is the radial position, φ is the angle in circumferential position, z is the axial position, T is the local temperature at (r, z, φ) (K) and $q_{ave}$ is the average loss of the winding at an average temperature (W/m$^3$).

Heat transfer can be propagated in different directions, the overall heat transfer being a series and parallel parts of (1) the insulation between the neighbouring conductors that are in direct contact with each other. This is in a radial direction. (2) The insulation paper and oil boundary layer between the conductor and the oil flow. This is in an axial direction. (3) The winding copper. This is located in the tangential direction and usually can be neglected.

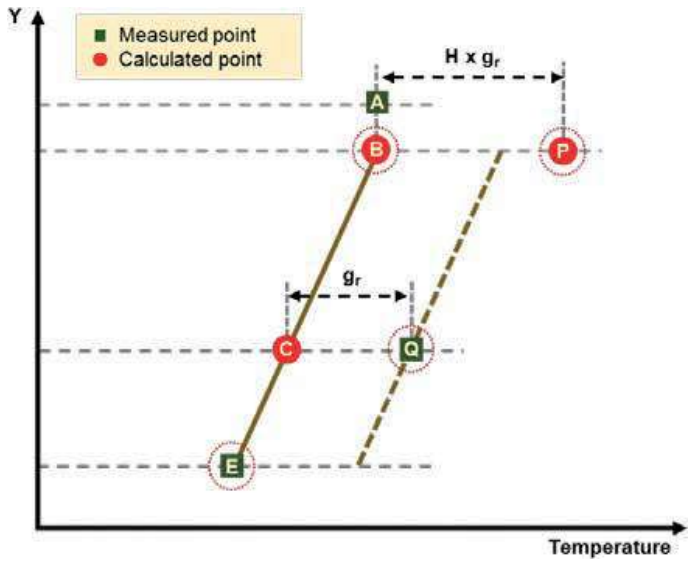


**Figure 4.** Transformer thermal diagram with the measured quantities highlighted. A—Top-oil temperature derived as the average of the tank outlet oil temperature and the tank oil pocket temperature. B—Mixed oil temperature in the tank at the top of the winding (often assumed to be the same temperature as A). C—Temperature of the average oil in the tank. D—Oil temperature at the bottom of the winding. E—Bottom of the tank. gr—Average winding to average oil (in tank) temperature gradient at rated current. H—Hot-spot factor. P—Hot-spot temperature. Q—Average winding temperature determined by resistance measurement.

For transformer manufacturers, a good thermal design is a very important issue. Aspects as material, winding geometry, oil paths through the windings, or oil velocity are very relevant. This design determines the cost and the insulation ageing (transformer life).

Mathematical models allow predicting transformer temperatures and winding hot-spot temperatures with good accuracy. Transformer manufacturers use these models to make their designs and any significant design variants. However, simulating the loss distribution in the structural metal parts of a transformer requires a very large number of small mesh elements. Nevertheless, calculating the temperature rise distribution in the structural metal parts requires a much higher resolution mesh density.

### 3.2. Computational fluid dynamics modelling

Tackling numerically, a complex physical problem using computational resources has only been able since few years ago. In fact, the current powerful computing resources allow us to discretize complex geometries. Then, the underlying governing equations, for example, differential equations (DEs), can be solved assuming small simplifications. The discretization process converts these DEs in a set of algebraic equations that can be solved using numerical algorithms. Regarding our topic, in which heat transfer and fluid dynamics physics are involved, the numerical method that carries out this process is named Computational Fluid Dynamics (CFD).

*3.2.1. CFD basic concepts*

CFD is based on the solution of the Navier-Stokes equations. These are a set of Partial Differential Equations (PDE) that state the mass, momentum and energy conservations, Eqs. (15)–(17). However, it is not possible to solve them in an exact way (except some scarce and special cases). CFD allows solving these PDE by means of the geometrical model discretization. The latter converts the PDE in a set of algebraic equations that can be solved using specialised numerical algorithms, such as Gauss elimination algorithm, on a computer. These algorithms obtain the solution (velocity, pressure, temperature, in the case of power transformers) at discrete points of the studied domain [5]

$$\nabla \cdot (\rho u) = 0 \tag{12}$$

$$\rho(u \cdot \nabla)\mathrm{u} = \nabla \left[ pI + \mu\left(\nabla u + (\nabla u)^T\right) - \frac{2}{3}\mu(\nabla \cdot u)I \right] + F \tag{13}$$

$$\rho C_p u \cdot \nabla T = \nabla \cdot (k \nabla T) + \mathrm{q} \tag{14}$$

where $\rho$, $\boldsymbol{u}$, $p$, $\mathbf{I}$, $\mu$, $\mathbf{F}$, $\mathrm{C_p}$ T and $q$ of Eqs. (12)–(14) are, respectively, density (kg/m$^3$), velocity vector (m/s), pressure (Pa), identity matrix, dynamic viscosity (Pa·s), body force vector (N/m$^3$), specific heat capacity (J/kg·K), temperature (K) and unitary heat transfer (W/m$^3$).

The first step in this kind of modelling is usually to determine the dimensions number of the geometrical model: 2D or 3D, generally. This is very important since the geometrical model is the first source of errors. For instance, if 2D models were considered in CFD, important edge effects that contribute to heat transfer and flow phenomena could be obviated.

Generally, CAD tools are used to draw the geometry (Solidworks, Inventor, etc.). These tools allow defining the geometry with a high-detail level. The latter is an essential aspect to be considered since a very detailed geometry can excessively complicate the numerical model without significant improvement in the problem definition. For instance, in the case of the power transformer shown in **Figure 5**, it was decided to simplify the phase using angular and plane symmetries since these simplifications did not affect the solution accuracy.

The physics involved in the problem analysed must be described. In CFD, many mathematical models can be used to define the heat transfer and flow phenomena. In fact, an adequate selection of the model and a correct setting of the boundary conditions supported by this model are a crucial task to avoid errors in the numerical solution obtained.

This task consists in the division of the geometric model in smaller parts (cells). This is the so-called discretization. There are mainly three discretization techniques: finite element, finite volume and finite difference. At the same time, these techniques generate structured and/or unstructured meshes.

Structured meshing is habitually used in simple geometries such as the one shown in **Figure 5**. This geometry consists in volumetric cells of six faces that can uniquely be identified using

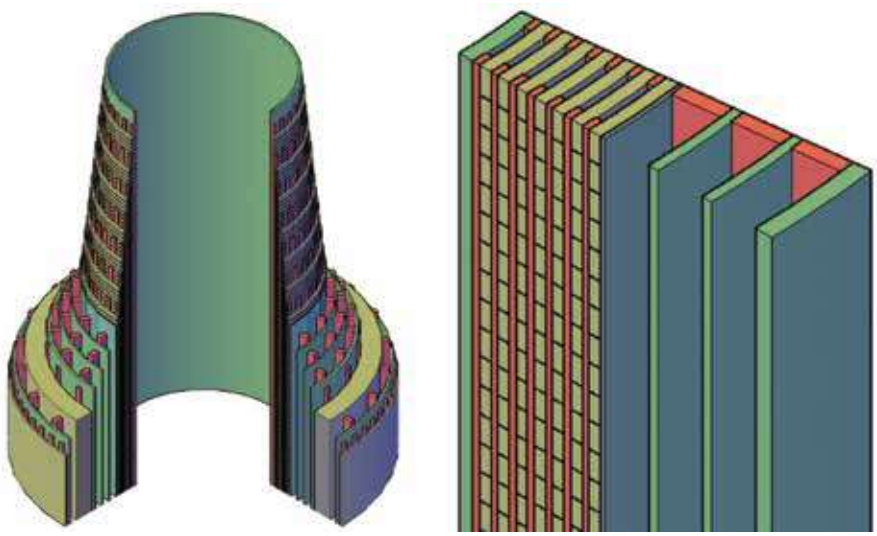

**Figure 5.** Geometry definition.

three indexes (i,j,k). The deformation grade (mesh quality) of the elements of this meshing type is generally smaller than in the other case. In addition, the cells can be oriented in the main flow direction, thus capturing the flow phenomena in a better way.

By contrast, unstructured meshing can be used in very complex geometries. The cells may have any shape (quadrilateral or triangular shapes in 2D, tetrahedral or hexahedral shapes in 3D), thus a better adaption to the geometry is obtained. However, this type of mesh generates a set of algebraic equations whose solution time is habitually higher. Finally, the mesh refinement grade affects the solution accuracy. Generally, the finer the mesh, the more accurate the solution is.

The solution of the set of algebraic equations resulting from the discretization of the geometric model is the last step. This can be done using direct or iterative methods. The latter are habitually used to solve the Conjugate Heat Transfer (CHT) problems since the computational requirements are smaller than that required by the former methods. For instance, CHT problems are commonly solved using iterative methods such as Conjugate gradient, Gauss-Seidel and Multigrid.

In addition, to solve the algebraic equations, a convergence criterion is needed to be considered. This is often implied to assume a maximum error in the residuals of the governing equations. That is, the solution obtained is not exact. In other words, another error appears in the numerical model solution.

In comparison with other numerical tools (for instance, THNM), a lot of computing time and a great amount of computational resources are needed by CFD. However, this technique allows knowing the fluid flow and heat transfer phenomena in fine detail.

### *3.2.2. Main research lines of CFD applied to transformer thermal modelling*

As can be seen in **Figure 6**, the cooling system of a power transformer is a closed loop that consists mainly of a heat source (windings), a heat sink (radiators) and a tank. Most CFD studies are focused on the thermal-fluid behaviour of the cooling system inside the windings. Nonetheless, some efforts have been put into the thermal modelling of the radiators too. The next subsections present a brief review of these topics.

### *3.2.3. Winding modelling*

As mentioned previously, the main goal of the winding CFD modelling is to numerically predict the hot-spot temperature and temperature distributions in oil-immersed transformers since their life span depends on it. First works were developed at the beginning of this century. For instance, Mufuta et al. and El Wakil et al. modelled two windings using this technique. The former characterises the oil flow through an array of discs with different spaces between discs and different inlet conditions [7]. The latter employed a 2D axisymmetric model of a power transformer with six different geometries and six different inlet velocities in order to study the heat transfer and oil flow through the windings [8]. In the same decade, other authors have contributed to this labour. For instance, Torriano performed 2D and 3D simulations of an LV winding (LVW) of a power transformer with zigzag cooling to determine the effects of several elements, such as sticks and inter-sticks, in the temperature distribution [6, 9]. In 2011, Gastelurrutia et al. carried out a study where they developed a 3D and a 2D model of an Oil Natural-Air Natural (ONAN) distribution transformer. They demonstrated the good capacity of the simplified 2D model to represent the thermal behaviour of the whole transformer [10]. In 2012, Tsili et al. established a methodology to develop a 3D model to predict hot-spot temperature [11]. In this year, Skillen et al. carried out a CFD simulation of a 2D non-isothermal flow axisymmetric model in order to characterise the oil flow in transformer winding with zigzag

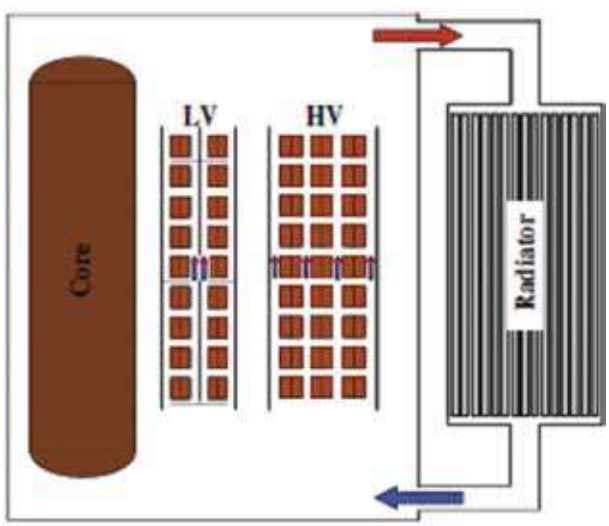


**Figure 6.** Schematic of oil circulation in a power transformer [6].

cooling [12]. In 2014, Yatsevsky carried out a 2D-axisymmetric simulation of a CHT model of a transformer, including the core, the tank and the radiator, in order to predict hot spots in an oil-immersed transformer with natural convection. The developed model has shown a good adequacy verified by experiments [13]. Recently, Torriano et al. have developed a 3D CHT model of an Oil Natural (ON) disc-type power transformer-winding scale model. An underestimation of the average and hot-spot temperatures was obtained in this model in comparison with the experimental setup when the entire cooling loop was considered. This is the reason why the authors chose to reduce the computational domain to the winding, setting the inlet boundary conditions. This way, the model accuracy was improved significantly [14].

The substitution of mineral oil by new biodegradable dielectric liquids is another research line in which CFD is used as an analysis tool. However, few experimental and theoretical works can be found in the study related with the cooling capacity of these new liquids. In 2015, Park et al. employed a 2D-CFD model to obtain temperature and velocity profiles of some alternative liquids used in a distribution transformer of 2.3 MVA and a power transformer of 16.5 MVA [15]. In the same year, Lecuna et al. carried out a 3D-CFD simulation of an ONAN distribution transformer comparing a natural ester, a synthetic ester, a high kinematic viscosity silicone oil and a low kinematic viscosity silicone oil with a mineral oil [16]. These works conclude that alternative liquids produce higher temperatures in the transformer windings designed for mineral oil. More recently, Santisteban et al. evaluated the cooling performance of two alternative vegetal liquids with that of a typical mineral oil. This task was carried out using a 2D-axisymmetric model of an LVW with zigzag cooling in which temperature distributions, hot-spot temperatures and their locations, and hot-spot factors were determined. In contrast to the results of the previous works, this work shows that the hot-spot temperature is lower for the vegetable oils in the initial design than that of mineral oil [17].

Finally, CFD is also used to analyse the advantage of using natural esters in the transformer insulation system. For instance, in 2016, Fernandez et al. published a work in which laboratory experiments and CFD simulations are combined to study the influence of vegetable oils in the life span of the winding insulation paper [18]. It was concluded that, even though the chapter suffers worse thermal conditions when it is immersed in vegetable oils, the physical properties of these oils extend the life span of this chapter, **Figure 7**. That is, in the long term, both effects tend to the balance and the degradation is similar to the one obtained in windings cooled by mineral oil.

### *3.2.4. Radiator modelling*

Most of the power transformers have fan-cooled radiators. CFD can be used to improve the cooling capability of these components. Few works can be found with this subject. In fact, this topic has mainly begun to be treated in this decade. For instance, Kim et al. presented in 2013, a predictive and experimental study about the cooling performance of the radiators used in oil-filled power transformers with two different cooling methods, ONAN and Oil-Directed Air Natural (ODAN) [19]. The aim was to experimentally evaluate the cooling capacity of the radiator and compare the results with those obtained with two different predictive methods. CFD was one of these methods. The authors stated that the radiator optimization could be

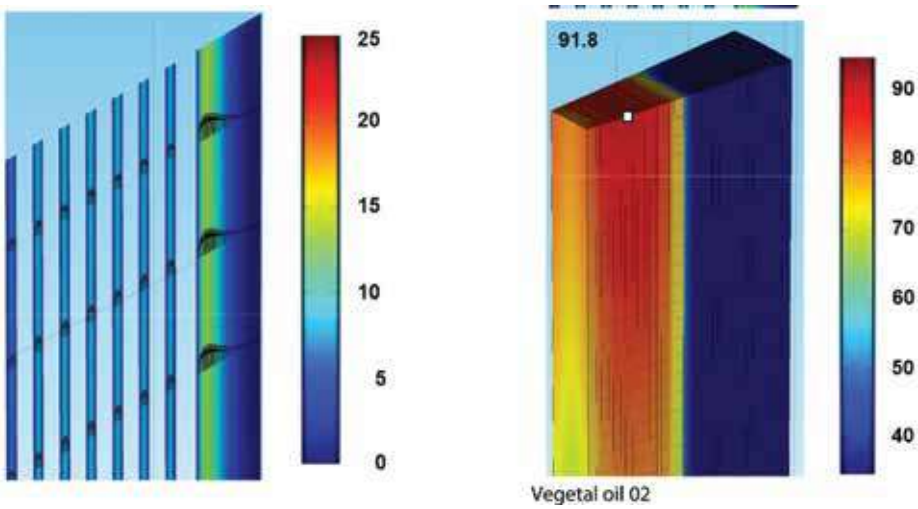


**Figure 7.** Velocities (mm/s) and temperatures (°C) distributions.

done in this way. On the other hand, to improve the cooling capacity of the radiators, the fan's location in the radiators has to be studied. Paramane et al. conducted this in 2014 using both CFD and experimental studies [20]. They considered horizontal and vertical blowing directions. For the transformer studied, they found that the horizontal blowing direction had a higher performance due to the lesser air sideway leakages that those of the vertical blowing case. Two years later, in 2016, the same authors carried out the same type of study [21]. However, as a novelty, they provide the effect of the blowing direction on the temperature and velocity distributions of the oil inside the radiators.

Finally, in 2017, Ríos et al.? presented the result comparison of two models (a semi-analytical model and a CFD model) with the experimental results of a radiator of a 30-MVA power transformer working in ONAN mode. The objective was to validate both models in order to use them in the optimization of the current radiator design [22]. This aim was accomplished. An extension of this work was presented the same year with the goal of analysing the thermal-fluid dynamic behaviour of the radiator working in ONAF mode with vertical blowing of the fans [23]. The results obtained, which were validated with experimental and CFD results, showed that the semi-analytical model they proposed was a useful tool for radiator design processes.

### 3.3. Thermal hydraulic network modelling, THNM

THNM is a technique for transformer thermal modelling that relies on three basic principles: mass conservation, momentum conservation and energy conservation. It implies a subdivision of the domain in multiple elements where the conservation principles are observed as a convergence condition.

This model describes the conservation principles by algebraic equation sets that makes the solving time shorter than CFD that describes the same principles into a set of partial differential

equations. These principles are applied to solve the temperature and oil flow fields in several parts of the transformer (windings, core, coolers). THNM applied on the windings can be useful for predicting the hot-spot temperature.

THNM models are the coupling of two different networks: the hydraulic network and the thermal network. The hydraulic network comprises the oil flows through channels and nodes. The oil flow is modelled using the electric circuit analogy where the oil flow and pressure correspond to, respectively, electrical current and voltage. The thermal network models the heat transfer between the active parts and the cooling circuit of the transformer. Temperature-dependent properties of the materials and heat transfer coefficients make both networks to be coupled.

### *3.3.1. Hydraulic network*

The hydraulic network corresponding to a disc winding with barriers is shown in **Figure 8**. The hydraulic network consists of eight nodes, four per axial side, where two of the nodes correspond to the entrance and exit of the coolant and the three remaining nodes per side are where the coolant branches or merges. The network is represented by its electrical circuit analogy where the physical quantity associated to each node corresponds to the sum of the static and dynamic pressures. In the circuit, resistances represent frictional pressure drops, and resistances in the nodes represent the local pressure drops as well. Buoyancy effect is represented by generators representing the gain of pressure due to gravitational effects. Since the hydraulic resistances depend on the flow, the hydraulic circuit proposed in **Figure 8** is a nonlinear circuit that has to be solved with an iterative procedure [24].

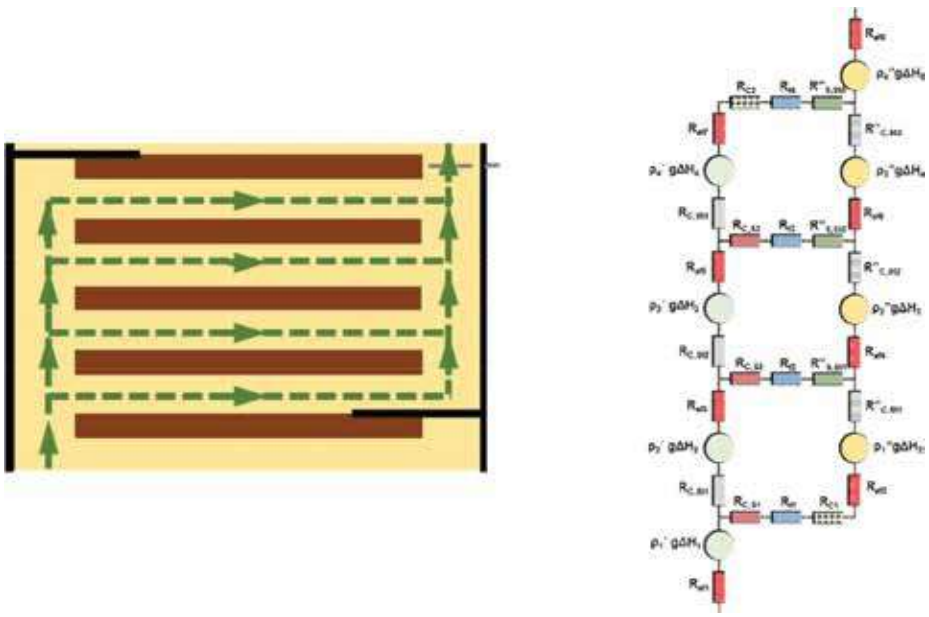

**Figure 8.** Analogy hydraulic circuit versus hydraulic network.

### *3.3.2. Thermal network*

Thermal network describes the heat transfer phenomena on the transformer and on the transformer elements. There are two main mechanisms of heat transfer in a transformer winding: heat conduction in the conductors and in the solid insulation, and convection from the active part to the cooling oil. The convection term highly depends on the oil flow distribution, which is given by the hydraulic network. In addition, hydraulic network depends on temperature buoyancy effect and temperature-dependent properties of the cooling oil. This coupling between networks enhances the necessity to apply iterative procedures to solve both networks.

An approach for the thermal part of a transformer winding is to build a thermal network. For the case of a disc winding, the analogy with electric circuits is useful to model the heat transfer in two directions, axial and radial. A resistive term is used for modelling heat conduction between conductor and solid insulation and a resistive term is used for the convective part, which depends on the oil flow distribution. A good approach consists in assuming that the thermal resistance of the conductor is negligible, considering only the resistance of the solid insulation. A voltage source represents the oil temperature and a current source represents the heat generation on each node. **Figure 9** represents the thermal network previously described, where the $R_{\lambda i}$ represents the thermal resistance for conductive terms, $R_{\alpha i}$ represents the thermal resistance for convective terms, $\theta_{bi}$ and $\theta_{ti}$ represent the temperature on the channels and $P_{\gamma i}$ represents the heat source in the conductors [24].

### *3.3.3. Complete loop modelling*

Other application of THNM is to model the complete oil loop of the transformer. It is based on the global pressure equilibrium of the oil loop, considering core, tank, winding and radiators, taking into account thermal driving forces, pump forces and pressure drops in the whole loop. Thermal driving forces appear due to density changes with temperature. Driving forces and pressure drop depend on the oil flow rate. The oil flow rate, $Q_o$, represents the equilibrium between driving forces and pressure drops.

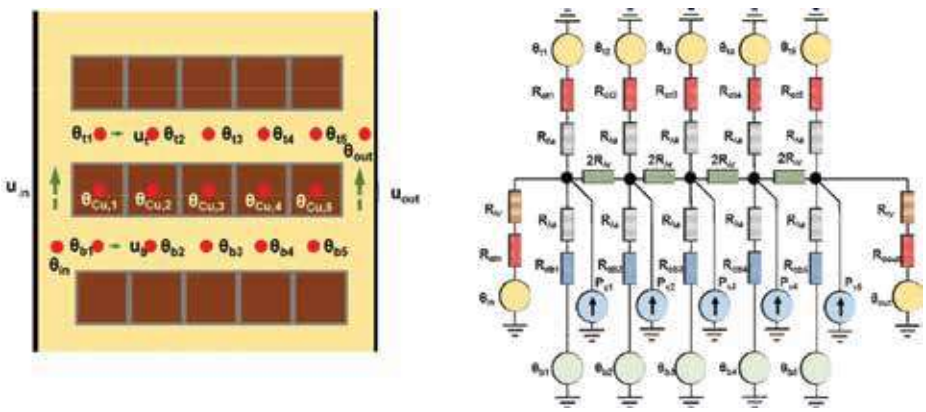

**Figure 9.** Thermal network of a transformer winding disc.

A simple way to imagine the oil loop of a transformer is described as follows: the oil is heated in the windings, then flows through a piping system reaching the radiator, where it is cooled and finally goes through another piping system to reach the starting point. Although there is heat exchange in the piping system, it is considered negligible compared to the heat exchanged in radiators and windings. It is represented in **Figure 10**.

Thermal driving force is generated due to density variations along the loop and can be expressed by Eq. (15)

$$p_T = \oint \rho \cdot \vec{g} \cdot \vec{dl} = \oint \rho \cdot g \cos\varphi \cdot dl \tag{15}$$

where $\rho$ is the oil density, $\vec{g}$ is the gravity vector, $\varphi$ is the angle between velocity and gravity vectors and $\vec{l}$ is the path vector.

For simplicity, Eq. (16) can be expressed as follows:

$$p_T = \rho_r \cdot g \cdot \beta \cdot \Delta\theta_{ol} \cdot \Delta H \tag{16}$$

where $\rho_r$ is the oil density at a reference temperature (kg/m$^3$), $\beta$ is the volume expansion coefficient of the oil (1/K), $\Delta\theta_{Ol}$ is the vertical temperature gradient (°C) and $\Delta H$ is the height difference between the centre point of the radiator and the centre point of the winding (m).

When the pump runs directly to the windings, the total driving pressure will be the sum of the thermal driving force and the pump driving force where the pump pressure is much higher than the thermal driving pressure.

The pressure drop can be subdivided into two different groups: major and minor losses. Major losses involve the frictional pressure drops and minor losses involve the local pressure drops due to accessories in the cooling circuit (valves, junctions, etc.).

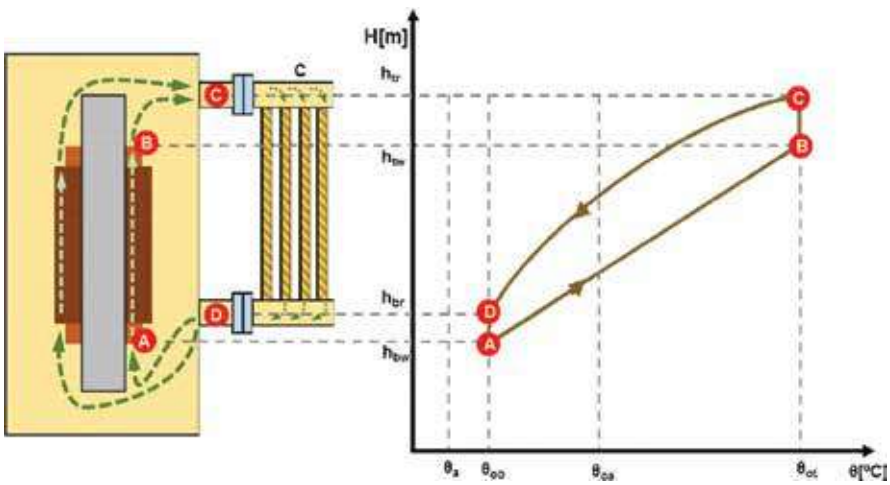


**Figure 10.** Oil loop of a transformer.

The driving pressure on the loop must be equal to the total pressure drop. Energy conservation is also applied to the loop. The energy balance of the winding is presented in Eq. (17)

$$p_\gamma = \rho \cdot c_p \cdot Q_o \cdot \Delta\theta_{ol} \tag{17}$$

where Pγ are the power losses in the winding (W), $c_p$ is the specific heat of the oil at average oil temperature (J/kg·K), $\rho$ is the density at bottom-oil temperature (kg/m$^3$) and $Q_o$ is the volume oil flow (m$^3$/s).

With these two equations, Eqs. (16) and (17), there are three variables that are volume oil flow $Q_o$, bottom-oil temperature $T_{Ob}$ and top-oil temperature $T_{Ot}$. Eq. (18) is added when considering the energy balance in the radiator

$$k_p \cdot O \cdot (T_0(x) - T_a)dx = -\rho \cdot c_p \cdot Q_0 \cdot dT_0(x) \tag{18}$$

where $k_p$ is the total heat transfer coefficient (HTC) (W/m$^2$K), O is the circumference of the outer radiator cross section (m), $T_O(x)$ is the oil temperature at position x (K) and $Q_O$ is the oil flow through the radiator (m$^3$/s).

Assuming that the HTC does not change along the radiator in a significant way, the solution of Eq. (19) is

$$T_0(x) = T_a + (T_{ot} - T_a) \cdot e^{-\frac{k_p \cdot O}{\rho \cdot c_p \cdot Q_o} x} \tag{19}$$

Then, integrating the cooling power in the radiator

$$P = \int_0^{L_R} (T_o(x) - T_a) \cdot k_p \cdot O \cdot dx \tag{20}$$

result in the following equation:

$$P = \rho \cdot c_p \cdot Q_o \cdot (T_{ot} - T_a) \cdot \left(1 - e^{-\frac{k_p \cdot O \cdot L_R}{\rho \cdot c_p \cdot Q_o}}\right) \tag{21}$$

In this explanation, it is assumed that there is no heat exchange in the tank and there are no core losses. Consequently, from Eqs. (16), (17) and (21), two unknown temperatures and the oil flow can be determined [24].

### *3.3.4. Detailed winding model*

THNM can be developed for predicting the temperature and oil flow distribution in a transformer winding in detail. For this type of modelling, bottom-oil temperature and oil flow rate have to be taken as inputs for the model. There is also the possibility to introduce a non-uniform power source in the active part of the winding.

Applying a special discretization and following THNM principles, there are some assumptions that are taken in this kind of models: perfect thermal mixing is considered at junctions, fully developed flows are assumed in oil channels and exterior walls are considered as adiabatic.

The accuracy of these models has been tested and resulted acceptable. In order to increase this accuracy, many authors have tried to focus into two different parameters that come from correlations from datasets that are local pressure drop coefficients and convective heat transfer coefficient.

The knowledge of these two parameters is small in this application since there is not much experience to define them. However, some authors have defined these parameters based on datasets obtained from CFD results. Using CFD to accurately these two parameters has improved the performance of detailed THNMs. These kinds of models are known as CFD calibrated THNMs and integrate both main techniques of transformer thermal modelling.

THNM modelling predicts temperature distribution and velocity in the channels of the windings of the transformer. Hot-spot and top-oil temperatures can be estimated using THNM in a fast calculation, taking less than 5 min in a normal computer. These results show small deviations with respect to the obtained CFD models that are below 5% of deviation in hot-spot and top-oil temperature.

#### *3.3.5. Detailed radiator model*

Other kinds of THNM modelling are the detailed radiator models. These models rely on the same principles than detailed winding models, but applied on the radiator part. Thermal modelling of radiators is complex, although radiators are mechanically simple, because of the following reasons: oil temperature varies in function of the height and per radiator panel, temperature variation is a function of the oil mass flow and the local heat flux, the local heat flux is dependent on the temperature difference between oil and ambient air and the local air velocity and the local air velocity are variable along the position in the radiator [25].

Especially, focus needs to be made on the air velocities distribution since there exist three possible configurations: air natural (AN), air forced (AF) with vertical air flow and air forced with horizontal flow. With AN configuration, the air flow through the panels is originated by buoyancy forces of the hot air. The buoyancy force will be in equilibrium with the pressure drop of the air flow through the panels.

In the case of AF, air flow distribution generated from the fans has to be previously defined in order to obtain the heat transfer coefficient in the radiator plates. In order to better understand and model the air distribution over the radiator panels, CFD simulations have been carried out. Determining that the air coming from a fan spread in a conic way, an effective air velocity can be calculated based on the volumetric air capacity of the fan and the cone surface. With these assumptions, thermal modelling of the radiator can be made.

## 4. Summary

In this chapter, different techniques for transformer thermal modelling have been introduced. The main goal of all of them is to predict the hot-spot temperature in the transformer windings with good accuracy. Due to the complex phenomena involved in transformer thermal modelling, the models have to be previously validated with experimental data. The first models are the dynamic models, which take into account different load factors to predict hot-spot and top-oil temperatures over time. These models are useful to predict hot-spot temperatures in scenarios of emergency load. The steady-state models predict the temperature and velocity profiles in the windings of the transformer for a selected load rate. These models, CFD and THNM, are useful for design steps to predict the thermal behaviour of the transformer. CFD is a more accurate method, whereas THNM is faster and requires less computational resources. Both are used for design steps of transformer windings. Steady-state models are also used to test the cooling performance of alternative dielectric liquids, such as natural esters, in power transformers by comparing hot-spot temperature and pressure drop over the windings.

## Author details

Agustín Santisteban*, Fernando Delgado, Alfredo Ortiz, Carlos J. Renedo and Felix Ortiz

*Address all correspondence to: santistebana@unican.es

ETSIIT University of Cantabria, Santander, Spain

## References

[1] IEC Power transformers—Part 7: Loading guide for oil-immersed power transformers. IEC 60076-60077, 2011

[2] Susa D. Dynamic thermal modelling of power transformers. IEEE Transactions on Power Delivery, 0, 1. Jan 2005;**20**(1):197-204. ISSN: 0885-8977

[3] Susa D. Dynamic thermal modelling of power transformers: Further development—Part I. IEEE Transactions on Power Delivery, 10. Oct 2006;**21**(4):1961-1970. ISSN: 0885-8977

[4] Susa D. Dynamic thermal modelling of power transformers: Further development—Part II. IEEE Transactions on Power Delivery, 10. Oct 2006;**21**(4):1971-1980. ISSN: 0885-8977

[5] COMSOL Multiphysics. COMSOL Multiphysics Reference Manual. 2013. pp. 1-1262

[6] Torriano F, Chaaban M, Picher P. Numerical study of parameters affecting the temperature distribution in a disc-type transformer winding. Applied Thermal Engineering. 2010;**30**(14): 2034-2044. ISSN: 1359-4311. DOI 10.1016/j.applthermaleng.2010.05.004

[7] Mufuta J, van den Bulck E. Modelling of the mixed convection in the windings of a disc-type power transformer. Applied Thermal Engineering. 2000;**20**(5):417-437. ISSN: 1359-4311. DOI: 10.1016/S1359-4311(99)00034-4

[8] Wakil NE, Chereches N, Padet J. Numerical study of heat transfer and fluid flow in a power Transformer. International Journal of Thermal Sciences. Jun 1, 2006;**45**(6):615. ISSN: 1290-0729. DOI: 10.1016/j.ijthermalsci.2005.09.002

[9] Torriano F, Picher P, Chaaban M. Numerical investigation of 3D flow and thermal effects in a disc-type transformer winding. Applied Thermal Engineering. Jul, 2012;**40**:121-131. ISSN: 1359-4311. DOI: 10.1016/j.applthermaleng.2012.02.011

[10] Gastelurrutia J. et al. Numerical modelling of natural convection of oil inside distribution transformers. Applied Thermal Engineering. 2011;**31**:493-505. ISSN 1359-4311. DOI: 10.1016/j.applthermaleng.2010.10.004

[11] Tsili MA, Amoiralis EI, Kladas AG, Souflaris AT. Power transformer thermal analysis by using an advanced coupled 3D heat transfer and fluid flow FEM model. International Journal of Thermal Sciences. Mar, 2012;**53**:188-201. CrossRef. ISSN: 1290-0729. DOI: 10.1016/j.ijthermalsci.2011.10.010

[12] Skillen A, Revell A, Iacovides H, Wu W. Numerical prediction of local hot-spot phenomena in transformer windings. Applied Thermal Engineering. Apr, 2012;**36**:96-105. ISSN: 1359-4311. DOI: 10.1016/j.applthermaleng.2011.11.054

[13] Yatsevsky VA. Hydrodynamics and heat transfer in cooling channels of oil-filled power transformers with multicoil windings. Applied Thermal Engineering. Feb, 2014;**63**(1):347-353. CrossRef. ISSN: 1359-4311. DOI: 10.1016/j.applthermaleng.2013.10.055

[14] Torriano F. Numerical and experimental thermofluid investigation of different disc-type power transformer winding arrangements. The International Journal of Heat and Fluid Flow. 2018;**69**:62-72. ISSN: 0142-727X

[15] Park T. Numerical analysis of local hot-spot temperatures in transformer windings by using alternative dielectric fluids. Electrical Engineering. 2015;**97**(4):261-268. ISSN: 0003-9039

[16] Lecuna R et al. Thermal-fluid characterization of alternative liquids of power transformers: A numerical approach. IEEE Transactions on Dielectrics and Electrical Insulation. 2015;**22**(5):2522-2529. ISSN: 1070-9878. DOI: 10.1109/TDEI.2015.004793

[17] Santisteban A et al. Numerical analysis of the hot-spot temperature of a power transformer with alternative dielectric liquids. IEEE Transactions on Dielectrics and Electrical Insulation. 2017;**24**(5):3226-3235. ISSN: 1070-9878. DOI: 10.1109/TDEI.2017.006228

[18] Fernández C et al. Thermal degradation assessment of kraft paper in power transformers insulated with natural esters. Applied Thermal Engineering. Jul 5, 2016;**104**:129-138. ISSN: 1359-4311. DOI: 10.1016/j.applthermaleng.2016.05.020

[19] Kim M, Cho SM, Kim J. Prediction and evaluation of the cooling performance of radiators used in oil-filled power transformer applications with non-direct and direct-oil-forced flow. Experimental Thermal and Fluid Science. Jan 1, 2013;**44**:392. ISSN: 0894-1777. DOI: 10.1016/j.expthermflusci.2012.07.011

[20] Paramane SB. CFD study on thermal performance of radiators in a power transformer: Effect of blowing direction and offset of fans. IEEE Transactions on Power Delivery. 2014; **29**(6):2596-2604. ISSN: 0885-8977

[21] Paramane SB. A coupled internal-external flow and conjugate heat transfer simulations and experiments on radiators of a transformer. Applied Thermal Engineering. 2016;**103**: 961-970. ISSN: 1359-4311

[22] Rodriguez GR. Numerical and experimental thermo-fluid dynamic analysis of a power transformer working in ONAN mode. Applied Thermal Engineering. 2017;**112**:1271-1280. ISSN: 1359-4311

[23] Garelli L. Reduced model for the thermo-fluid dynamic analysis of a power transformer radiator working in ONAF mode. Applied Thermal Engineering. 2017;**124**:855-864. ISSN: 1359-4311

[24] Radakovic Z, Sorgic M. Basics of thermal-hydraulic model for thermal design of oil power transformers. IEEE Transactions on Power Delivery. 2010;**25**(2):790-802. ISSN: 0885-8977. DOI: 10.1109/TPWRD.2009.2033076

[25] van der Weken W, Paramane SB, Mertens M, Chandak V, Coddé J.. Increased efficiency of thermal calculations via the development of a full thermohydraulic radiator model. IEEE Transactions on Power Delivery. 2016;**31**(4):1473-1481. ISSN: 0885-8977. DOI: 10.1109/TPWRD.2015.2501431

Chapter 3

# Modeling and Simulation of Rotating Machine Windings Fed by High-Power Frequency Converters for Insulation Design

Fermin P. Espino Cortes, Pablo Gomez and
Mohammed Khalil Hussain

Additional information is available at the end of the chapter

http://dx.doi.org/10.5772/intechopen.78064

**Abstract**

Modern power systems include a considerable amount of power electronic converters related to the introduction of renewable energy sources, high-voltage direct current (HVDC) systems, adjustable speed drives, and so on. These components introduce repetitive pulses generated by the commutation of semiconductor switches, resulting in overvoltages with very steep fronts and high dielectric stresses. This phenomenon is one of the main causes of accelerated insulation aging of motors in power electronic-based systems. This chapter presents state-of-the-art computational tools for the analysis of motor windings excited by fast-front pulses related to the use of frequency converters based on pulse-width modulation (PWM). These tools can be applied for the accurate prediction of overvoltages and dielectric stresses required to propose insulation design improvements. In the case of the stress-grading system used in medium-voltage (MV) motors, transient finite-element method (FEM) is used to study the effect of fast pulses. It is shown how, by controlling the material properties and the design of the stress-grading systems, solutions to reduce the adverse effects of fast pulses from PWM-type inverters can be proposed.

**Keywords:** dielectric stress, fast-front pulses, motor windings, pulse-width modulation

## 1. Introduction

The detrimental effect of steep voltage surges propagating along the windings of power components such as transformers, reactors, motors, generators, and so on has been a topic of great interest for almost a century (see for instance [1–6]). In the case of motors, these surges

have been traditionally associated with energization, re-energization, or incoming lightning pulses [7]. Over the last decades, this has become a larger issue with the increasing use of frequency converters for speed and torque control, which introduce repetitive steep-front voltage impulses and associated partial discharges into the machine windings (see **Figure 1**). The insulation of this type of devices is subjected to high and sustained electric and thermal stresses [8, 9]. This effect is further amplified by the use of long connection cables [10].

Industrial surveys and other studies show that 20–40% of rotating machine failures are due to stator winding problems, and 70% of these are due to insulation failures [11–16]. Dielectric stress along motor's windings associated with the propagation of fast-front voltage surges is a major source of premature deterioration or failure of the insulation system of these devices [9, 17].

Early motor representations for fast-transient studies consisted of approximating the surge impedance of the motor as a simple lumped termination of the feeding cable [18]. This allowed understanding and predicting the transient overvoltages produced at the cable/motor connection. However, overvoltages can appear at several points inside the machine coils during the transient period. Models that are more detailed were later introduced to consider the transient potential distribution along windings. These models are known as white box models and can be classified in lumped and distributed parameter representations [7]. Although the former are easier to implement and less computationally expensive, the latter are more accurate since the wave propagation along the winding coils is introduced in a more precise manner.

Rudenberg first introduced the application of traveling wave theory to study the fast-transient behavior of windings [19]. A more rigorous approach based on a multi-conductor line model and applied to transformer windings was described by Rabins in 1960 [20]. Oraee [4] and Guardado [5] independently developed this approach for electrical machines in the 1980s. The main idea of their modeling approach is that a coil can be approximated by a multi-conductor transmission line (MTL): each conductor represents a turn (or group of turns) of the coil, and the continuity between the end of one turn and the beginning of the next one is preserved by

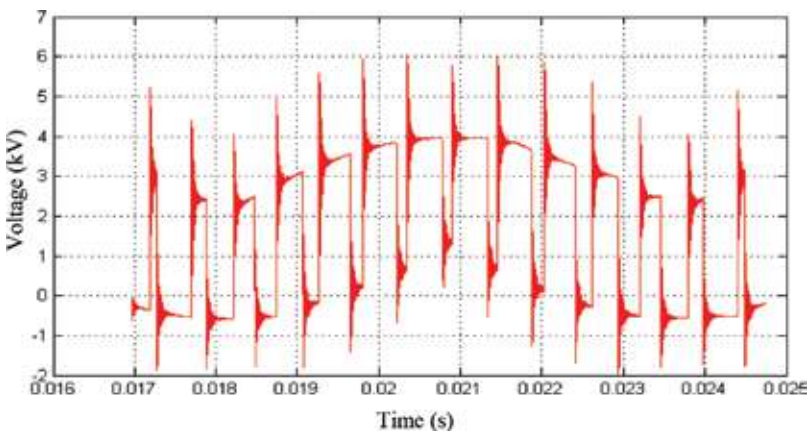


**Figure 1.** Typical voltage to ground of a medium-voltage winding fed by a three-level converter.

http://dx.doi.org/10.5772/intechopen.78064

means of a topological connection between the corresponding nodes. This is called a zig-zag connection and is shown in **Figure 2**.

The distributed parameter model of an MTL is completely characterized by its electrical parameter matrices: series impedance matrix **Z** and shunt admittance matrix **Y**. For the case of machine windings, these matrices are obtained from the geometrical configuration of the machine. Considering the typical stator coil diagram depicted in **Figure 3**, the incident surge

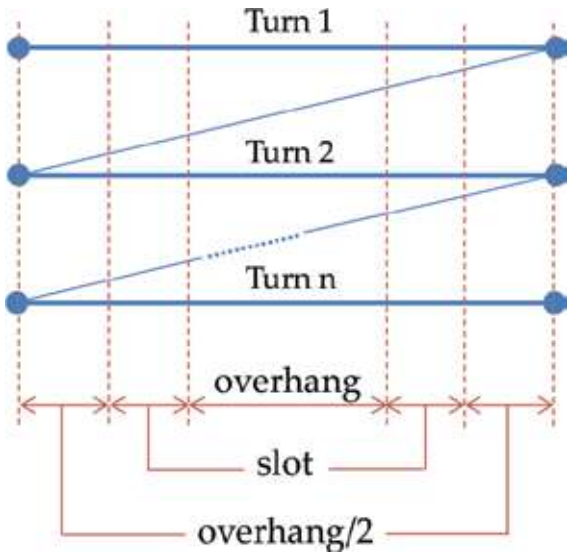


**Figure 2.** Multi-conductor transmission line model of the coil with a zig-zag connection (three turns are considered for the purpose of illustration) [21].

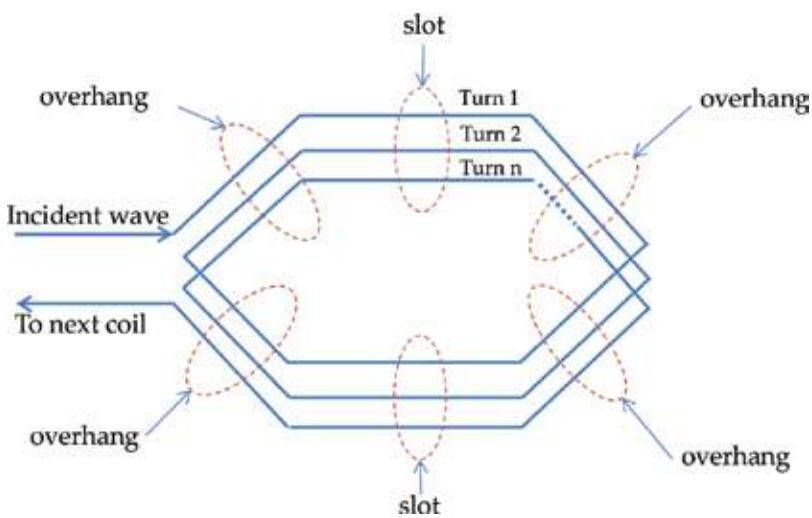


**Figure 3.** Coil sections in the stator frame [21].

will propagate along two different regions: slot and overhang. Due to the variation in the electromagnetic field distribution in these two regions, the corresponding parameter matrices will also be different [5].

Another challenging aspect of machine-winding modeling is the computation of electrical parameters. Common approaches followed for this task are (1) measuring the parameters, (2) applying analytical expressions, and (3) applying numerical methods. Analytical and numerical methods are the only possible choices for new designs. However, since machine windings have complex geometrical features, the available analytical expressions rely on numerous approximations and assumptions and are therefore restricted to particular geometries. Numerical methods are applicable in a more general sense as long as detailed geometrical and electrical data are available, which is the case at the design stage [22].

One of the first insulation problems stemming from the use of power frequency converters with medium-voltage (MV) motors was associated with the electric stresses on the surface of the coils. Partial discharge (PD) and heat can erode the coatings of the stress-grading (SG) system [23], aggravating the problem and, perhaps, eventually destroying the ground-wall insulation. This process can take a long time to produce a critical failure, but the ozone produced as a byproduct of surface PD [24] may accelerate the degradation and hence the need to rewind the motor [23].

The SG system in MV-rotating machines is composed of two coatings: the conductive armor coating and the semi-conductive stress-grading coating. The conductive armor coating is a relatively conductive layer that is usually applied in the form of a tape to the surface of the ground-wall insulation in form-wound coils that lies inside the stator slot of a rotating machine. The function of this coating is to limit the surface potential of the coil to a value equal or close to ground potential, thereby avoiding the possibility of discharges between the coil insulation and the slot wall. The length of the conductive armor coating extends beyond the end of the slot [25], as illustrated by part A in **Figure 4**. The semi-conductive-grading coating starts at the end of the conductive armor coating, part B, also in the form of a tape, and they are often overlapped by a couple of centimeters, shown as region E. The purpose of the semi-conductive-grading coating is to produce a smooth transition from the potential in the conductive armor coating to the high voltage (HV) on the surface of the coil insulation outside of the slot, shown as part C in **Figure 4**. The graded voltage drop along the surface of the coil avoids harmful high electric field concentrations.

The conductive armor coating is commonly a composite of either varnish or polyester resin filled with graphite or carbon black. It is considered as a constant conductivity layer with values between 10 and 0.01 S/m. The semi-conductive-grading coating of coils is a composite of silicon carbide (SiC) and varnish or polyester resin, with a field-dependent conductivity. A profile of the voltage from the slot exit to the end of the semi-conductive-grading tape (SGT) measured using an alternating current (AC) electrostatic voltmeter is shown in **Figure 5**. The coil was energized with 8 kVrms at 60 Hz. The conductive armor tape (CAT) is at ground potential (first 10 cm in the plot of **Figure 5**) while along the SGT the voltage increases smoothly (after 10 cm), something that is accomplished by the generation of resistive heat as

http://dx.doi.org/10.5772/intechopen.78064

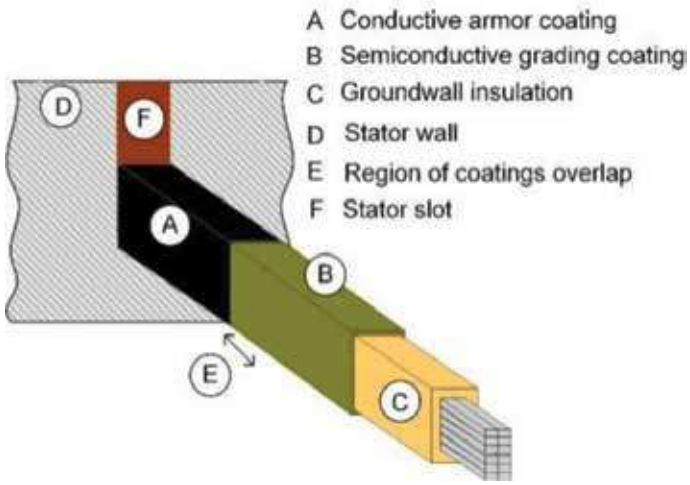


**Figure 4.** Illustration showing conductive armor and semi-conductive-grading coatings on a form-wound coil [26].

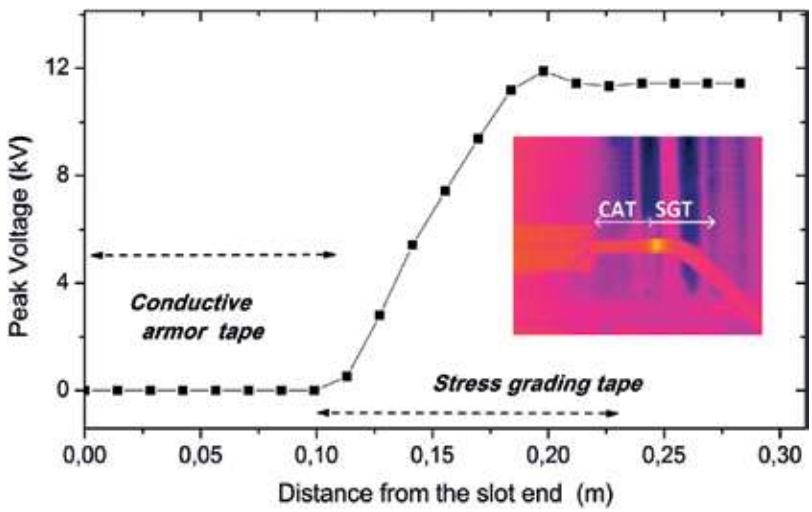


**Figure 5.** Illustration showing conductive armor and stress-grading coatings on a form-wound coil under sinusoidal 60-Hz voltage [26].

seen in the inserted infrared image of **Figure 5**, where the section of the SG presents a hot spot. The slope of the voltage defines the tangential electric field on the surface of the stress-grading region. Overvoltages and pulses having steep fronts, like those from PWM-type inverters, considerable modify the stress relief in the SGT and in the portion of the CAT that is outside of the slot. The design of the stress grading and the conductive armor coatings has become difficult under this condition, and modeling had resulted in a useful tool in understanding the influence of the various design parameters.

The remaining of this chapter is divided as follows: Section 2 describes the modeling and parameter determination of motor windings excited by the fast pulses produced by an inverter. Section 3 describes a finite-element method (FEM)-based approach to analyze the performance of stress-grading systems. Finally, Section 4 presents the conclusions and final remarks of this chapter.

## 2. Fast-transient modeling of rotating machine windings for inverter excitation

The computer model described in this section for the prediction of the fast-transient response of the machine winding is a non-uniform, multi-conductor, distributed-parameter model defined in the frequency domain. This model is selected over other alternatives given its good balance between high accuracy and practicality, as explained below:

1. *Why non-uniform?* The distribution of electric and magnetic fields is different in the slot and overhang regions, resulting in different electrical parameters for each region that should be considered to accurately reproduce the pulse propagation. In this case, the non-uniform model consists of five segments considering the typical geometry of a wound-form motor, as shown in **Figures 3** and **6**.
2. *Why multi-conductor?* This modeling approach of the winding allows natural inclusion of the inductive and capacitive coupling between turns [21].
3. *Why based on distributed parameters?* A distributed parameter model based on transmission line theory can represent the propagation of a fast pulse along windings in a more rigorous manner than a lumped parameter model based on circuit theory [27].
4. *Why defined in the frequency domain?* The partial differential equations describing wave propagation in time domain become ordinary differential equations in the frequency domain, making the solution more straightforward. In addition, including frequency dependence of the system parameters is substantially easier in the frequency domain than in the time domain [28].

The winding electrical parameters (capacitance, inductance, and losses) in the overhang and slot regions of the coil are calculated using the finite-element method (FEM)-based software COMSOL Multiphysics [29], as described in Section 2.2.

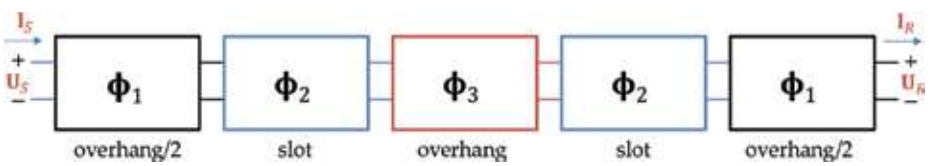


**Figure 6.** Cascaded connection of chain matrices to model all coil regions [22].

### 2.1. Winding model

Wave propagation along the non-uniform multi-conductor transmission system representing the winding is defined by the Telegrapher equations in the Laplace domain as follows [30, 31]:

$$\frac{d}{dx}\begin{bmatrix}\mathbf{U}(x,s)\\ \mathbf{I}(x,s)\end{bmatrix}=\begin{bmatrix}0 & -\mathbf{Z}(x,s)\\ -\mathbf{Y}(x,s) & 0\end{bmatrix}\begin{bmatrix}\mathbf{U}(x,s)\\ \mathbf{I}(x,s)\end{bmatrix} \tag{1}$$

In Eq. (1), $\mathbf{U}(x,s)$ and $\mathbf{I}(x,s)$ are the voltage and current vectors at point $x$ along the line, $\mathbf{Z}(x,s)$ and $\mathbf{Y}(x,s)$ are the series impedance and shunt-admittance matrices of the line per unit length, respectively. According to Eq. (1), the winding electrical parameters are a function of both space and time. Voltages and currents at the terminals of the segment can be related using the chain matrix definition, assuming constant parameters over a segment $\Delta x$ and applying boundary conditions at $x$ and $x+\Delta x$ [31]:

$$\begin{bmatrix}\mathbf{U}(x+\Delta x,s)\\ \mathbf{I}(x+\Delta x,s)\end{bmatrix}=\boldsymbol{\phi}(\Delta x,s)\begin{bmatrix}\mathbf{U}(x,s)\\ \mathbf{I}(x,s)\end{bmatrix} \tag{2}$$

where the chain matrix of the segment is defined as

$$\boldsymbol{\phi}(\Delta x,s)=\begin{bmatrix}\cosh(\boldsymbol{\psi}\Delta x) & -\mathbf{Y}_0^{-1}\sinh(\boldsymbol{\psi}\Delta x)\\ -\mathbf{Y}_0\sinh(\boldsymbol{\psi}\,\Delta x) & \mathbf{Y}_0\cosh(\boldsymbol{\psi}\Delta x)\mathbf{Y}_0^{-1}\end{bmatrix} \tag{3}$$

In Eq. (3), $\boldsymbol{\psi}$ is the propagation constant matrix of the line, given by $\boldsymbol{\psi}=\mathbf{M}\sqrt{\boldsymbol{\lambda}}\mathbf{M}^{-1}$, where $\mathbf{M}$ and $\boldsymbol{\lambda}$ are the eigenvalue and eigenvector matrices of the $\mathbf{Z}(x,s)\mathbf{Y}(x,s)$ product, respectively. In addition, $\mathbf{Y}_0$ is the characteristic admittance matrix of the line segment, given by $\mathbf{Y}_0=\mathbf{Z}(x,s)^{-1}\boldsymbol{\psi}$. The two-port representation defined by Eq. (2) is the basis of the non-uniform model of the machine-winding coil, according to the following procedure [21]:

1. The coil is divided into five segments, as shown in **Figures 2** and **6**.
2. Each of the five chain matrices is obtained from Eq. (3) as a function of parameters **Z** and **Y**, which are different in the geometrical regions identified as overhang and slot.
3. The chain matrices are multiplied according to the cascaded connection shown in **Figure 6** in order to obtain a single chain matrix representing the complete coil.

Voltages and currents at the sending ($S$) and receiving ($R$) nodes of the complete coil are related as follows:

$$\begin{bmatrix}\mathbf{U}_R\\ \mathbf{I}_R\end{bmatrix}=\boldsymbol{\phi}_1\boldsymbol{\phi}_2\boldsymbol{\phi}_3\boldsymbol{\phi}_2\boldsymbol{\phi}_1\begin{bmatrix}\mathbf{U}_S\\ \mathbf{I}_S\end{bmatrix}=\begin{bmatrix}\boldsymbol{\Phi}_{11} & \boldsymbol{\Phi}_{12}\\ \boldsymbol{\Phi}_{21} & \boldsymbol{\Phi}_{22}\end{bmatrix}\begin{bmatrix}\mathbf{U}_S\\ \mathbf{I}_S\end{bmatrix} \tag{4}$$

In Eq. (4), $\boldsymbol{\Phi}_{11}$, $\boldsymbol{\Phi}_{12}$, $\boldsymbol{\Phi}_{21}$, and $\boldsymbol{\Phi}_{22}$ are the elements of the complete chain matrix representation of the coil. This representation is transformed into an equivalent admittance matrix form to

include the zig-zag connection in order to preserve continuity between turns as a pulse propagates along the coil (see **Figure 2**) [32, 33]. This yields

$$\begin{bmatrix} \mathbf{U}_S \\ \mathbf{U}_R \end{bmatrix} = \begin{bmatrix} \mathbf{Y}_{SS} + \mathbf{Y}_{con11} & -(\mathbf{Y}_{SR} + \mathbf{Y}_{con12}) \\ -(\mathbf{Y}_{SR} + \mathbf{Y}_{con21}) & \mathbf{Y}_{RR} + \mathbf{Y}_{con22} \end{bmatrix}^{-1} \begin{bmatrix} \mathbf{I}_S \\ \mathbf{U}_R \end{bmatrix} \tag{5}$$

The admittance matrix and chain matrix elements are related according to the following expressions:

$$\mathbf{Y}_{ss} = -\mathbf{\Phi}_{12}^{-1}\mathbf{\Phi}_{11}, \mathbf{Y}_{SR} = -\mathbf{\Phi}_{12}^{-1} = -\mathbf{\Phi}_{22}\mathbf{\Phi}_{12}^{-1}\mathbf{\Phi}_{11} + \mathbf{\Phi}_{21}, \mathbf{Y}_{RR} = -\mathbf{\Phi}_{22}\mathbf{\Phi}_{12}^{-1} \tag{6}$$

In Eq. (5), admittance submatrices $\mathbf{Y}_{con11}$, $\mathbf{Y}_{con12}$, $\mathbf{Y}_{con21}$, and $\mathbf{Y}_{con22}$ are included to connect the end of each turn to the beginning of the next one (zig-zag connection), as well as the source and load admittances representing winding terminal connections.

The Laplace-domain voltages at each turn of the coil are obtained from Eq. (5). These voltages are finally transformed into transient voltage responses in the time domain by means of the application of the inverse numerical Laplace transform [28].

### 2.2. Parameter computation

FEM-based simulation program COMSOL Multiphysics is used to compute the capacitance and inductance matrices in the overhang and slot regions of the machine winding [29]. For the calculation of inductance in the slot region, it is assumed that the slot walls behave as magnetic insulation due to eddy currents at the high frequencies related to the pulses produced by frequency converters, meaning that the flux is normal to the boundary and does not penetrate the core. In the overhang region, these walls are replaced by an open-boundary condition.

#### *2.2.1. Capacitance*

Capacitance matrix **C** is calculated using the electrostatics module of COMSOL using the forced voltage method as follows [22]:

$$\begin{bmatrix} Q_1 \\ \vdots \\ Q_n \end{bmatrix} = \begin{bmatrix} C_{11} & \cdots & C_{1n} \\ \vdots & \ddots & \vdots \\ C_{n1} & \cdots & C_{nn} \end{bmatrix} \begin{bmatrix} U_1 \\ \vdots \\ U_n \end{bmatrix} \tag{7}$$

The charge in all $n$ elements due to conductor $i$ is obtained by exciting conductor i with a fixed voltage while defining all other conductors at zero potential, thus obtaining the $i$-th column of the capacitive matrix. This process is repeated for each conductor to obtain the complete matrix.

#### *2.2.2. Inductance*

Inductance matrix **L** is computed from the magnetic energy method [22]. The current is nonzero in one or two terminals at a time and the energy density is integrated over the whole

geometry. Self-inductance $L_{ii}$ is obtained from the magnetic energy $W_{m,i}$ due to the injection of a current $I_i$ to turn $i$:

$$L_{ii} = \frac{2W_{m,i}}{I_i^2} \tag{8}$$

Mutual inductance $L_{ij}$ is obtained from the magnetic energy $W_{m,ij}$ due to the simultaneous injection of current to turns $i$ and $j$:

$$L_{ij} = \frac{W_{m,ij}}{I_i I_j} - \frac{1}{2}\left(\frac{I_i}{I_j}L_{ii} + \frac{I_j}{I_i}L_{jj}\right) \tag{9}$$

When using this method, all self inductances must be computed first and then applied for the computation of mutual inductances.

#### *2.2.3. Losses*

The series losses matrix (**R**) of the winding is considered frequency-dependent and obtained from the concept of complex penetration depth [22]. The dielectric losses matrix (**G**) is computed using the "electric currents" module in COMSOL [29]. Finally, the series impedance and shunt admittance matrices required by the winding model are computed according to $\mathbf{Z} = \mathbf{R} + s\mathbf{L}$ and $\mathbf{Y} = \mathbf{G} + s\mathbf{C}$.

### 2.3. Case study

A schematic cross-section of the coil considered in this study is shown in **Figure 7**. The main parameters of the stator coil are summarized in **Table 1**. **Figure 8** shows a schematic representation and a picture of the experimental setup. Besides the MV form-wound coil under test, it includes a waveform generator (Keysight 33500B), an oscilloscope (Agilent DSO-X 2014A), and a 100-Ω load connected at the end of the coil. Steel plates were included to emulate the EM field distribution in the slot region [34]. The experimental setup was placed in a laboratory facility free of EM interference. More details of this test case can be found in [35].

The capacitance and inductance matrices are computed from FEM simulations using COMSOL Multiphysics, as explained in Section 2.2. Sample simulations are shown in **Figures 9** and **10** for the first turn.

**Figure 9** shows the distribution of electric potential when turn 1 (top turn) is excited with 1 V, while all other turns and the slot walls are grounded. This allows the calculation of the first column of the capacitance matrix of the coil using Eq. (7). **Figure 10** shows the distribution of magnetic energy density when turn 1 is excited with 1 A, while all other turns are left unexcited. Integrating this magnetic energy density results in the magnetic energy required in Eq. (8) to compute the self-inductance of turn 1.

The winding model is validated considering a PWM-type excitation with different rise times between 100 and 500 ns connected to the first turn of the coil. The rest of winding is represented

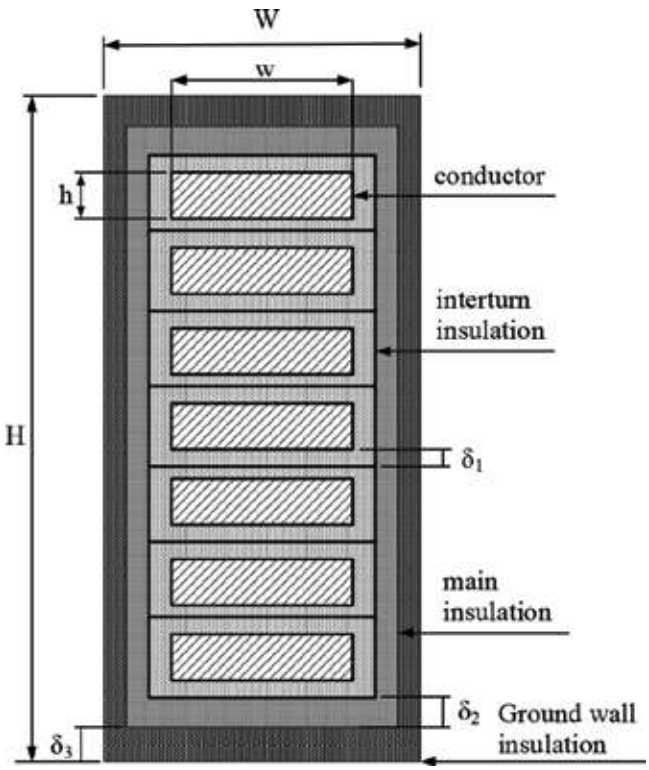


**Figure 7.** Cross section of the coil with three insulation layers [35].

| | |
|---|---|
| Turns per stator coil | 7 |
| Length of overhang region | 0.33 m |
| Conductor width (w) | 5.35 mm |
| Conductor height (h) | 2.85 mm |
| Resistivity of stator bar conductor | $1.7 \times 10^{-8}$ Ω·m |
| Thickness of interturn insulation (δ1) | 0.2 mm |
| Thickness of main insulation (δ2) | 1.41 mm |
| Thickness of ground-wall insulation (δ3) | 0.36 mm |
| Relative permittivity of the interturn insulation | 2.5 |
| Relative permittivity of the main insulation | 2 |
| Relative permittivity of the ground-wall ins | 2.8 |
| Slot width (W) | 8.9 mm |
| Slot height (H) | 24.2 mm |
| Slot length | 0.45 m |

**Table 1.** Rotating machine parameters [35].

http://dx.doi.org/10.5772/intechopen.78064

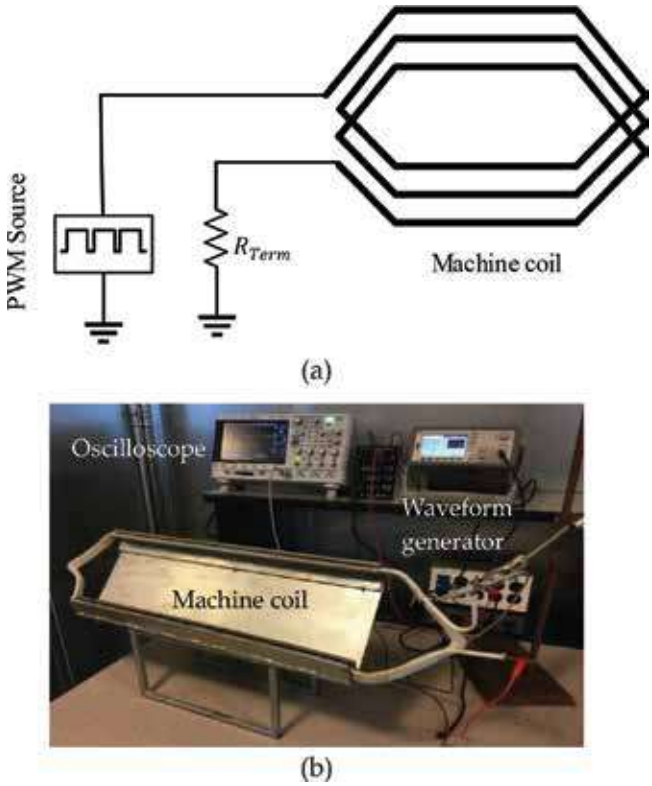


**Figure 8.** Experimental setup for validation of the inverter-coil setup: (a) schematic diagram showing main parts and (b) photography of laboratory components [35].

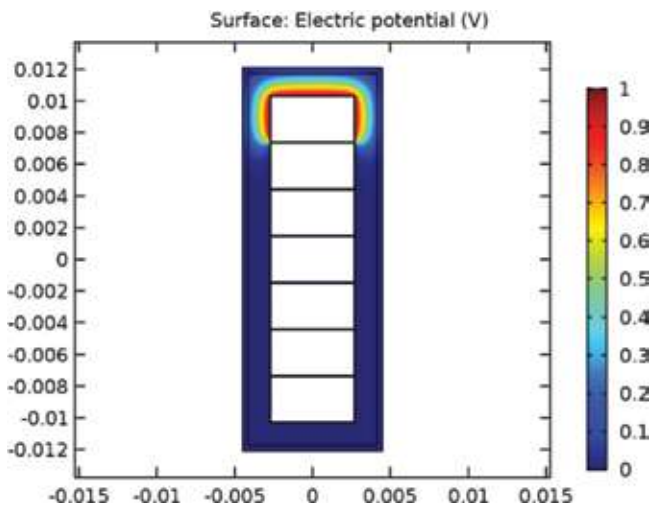


**Figure 9.** Capacitance calculation using forced voltage method in FEM [35].

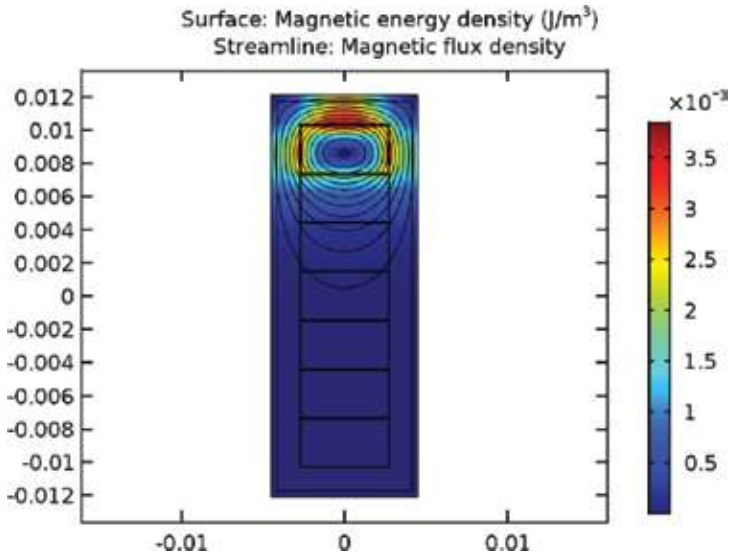


**Figure 10.** Inductance calculation using magnetic energy method in FEM [35].

by a 100-Ω load. This type of excitation is obtained from the waveform generator emulating the phase-to-ground voltage from a voltage source inverter.

**Figure 11** shows the comparison of the simulated and measured transient voltage at the first winding turn for excitations with different rise times. It can be noticed that the magnitude of the overshoot produced depends on the rise time of the excitation. A second assessment of the winding corresponds to a similar setup, but with an open-ended condition of the coil. This results in noticeable oscillations, which are reproduced in a very accurate manner by the winding model, as shown in **Figure 12**, which illustrates the transient response at the far end

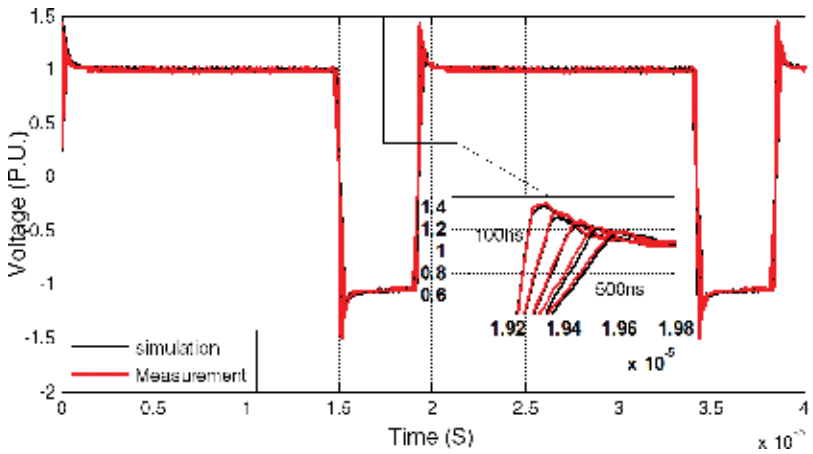


**Figure 11.** Transient overvoltage at the first turn of the coil terminated in 100-Ω load [35].

http://dx.doi.org/10.5772/intechopen.78064

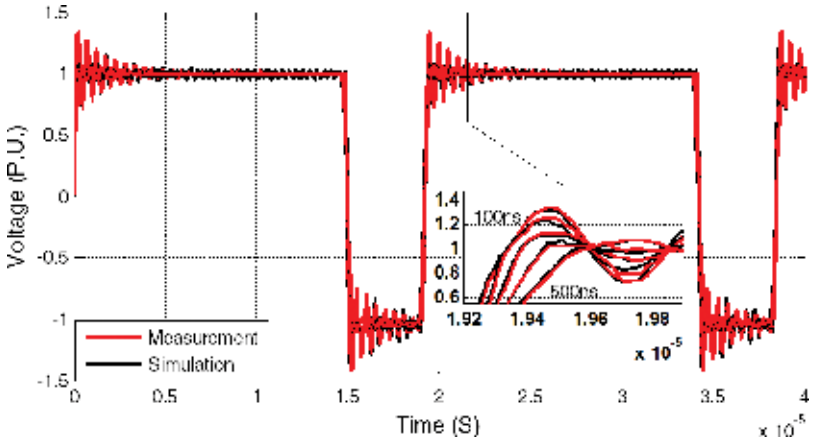


**Figure 12.** Transient overvoltage at the last turn of the coil for open-ended case [35].

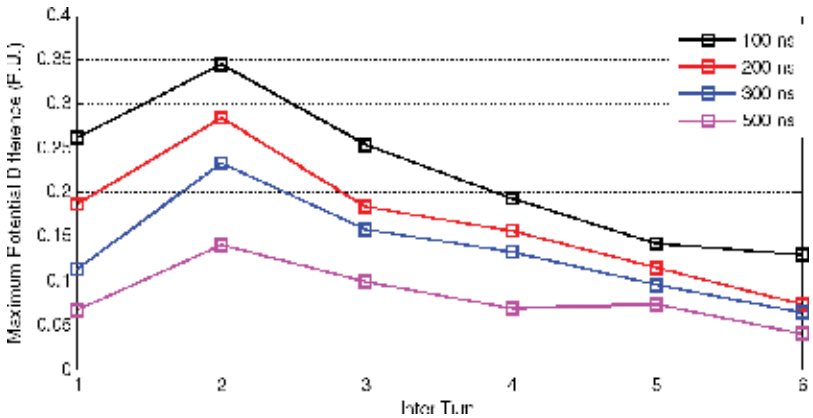


**Figure 13.** Potential difference between turns considering different rise times of the excitation [35].

of the winding. As in the previous case, the maximum overvoltages are related to the highest rise time of the excitation.

The effect of the excitation rise time is analyzed in a more general manner in **Figure 13**, which shows the potential difference between turns for different rise times. According to this figure, the potential difference is inversely proportional to the rise time of the excitation.

## 3. Modeling of stress-grading systems from rotating machines

Modeling of stress-grading systems of MV rotating machines is an essential tool for their design and optimization. An accurate model can serve several purposes, such as [36]:

**1.** describing how the system is likely to behave under certain conditions;

2. modifying the material characteristics to match specific requirements;
3. predicting the effects of aging and determining the material's life time in order to establish a maintenance policy.

FEM has become one of the most commonly used techniques for modeling stress-grading systems [37–39]. With FEM, the geometry can be considered including most of the details that influence the electric field distribution. To determine how the electric field stress is distributed during PWM voltage excitation, the problem must be solved in the time domain with considerably small time steps. This, together with the high nonlinearity of the semi-conductive stress-grading coating, makes modeling of SG systems a complicated task [40, 41].

### 3.1. Modeling of stress-grading systems

In the general case, problems with stress-grading systems can be represented with subdomains of conductors, subdomains of perfect dielectrics (air or another surrounding medium and main insulation), and subdomains of stress-grading materials [42]. Conductors can be considered perfect conducting regions of known potential. Neglecting the dielectric loss component of the materials, the equation to be solved is of the form [43]

$$\nabla\cdot[-\sigma(\mathbf{E})\nabla U] + \frac{\partial[\nabla\cdot(\varepsilon_r\varepsilon_0(-\nabla U))]}{\partial t} = 0 \tag{10}$$

where $\sigma$ is the electrical conductivity, $\varepsilon_r$ is the relative permittivity, and $\varepsilon_0$ is the vacuum permittivity. The electric field dependency ($\sigma(\mathbf{E})$) of the semi-conductive-grading coating helps to limit the maximum electric field on the surface of the coil giving adaptability to different designs and voltage levels [44]. For proper FEM simulations, it is required to know the nonlinearity of the electrical conductivity at high electric stress for the semi-conductive-grading material. One of the most common expressions used to define the electric field dependency in S/m of this coating is given by [45, 46]

$$\sigma(E_t) = \sigma_0 \exp(\alpha {E_t}^n) \tag{11}$$

where $\sigma_0$ = 1.85 x $10^{-9}$ S/m, $\alpha$= 0.00112, and $n$ = 0.67. Eq. (10) can be solved analytically or numerically. FEM or an Equivalent Electric Circuit Model [36] can be used for this purpose. FEM is widely used to model the SG coatings due to some advantages over, for example, equivalent circuit models. With circuit models, some geometric aspects of the SG systems, like overlapping of coatings or the sharp end of the slot exit, are difficult to be considered. In addition, with FEM, the thermal field problem can be solved using the same geometry, taking as a source of heat the ohmic losses from the electric solution.

Transient FEM with efficient algorithms needs to be used in order to solve the highly nonlinear problem associated with SG coatings. Nowadays, FEM software provides new capabilities that allow performing highly nonlinear simulations. The "electric currents" module of the FEM-based software COMSOL Multiphysics [29] is used in the next sections to compute the electric

http://dx.doi.org/10.5772/intechopen.78064

field distribution and resistive heat produced in the CAT and SGT of form-wound coils under the application of fast rise time pulses.

### 3.2. FEM modeling of stress-grading coatings under PWM voltage waveforms

With the aid of an infrared camera, it is possible to observe the heat generated because of the electric stress grading under fast pulses. In order to show this condition, a 4.2-kV form wound coil was energized with 4-kV squared pulses with a repetition rate of 2000 pulses per second, and the temperature was registered using an infrared camera model Flir-SC500. As it can be seen in **Figure 14**, the heat distribution is different in comparison to that presented in **Figure 5** for power frequency (60 Hz); under this condition, the high electric stress moves from the SGT to the CAT at slot exit. Something important to notice in the infrared image is the presence of hot spots that follow the patterns of the CAT tapping; this will be discussed in Section 3.4.

Usually, modeling of the conductive armor coating and the semi-conductive-grading coatings is done separately; however, under fast pulses, it is important to understand the combined performance of both coatings. Therefore, the analysis of coil ends working with PWM voltages requires the simultaneous simulation of both coatings.

#### *3.2.1. Finite-element dimension reduction on the stress-grading coatings*

A useful tool in FEM modeling is the ability of reducing the dimension of the elements used to discretize the stress-grading coating subdomain [29]. These coatings are applied in thin layers that require a very fine element discretization; otherwise, if a coarse discretization of the subdomains is used, numerical instability may result [47]. Assuming that the conductivity of the semi-conductive coating depends only on the tangential component of the electric field, the elements used in the SG coatings can be reduced to one dimension (1D) [48]. If the geometry of the problem is considered in two dimensions (2D), as shown in **Figure 15(a)**, the subdomains

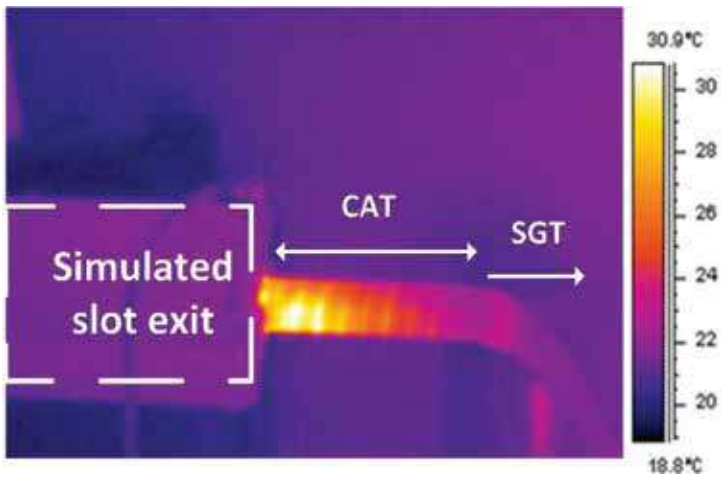


**Figure 14.** Temperature profile on a 4.2-kV coil end under 650-ns rise time pulses with a repetition rate of 2000 pulses per second. Peak voltage: 4.0 kV [26].

for the CAT and SGT can be discretized using one-dimensional elements (electric shielding boundary in COMSOL), thereby considerably reducing the total number of elements and, in most cases, making it easier for the solution to converge.

Consider for simulation the 2D geometry of the coil end shown in **Figure 15(a)** and the transient voltage of a leading edge of one PWM pulse, shown in **Figure 15(b)**. The pulse has a rise time of 1 μs and an overshoot of around of 1.6 times the nominal phase to ground peak voltage for a 6.6-kV coil. The thickness of the ground-wall insulation is 3 mm, the CAT and SGT are 0.5 mm thick, and their lengths are 50 and 100 mm, respectively. The CAT conductivity is 0.01 S/m, and the conductivity of the SGT is given by Eq. (11). The relative permittivities ($\varepsilon_r$) of the CAT and the SGT are, respectively, 50 and 20. A comparison of the results for the electric field on the CAT and SGT using 1D and 2D elements is presented in **Figure 16**. As it can be seen in this figure, this 1D simplification does not modify the results when compared to the solution obtained considering 2D elements.

In addition, the simplification from a 2D to a 1D modeling can be indeed useful, especially when non-axial-symmetric geometries need to be modeled in three dimensions. For example, form-wound coils can be modeled in 3D, when considering 2D elements in the stress-grading subdomains [49]. One problem that occurs with this simplification is that geometrical details like overlapping in multilayer systems are sometimes difficult to implement.

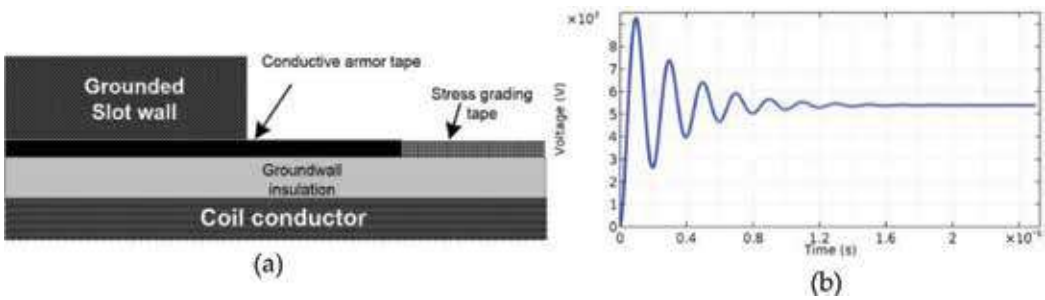


**Figure 15.** (a) Cross-section illustration of the form-wound coil and (b) transient pulse voltage waveform considered in the transient FEM simulations [26].

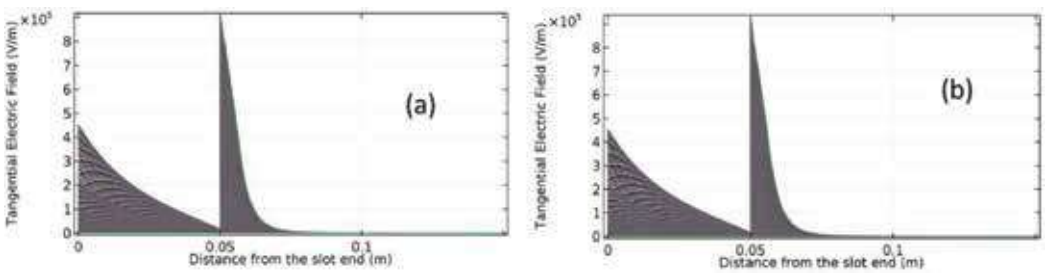


**Figure 16.** Tangential electric field distribution along the stress-grading coatings computed using (a) 2D elements and (b) 1D elements.

http://dx.doi.org/10.5772/intechopen.78064

However, simulations using discretization of the CAT and SGT with one dimension elements reduction can give a sufficiently good approximation when these details are not required in the simulations.

When the response of an SG system during a PWM waveform needs to be modeled, a large computing time is generally required, since the time step is defined by the fast rise time of the pulses (1 μs or less) and the simulation time is in the order of several milliseconds. Using reduced dimension elements in the CAT and SGT domains makes the simulation computationally more efficient. One example of the convenience of this dimension reduction is shown with the transient simulation of electric field and heat in a coil with 3-mm thickness of the ground-wall insulation, and 1 mm CAT and SGT thickness; the length of the CAT is 50 mm from the slot exit. The CAT conductivity is 0.01 S/m, and the relative permittivity is 100. The length of the SGT is 100 mm. The SGT has a relative permittivity of 20 and a nonlinear conductivity given by Eq. (11). Considering a phase-to-ground three-level PWM voltage [50], which waveform is shown in the inset of **Figure 17(a)**, the magnitude of the tangential electric stress versus time is present along both coatings, as it can be observed in **Figure 17(a)**. The magnitude of the resistive heat density along the CAT and SGT as a function of time and electric field is presented in **Figure 17(b)**. According to this figure, the heat is concentrated mainly in the CAT.

The tangential component of the electric field in the CAT is well below the tangential electric field in the SGT (**Figure 17(a)**), but the heat generated in this coating is considerably higher (**Figure 17(b)**). Experimental work on form-wound coils stressed by fast pulses has shown that this condition can damage the CAT, allowing surface PD to appear right at the slot exit [51, 52]. The next section introduces the use of FEM modeling to investigate possible solutions to this problem.

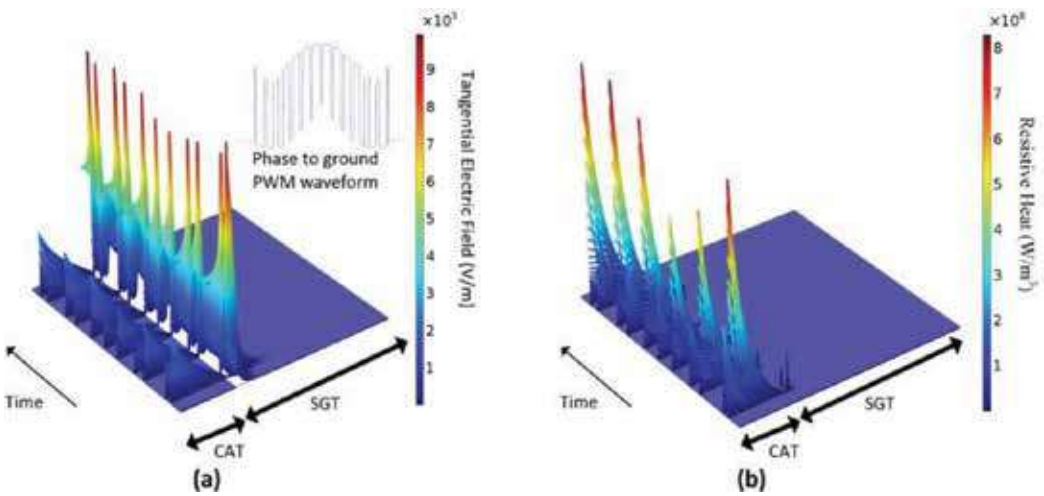


**Figure 17.** (a) Tangential electric field distribution along the surface from the slot end of the coil under a phase to ground PWM waveform and (b) resistive heat [53].

### 3.3. Modeling for the design of stress-grading coatings under PWM voltages

As mentioned before, the SG systems in motor coil ends can fail because of the excessive heat generated when they operate under fast rise time pulses like those produced by adjustable speed drives. The excessive heat produced in the CAT can be considered the first problem to be solved in order to improve the performance of these coatings under fast pulses. **Figure 18** shows the resistive heat density for the same case presented in **Figure 16**. It can be noticed that the heat is produced mainly in the CAT. The heat and electric field in the CAT can be reduced by increasing the conductivity of this coating; however, the high stress will be now moved to the SGT. A possible solution consists of controlling both the material properties and the designs of stress-grading system [26]. For example, a sectionalized stress-grading system consisting of two coatings with different conductive properties can be used in the CAT in addition to the SGT in order to divide the electric field and ohmic losses at the coil end. The first part, starting from the slot end, is a highly conductive coating, and the second part is now referred to as stress-grading coating for high-frequency components ($SG_{HF}$). The $SG_{HF}$ coating is designed to filter and relieve the fast rise front of the pulses, while a third coating ($SG_{LF}$) is used to grade the lower frequency components of the PWM voltage waveform.

As an example, consider a sectionalized stress-grading system where the thickness of the $SG_{HF}$ and $SG_{LF}$ layers is duplicated (1 mm), and the electric properties of the first layer are conductivity of 0.5 S/m, and $\varepsilon_r = 50$, for the second conductive layer ($SG_{HF}$): conductivity of 0.05 S/m, and $\varepsilon_r = 50$. The third layer SGT is an with the same nonlinear characteristic given by Eq. (11), but with a value of $\sigma_0 = 1.85 \times 10^{-8}$ S/m.

The distribution of resistive heat and electric field is modified, as it can be seen in **Figure 19**. With the first conductive layer, the maximum heat is moved to the $SG_{HF}$ and $SG_{LF}$ layers and reduced in around 50%, see **Figure 19(a)**. The electric field is not increased in the $SG_{LF}$ in comparison with the electric field in the original design presented in **Figure 16**, as shown in **Figure 19(b)**. This is an example of how modeling allows modifying the properties and dimensions of the stress-grading coatings in order to obtain the desired stress grading.

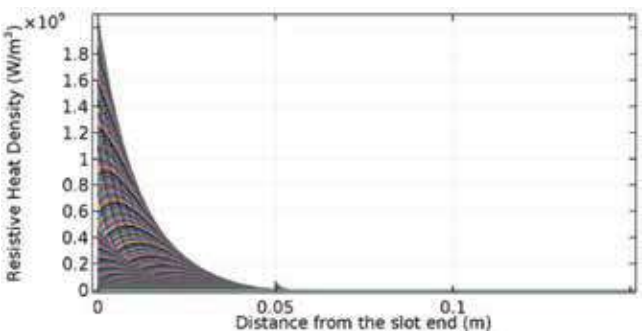


**Figure 18.** Resistive heat distribution along the stress-grading coatings for the same case of the results presented in **Figure 14**.

http://dx.doi.org/10.5772/intechopen.78064

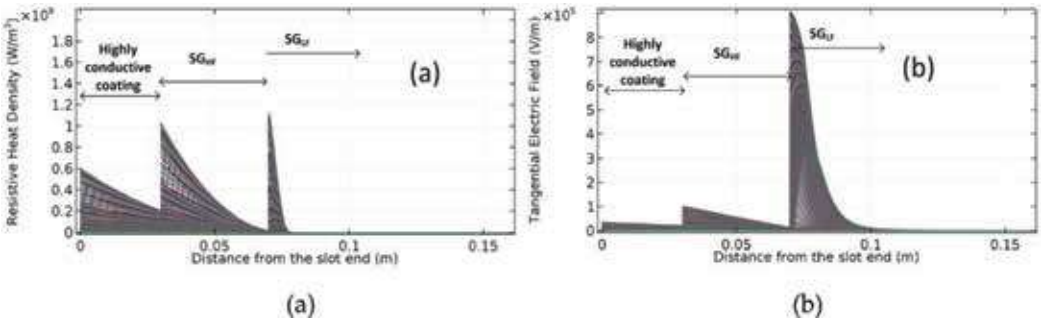


**Figure 19.** (a) Resistive heat and (b) electric field distribution along the sectionalized stress-grading system.

### 3.4. Simulation of the tapping of stress-grading systems under fast pulses

As mentioned before, an important characteristic of FEM modeling of stress-grading systems is the possibility of taking into account some details of the geometry that can influence the stress distribution under fast rise time pulses. In tape-based SG systems, the SGT usually overlaps the CAT a couple of centimeters, with one or two full-lapped turns followed by half-lapped turns until it reaches the desired length. During FEM modeling, the overlapping interfaces can be reproduced as in the real condition; however, it is not usual to consider the tape interfaces. Optical micrographs of the overlapping tape sections, obtained from form-wound coils, have shown that there are transition sections of the coatings with only one tape thickness between segments with two tape thickness [54].

Two-dimensional FEM simulations of the stress-grading system are performed considering the coatings configuration and the voltage waveform from **Figure 15**, but now the geometrical shape of the half overlapping between tape turns is included. For this case, the conductivity of the CAT was considered as 0.01 S/m, with a relative permittivity of 50,

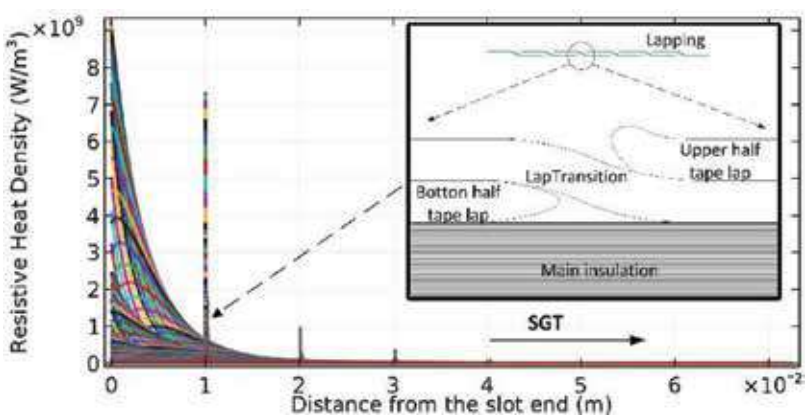


**Figure 20.** Heat in the CAT and SGT coatings considering the tape overlappings.

and the CAT-CAT overlappings occurring every centimeter. The conductivity of the SGT is given by Eq. (11). The shape considered for the tape overlappings is shown in the inset of **Figure 20**. In the same figure, the simulation results show how the CAT-CAT overlappings present high values of heat, behavior that is experimentally confirmed by the temperature distribution presented in **Figure 14**. These results demonstrate how the quality of the application of these tape-based coatings must be guaranteed to avoid early problems with the machines fed by PWM drives.

## 4. Conclusions

Two crucial topics for the proper insulation design of MV motors excited by PWM drives have been reviewed in this chapter: modeling of the windings for pulse propagation analysis and modeling of the stress-grading system.

A frequency domain non-uniform multi-conductor transmission line approach has been used to study the fast-front transient response of a machine-winding coil when a PWM-type excitation from an inverter is applied. The parameters of the coil were calculated using the finite-element method. The results when applying a PWM-type excitation to the coil show that the rise time of the source and the length of the cable has an important effect on the transient overvoltage produced at different turns of the coil, as well as in the potential difference between adjacent turns. The comparison between simulation and experimental results, in terms of oscillatory behavior and magnitude, demonstrates that both the winding model and the cable model selected result in a very accurate prediction of the fast-transient response related to the use of inverters in medium-voltage induction machines. Since the winding model is considered as linear for high frequencies, a frequency domain-modeling approach is a very good option to study the fast-transient response of machine windings.

On the other hand, the conductive armor and semi-conductive-grading coatings are important parts of the insulation system in rotating machines. The correct design of these coatings becomes difficult when PWM voltages feed the machine from adjustable speed drives. The stress-grading coatings often cannot effectively relieve the stress during repetitive surge voltages and, in the extreme case, hot spots and/or PDs will gradually destroy the coatings, making the problem worse. FEM modeling is a useful tool in understanding the influence of the various design parameters eliminating the trial and error methods that usually require more time and other resources. By reducing the dimension of the elements used to discretize the stress-grading coatings subdomains, it is possible to reduce the computational burden, but when a detailed geometry of the stress-grading system needs to be included in the simulation, this option cannot be considered. By using FEM modeling, it is possible to compute the maximum electric field, power loss, or voltage at the end of the SGT and use these variables in conjunction with optimization subroutines to obtain improved designs.

## Author details

Fermin P. Espino Cortes[1], Pablo Gomez[2*] and Mohammed Khalil Hussain[2,3]

*Address all correspondence to: pablo.gomez@wmich.edu

1 Instituto Politecnico Nacional, Mexico City, Mexico

2 Western Michigan University, Kalamazoo, MI, USA

3 University of Baghdad, Baghdad, Iraq

## References

[1] Calvert JF. Protecting machines from line surges. Transactions of the American Institute of Electrical Engineers. 1934;**53**(1):139-146

[2] Abetti PA, Maginniss FJ. Fundamental oscillations of coils and windings. Transactions of American Institute of Electrical Engineers. Part III: Power Apparatus and Systems. 1954; **73**(1):1-10

[3] Cornick KJ, Thompson TR. Steep-fronted switching voltage transients and their distribution in motor windings. Part 2: Distribution of steep-fronted switching voltage transients in motor windings. IEE Proceedings B – Electric Power Applications. 1982;**129**(2):56-63

[4] Oraee H, McLaren PG. Surge voltage distribution in line-end coils of induction motors. IEEE Transactions on Power Apparatus and Systems. 1985;**PAS-104**(7):1843-1848

[5] Guardado JL, Cornick KJ. A computer model for calculating steep-fronted surge distribution in machine windings. IEEE Transactions on Energy Conversion. 1989;**4**(1):95-101

[6] Guardado JL, Cornick KJ, Venegas V, Naredo JL, Melgoza E. A three-phase model for surge distribution studies in electrical machines. IEEE Transactions on Energy Conversion. 1997;**12**(1):24-31

[7] Su CQ, editor. Electromagnetic Transients in Transformer and Rotating Machine Windings. 1st ed. Hersey: IGI Global; 2013

[8] Stranges MKW, Stone GC, Bogh DL. Progress on IEC 60034-18-42 for qualification of stator insulation for medium-voltage inverter duty applications. In: Proceedings of IEEE Petroleum and Chemical Industry Technical Conference (PCIC'07); 17–19 Sept. 2007; Calgary, Canada. US: IEEE; 2007. pp. 1-7

[9] Stone GC, Culbert I. Review of stator insulation problems in medium voltage motors fed from voltage source PWM drives. In: Proceedings of International Symposium on Electrical Insulating Materials (ISEIM'14); 1–5 June 2014; Niigata, Japan. US: IEEE; 2014. pp. 50-53

[10] He J, Sizov GY, Zhang P, Demerdash NAO. A review of mitigation methods for overvoltage in long-cable-fed PWM AC drives. In: Proceedings of IEEE Energy Conversion Congress and Exposition (ECCE'11); 17–22 Sept 2011; Phoenix, AZ. US: IEEE; 2011. pp. 2160-2166

[11] Nussbaumer P, Mitteregger A, Wolbank TM. Online detection of insulation degradation in inverter fed drive systems based on high frequency current sampling. In: Proceedings of 37th Annual Conference on IEEE Industrial Electronics Society (IECON'11); 7–10 Nov. 2011; Melbourne, Australia. US: IEEE; 2012. pp. 1954-1959

[12] Moreira FS, D'Angelo MFSV, Palhares RM, Caminhas WM. Incipient fault detection in induction machine stator-winding using a fuzzy-Bayesian two change points detection approach. In: Proceedings of 9th IEEE/IAS International Conference on Industry Applications (INDUSCON); 8–10 Nov. 2010; Sao Paulo, Brazil. US: IEEE;2011. pp. 1-6

[13] Gandhi A, Corrigan T, Parsa L. Recent advances in modeling and online detection of stator interturn faults in electrical motors. IEEE Transactions on Industrial Electronics. 2011; **58**(5):1564-1575

[14] Refaat SS, Abu-Rub H, Saad MS, Aboul-Zahab EM, Iqbal A. Detection, diagnoses and discrimination of stator turn to turn fault and unbalanced supply voltage fault for three phase induction motors. In: Proceedings of IEEE International Conference on Power and Energy (PECon); 2–5 Dec. 2012; Kota Kinabalu, Malaysia. US: IEEE; 2013. pp. 910-915

[15] Nussbaumer P, Vogelsberger MA, Wolbank TM. Induction machine insulation health state monitoring based on online switching transient exploitation. IEEE Transactions on Industrial Electronics. 2015;**62**(3):1835-1845

[16] Chaturvedi DK, Iqbal MS, Singh MP. Health monitoring techniques of induction motor: An overview. In: Proceedings of the International Conference on Emerging Trends in Engineering& Technology; 25–27 Oct. 2013; Kurukshetra, India. Netherlands: ACEEE; 2013. pp. 469-477

[17] Fabiani D, Cavallini A, Montanari GC. Aging investigation of motor winding insulation subjected to PWM-supply through PD measurements. In: Annual Report Conference on Electrical Insulation and Dielectric Phenomena (CEIDP), 16–19 Oct., Nashville, TN. USA: IEEE; 2005. pp. 434-437

[18] Greenwood A. Electrical Transients in Power Systems. 2nd ed. New York: Wiley; 1991

[19] Rudenberg R. Performance of traveling waves in coils and windings. Electrical Engineering. 1940;**59**(12):1031-1040

[20] Rabins L. A new approach to the analysis of impulse voltages and gradients in transformer windings. Transactions of American Institute of Electrical Engineers. 1960;**79**(4): 1784-1791

[21] Hussain MK, Gomez P. Modeling of machine coils under fast front excitation using a non-uniform multiconductor transmission line approach. In: Proc. of North American Power Symposium (NAPS'16); 18–20 Sept. 2016; Denver, CO. US: IEEE; 2016. pp. 1-6

[22] de León F, Gomez P, Martinez-Velasco JA, Rioual M. Transformers. In: Martinez-Velasco JA, Editor. Power System Transients: Parameter Determination. 1st ed. Boca Raton: CRC Press. pp. 177-250

[23] Stone GC, Boulter EA, Culbert I, Dhirani H. Electrical Insulation for Rotating Machines, Design, Evaluation, Aging, Testing, and Repair. 2nd ed. Hoboken: Wiley - IEEE Press; 2014

[24] Haque SM, Ardila-Rey JA, Masud AA, Umar Y, Albarracín R. Electrical properties of different polymeric materials and their applications: The influence of electric field. In: Boxue D, editor. Properties and Applications of Polymer Dielectrics. Rijeka, Croatia: InTech; 2017 Chapter 3

[25] Kielmann F, Speck J. Behaviour of the stress grading systems in converter operated H.V. Machines. In: Proceedings of 10th International Insulation Conference (INSUCON); 24–26 May 2006; Birmingham, UK. US: IEEE; 2006. pp. 99-104

[26] Espino-Cortes FP, Cherney EA, Jayaram SH. Impact of inverter drives employing fast switching devices on form-wound AC machine stator coil stress grading. IEEE Electrical Insulation Magazine. 2007;**23**(1):16-28

[27] Luna Z, Gómez P, Espino-Cortes FP, Peña R. Modeling of transformer windings for fast transient studies: Experimental validation and performance comparison. IEEE Transactions on Power Delivery. August 2017;**32**(4):1852-1860

[28] Gómez P, Uribe FA. The numerical Laplace transform: An accurate technique for analyzing electromagnetic transients on power system devices. International Journal of Electrical Power & Energy Systems. 2009;**31**(2):116-123

[29] COMSOL. Introduction to COMSOL Multiphysics 5.3a [Internet]. 2017. Available from: https://cdn.comsol.com/documentation/5.3.1.180/IntroductionToCOMSOLMultiphysics.pdf [Accessed: February 09, 2018]

[30] Gomez P, Moreno P, Naredo JL. Frequency-domain transient analysis of nonuniform lines with incident field excitation. IEEE Transactions on Power Delivery. 2005;**20**(3):2273-2280

[31] Moreno P, Gomez P, Davila M, Naredo JL. A uniform line model for non-uniform single-phase lines with frequency dependent electrical parameters. In: Proceedings of IEEE Transmission & Distribution Conference and Exposition; 15–18 Aug 2006; Caracas, Venezuela. US: IEEE; 2007. pp. 1-6

[32] Gomez P, Escamilla JC. Frequency domain modeling of nonuniform multiconductor lines excited by indirect lightning. International Journal of Electrical Power & Energy Systems. 2013;**45**(1):420-426

[33] Nuricumbo-Guillen R, Gomez P, Espino-Cortes FP. Computation of transient voltage profiles along transmission lines by successive application of the numerical Laplace transform. In: Proceedings of North American Power Symposium (NAPS); 22–24 Sept 2013; Manhattan, KS. US: IEEE; 2013. pp. 1-6

[34] Ul Haq S, Stranges MKW, Wood B. A proposed method for establishing partial discharge acceptance limits on API 541 and 546 sacrificial test coils. IEEE Transactions on Industry Applications. 2017;**53**(1):718-722

[35] Hussain MK, Gomez P. Modeling and experimental analysis of the transient Overvoltages on machine windings fed by PWM inverters. In: Proceedings of International Conference on Power System Transients; 26–29 June. Vol. 2017. South Korea: Seoul; 2017. pp. 1-6

[36] Rivenc JP, Lebey T, Loubiere A, Biron M, Warnant J. A discussion of current-voltage and surface potential measurements to test stress grading materials. J. Physics D: Appl. Phys. 1998;**31**:2612-2621

[37] Staubach C, Hildinger T, Staubach A. Comprehensive electrical and thermal analysis of the stress grading system of a large hydro generator. IEEE Electrical Insulation Magazine. 2018;**34**(1):37-49

[38] Kone G, Volat C. Numerical investigation of transient potential distribution along stress-grading on stators bars (Roebel type). IEEE Electrical Insulation Conference (EIC), Montreal, QC, CA: IEEE. 2016;**2016**:9-12

[39] Umemoto T, Tsurimoto T, Kisakibaru T, Sakurai T, Tsuda T, Karasawa K. Novel evaluation methods of end-turn stress grading materials for converter-fed high voltage rotating machines. Conference on Electrical Insulation and Dielectric Phenomena (CEIDP), Toronto, ON, CA: IEEE. 2016:307-310

[40] Zhang L, Calebrese C. Karakus Y, Dickens K, Yin W. Inverter fed motor stress grading system design consideration. 13th International Electrical Insulation Conference (INSUCON), Birmingham, UK. 2017:1-5

[41] Sharifi E, Jayaram SH, Cherney EA. Temperature and electric field dependence of stress grading on form-wound motor coils. IEEE Transactions on Dielectrics and Electrical Insulation. 2010;**17**(1):264-270

[42] Egiziano L, Tucci V, Petrarca C, Vitelli M. A Galerkin model to study the field distribution in electrical components employing nonlinear stress grading materials. IEEE Transactions on dielectrics and electrical insulation. 1999;**6**(6):765-773

[43] Bayon L, Buret F, Koelblin C, Toledo T. Field distribution measurement and simulation of stress control materials for cable accessories. In: Proceedings of the 2004 IEEE International Conference on Solid Dielectrics ICSD 2004, Toulouse, France. 2004, 2. pp. 534-537

[44] Allison JA. Understanding the need for anti-corona materials in high voltage rotating machines. In: Proceedings of 6th International Conference on Properties and Applications of Dielectric Materials; 21–26 June 2000; Xi'an, China. US: IEEE; 2002. pp. 860-863

[45] Nam NN, Matsumoto S. Electrical and thermal computation of stress grading system in inverter-driven medium voltage motors. IEEJ Transactions on Fundamentals and Materials. 2013;**133**(11):591-597

[46] Kumada A, Nakamura T, Ikeda H, Hidaka K, Tsuboi Y, Kisakibaru T, Yoshimitsu T. Transient potential distribution on stress grading system of rotating machines under repetitive impulse voltages. In: Proceedings of Electrical Insulation Conference (EIC); 8–11 June 2014; Philadelphia, PA. US: IEEE; 2014. pp. 368-372

[47] Baker AE, Gully AM, Wheeler JCG. Finite element modeling of non-linear stress grading materials for machine end windings. In: Proceedings of IEE Conference on Power Electronics, Machines and Drivers; 4–7 June 2002; Santa Fe, NM. US: IEEE; 2002. pp. 265-268

[48] Yeo Z, Buret F, Krahenbuhl L, Auriol P. A nonlinear model for surface conduction. IEEE Transactions on Magnetics. 1998;**34**(5):2617-2620

[49] Wheeler JCG, Gully AM, Baker AE, Perrot FA. Novel stress grading systems for converter-fed motors. IEEE Electrical Insulation Magazine. 2007;**23**(1):29-35

[50] Espino-Cortés FP, Gómez P, Betanzos Ramírez D. Modeling of the heat generation on stress grading coatings of motors fed by multilevel drives. IEEE Transactions on Dielectrics and Electrical Insulation. 2011;**18**(4):1328-1333

[51] Sharifi E, Fink H. Slot corona protection systems for medium voltage rotor windings subjected to PWM voltage in doubly fed induction generators. In: Proceedings of Electrical Insulation Conference (EIC); 8–11 June 2014; Philadelphia, PA. US: IEEE; 2014. pp. 378-381

[52] Chen W, Gao G. Using multi-stress aging test to evaluate and improve medium-voltage stator insulation for adjustable speed drive applications. In: In: Proceedings of IEEE Petroleum and Chemical Industry Technical Conference (PCIC'11); 19–21 Sept. Vol. 2011. Toronto, Canada. US: IEEE; 2011. pp. 1-7

[53] Espino-Cortés FP, Asiain-Olivares TI, Gómez P. Simulation of the effect of armor coating conductivity on the stress grading coating performance under PWM multilevel waveforms. Electrical Insulation Conference (EIC), Seattle, Washington, USA: IEEE; 7–10 June. 2015;**2015**:172-175

[54] Ramirez-Serrano JC, Espino-Cortes FP, Hernandez-Ramirez EJ. Electric field and heat at the CAT-SG coatings interface under fast rise pulses. In: Proceedings of electrical insulation conference (EIC); 17-20 June 2018; San Antonio TX. US: IEEE; to be published

Section 2

# Environmentally Friendly Insulation Gases as Alternatives to Sulfur Hexafluoride Gas

Chapter 4

# Development Prospect of Gas Insulation Based on Environmental Protection

Dengming Xiao

Additional information is available at the end of the chapter

http://dx.doi.org/10.5772/intechopen.77035

**Abstract**

The research situation of environmentally friendly gas insulation is expounded in this paper. The basic physical and chemical properties of the insulating gases are analysed, to propose several environment-friendly insulating gas of potential alternative to sulphur hexafluoride ($SF_6$). The insulation characteristics of different components gas mixtures with 90% of nitrogen ($N_2$) and carbon dioxide ($CO_2$) as buffer gas and 10% octafluorocyclobutane (c-$C_4F_8$), Trifluoroiodomethane ($CF_3I$) and heptafluorobutyronitrile ($C_4F_7N$) as the main insulating gas had been tested with 5–20 mm sphere-plane electrode gaps in non-uniform electric field under the power frequency voltage and positive and negative lightning impulse breakdown. The development prospects of environmentally friendly gas insulation are forecasted. Further analysis of c-$C_4F_8$,$CF_3I$ and $C_4F_7N$ (some friendly gases, which have the potential to replace $SF_6$) are conducted trying to points out the further research direction.

**Keywords:** electrical equipment insulation, environmentally friendly gases, alternatives gases, $SF_6$

## 1. Introduction

Because of its good electrical insulating properties, sulphur hexafluoride ($SF_6$) can satisfy the insulating demands of the electrical apparatus. $SF_6$ is nontoxic and non-combustible, which guarantees the security of its application in the gas insulating apparatus. What is more, the chemical properties of $SF_6$ are stable and it can be compatible with most mental and solid insulating materials. There is little decomposing by-products after discharge or arc, which guarantees the following insulating function and protects apparatus. Nowadays, $SF_6$ has been an important industrial gas with more than 20,000 tons' produced every year all over the

world, and 80% of that is applied as insulating gas in electrical apparatus [1]. With the continuous increase of China's electrical demand and the expansion of the electrical grid, the demand for insulating gas will continuously increase [2–4].

Although the characteristics of $SF_6$ can satisfy the requirements as insulation gas in electrical apparatus, such as gas-insulated substations, scientists have recognised that it can influent and aggravate the greenhouse effect in recent years. $SF_6$ is a strong greenhouse gas that will cause serious harm to the environment. The Global Warming Potential GWP of $SF_6$ is 23,900 times stronger than that of $CO_2$ [5], which means that under the computing period of 100 years. Far more serious is that because of the extremely stable chemical properties, it is very hard to decompose $SF_6$ in nature and it can exist for 3200 years in atmosphere [6], which will make the environmental influence and greenhouse effect continuously accumulated.

In the *Kyoto Protocol to the United Nations Framework Convention on Climate Change* signed in 1997 in Kyoto of Japan [2], $SF_6$ was regarded as one of the six-kinds of greenhouse gas ($CO_2$,$CH_4$,$N_2O$,PFC,HFC and $SF_6$) and it demanded that developed countries should stop and reduce the total emission of greenhouse gas. With signing the *Paris Agreemen*t [3], international society are making efforts to reduce carbon emissions, which means that the application of $SF_6$ in industry will be limited more and more [4, 5, 7]. Therefore, researching new method of gas insulating to replace $SF_6$ becomes an urgent work.

It is important to look for environmentally insulating gas with similar insulating characteristics and physicochemical properties of $SF_6$ to replace $SF_6$. $SF_6$ belongs to inorganic fluorinated gases, and its molecular geometry is octahedron with six-fluorine (F) atoms in outer surface and one sulphur (S) atom in centre. Because of fluorine belongs to the halogens, its peripheral electronic layer is occupied by seven electrons and can become stable structure with one more electron, which allows it to strongly attract electron. Moreover, in the molecule of $SF_6$, F atoms and S atom form more stable covalent bonds by sharing electrons. However, F atoms also have the trend to attract electrons so that the entire molecule has a trend to attract electron. Therefore, it has better insulating characteristics than other gaseous molecular without electronegativity. In addition, although the gas characteristics showed by the structure of macro element cannot show the insulation strength of gas exactly, even counterexample existing, researchers have attached importance to that and the researching emphasis of alternative gas is concentrated on the halogenated gas [8]. In 1997, the research report about the insulation characteristics and arc quenching of alternative gas of $SF_6$ written by the National Bureau of Standards of the U.S.A [9] introduced many potential alternative gases. Besides, in this work was studied the breakdown voltage under direct current (DC) uniform field of gases, such as organic fluorinated ones, compared with $SF_6$, and this comparison is shown in **Table 1**. The result of the report shows that most fluorinated gases have good electronic adsorption, which it is related to the addition of fluorine, but not all the organic fluorinated gases have good insulation characteristics. Besides, it is not correct to evaluate the insulation characteristics just based on the elements that constitute a gas, so it is necessary to analyse different gases in detail for comparison. Because the physicochemical properties of octafluorocyclobutane (c-$C_4F_8$) are close to $SF_6$, its cost is low and Greenhouse Warming Potential (GWP) is lower than $SF_6$, the report has specially indicated that c-$C_4F_8$ and its mixture can be the study subject for long time [10], so that researchers are focused on the study of this gas.

| Gas | Relative breakdown voltage | Remarks |
|---|---|---|
| $SF_6$ | 1 | As reference of gas<br>Relative breakdown voltage is 1 |
| $C_3F_8$ | 0.90 | With strong absorption to free electron, especially low-power free electron |
| c-$C_4F_8$ | About 1.35 | |
| 2-$C_4F_8$ | About 1.75 | |
| 1,3-$C_4F_6$ | About 1.50 | |
| Hexafluorobutadiene (2-$C_4F_6$) | About 2.3 | |
| $CHF_3$ | 0.27 | With weaker absorption to free electron |
| $CF_4$ | 0.39 | |

**Table 1.** Relative direct current (DC) breakdown voltages of some fluorination gases [1, 8, 12].

Besides c-$C_4F_8$, organic halogenated gas, trifluoroiodomethane ($CF_3I$), contains fluorine (F) and iodine (I) has been concentrated by researchers for its much lower GWP and better insulation characteristics. At the same time, ALSTOM company in France and 3M company in US produce an electrical insulation gas mixtures together, named G3, whose main ingredient is heptafluorobutyronitrile ($C_4F_7N$), a kind of fluorinated nitrile with Novec 4710 as trade name [11]. Besides, ABB company produces electrical insulation gas mixtures whose main ingredient is fluorinated ketone such as Heptafluoropropyl trifluorovinyl ether ($C_5F_{10}O$) and Undecafluorohexanoyl Fluoride ($C_6F_{12}O$). Properties of some potential alternative gases to $SF_6$ are shown in **Table 2**.

| Gas | Physicochemical properties | | Environmental characteristics | Electrical characteristics | |
|---|---|---|---|---|---|
| | Toxicity | Boiling point (unit: °C) | Relative GWP | Relative insulation characteristics [15] | Relative rising rate of recovery voltage (RRRV) characteristics |
| $SF_6$ | Nontoxic | −64 | 1 | 1.00 | 1.00 |
| $CF_3I$ | Low-toxicity | −22.5 | ≈0 | 1.20 | 0.90 |
| c-$C_4F_8$ | Nontoxic | −6 | 0.3 | 1.30 | — |
| $g^3(C_4F_7N/CO_2)$ | Low-toxicity | 24 (Pure) | 0.02 | 0.85–1 | — |
| $C_5F_{10}O$/air | Nontoxic | 26.9 (Pure) | ≈0 | 0.75–0.85 | — |
| Hexafluoropropylene ($C_3F_6$) | Toxic | −29.6 | ≈0 | 1.01 | — |
| Fluorinated 1,3-butadiene ($C_4F_6$) | Toxic | 6~7 | ≈0 | 1.4 | — |
| Fluorinated 2-butyne ($C_4F_6$) | Toxic | −25 | ≈0 | 1.7 | — |
| Fluorinated 2-butene ($C_4F_8$) | Toxic | 1.2 | — | 1.8 | |

**Table 2.** Properties of potential alternative gas to sulphur hexafluoride ($SF_6$) [8, 13, 14].

## 2. Analysis of potential alternative gas

### 2.1. Octafluorocyclobutane (c-$C_4F_8$)

Octafluorocyclobutane, c-$C_4F_8$ is an important industrial gas. Nowadays, it is used in plasma etching technology or as refrigerant [16]. Similar to $SF_6$ gas, the performance to absorb electron easily of fluorine in c-$C_4F_8$ is shown in the characteristics of the whole molecule, so that c-$C_4F_8$ has a stronger absorption to free electron. c-$C_4F_8$ is colourless, odourless, nontoxic to human bodies at low concentration, non-combustible, nonexplosive and with GWP of about 8700 relative to $CO_2$. Though it belongs to greenhouse, but in the same conditions, its negative effects are just one third of $SF_6$ [17]. In addition, as organic halogenated gas, c-$C_4F_8$ does not contain chlorine or bromine, so it is not harmful to the ozone layer. The molecule of c-$C_4F_8$ is circular with a stable chemical structure and does no harm to other solid materials in electrical apparatus, such as aluminium alloy, copper contact and epoxy supporting insulators. Recently, the price of c-$C_4F_8$ differs with the purity of gas. The price of this gas with 99.9% purity is about 200 RMB/kg [8] (1 RMB ≈ 0.16 dollar≈0.13 euro, the same below), as the price of gas with 99.999% purity is about 500 RMB/kg, and that has obviously reduced compared with the price of about thousand RMB per kilogramme 10 years ago. This is related to more applications, such as refrigerant [18], that are using c-$C_4F_8$ and the rise of production. Nowadays, the price of c-$C_4F_8$ is only a little bit higher than that of $SF_6$, but if c-$C_4F_8$ is applied widely in electrical domain, its price still can be reduced, so the cost is not the obstacle to be applied in electrical apparatus.

Long before, Japanese researchers began to research the electrical properties of c-$C_4F_8$ and indicated that it had the feasibility to replace $SF_6$ in electrical apparatus. Then, the researchers of plasma and electric-related domains from the U.S.A. and Mexico began to use Boltzmann equation, calculation of parameter of discharge particle and breakdown test to research the insulation characteristics of c-$C_4F_8$. Shanghai Jiao Tong University, Xi'an Jiao Tong University and other high schools in China began the researches about calculation of academic simulation and breakdown test of c-$C_4F_8$. The results of researches have shown that the insulation characteristics of pure c-$C_4F_8$ are better than $SF_6$, in air pressure at 0.3 MPa and over. The breakdown voltage of the gas mixtures of c-$C_4F_8$ and $N_2$ or $CO_2$ is higher than the gas mixtures of $SF_6$ with the same contents, and in low air pressure or atmospheric pressure, the breakdown voltage of the gas mixtures of c-$C_4F_8$ can approach the gas mixtures of $SF_6$ with the same contents. In conclusion, c-$C_4F_8$ and its gas mixtures have similar insulation characteristics with $SF_6$, and the breakdown voltage differs a little with the composition, mixture ratio and gas pressure, so it can satisfy the demands of actual application.

The relative molecular mass of c-$C_4F_8$ is 200, higher than that of $SF_6$ (146.06), and it means that the condensing temperature of c-$C_4F_8$ will be high, is about −6°C, higher than −63.6°C of $SF_6$. The insulating gas should exist in gaseous state in the electrical apparatus, thus need to have a low enough liquefaction temperature. One way to reduce its liquefaction point is to add some buffer gas including nitrogen ($N_2$) or carbon dioxide ($CO_2$), which may lead to a weaker insulation strength. So we need to take a balance between the low liquefaction temperature and good insulation property when considering the mixture ratio for c-$C_4F_8$

gas mixtures. Therefore, c-$C_4F_8$ is not suited to be applied in apparatus as pure gas, or it cannot satisfy the demand of arctic alpine regions. Thus, it should be mixed with other gas in some ratios to reduce the condensing temperature of the gas mixtures and be used as gas mixtures.

### 2.2. Trifluoroiodomethane ($CF_3I$)

Trifluoroiodomethane ($CF_3I$) is colourless, odourless, non-combustible and nonexplosive. $CF_3I$ is a new industrial gas that can be used as an environmental refrigerant and alternative fire-extinguishing agent. It can be used as additive or mixed composition to replace traditional refrigerant Freon and fire-extinguishing material "Halon." Because its GWP is very low, about 1–5 relative to $CO_2$ is much lower than most organic halogenated gases, so its influence on greenhouse is very small. At the same time, it does not contain chlorine and bromine that is commonly present in most refrigerants, so it will not damage the ozone layer, thus the United Nations regards it as new refrigerant to replace Freon [19]. This can prove that $CF_3I$ is a kind of environmentally friendly gas, and has related basis in industrial application. As a kind of fire-extinguishing material, its efficiency is outstanding and has little negative influence on environment, and it is well compatible with normal industrial materials, so that it will not cause chemical reaction or erosion. Therefore, it has passed some related standards of the U.S.A [20]. and can be used in aerospace and other areas. In addition, it can rise the security of the electrical apparatus by applying $CF_3I$ in electrical apparatus such as cubicle gas insulating switchgear (C-GIS) or compact transformer. It is especially appropriate to be used in populous regions of central city in order to reduce the conflagration or explosion caused by the bug of electrical apparatus. The molecular structure of $CF_3I$ is shown in **Figure 1** RMB. It is affected by halogens such as F and I, so it has strong absorption to free electron. So that it can absorb free electron at the beginning of discharge when electron avalanche forms, and then it can restrain the formation of collision ionisation, which enhances its insulation property. What is worthy to indicate, that the difference between $CF_3I$ and $SF_6$, as well as c-$C_4F_8$, comes from the asymmetry of its structure, which makes the polarity effect of the molecule stronger. The three-F atoms in the molecule has stronger absorption to electron than I atom, so the electron cloud in the molecule trends to F atoms, and the density of the electron cloud around the carbon-iodine covalent bond formed by I atom and carbon (C) atom is reduced, and the energy barrier to absorb electron is also reduced. Therefore, the whole molecule has a strong ability to absorb electron.

Because of $CF_3I$ is a new industrial gas, its application in China is not widely extended, the production in China is low. Currently, $CF_3I$ produced in China costs about 2000 RMB/kg, the price is much higher than $SF_6$ [1]. The main reason why the price of $CF_3I$ in China is higher than that for $SF_6$ [1] is that the demand is very low. According to the producers of $CF_3I$ (Beijing Yuji Science & Technology Co., Ltd.), after $CF_3I$ will be used widely and will be mass-produced, the constant cost of $CF_3I$ will reduce a lot with the actual cost lower than 600 RMB/kg. Moreover, by optimising and upgrading, its price will be reduced continuously like that for c-$C_4F_8$.

Since year 2000, many researchers in China and abroad begin to research this new insulating gas [21, 22]. Researchers of plasma from Mexico have calculated and measured the ionisation

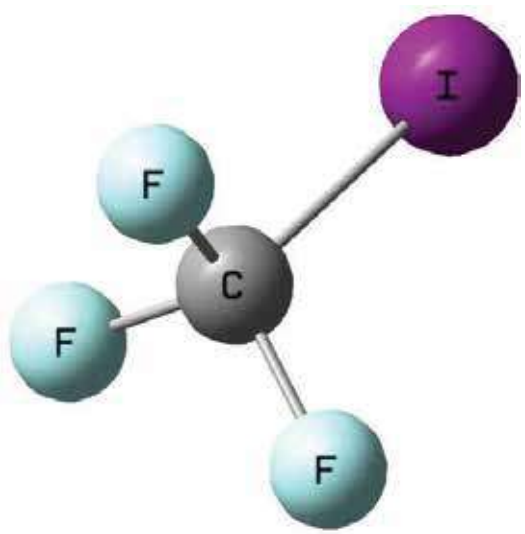


**Figure 1.** Molecule structure of $CF_3I$.

coefficient, attachment coefficient and electron drift velocity during the process of discharge of $CF_3I$ and its gas mixtures with $N_2$, $SF_6$ and other gases [23, 24]. The aforementioned work has quantified the reaction between free electron and gas molecule during the process of discharge, and has analysed the insulation strength of gas mixtures from the perspective of the parameters of discharge. Tokyo University of Japan, Tokyo Denki University and Japan Electric Power Company have researched $CF_3I$ by testing [25, 26]. They make the breakdown test to $CF_3I$ and its gas mixtures with $N_2$, $CO_2$ and air by using lighting impulse. The results show that the insulation strength of pure $CF_3I$ is better than that in $SF_6$, about 1.2 times than $SF_6$, and $CF_3I$-$CO_2$ gas mixtures with high content also has better insulation characteristics to be able to replace $SF_6$. Many universities and academies in Europe also research the gas mixtures of $CF_3I$-$CO_2$ and $CF_3I$-$N_2$ in different conditions [24]. The results show that the positive synergistic effect of the gas mixtures of $CF_3I$ and $N_2$ is less obvious than that of the gas mixtures of $SF_6$ and $N_2$, which means that in the same mixture ratio, the insulation strength of the gas mixtures of $CF_3I$-$CO_2$ cannot increase with the rising content of $CF_3I$ because of the synergistic effect [22]. In addition, the gas mixtures of $CF_3I$ and $CO_2$ with low content show better positive synergistic effect. Shanghai Jiao Tong University, Xi'an Jiao Tong University and Chongqing University in China has researched $CF_3I$ and its gas mixtures by academic calculation and testing research [27–29]. Shanghai Jiao Tong University uses Boltzmann's equation to calculate and analyse the discharge parameters and insulation characteristics of the gas mixtures of $CF_3I$ and $N_2$, $CO_2$, He and so on and get the alternating current (AC) breakdown voltage in non-uniform electric field and slightly non-uniform electric field by testing [28, 30]. Other researchers have measured partial discharge voltage and other insulation characteristics of the gas mixtures of $CF_3I$ [31, 32]. The results show that $CF_3I$ has good electrical insulation characteristics, but the positive synergistic effect of the mixture of $CF_3I$ and normal buffering gas is not obvious, so that the

insulation characteristics of its gas mixtures are lower than $SF_6$. Therefore, the research about the synergistic effect of $CF_3I$ and other gas is the key to be applied in the future.

### 2.3. Fluorinated nitrile gas and G3 gas mixtures

ALSTOM company in France and 3M company in U.S.A. have joined to research the alternative to $SF_6$ gas. Among many organic fluorinated gases, they choose the gas, which is also alternative refrigerant, and organic chemical compound that contains four-C atoms and seven-F atoms, with a trade name of Novec 4710 [11] and chemical formula of $C_4F_7N$, named G3. Besides, its molecular structure is shown in **Figure 2**. The gas has replaced a fluorine atom with nitrile group (—C≡N) on the basis of the fluorinated hydrocarbon gas, and becomes fluorinated nitrile gas. This nitrile group containing carbon-nitrogen triple bond has a special chemical structure to make $C_4F_7N$ have very good insulation performance, which can reach about two-times of that of $SF_6$. The chemical features of this gas are similar to the organic fluorinated gas with stable chemical characteristics and can be well compatible with other materials used in electrical assets. The relative molecular mass of $C_4F_7N$ is 195, with a high condensing temperature of −4.7°C, so that it cannot replace $SF_6$ as a single gas, it should become gas mixtures with buffering gas such as $N_2$ or $CO_2$. Because of it is a new insulating gas, related testing research is lacking. According to research result obtained by now, the insulation characteristics of its gas mixtures with $CO_2$ is about 90% of the $SF_6$ mixtures with the same amount of $CO_2$, and this gas can also be used as arc quenching medium being applied in circuit-breakers [33]. Nowadays, this gas is researched and produced by 3M company and its cost is dozens of times higher than other gases [33], so the cost is one of the obstacles for its industrial application. With the accomplishment of the production technology of the gas and the development of the producers at home, the price could be reduced.

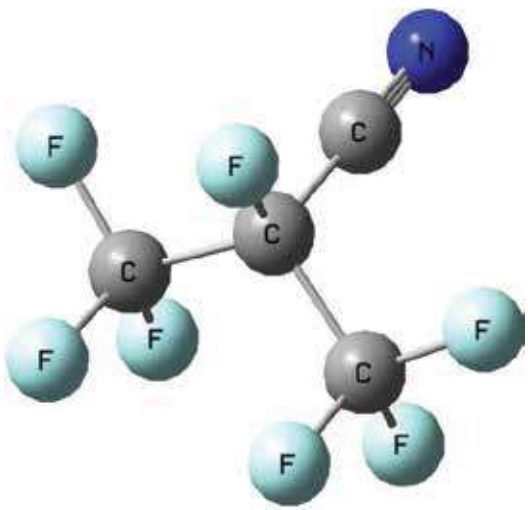


**Figure 2.** Molecule structure of $C_4F_7N$.

The gas with the chemical formula of $C_4F_7N$ has two-isomeric compounds, their chemical formulas and element compositions are the same, but for the different positions of nitrile groups, their molecular structures and microcosmic natures are different. For Novec 4710 gas used in G3 gas, its nitrile group is located in the carbon atom in the middle of the organic carbon-chain, and the other isomeric compound has a nitrile group located in the carbon atom at one end of the carbon-chain, which constitute a virulent gas that cannot be used in industry. In addition, during the production of Novec 4710, by avoiding the production and the mixture of the virulent isomeric compound is key to apply this gas in a real environment. What is more, any gas will be decompounded to produce decomposed by-products in the condition of high temperature and pressure during the discharge process. Moreover, it should be continuously researched about how to guarantee that this gas will not produce toxic isomeric compounds or other gases during the process of discharge or arc interruption.

### 2.4. Fluorinated ketone gas

ABB company in Switzerland has supported a method for evaluating the greenhouse effect of $SF_6$ [34, 35], and it is to take advantage of fluorinated ketone gas as the main ingredient of gas mixtures, which contains organic fluorinated gas with carbonyl group (C〓O) such as $C_5F_{10}O$ and $C_6F_{12}O$. This kind of gas is similar to fluorinated nitrile gas. It is a chemical compound, which uses the carbonyl group to replace one F atom of fluorinated hydrocarbon based on fluorinated hydrocarbon. Because of carbonyl group has carbon-oxide double bond, which is unsaturated bond as the same as the carbon-nitrogen triple bond, it has good absorption to free electron, and it shows higher insulation characteristics in macro-performance [36]. According to the existing testing data in China and abroad, the insulation characteristics of pure $C_5F_{10}O$ and $C_6F_{12}O$ are about two-times higher than $SF_6$ and their GWP value approaches zero, physicochemical properties are stable and they have good compatibility with materials and industrial applicability. The fluorinated carbonyl, which ABB has applied in the gas mixtures has more than five-carbon atoms, so its relative molecular mass is bigger than other insulating gases, such as $C_5F_{10}O$ with 266 and $C_6F_{12}O$ with 316. Besides,the condensing temperature of $C_5F_{10}O$ and $C_6F_{12}O$ is very high with 24 and 49°C at room condition, which means that they are liquid at normal temperature and gas pressure. Therefore, this gas cannot be used in any electrical insulating domains as single gas, and it can only be applied as gas mixtures. Limited by its high-condensing temperature, it will have low content in the gas mixtures, which causes the limitation of the insulation strength of the whole gas mixtures, so the synergistic effect of this gas and other gas mixtures is very important. Therefore, the use of this kind of gas forming gas mixtures, which allows it keep high insulation characteristics at low concentrations, is the emphasis of research in the future.

## 3. The power frequency AC breakdown characteristics of the c-$C_4F_8$, $N_2$, $CO_2$ gas mixtures

The breakdown voltage under AC voltage of the gas mixtures with a constant content of 10% of c-$C_4F_8$ and different content of $N_2$ and $CO_2$ has been measured by testing. **Figures 3** and **4** show the variety of the AC-breakdown voltage and maximum electric strength of the c-$C_4F_8$, $N_2$, $CO_2$ gas mixtures with the variety of gap distance under different air pressure. The gas discharge test chamber and other internal structure are the same with that in Ref. [37]. The

method to inflate gas mixtures to test chamber is introduced in Ref. [17]. The gases tested in the present paper are listed in **Table 3**.

From **Figures 3** and **4**, it can be observed that the behaviour of c-$C_4F_8$ mixtures is similar to the $SF_6$ gas mixtures, the AC-breakdown voltage of the c-$C_4F_8$, $N_2$, $CO_2$ gas mixtures gets higher values as the gap distance gets bigger, and it shows saturation effect. The maximum electric strength of the gas mixtures gets lower values as the gap distance gets bigger, and it shows that the gas mixtures has some sensitivity to the non-uniformity of the electric field. As the non-uniformity of the electric field increases, the maximum electric field able to be tolerated reduces, and the trend of change is similar to $SF_6$, $N_2$ and $CO_2$ in Appendix **Figures A1** and **A2**.

**Figure 5** shows that under different gap distances, the variety of the AC-breakdown voltage of the c-$C_4F_8$, $N_2$, $CO_2$ gas mixtures as the gas pressure changes. The AC-breakdown voltage of c-$C_4F_8$ gas mixtures increases linearly as the air pressure increases without hump effect, and this trend is the same to $SF_6$ gas mixtures. From **Figures 3–5**, we can see that the variety of the breakdown voltage of the c-$C_4F_8$ gas mixtures with the same content as the air pressure and the electrodes gap changes is the same to $SF_6$ gas mixtures. However, the curves of breakdown voltage of c-$C_4F_8$ gas mixtures with different contents in the graphs are more concentrated than $SF_6$. That is to say, the breakdown voltages of gas mixtures have little difference with different contents, at the same time, it shows that the breakdown voltage of the gas mixtures of c-$C_4F_8$ and $CO_2$ is the highest and the gas mixtures with $N_2$ is lower, this is different from the properties of $SF_6$ gas mixtures. When the gap distance is 20 mm, the AC-breakdown voltage of 10%c-$C_4F_8$+90%$CO_2$ is about 10% higher than that of 10%c-$C_4F_8$+90%$N_2$.

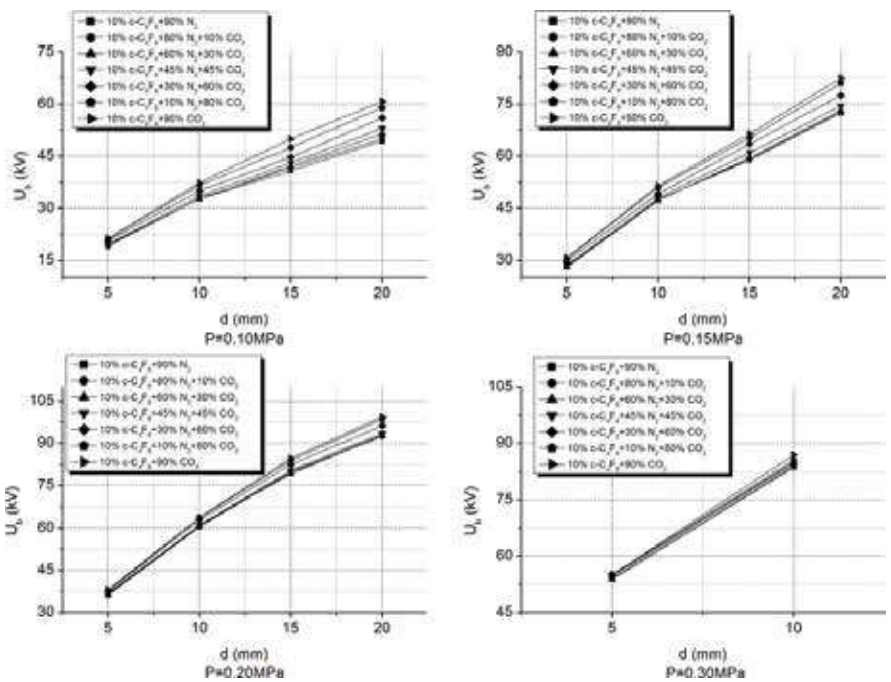


**Figure 3.** AC-breakdown voltage of c-$C_4F_8$, $N_2$, $CO_2$ gas mixtures with different gas pressures.

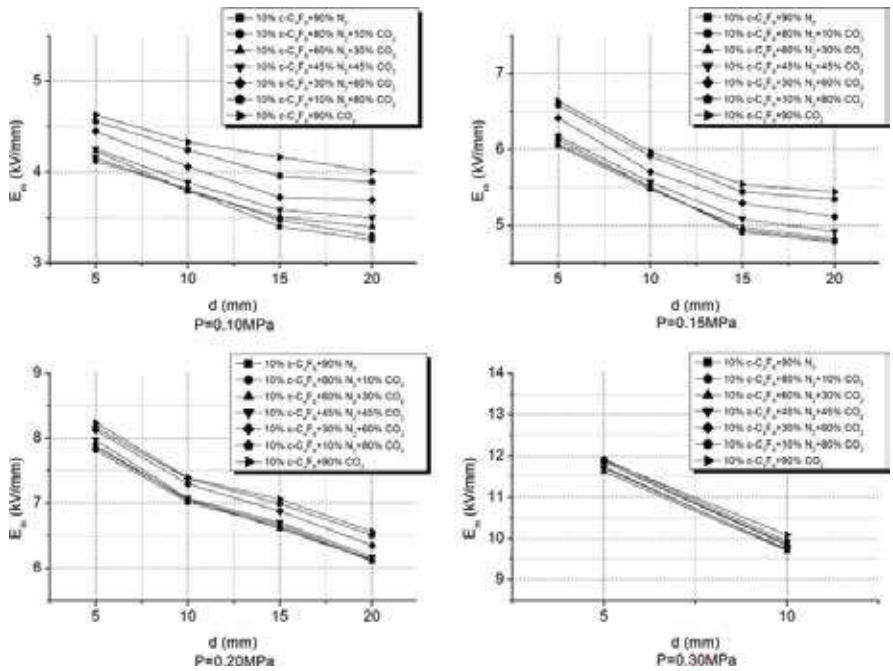


**Figure 4.** Maximum electric strength of c-$C_4F_8$, $N_2$, $CO_2$ gas mixtures with different gas pressures.

| Number | c-$C_4F_8$/$CF_3I$ mixing ratio (%) | $N_2$ mixing ratio (%) | $CO_2$ mixing ratio (%) |
|---|---|---|---|
| 1 | 10 | 90 | 0 |
| 2 | 10 | 80 | 10 |
| 3 | 10 | 60 | 30 |
| 4 | 10 | 45 | 45 |
| 5 | 10 | 30 | 60 |
| 6 | 10 | 10 | 80 |
| 7 | 10 | 0 | 90 |

**Table 3.** Test gas mixtures for power frequency AC breakdown experiments.

**Figure 6** shows under different gas pressures, the variety of the AC-breakdown voltage of the c-$C_4F_8$, $N_2$, $CO_2$ gas mixtures as the content changes. If it is make the gas mixtures of 10%c-$C_4F_8$ + 90%$N_2$ as the initial matched group, it can be seen that the breakdown voltage of the gas mixtures increases as the content of $CO_2$ increases, and when the content of $CO_2$ exceeds 60%. In other words, with a content of $N_2$ lower than 30%, the increase of the breakdown voltage is more noticeable.

Because of during the process of discharge, $N_2$ will make the ionisation probability of $CO_2$ increase as well, when reducing $N_2$ and increasing $CO_2$ of the c-$C_4F_8$ gas mixtures, the breakdown voltage of the triple gas mixtures in **Figure 6** does not has an obvious increase

http://dx.doi.org/10.5772/intechopen.77035

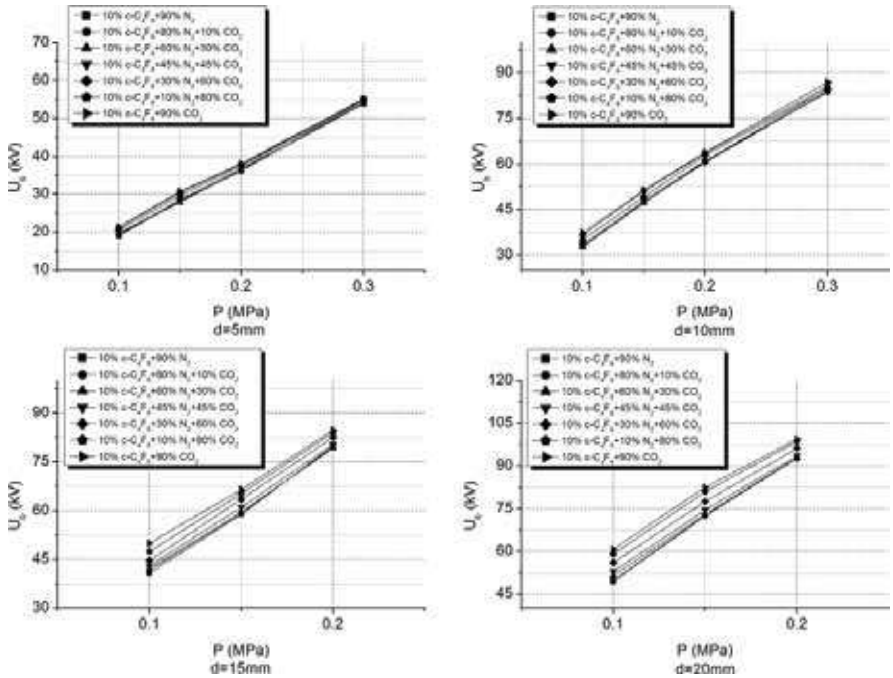


**Figure 5.** AC-breakdown voltage of c-$C_4F_8$, $N_2$, $CO_2$ gas mixtures with different electrodes gap distances.

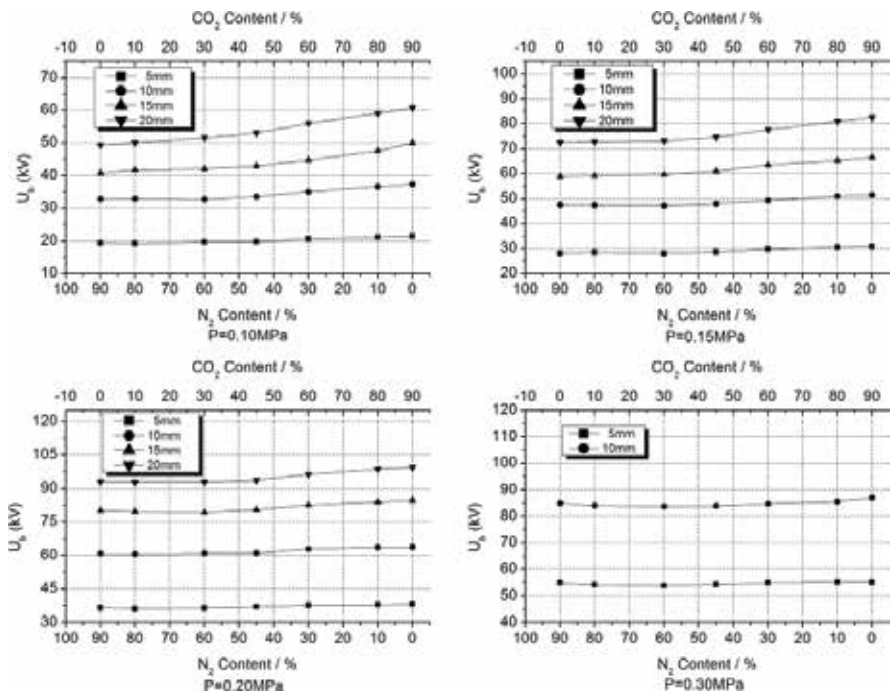


**Figure 6.** Relationship between AC-breakdown voltage and mixing contents of c-$C_4F_8$, $N_2$, $CO_2$ gas mixtures.

immediately, and even it has a trend to reduce a little. Only after the content of $N_2$ is lower than 30% and the content of $CO_2$ is higher than 60%, the breakdown voltage can increase significantly.

## 4. Power frequency AC-breakdown characteristics of the $CF_3I$, $N_2$, $CO_2$ gas mixtures

To $CF_3I$, it has been measured the breakdown characteristics for a constant content of 10% $CF_3I$ and with different concentrations of $N_2$ and $CO_2$ under AC-voltage applied during the tests. The test method and experiment setup are similar to that in Section 2. The gas mixtures and mixing ratio are listed in **Table 1**. **Figures 7** and **8** show that under different air pressures, the variety of the AC-breakdown voltage applied and the maximum electric strength of the $CF_3I$, $N_2$, $CO_2$ gas mixtures as the gap changes. From **Figure 7**, it can be seen that the breakdown voltage of $CF_3I$ gas mixtures gets higher as the electrodes gap gets bigger, but curves of different gas mixtures are more approached even closer compared with $SF_6$ and c-$C_4F_8$. The breakdown voltage of $CF_3I$ gas mixtures has little difference with different contents of $N_2$ and $CO_2$. Moreover, $N_2$, which has better insulation strength, does not perform better than $CO_2$ when it is mixed with $CF_3I$. In **Figure 8**, the maximum electric strength of $CF_3I$ gas mixtures has a trend to reduce as the electrodes gap increases, but the curves are smoother than c-$C_4F_8$, which shows that the sensitivity to the electric non-uniformity of $CF_3I$ is lower than c-$C_4F_8$.

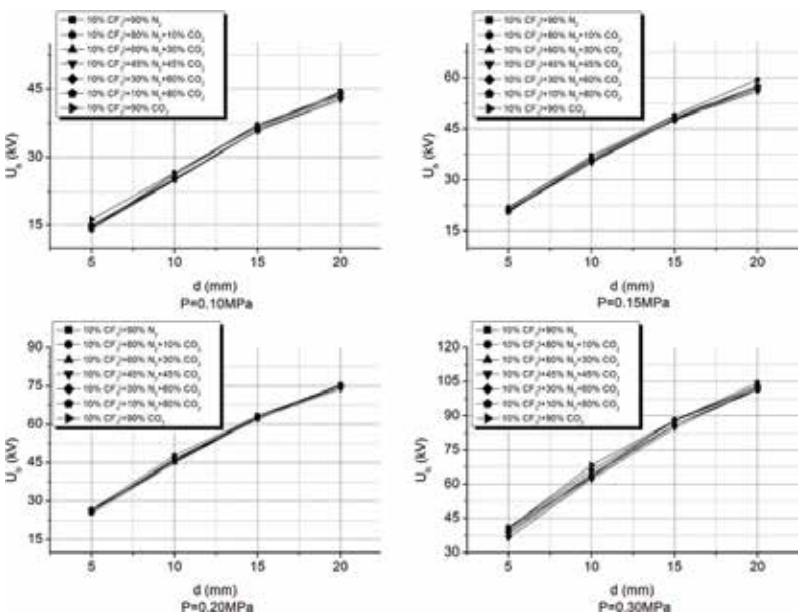


**Figure 7.** AC-breakdown voltage of $CF_3I$, $N_2$, $CO_2$ gas mixtures with different gas pressures.

http://dx.doi.org/10.5772/intechopen.77035

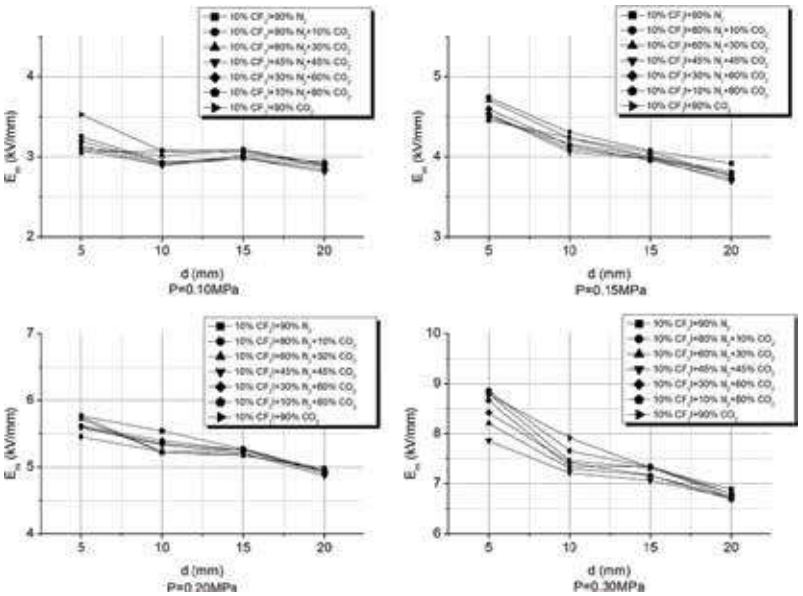


**Figure 8.** Maximum electric strength of $CF_3I$, $N_2$, $CO_2$ gas mixtures with different gas pressures.

**Figure 9** shows, under different gaps of electrode, the variety of the AC-breakdown voltage for $CF_3I$, $N_2$, $CO_2$ gas mixtures as the gas pressure changes. Similar to the gas mixtures of $SF_6$ and c-$C_4F_8$, the AC-breakdown voltage increases linearly as the air pressure increases, and without

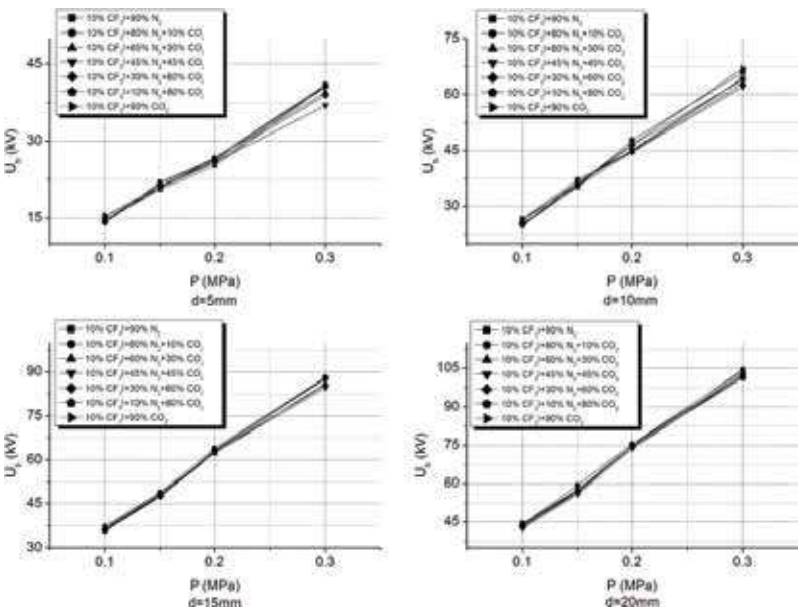


**Figure 9.** AC-breakdown voltage of $CF_3I$, $N_2$, $CO_2$ gas mixtures with different electrodes gap distances.

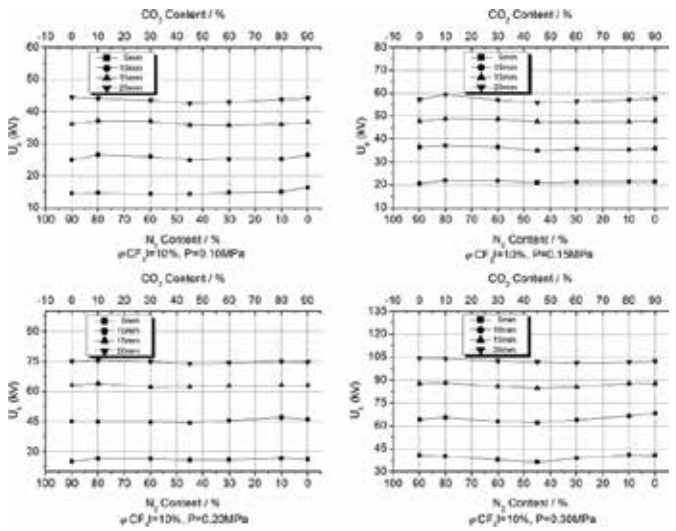

**Figure 10.** Relationship between AC-breakdown voltage and mixing contents of $CF_3I$, $N_2$, $CO_2$ gas mixtures.

hump effect or trend of saturation. Curves in **Figure 9** are similar to these in **Figure 7**, the superposition of the curves of gas mixtures with different contents is very high and the performed insulation characteristics are little different.

**Figure 10** shows that under different gas pressures, the curves of the variety of the AC-breakdown voltage for $CF_3I$, $N_2$, $CO_2$ gas mixtures changes as the content changes. Generally, with the same mixing ratio of CF3I, the breakdown strength becomes stronger with the increasing ratio of $CO_2$. The same as the judge of the foregoing, the change of the gas mixtures of $CF_3I$ is not obvious as the contents of $N_2$ and $CO_2$ change. What is worthy to be concentrated, it is that $N_2$ has higher insulation strength than $CO_2$, but it does not perform in the $CF_3I$ gas mixtures.

## 5. Power frequency AC-breakdown characteristics of $C_3F_7CN/CO_2$

AC-breakdown characteristics of $C_4F_7CN$ mixed with $CO_2$ are tested for different concentrations. **Figure 11** shows that AC-breakdown voltage of $C_3F_7CN/CO_2$ gas mixtures varies as the mixture ratio changes between 0 and 10% under different air pressures. Under the same gas pressure, as the mixture ratio of $C_4F_7CN$ *k* increases, the AC-breakdown voltage of gas mixtures shows the saturated trend to increase. The lower the gas pressure is, the smaller the growth is. It has to be said that the influence of the mixture ratio *k* on the $C_3F_7CN/CO_2$ gas mixtures is less under low gas pressure. In addition, under high-gas pressure, increasing the mixture ratio k can increase the insulation properties of the gas mixtures. When the proportion of $C_3F_7CN$ increases to 20%, the insulation properties of $C_3F_7CN/CO_2$ gas mixtures can approach that of pure $SF_6$ under the same condition.

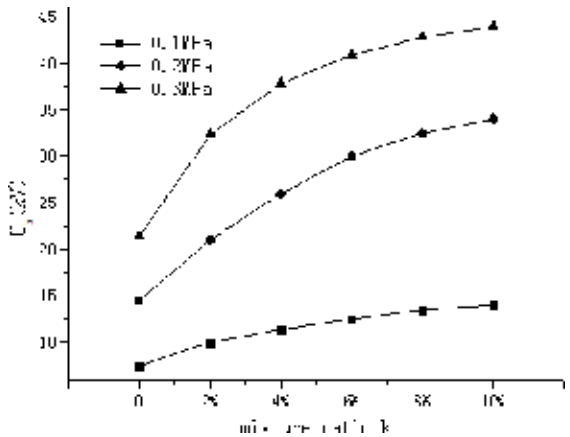

**Figure 11.** Relationship between power frequency breakdown voltage and mixture ratio of $C_3F_7CN/CO_2$.

## 6. Lightning impulse characteristics of c-$C_4F_8$, $N_2$, $CO_2$ gas mixtures

**Figures 12** and **13** show the testing curves of the positive lightning impulse voltage of gas mixtures of 10% c-$C_4F_8$ with $N_2$ and $CO_2$. The positive lightning impulse voltage increases as the electrodes gap increases without the performance of the trend to saturation in $SF_6$ gas mixtures, and the breakdown voltage increases nearly linearly as the air pressure increases. From the perspective of the excitation energy and the ionisation energy of the microcosmic parameters, c-$C_4F_8$ is more appropriate to be mixed with $CO_2$ and the positive lightning impulse breakdown voltage of $CO_2$ is higher than $N_2$. According with **Figures 12** and **13**, it can be

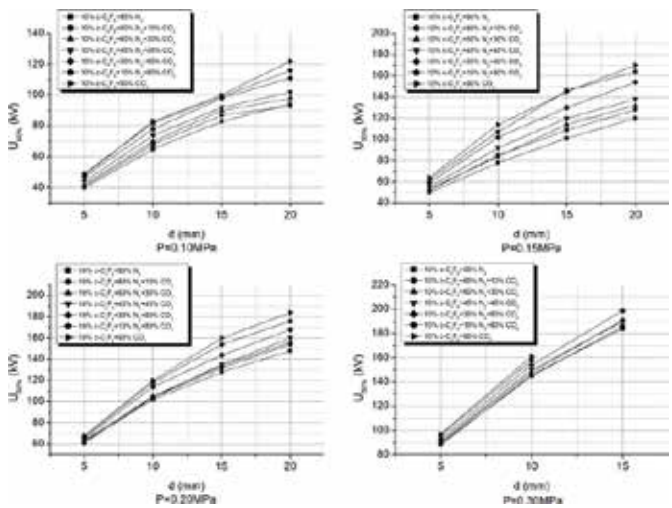

**Figure 12.** Positive lightning impulse breakdown voltage of c-$C_4F_8$, $N_2$, $CO_2$ gas mixtures with different gas pressures.

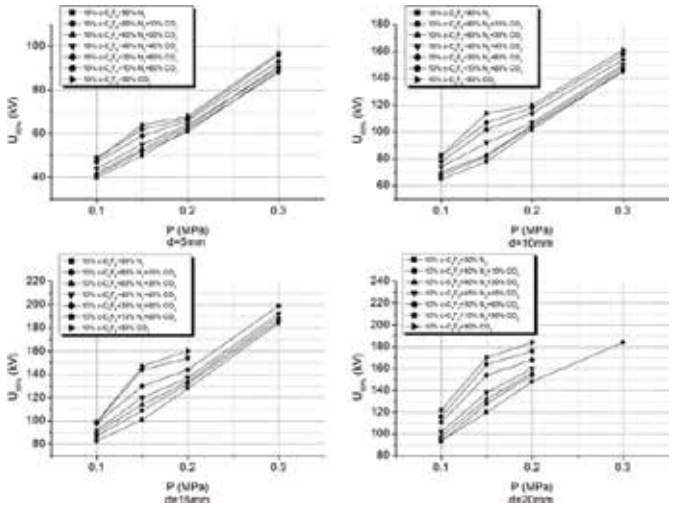

**Figure 13.** Positive lightning impulse breakdown voltage of c-$C_4F_8$, $N_2$, $CO_2$ gas mixtures with different electrodes gap distances.

seen that 10%c-$C_4F_8$ + 90%$CO_2$ gas mixtures have the highest breakdown voltage and 10%c-$C_4F_8$ + 90%$N_2$ gas mixtures have the lowest breakdown voltage.

**Figure 14** shows the different curves of positive lightning impulse breakdown voltage of the gas mixtures of 10%c-$C_4F_8$ with $N_2$ and $CO_2$ as the content of $N_2$ and $CO_2$ changes. Because of $CO_2$ itself has stronger ability to tolerate positive lightning impulse and it will not have obvious ionisation with c-$C_4F_8$ compared with $N_2$, the breakdown voltage increases as the content

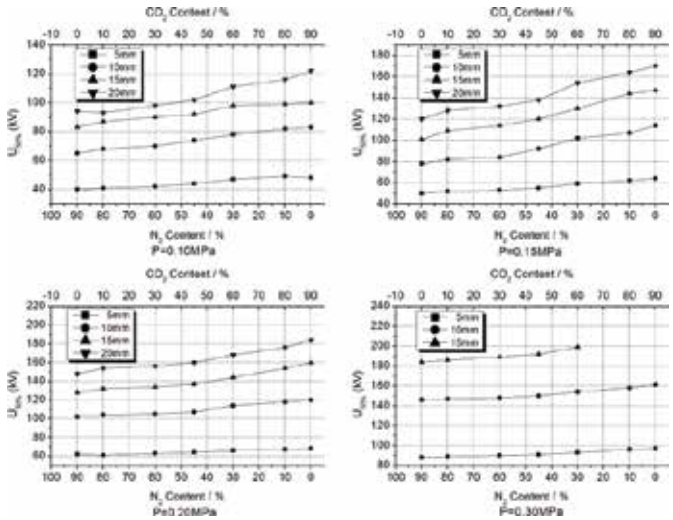

**Figure 14.** Relationship between positive lightning impulse breakdown voltage and mixing contents of c-$C_4F_8$, $N_2$, $CO_2$ gas mixtures.

of $CO_2$ in the gas mixtures increases. Because of the high resonance excitation, energy of $N_2$ in the gas mixtures will have negative impact on $CO_2$ when the content of $N_2$ exceeds 30%. The increase of breakdown voltage of the gas mixtures is not obvious, and when the content of $N_2$ is lower than 30%, the positive lightning impulse breakdown voltage shows more obvious trend to increase as the content of $CO_2$ increases. Comparing 10%c-$C_4F_8$ + 90%$N_2$ and 10%c-$C_4F_8$ + 90%$CO_2$, it is not hard to find that 10%c-$C_4F_8$ + 90%$CO_2$ has obviously higher positive lightning impulse breakdown voltage.

## 7. Lightning impulse characteristics of the $CF_3I$, $N_2$, $CO_2$ gas mixtures

**Figures 15** and **16** show the curves of the positive lightning impulse (means that the impulse voltage is applied to sphere electrode, and the plane electrode is connected to ground) breakdown voltage of 10% $CF_3I$ with $N_2$ and $CO_2$ of different contents. The positive lightning impulse voltage of $CF_3I$ gas mixtures increases with a little saturation as the electrodes gap and air pressure increase. From the difference of breakdown voltages of gas mixtures with different contents and ratios, it can be seen that $CF_3I$ has the similar properties with c-$C_4F_8$ and it is more appropriate to mix with $CO_2$.

**Figure 17** shows the variation of the positive lightning impulse breakdown voltage of the gas mixtures consisting of 10% $CF_3I$ and $N_2$ as well as $CO_2$ as the mixture ratio changes. The curves in **Figure 17** have the same change with the c-$C_4F_8$ gas mixtures, when the content of $N_2$ is lower than 30%, the excitation energy can weaken the ionisation of $CF_3I$ and $CO_2$, and the breakdown voltage of the gas mixtures increases obviously and this is the same with the changing trend of c-$C_4F_8$ gas mixtures.

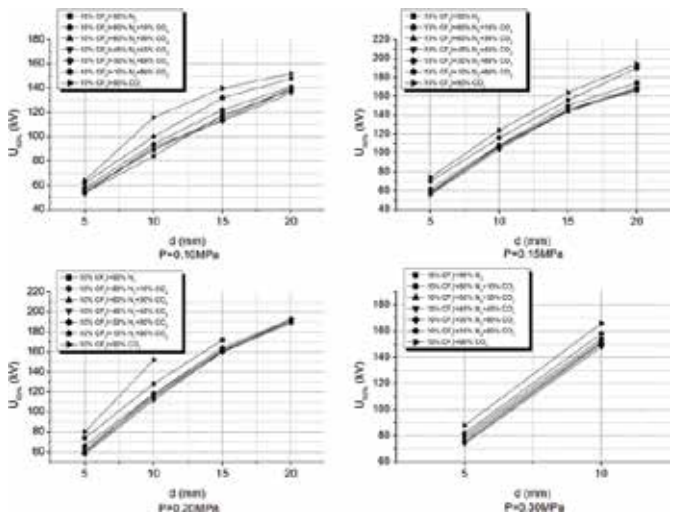

**Figure 15.** Positive lightning impulse breakdown voltage of $CF_3I$, $N_2$, $CO_2$ gas mixtures with different gas pressures.

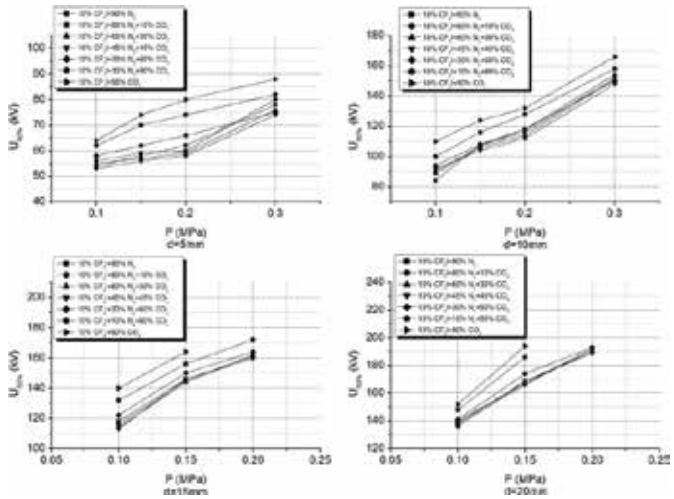

**Figure 16.** Positive lightning impulse breakdown voltage of $CF_3I$, $N_2$, $CO_2$ gas mixtures with different electrodes gap distances.

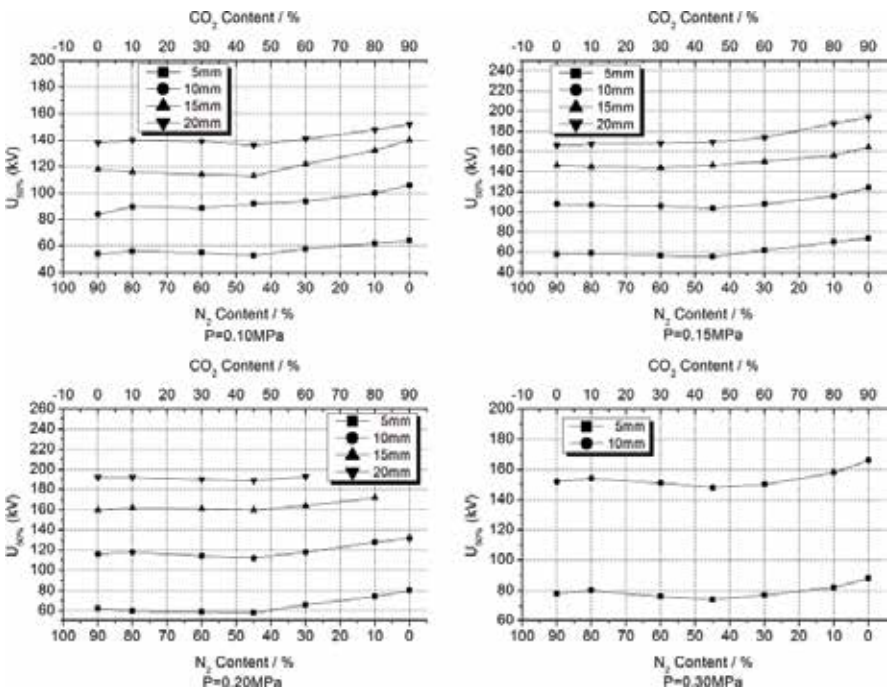


**Figure 17.** Relationship between positive lightning impulse breakdown voltage and mixing contents of $CF_3I$, $N_2$, $CO_2$ gas mixtures.

## 8. Conclusion

**1.** In the consideration of insulation strength, c-$C_4F_8$ gas mixtures with $N_2$, $CO_2$ is prior than current $SF_6/N_2$ gas mixtures and pure $SF_6$. Moreover, c-$C_4F_8$ gas mixtures can solves the problem of c-$C_4F_8$ gas tending to liquefaction and carbon decomposition. Traditional c-GIS is widely used in the range of middle voltage, mainly in electric power substation and among consumers. Vacuum circuit breaker and grounded switchgear are both installed in a gas cavity shell, which is full with gas at 0.1–0.3MPa. Therefore, c-$C_4F_8$ gas mixtures can be applied to the gas switchgear of relative low voltage whose working pressure is low and function is not to break current arc, which can not only guarantee the insulation strength, but also greatly reduce the effect of insulation gas on the environment. Therefore, it has a good potential to substitute $SF_6$ and $SF_6/N_2$ as insulation media.

Moreover, for the areas with warm climate, electric apparatus such as transformer and high voltage power transmission wire are promising to use c-$C_4F_8$ gas mixtures as insulation media forming gas insulation transformer (GIT), gas insulation line (GIL) and cabinet Gas Insulated Switchgear at middle and low voltage (C-GIS).

**2.** Above comprehensive of analysis, under the same pressure conditions, the insulating strength of $CF_3I$ is higher than that of $SF_6$ while ensuring $CF_3I$ not to be liquefied. Compared with compressed air or compressed $N_2$ insulated in C-GIS, $CF_3I$ can lower the pressure, in order to reduce the sealing technology and easy to manufacture. The shortcomings of high price also can be relief after mixed with buffer gas. Therefore, using $CF_3I$ as insulating gas in C-GIS has better comprehensive performance than that of the present C-GIS.

$CF_3I$ and $N_2$ mixed gas can be used as replacement of $SF_6$ gas in the C-GIS at a low pressure, which has bigger advantage on the dielectric strength, liquefaction temperature and cost, especially in 30% proportion of $CF_3I$ in mixed gases, that is the most likely to be feasible.

As environmentally friendly insulation gas, $CF_3I$ and its gas mixtures is a hot-topic on the global scope for gas insulating systems. The application of $CF_3I$ and its gas mixtures in high-voltage apparatus not only meets the requirements and current trends on environmental protection in the international community, but also is a new direction in the field of electrical insulation.

To sum up, taking into account environmental characteristics, insulating properties and liquefaction temperature, $CF_3I$ gas mixtures can be applied prior to C-GIS in the middle, low voltage system as well as GIL, GIT and other electrical devices in high-voltage system.

**3.** Power-frequency breakdown voltage of $C_3F_7CN/CO_2$ gas mixtures increases with the increase of mixing ratio from 0 to 10%. The relative dielectric strength of the gas mixtures showed a trend of saturated growth with the increase of mixing ratio, and power-frequency

breakdown voltage of $C_3F_7CN/CO_2$ gas mixtures when $C_3F_7CN$ is 8% ratio can reach 75% of that of pure $SF_6$ under the same condition. $C_3F_7CN/CO_2$ gas mixtures have potential of application of substitute for $SF_6$ in the electric power equipment, and the insulation of the other characteristics need further study. A deep insight into the partial discharge properties and corona stabilisation behaviour under strong inhomogeneous fields is needed for a full understanding.

## Acknowledgements

This work is supported by the National Natural Science Foundation of China (Grant No. 51337006).

## Appendix

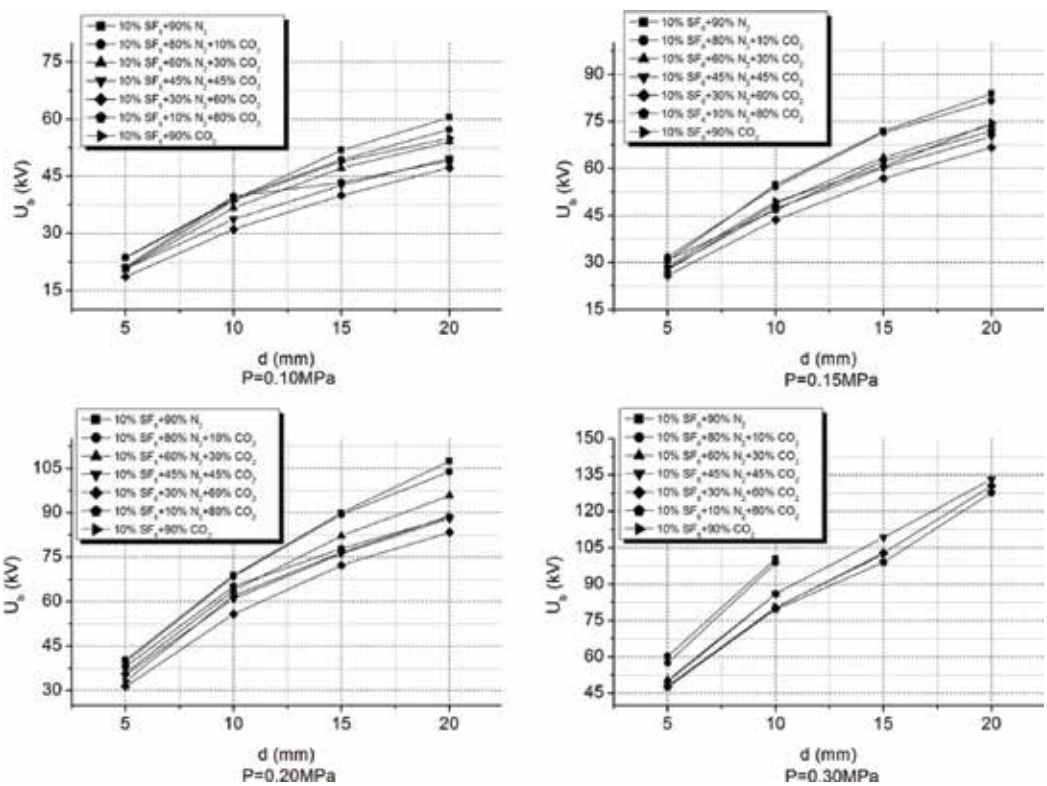


**Figure A1.** AC breakdown voltage of $SF_6$, $N_2$, $CO_2$ gas mixtures with different gas pressures.

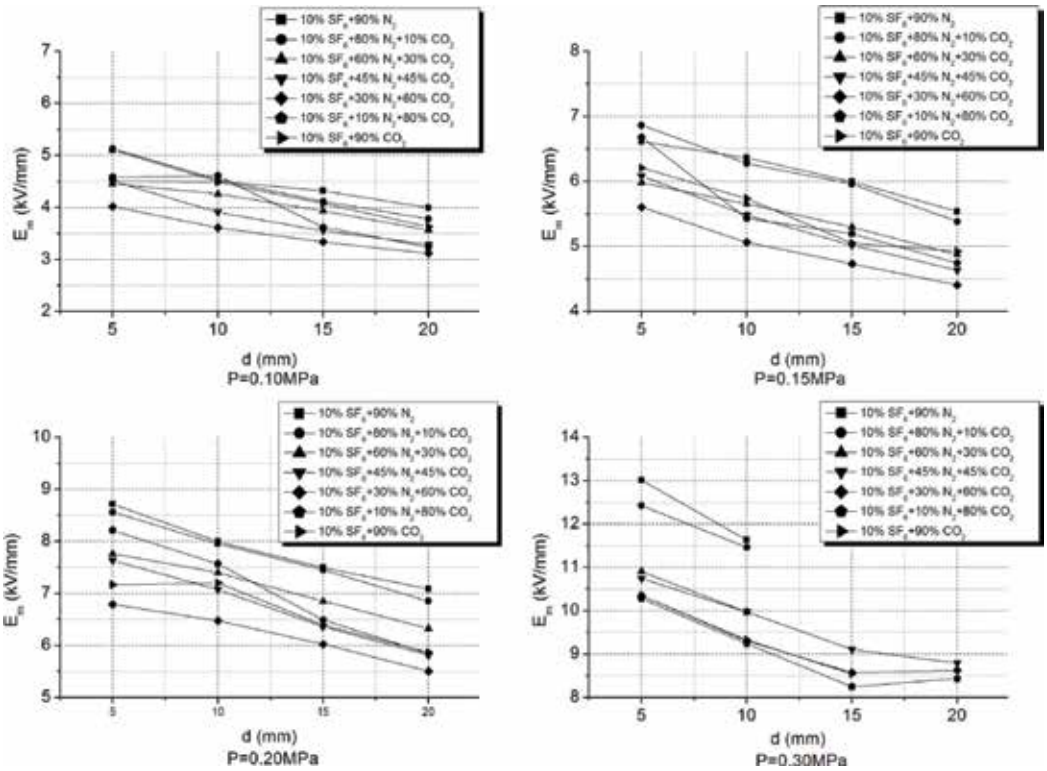


**Figure A2.** Maximum electric strength of $SF_6$, $N_2$, $CO_2$ gas mixtures with different gas pressures.

## Author details

Dengming Xiao

Address all correspondence to: dmxiao@sjtu.edu.cn

Shanghai Jiao Tong University, Shanghai, China

## References

[1] Yunkun D. Basic research of the environmentally friendly insulating gas $CF_3I$ for its application in electric power apparatus [PhD thesis]. Shanghai: Shanghai Jiao Tong University; 2016

[2] Reilly J, Prinn R, Harnisch J, Fitzmaurice J, Jacoby H, Kicklighter D, et al. Multi-gas assessment of the Kyoto protocol. Nature. 1999;**401**:3466-3469

[3] Qingchen C, Yongxiang Z, Gao X, Wang M. Paris agreement: A new start for global governance on climate. Progress in Climate Change Research. 2016;**12**:61-67

[4] National Development and Reform Commission. China's Policy and Action on Climate Change 2017. Beijing: China Government; 2017

[5] WMO. The state of greenhouse gases in the atmosphere based on global observations through 2016. WMO Greenhouse Gas Bulletin (GHG Bulletin). October 2017;**13, 30**:1

[6] CE. Why Climate Policy-Makers can't Afford to Overlook Fully Fluorinated Compounds. Washington: World Resources Institute; 1995

[7] Xiangwan D. Opening a new stage of global green low-carbon development. China Awards for Science and Technology. 2016:6-6

[8] Dengming Xiao. Gas Discharge and Gas Insulation. China: Springer; 2016

[9] Wwvh W, Wwvl W, Connor JT, Astin AV, Engineerin SK. National Bureau of Standards. IRE Transactions on Aeronautical & Navigational Electronics. 2012;**2**:111-114

[10] Liu X, Wang J, Wang Y, Zhang Z, Xiao D. Analysis of the insulation characteristics of c-$C_4F_8$/$CO_2$ gas mixtures by the Monte Carlo method. Journal of Physics D: Applied Physics. 2008;**41**:015206

[11] Costello MG, Flynn RM, Bulinski MJ. Fluorinated nitriles as dielectric gases. Google Patents; 2013

[12] Nishimura H, Huo WM, Ali MA, Kim YK. Electron-impact total ionization cross sections of $CF_4$, $C_2F_6$, and $C_3F_8$. Journal of Chemical Physics. 1999;**110**:3811-3822

[13] Devins J. Replacement gases for SF6. IEEE Transactions on Electrical Insulation. 1980: 81-86

[14] Christophorou LG, Olthoff JK, Green DS. Gases for electrical insulation and arc interruption: Possible present and future alternatives to pure SF6. NIST TN-1425. 2011;**8**:391

[15] Xiao D, Zhu L, Li X. Electron transport coefficients in SF6 and xenon gas mixtures. Journal of Physics D: Applied Physics. 2000;**33**:L145

[16] Christophorou LG, Olthoff JK. Electron interactions with c-C4F8. Journal of Physical and Chemical Reference Data. 2001;**30**:449-473

[17] Zhao S, Jiao J, Zhao X, Zhang H, Xiao D, Yan JD. Synergistic effect of c-$C_4F_8$/$N_2$ gas mixtures in slightly non-uniform electric field under lightning impulse. In: IEEE Electrical Insulation Conference; 2016. pp. 531-534

[18] Wu B-T, Xiao D-M, Liu Z-S, Zhang L-C, Liu X-L. Analysis of insulation characteristics of c-$C_4F_8$ and $N_2$ gas mixtures by the Monte Carlo method. Journal of Physics D: Applied Physics. 2006;**39**:4204

[19] Macko WMJ. Toxicity review for Iodotrifluoromethane ($CF_3I$). In: Halon Options Technical Working Conference. US. 1999

[20] NFP Association. Standard on Clean Agent Fire Extinguishing Systems. In: NFPA 2001. New Orleans, LA, U.S.: Technical Committee on Halon Alternative Protection Options; 2000. p. 109

[21] De Urquijo J. Is $CF_3I$ a good gaseous dielectric? A comparative swarm study of $CF_3I$ and $SF_6$. Journal of Physics: Conference Series 86, 2007:012008

[22] Yun-Kun D, Deng-Ming X. The effective ionization coefficients and electron drift velocities in gas mixtures of $CF_3I$ with $N_2$ and $CO_2$ obtained from Boltzmann equation analysis. Chinese Physics B. 2013;**22**:035101

[23] Kimura M, Nakamura Y. Electron swarm parameters in $CF_3I$ and a set of electron collision cross sections for the $CF_3I$ molecule. Journal of Physics D: Applied Physics. 2010;**43**:145202

[24] Cressault Y, Connord V, Hingana H, Teulet P, Gleizes A. Transport properties of $CF_3I$ thermal plasmas mixed with $CO_2$, air or $N_2$ as an alternative to $SF_6$ plasmas in high-voltage circuit breakers. Journal of Physics D: Applied Physics. 2011;**44**:495202

[25] De Urquijo J, Mitrani A, Ruíz-Vargas G, Basurto E. Limiting field strength and electron swarm coefficients of the $CF_3I$–$SF_6$ gas mixture. Journal of Physics D: Applied Physics. 2011;**44**:342001

[26] De Urquijo J, Juárez A, Basurto E, Hernández-Ávila J. Electron impact ionization and attachment, drift velocities and longitudinal diffusion in $CF_3I$ and $CF_3I$–$N_2$ mixtures. Journal of Physics D: Applied Physics. 2007;**40**:2205

[27] Xiaoxing Z, Junjie Z, Ju T, Song X, Yefei H."Experimental research on the partial discharge insulation properties of $CF_3I/CO_2$ and $CF_3I/N_2$ gas mixtures," Proceedings of the CSEE, vol. 34, pp. 1948-1956, 2014

[28] ZHAO Su, XIAO Dengming, ZHANG Hui, and DENG Yunkun, "Investigation on discharge polarity effect of $CF_3I/N_2$ gas mixtures under lightning impulse," Proceedings of the CSEE, vol. 37, pp. 3636-3642, 2017

[29] Li X, Zhao H, Wu J, Jia S. Analysis of the insulation characteristics of $CF_3I$ mixtures with $CF_4$, $CO_2$, $N_2$, $O_2$ and air. Journal of Physics D: Applied Physics. 2013;**46**:345203

[30] Zhao X, Li B, Xiao D, Deng Y. Breakdown characteristics of $CF_3I$-$N_2$ gas mixtures in a needle-plate geometry. IEEE Transactions on Dielectrics and Electrical Insulation. 24 April 2017;**24**:869-875

[31] Xiao S, Cressault Y, Zhang X, Teulet P. The influence of Cu, Al, or Fe on the insulating capacity of $CF_3I$. Physics of Plasmas. 2016;**23**:123505

[32] Kochetov I, Napartovich A, Vagin N, Yuryshev N. Mechanism of pulse discharge production of iodine atoms from $CF_3I$ molecules for a chemical oxygen–iodine laser. Journal of Physics D: Applied Physics. 2009;**42**:055201

[33] Kieffel Y. Characteristics of G3—An alternative to SF6. In: IEEE International Conference on Dielectrics; 2016. pp. 880-884

[34] Switzerland: ABB achieves breakthrough in switchgear technology with eco-efficient insulation gas. Tendersinfo News. 2014

[35] Rabie M, Franck CM. Assessment of eco-friendly gases for electrical insulation to replace the most potent industrial greenhouse gas $SF_6$. Environmental Science & Technology. 2017:369-380

[36] Stoller PC, Doiron CB, Tehlar D, Simka P, Ranjan N. Mixtures of $CO_2$ and $C_5F_{10}O$ perfluoroketone for high voltage applications. IEEE Transactions on Dielectrics & Electrical Insulation. 2017;**24**:2712-2721

[37] Zhao S, Xiao D, Jiao J, Zhao X. Discharge characteristics of c-$C_4F_8/N_2$ with and without insulator under standard lightning impulse. Presented at the IEEE Electrical Insulation Conference; 2016

Chapter 5

# Typical Internal Defects of Gas-Insulated Switchgear and Partial Discharge Characteristics

Fuping Zeng, Ju Tang, Xiaoxing Zhang,
Siyuan Zhou and Cheng Pan

Additional information is available at the end of the chapter

http://dx.doi.org/10.5772/intechopen.79090

**Abstract**

Gas-insulated switchgear (GIS) is a common electrical equipment, which uses sulfur hexafluoride ($SF_6$) as insulating medium instead of traditional air. It has good reliability and flexibility. However, GIS may have internal defects and partial discharge (PD) is then induced. PD will cause great harm to GIS and power system. Therefore, it is of great importance to study the intrinsic characteristics and detection of PD for online monitoring. In this chapter, typical internal defects of GIS and the PD characteristics are discussed. Several detection methods are also presented in this chapter including electromagnetic method, chemical method, and optical method.

**Keywords:** GIS, internal defects, PD, intrinsic characteristics, electromagnetic detection method, chemical detection method, optical detection method

## 1. Introduction

Gas-insulated switchgear (GIS) is an electrical equipment that conceals traditional electrical devices in a chamber. GIS has obvious advantages over traditional air-insulated switchgear (AIS). Firstly, GIS demands less area thus reducing the cost; secondly, GIS has a longer overhaul period; and finally, GIS has higher reliability. For these reasons, GIS has been widely used in the world nowadays [1–4]. However, GIS has a complex structure that internal defects may come into being during process of manufacturing, transferring, and installing [5, 6]. These defects will induce partial discharge (PD) [7–9], which causes potential internal insulation aging. The insulation aging may develop into serious fault and blackout [10, 11]. PD also reflects GIS insulation state. By monitoring PD signals, potential defects can be recognized.

### 1.1. Typical types of GIS internal defects

There are several types of GIS internal defects, namely high-voltage (HV) conductor protrusions, free metal particles, floating potential, insulator metal pollution, and insulator gap [7]. The various defects in GIS are shown in **Figure 1**.

In recent decades, GIS has also been deployed widely in China. However, operating experience shows that although GIS equipment has high reliability, inevitable internal defects will still lead to failure and gradually major accidents. This has become a hot topic in power system [12].

According to statistics, the State Grid Corporation of China had a total of 48,498 GIS equipment in operation by the end of 2013, with a growth of 17.8% of the previous year. In the same year, 11 trips occurred in the GIS operation of the national grid system in China. CIGRE 23.10 Working Group GIS Fault Investigation Report shows that in all failures of GIS that occurred before 1985, the insulation failure accounted for 60 and 51% after 1985. According to operation analysis of the State Grid of China, at the end of June in 2008, 33 GIS accidents occurred including 24 insulation accidents, while operation failure occurred 74 times including 13 insulation accidents [4]. GIS insulation failure accidents are diverse. According to **Figure 2**, insulation faults caused by bad contact and defects of metal particles occupy a larger proportion [12].

In this chapter, we will focus on four typical types of GIS internal insulation defect, that is, free-metal particles, conductor protrusions, insulator gap, and insulator metal pollution.

#### *1.1.1. Free metal particles defect (denoted as P-type defect)*

Free-metal particles defects in GIS are one of the main causes of insulation failure. During the GIS assembling, installation or operation process, its metal parts may rub against each other, thus creating free metal particles. Due to their small size, these metal particles will move and beat under the electric field forces. If the range of particle movement is large enough, it is possible to form conductive paths or arc passages between the HV conductor and the shell, causing serious damage to the GIS. The path forming depends on many factors including applied voltage, shape and size of particles, and the position of the particles [12].

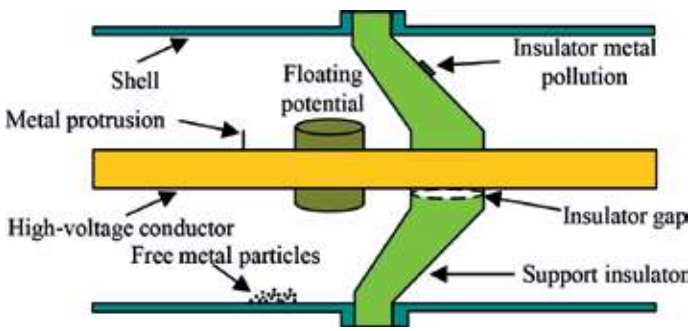


**Figure 1.** GIS internal insulation-defect type diagram.

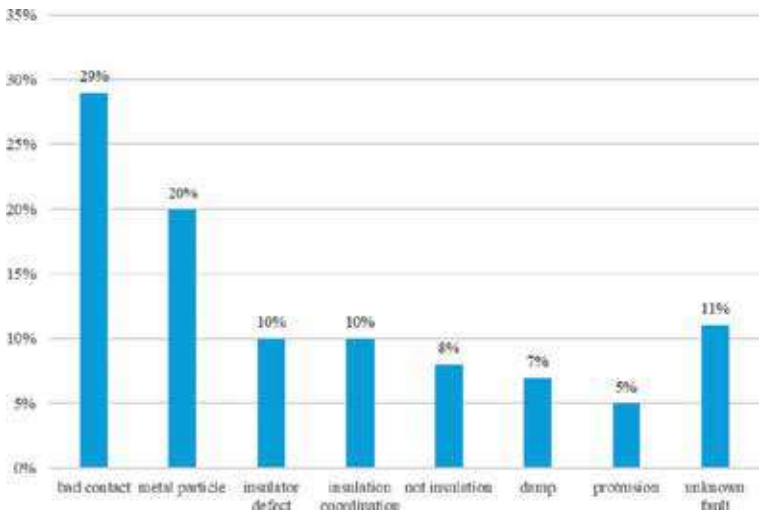


**Figure 2.** GIS equipment-defect type statistics.

### *1.1.2. Metal protrusions defect (denoted as N-type defect)*

Metal protrusion defects refer to the defects that form on the protruding parts such as HV conductor inside GIS. Just like free-metal particles defect, these protrusions are usually formed during process of assembling, installation, or operation. Due to the sharp tip of the protrusions, the electric field will be distorted and strong electric field will then come into being. Under the rated working voltage, the strong electric field will induce a stable PD, but under some overvoltage, it may cause breakdown and GIS fault.

The discharge characteristics of protrusion on HV conductor and that on inner wall of shell are different. Protrusions on the HV conductor usually discharge in the negative half-cycle of the power frequency, while protrusions on the inner wall of the shell usually discharge in the positive half-cycle of the power frequency. Some tiny protrusions will be ablated in long-term discharge and will not threaten the insulation of GIS. However, larger protrusions will persist for a long-time and damage the operation insulation of GIS [12].

### *1.1.3. Insulator gap defect (denoted as G-type defect)*

Insulator gap defects in GIS mainly happen on the basin-type insulator, which can be classified into two types. One type is due to internal bubbles of epoxy resin resulting during process of manufacturing. Then during operation, PD will take place in these bubbles under strong electric field, resulting in gradual insulation deterioration of the basin-type insulator, and serious insulation breakdown may follow;

The other type is due to electric force in the long-term operation. Mechanical vibration process may result in connection loosening of basin-type insulator and HV conductive rod connection loosening. Then an insulator gap defect forms and induces PD, resulting in deterioration of the insulating properties of the basin-type insulator [13].

*1.1.4. Insulator metal pollution defect (denoted as M-type defect)*

The surface of the insulator sometimes adsorbs some metal particles which move under the electric field force. Some of the particles may not be dangerous at first, but due to the mechanical vibration under electrostatic force, their movement facilitates the discharge and then induces the PD.

Due to strong adsorption, some of the particles will not move. Particles fixed on the insulator surface forms insulator surface pollution defects. These fixed metal particles have the following characteristics: on their surface, charges will accumulate, and these surface charges sometimes aggravate the distortion of the electric field, causing PD. Particle-induced discharge will cause insulator surface damage, resulting in surface tree marks. Eventually, it may cause serious insulation breakdown and flashover [14].

## 1.2. Typical detection methods of PD

Under the operating voltage, the insulation defect will cause the local electric field distortion in the insulation medium. When the local electric field reaches the critical breakdown field strength, PD will be induced and a large amount of charged particles will be generated. Charged particles under electric field will migrate, recombine, and adhere, resulting in pulse current, and accompanied by optical, electrical, thermal, and acoustic effects. By effective detection of these signals, PD can be measured in the GIS. At present, there are five commonly used PD signal detection methods, that is, pulse current method [15], ultra-high frequency (UHF) method [16], ultrasonic method, chemical detection method, and optical detection method [17, 18]. In this chapter, we will focus on the following three PD signal detection methods:

*1.2.1. UHF method*

When a PD occurs, a non-periodically changing current pulse excites a changing magnetic field and radiates a high-frequency electromagnetic (EM) wave through the insulator. Due to the short-duration of the PD current pulse and the steep rising edge, the excitation frequency of the EM wave ranges from several MHz to several GHz [19, 20].

Because GIS is a good coaxial waveguide structure, high-frequency EM waves can be effectively transmitted within the GIS. Through the high-frequency sensors installed inside or outside GIS, the detection of these EM signals and PD signals can be achieved. This method is called UHF method.

The UHF method has many advantages. Firstly, it uses the UHF signal to avoid EM interference due to low frequency in the power grid and has strong anti-interference ability. Secondly, it can pinpoint the location of the PD [21]. Finally, this method has a large detection range and requires fewer sensors to be installed [11, 22].

*1.2.2. Chemical detection method*

Many studies show that the $SF_6$ gas will decompose under PD and the decomposed components will further react with moisture and oxygen in the gas chamber of GIS to generate a

series of chemical substances including $SO_2F_2$, $SOF_2$, $CF_4$, $SO_2$, $SOF_4$, $S_2F_{10}$, $SiF_4$, HF, CO, $CO_2$, $CH_4$, and $SF_4$. By detecting these decomposed components in the GIS gas chamber, it is possible to determine whether there is a PD source [23, 24].

Studies have shown that PD sources caused by different types of defects differ in $SF_6$ decomposition components, their ratio, and gas generating rate. So one can also identify the PD type by detecting $SF_6$ decomposition components.

$SF_6$ decomposition component method is able to locate the fault to find fault gas chamber, response accurately and timely to sudden failure, and judge the type of defect. It is also free from the scene of EM and noise interference, and regular detection can reflect the development of PD in GIS.

*1.2.3. Optical detection method*

In the process of PD, molecular ionization, ion recombination, and atomic energy level transition will excite and radiate optical signals. Optical detection methods of PD based on ultraviolet light (UV), infrared ray (IR), and visible light have been developed.

The spectral range of optical signal generated by PD in $SF_6$ gas is roughly 460–550 nm, which is mainly visible light. The basic principle of optical detection method is to use optical sensors to receive optical signals generated by the PD source and convert optical signals into electrical signals through the optical converter [17, 18].

Optical detection is not affected by strong EM interference on site, its anti-interference ability is more outstanding than the other two methods, and real-time monitoring of GIS PD phenomenon can be achieved. However, due to poor-optical signal transmission and GIS is a closed structure of equipment, the optical method cannot be used for outer GIS detection; optical sensors must be installed inside the GIS.

## 2. Physical model of typical defects and the electrical field simulation

In order to simulate GIS insulation defects and PD, what we choose for the physical model of insulation defect designed in this chapter is stainless steel, aluminum, and brass, and the solid insulation material is epoxy resin [25].

### 2.1. Typical detection methods of PD construction of insulation defect physical model

*2.1.1. N-type defect*

Under steady-state AC voltage, the prominent parts are distributed in the electric field and form the local high field strength zone. This corona sometimes appears to be relatively stable as the discharge only occurs in a local area instead of throughout the entire electrode. In this chapter, pin-plate electrodes are used to simulate N-type defects. As shown in **Figure 3**, the pin electrodes are used to simulate abnormal protrusions on HV conductors and the plate electrodes simulate the metal shell of GIS.

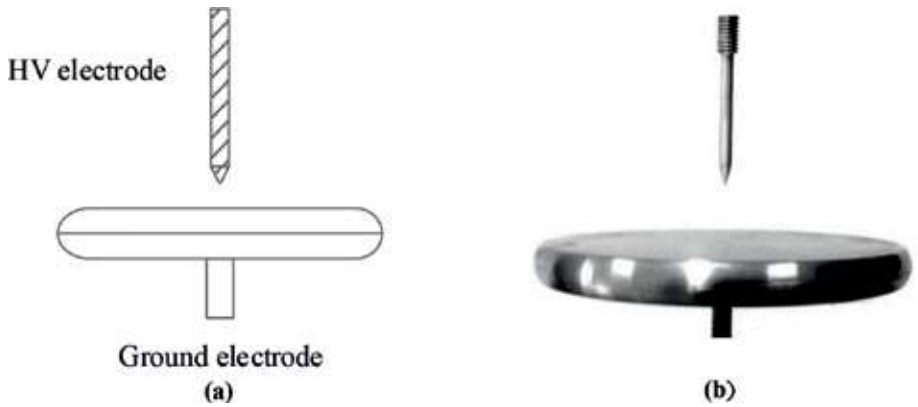


**Figure 3.** N-type insulation defect model. (a) Model diagram and (b) physical diagram.

In order to obtain a stable PD, an electrode is adopted with a tip radius of curvature of about 0.3 mm as well as a cone angle of 30°, and a ground plate electrode diameter of 120 mm as well as 10 mm thickness. Aluminum needle electrodes are designed and manufactured, with ground electrode material stainless steel, and electrode surface all were well polished.

*2.1.2. P-type defect*

Conductive particles have the shape of powder, flake or large solid particles, etc.; they get the charge in the electric field and will move or beat under electrostatic force. If the electric field is strong enough and the energy obtained by the conductive particles is large enough, particles are possible to cross the gap between the shell and the HV conductor or move to a point where the insulation is damaged.

The motion intensity of the conductive particles depends on the material, the shape, and the applied voltage, as well as the strength and duration of the external electric field strength and the location of the particles in GIS cavity. When the metal particles come close without touching the HV conductor, then PD arises as the electrical characteristics. Half of the actual GIS equipment uses a structure with a coaxial cylinder between the HV conductor and the shell, that is, a slightly uneven electric field structure [26]. In order to effectively simulate the slightly heterogeneous electric field structure of the coaxial cylinder inside the real GIS, the ball-bowl electrode shown in **Figure 4** is selected in this chapter. The bowl electrode is cut by a half of a stainless steel hollow sphere. In order to ensure the steady PD experiment, it is necessary to limit the beating range of the copper scrap. HV terminal ball electrode diameter is designed to be 44 mm, the ground bowl diameter is designed to be 120 mm, and particle maximum beating range up to 40 mm.

*2.1.3. M-type defect*

Due to electric force, some metal particles are absorbed on the insulator, thus distorting the insulator surface electric field and causing PD. Some metal particles on the insulator may not be dangerous at first, but under mechanical vibration and electric force, there will be slight movement and potential danger. Metal particles on the surface of the insulator will form surface charge aggregation, thereby increasing the possibility of failure. Particle discharge can cause

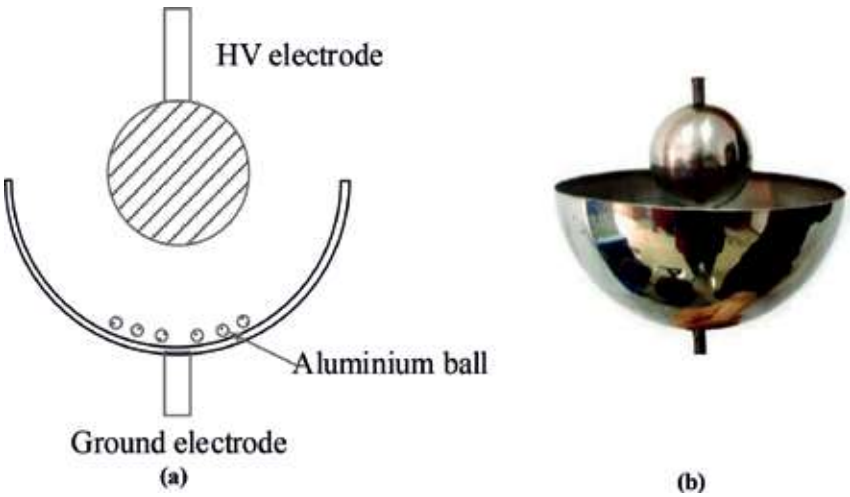


**Figure 4.** P-type insulation defect model. (a) Model diagram and (b) physical diagram.

damage to the surface of the insulator, causing surface tree marks in the power frequency field. Once the discharge channel is formed, a serious insulation accident will be caused.

In this chapter, rectangular copper cutting (5 × 18 $mm^2$) is used to stimulate M-type defect. The contact surface of electrodes and cylindrical insulator is polished to avoid potential air gap discharge. The model structure is shown in **Figure 5**. The plate diameter is 120 mm, the epoxy resin cylindrical insulator diameter is 60 mm, and the thickness is 25 mm. The HV electrode material is aluminum, and the ground plate electrode material is stainless steel.

*2.1.4. G-type defect*

G-type defects are often formed in the manufacturing process such as epoxy curing shrinkage and internal voids [17]. The mechanism of air gap discharge is complicated, and it is generally believed that there are three ways of air gap discharge, that is, the throughout discharge, the discharge along the surface of the upper and lower electrode and the discharge along the air gap wall. In this chapter, G defects model is shown in **Figure 6**. The cylindrical insulator and the grounding electrode are closely adhered with epoxy glue to ensure that there are no gaps or bubbles between them. The air gap size at the interface between the high voltage plate electrode, and the insulator is about 1–3 mm. In order to reflect the real air gap situation, the insulator is slightly concave at the center of the upper surface, and the edge of the air gap is arc shaped.

## 2.2. Insulation defect electric field simulation

In this chapter, the finite-element analysis software COMSOL is used to simulate the electric field distribution of four insulation defect models. The simulation results are used to evaluate the feasibility of the model and provide the preliminary data reference for the following PD test.

In the simulation, a cylindrical cavity is used to simulate the $SF_6$ discharge gas chamber. The solution domain is set as $SF_6$ and the boundary conditions are grounded. The specific technical parameters of the simulation model and the relative dielectric constants are shown in **Tables 1** and **2**.

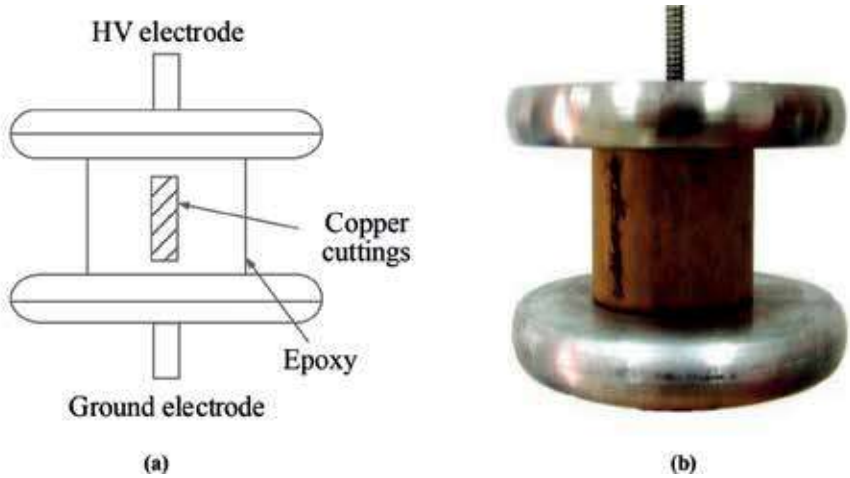


**Figure 5.** M-type insulation defect model. (a) Model diagram and (b) physical diagram.

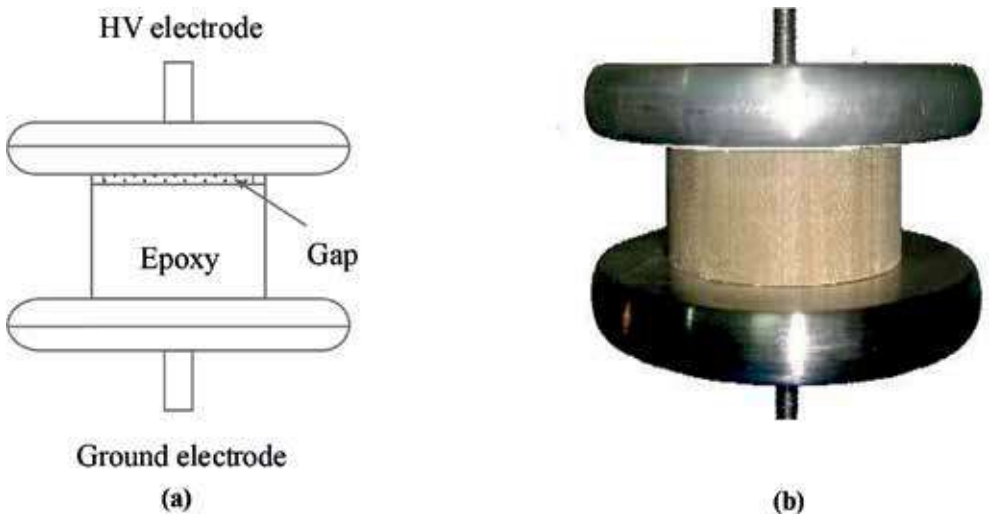


**Figure 6.** G-type insulation defect model. (a) Model diagram and (b) physical diagram.

*2.2.1. N-type insulation defect*

Due to the axial symmetry of N-type insulation defect, a two-dimensional axisymmetric model is adopted in this chapter. The HV-terminal needle electrode potential is set to 25 kV, the plate electrode with the cavity shell boundary is set to ground, and the needle-plate spacing is set to 10 mm.

The results of the electric field simulation of N-type insulation defect are shown in **Figure 7**. It can be seen from the figure that the distribution of the electric field between the needle and plate is extremely uneven. The electric field strength value at the tip of the needle electrode is high, and the electric field distortion at the tip of the needle electrode reaches up to 351 kV/cm.

| Cavity height/mm | Cavity diameter/mm | Plate electrode diameter/mm | Plate electrode thickness/mm | Needle curvature radius/mm | Cone sharp corners/° | Insulator diameter/mm | Insulator thick-ness/mm |
|---|---|---|---|---|---|---|---|
| 350 | 180 | 120 | 10 | 0.3 | 30 | 60 | 25/20 |

**Table 1.** Model technical parameters.

| Material | SF6 | Aluminum | Stainless steel | Aerosols (Copper) | Epoxy resin |
|---|---|---|---|---|---|
| Relative permittivity | 1.002 | 1.0 | 1.0 | 8000 | 3.8 |

**Table 2.** Relative dielectric constant of each part of the material.

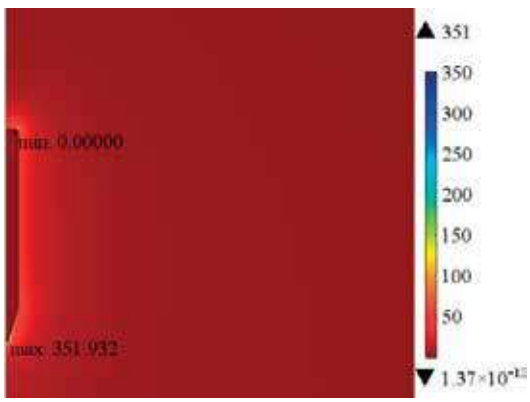


**Figure 7.** N-type insulation defect space electric field simulation output (mm).

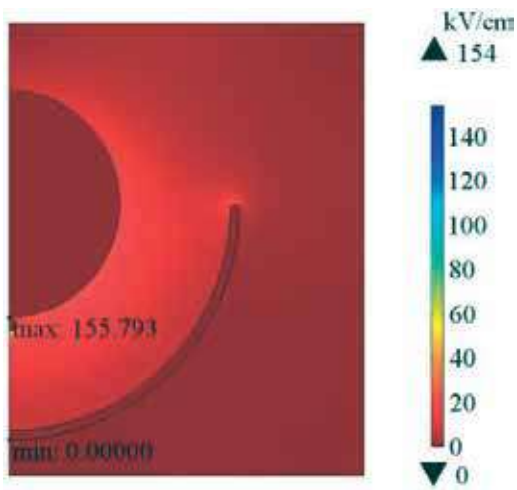


**Figure 8.** P-type insulation defect space electric field simulation output.

*2.2.2. P-type insulation defects*

Like N-type insulation defect, P-type insulation defect is also axisymmetric, so a two-dimensional axisymmetric model is adopted again for P-type insulation defect. In the simulation, the potential of the HV terminal ball electrode is set to be 30 kV, and the potential of the bowl electrode is set to be grounded. The distance between the ball and the bowl is set to 30 mm, and metal particles with a diameter of about 2 mm are placed in the bowl electrode. The floating particles are treated with the virtual large dielectric constant method.

The results of the electric field simulation of the P-type insulation defects are shown in **Figure 8**. The metal particles cause a distortion of the electric field between the electrodes. When the electric force is greater than the gravity of the metal particles, the particles will move or beat under the force. It can be seen from the figure that the electric field on the surface of metal particles close to the high voltage end is seriously distorted, and the maximum field strength reaches 155 kV/cm.

*2.2.3. M-type insulation defects*

In the simulation, the electrode potential of the HV terminal plate is set to be 30 kV, the boundary of the lower plate electrode and the cavity are set to be grounded, the thickness of the cylindrical insulator is set to 25 mm, and the surface is pasted with a metal copper cuttings of about 5 × 18 $mm^2$.

As shown in **Figure 9**, the simulation results show that the electric field at the surface of the insulator where the metal pollutants are located has been distorted, forming a very uneven field with the maximum field strength of 192 kV/cm. Based on the simulation results, insulator surface metal contamination will lead to PD before the insulator flashover.

*2.2.4. G-type insulation defects*

In the simulation, the potential of HV board is set to 60 kV. The boundary between lower board electrode and cavity is grounded. The upper surface of insulator is slightly concave with an average thickness of 20 mm. Between the HV board is arc-shaped air gap, with maximum gap 2 mm.

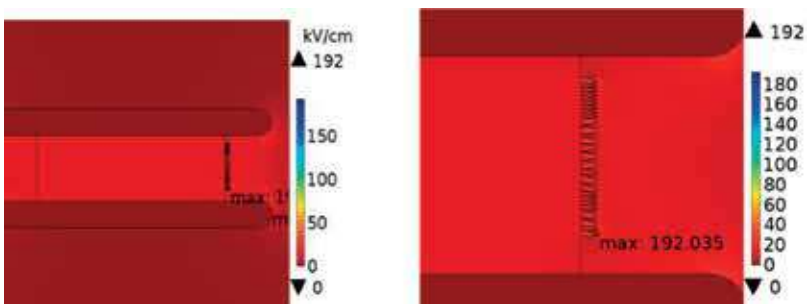


**Figure 9.** M-type insulation defect space electric field simulation output.

http://dx.doi.org/10.5772/intechopen.79090

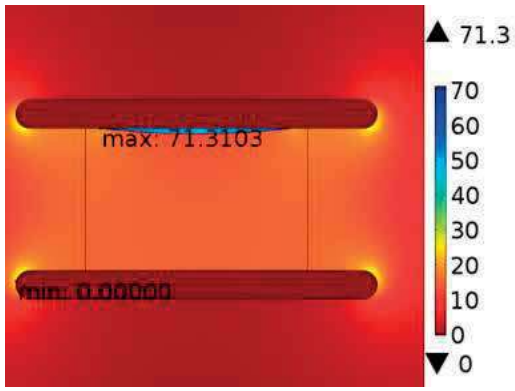


**Figure 10.** G-type insulation defect space electric field simulation output.

As shown in **Figure 10**, the simulation results of the electric field are mainly concentrated in the air gap between the high-voltage conductor and the insulator. The maximum field strength is 71.3 kV/cm. From the simulation results, G-type insulation defect has higher initial discharge voltage.

## 3. UHF characteristics of typical defects PD

As mentioned in Section 1, PD can be detected by UHF method. In this section, UHF characteristic of PD will be discussed. Experiments and analysis will be shown as follows.

### 3.1. Experimental setup

The detecting and measuring platform for PD is shown in **Figure 11**. The regulator (T1) input voltage is 220 V, the output voltage is adjustable from 0 to 250 V, the regulator output voltage through non-halo test transformer (T2: 10 kVA/50 kV) is boosted as the test voltage and is applied to the test object through a 10 kΩ protection resistor ($R_r$). The protection resistor is used to limit the amplitude of the short circuit current which may appear after the breakdown of the test object. To measure the test voltage, a capacitor divider in parallel on both ends of the test object is used [27]. The experimental voltage is acquired by outer UHF antenna developed by the authors (ultra-high frequency microstrip antenna, with 340–440 MHz bandwidth) and displayed on the digital storage oscilloscope (DSO: Lecroy WavePro 7100). The DSO has the largest sample rate of 20 GS/s.

### 3.2. Data acquiring and processing

Experiments can be done on the platform in **Figure 15**. Large numbers of data can then be acquired and processed. All sampling data are unified and normalized, so that the resulting mathematical models are more universal [28]. Unification means that each PD signal consists of 10,000 sampling points at a sampling rate of 20 GS/s (i.e., the sampling time is 500 ns, the sampling step is 0.05 ns, and the trigger point is set at the 4000th point). Normalization means that each value of the sample points is divided by the maximum absolute value.

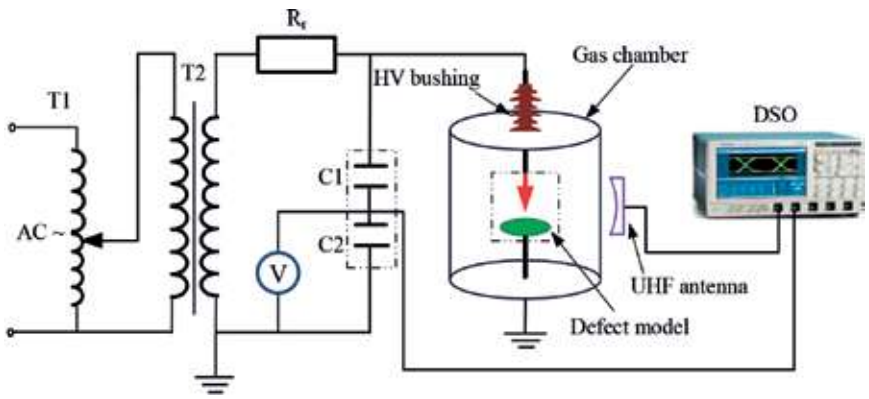


**Figure 11.** Detecting and measuring platform.

| Types of defects | Coefficients | Value | Coefficients | Value | Coefficients | Value |
|---|---|---|---|---|---|---|
| N-type | a1 | 0.2002 | b1 | 4852 | c1 | 435.3 |
| | a2 | 0.1863 | b2 | 4444 | c2 | 215.2 |
| | a3 | −0.9328 | b3 | 3998 | c3 | 19.2 |
| | a4 | 0.3613 | b4 | 6097 | c4 | 769.7 |
| | a5 | −0.3475 | b5 | 5767 | c5 | 119 |
| P-type | a1 | 0.2858 | b1 | 4305 | c1 | 39.6 |
| | a2 | 0.2332 | b2 | 4531 | c2 | 97.7 |
| | a3 | 0.1117 | b3 | 4762 | c3 | 104.1 |
| | a4 | −0.9565 | b4 | 3998 | c4 | 19.1 |
| | a5 | 0.0454 | b5 | 6181 | c5 | 211.8 |
| M-type | a1 | 0.9757 | b1 | 4000 | c1 | 23.2 |
| | a2 | 0.7679 | b2 | 5298 | c2 | 521.2 |
| | a3 | 0.7750 | b3 | 6661 | c3 | 606.1 |
| | a4 | 1.1040 | b4 | 5951 | c4 | 591.9 |
| | a5 | −1.5420 | b5 | 5981 | c5 | 1006.0 |
| G-type | a1 | 1.0100 | b1 | 3998 | c1 | 30.3 |
| | a2 | 0.0588 | b2 | 5156 | c2 | 358.2 |
| | a3 | 0.8981 | b3 | 4368 | c3 | 177.9 |
| | a4 | −1.0730 | b4 | 4358 | c4 | 201.4 |
| | a5 | 0.0232 | b5 | 7225 | c5 | 152.5 |

**Table 3.** Parameters of different types of defect.

Mathematical models of PD for VHF measurement are established by fitting to Gaussian plots function, the selected mathematical model is [28]:

$$f(x)=\sum_{i=1}^{n} a_i \bullet e^{\frac{(x-b_i)^2}{c_i^2}} \tag{1}$$

where $a_i$, $b_i$, and $c_i$ are parameters and different of defects have different parameters. Based on massive experiment data, these parameters can be calculated as shown in **Table 3**.

**Figures 12–15** show time domain and frequency domain UHF PD characteristics, and they, respectively, denote G-type defect, M-type defect, N-type defect, and P-type defect. In time domain, the unit of x-axis is nanosecond, while in frequency domain, the unit of x-axis is gigahertz. Notice that the y-axis in time domain and frequency domain has no unit because it represents normalized data, that is, the U* and A* both stand for per unit.

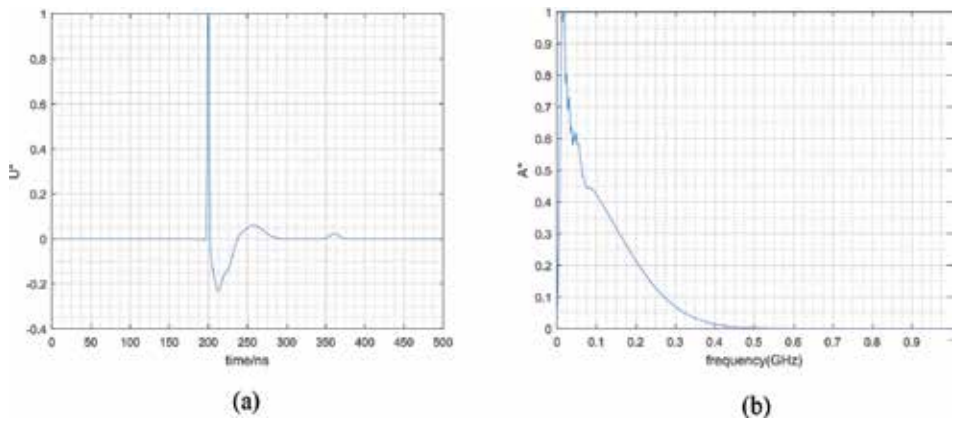


**Figure 12.** G-type defect UHF PD characteristics. (a) Time domain and (b) frequency domain.

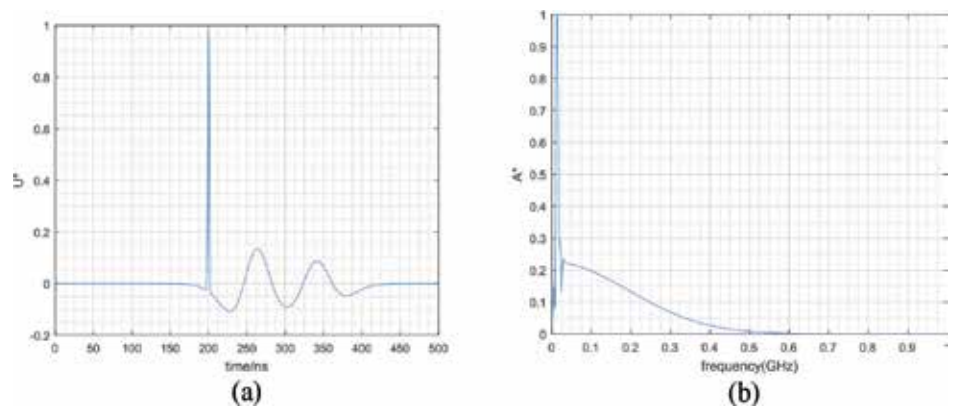


**Figure 13.** M-type defect UHF PD characteristics. (a) Time domain and (b) frequency domain.

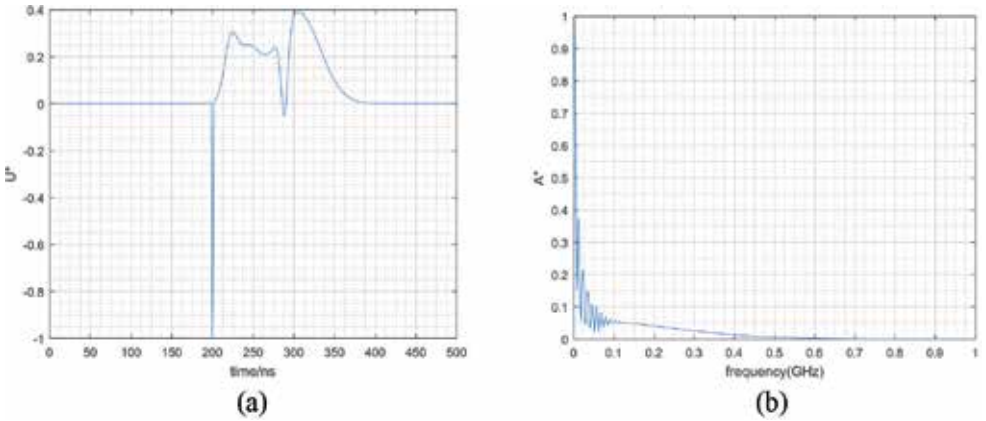


**Figure 14.** N-type defect UHF PD characteristics. (a) Time domain and (b) frequency domain.

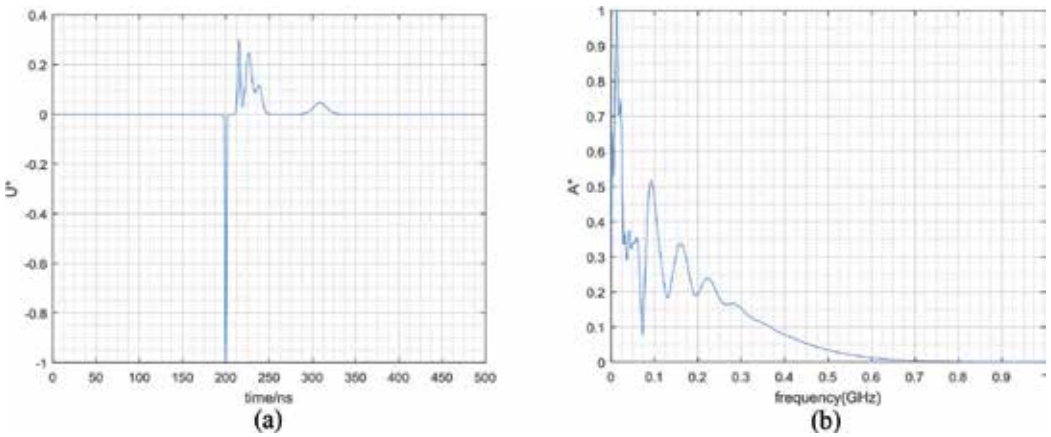


**Figure 15.** P-type defect UHF PD characteristics. (a) Time domain and (b) frequency domain.

For G-type defect characteristics curve, in time domain, there is a sharp jump at the 4000th point, and the curve is smooth after the jump; while in frequency domain, there is a jump after the original point, and the curve is smooth after the jump except for some protuberant points. For M-type defect characteristics curve, in time domain, there is a sharp jump at the 4000th point, and the curve is smooth after the jump with two peaks; while in frequency domain, there is a jump after the original point with a smaller jump afterwards, and the curve is smooth except for some protuberant points. For N-type defect characteristics curve, in time domain, there is a sharp jump at the 4000th point toward the negative direction, and the curve is smooth after the jump with a flat segment and then two peaks; while in frequency domain, there is oscillation on the whole frequency axis. For P-type defect characteristics curve, in time domain, there is a sharp jump at the 4000th point toward the negative direction, and several peaks follow afterwards; while in frequency domain, there is a jump after the original point with several oscillations afterwards.

http://dx.doi.org/10.5772/intechopen.79090

## 4. Chemical characteristics of typical defects PD

In GIS, PD takes place accompanied by $SF_6$ decomposition. In addition, different defects will lead to different decomposition components. Based on this idea, chemical methods can be used to detect PD [23].

### 4.1. Experimental setup

The detecting and measuring platform for PD is shown in **Figure 16**. The measuring platform is similar to that in Section 3.1, but the UHF antenna will be replaced by gas chromatography mass spectrometry (GCMS), with its type Shimadzu QP-2010 Ultra.

The experiment is carried out in the gas chamber, which is closed filled of $SF_6$ gas with a specific pressure. Certain type of insulation defects for PD is also placed in the chamber. The coupling capacitor (Ck: 500 pF/100 kV) provides a high frequency and low-impedance path to the pulsed current and is converted to a voltage signal via a sense-less impedance ($Z_m$: 50 Ω), and it is displayed by digital storage oscilloscope. The decomposed components generated under PD are detected by GCMS.

### 4.2. Experimental steps

In this chapter, $SF_6$ decomposition experiments under four types of insulation defects are carried out. Under each type, the experiments last for 96 h. The decomposition gas is collected every 12 h, and the concentration of characteristic decomposition components $CF_4$, $CO_2$, $SO_2F_2$ is measured. The initial discharge voltage and the test voltage of various insulation defects are shown in **Table 4**. The experimental process is as follows:

1. The insulation defect model is installed in $SF_6$ partial discharge decomposition gas chamber, the vacuum chamber is first evacuated and then filled with fresh SF6 gas, and then evacuated. Repeat the process until the chamber is filled with pure 0.2 MPa $SF_6$.
2. Connect the test circuit according to **Figure 20**, and then adjust the regulator to slowly increase the test voltage until the oscilloscope can detect PD on the defect model. Record the experimental voltage $U_0$ at this time, that is, the initial discharge voltage. Then, continue to raise at the experimental voltage.
3. Every 12 h, $SF_6$ gas is collected. The single collection gas volume is about 100 mL. Gas chromatograph is used to analyze the concentration of gas components.
4. After a 96-h continuous experiment on a defect model, another model of the defect will replace it and continue the experiment according to the aforementioned steps until all four types of defects are all done.

### 4.3. $SF_6$ decomposition characteristics

The decomposition components under the four types of defects are shown in **Figure 17(a)–(d)**, that is, N-type, M-type, P-type, and G-type defect, respectively. Four characteristic

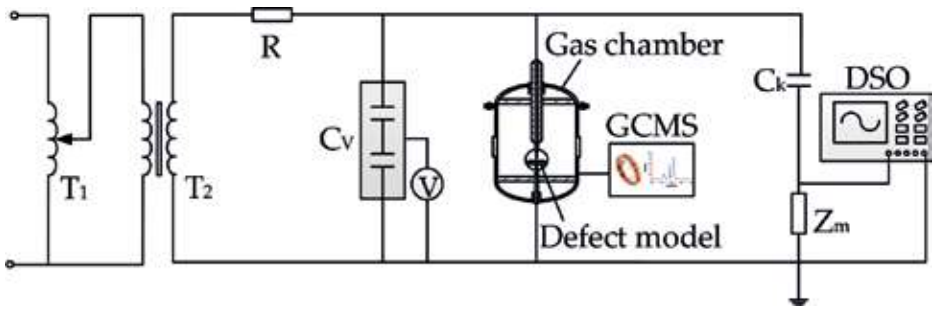


**Figure 16.** Detecting and measuring platform.

| Voltage | Defect type | | | |
|---|---|---|---|---|
| | N-type (kV) | M-type (kV) | P-type (kV) | G-type (kV) |
| Starting discharge voltage | 16.2 | 21.6 | 17.5 | 25.7 |
| Experimental voltage | 19.4 | 25.9 | 21.0 | 30.8 |

**Table 4.** Test voltage under different insulation defects.

decomposition components are generated, but the amounts of different characteristic components are quite different.

Under the N-type defect, at the end of the experiment, that is, at 96 h, concentration of $SOF_2$ was as high as 1114.5 μL/L, $SO_2F_2$ was 471.2 μL/L, $CO_2$ was 124.8 μL/L, and $CF_4$ was only a few μL/L. It was detected in the experiment that the concentration of components in ascending order is $SOF_2 > SO_2F_2 > CO_2 > CF_4$. Concentrations of $SOF_2$, $SO_2F_2$, and $CO_2$ all have an almost linear increase, indicating that PD is stable. The gas production rate dropped within a few tens of hours before the end of the experiment. It is preliminarily inferred that the moisture and oxygen in the gas chamber decreased after being consumed in experiment, resulting in a corresponding slowdown of various chemical reaction rates. Although the concentration of $CF_4$ generally increases, it does not increase simply linearly, and even decreases sometimes. The reason for this is that concentration of $CF_4$ is too low. Although the gas chromatograph detector sensitivity is very high, the final calculation of the test results needs to be integrated on the resulting chromatographic peak, when the concentration result is low, the impact of integral error will be greater.

The decomposition components under the M-type defect are shown in **Figure 17(b)**. The amounts of different characteristic components are also different. However, compared with the N-type defect, the difference is much smaller. At 96 h, concentration of $SOF_2$ was 42.78 μL/L, concentration of $SO_2F_2$ was 14.95 μL/L, concentration of $CO_2$ was 2.18 μL/L, and concentration of $CF_4$ was 6.18 μL/L. In the experiment, the concentration of components in ascending order is $SOF_2 > SO_2F_2 > CF_4 > CO_2$. Concentration of $SOF_2$ and $SO_2F_2$ gradually increased, but their increasing rate gradually decreased, especially $SO_2F_2$. Its concentration almost stopped increasing at the end of the experiment. That is because the insulator

http://dx.doi.org/10.5772/intechopen.79090

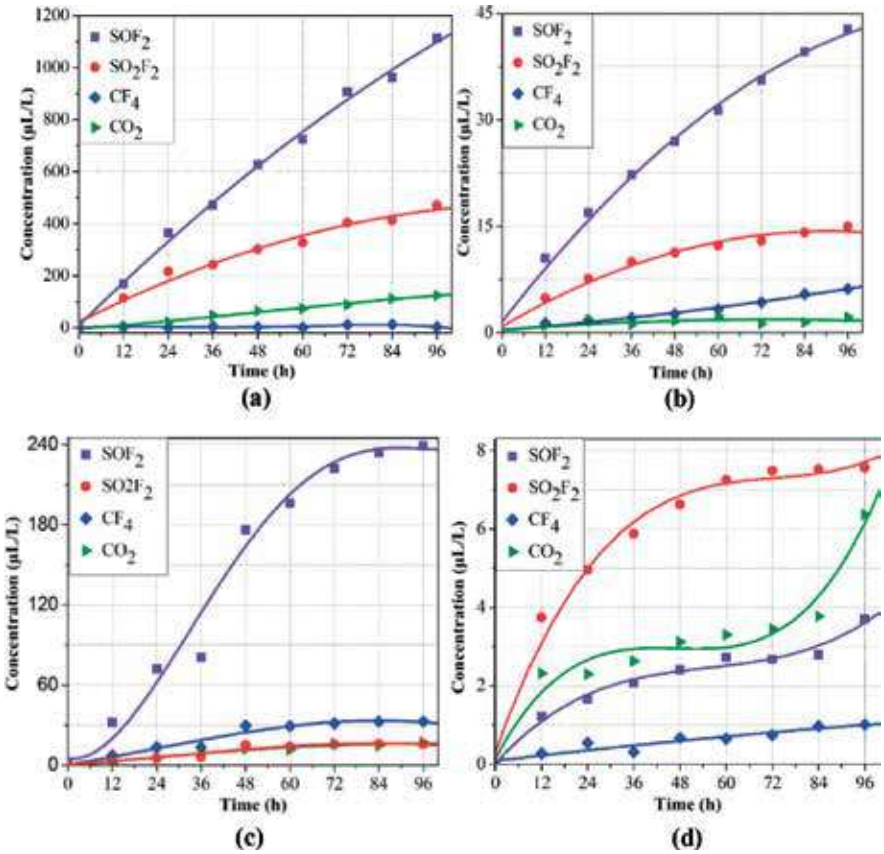


**Figure 17.** Decomposition concentration under four types of defects. (a) N-type defects, (b) M-type defects, (c) P-type defects, and (d) G-type defects.

surface contamination is gradually ablated by discharge; its effect on the electric field distortion becomes weaker and weaker, resulting in gradual decrease in discharge intensity. Because of sufficient fluorine atoms generated by the discharge and carbon atoms provided by the insulator, $CF_4$ is relatively less affected by the discharge intensity and its concentration increases substantially linearly with time. The increase of $CO_2$ does not simply grow linearly, and sometimes even decreases. The main reason for this is the concentration of $CO_2$ is low under M-type defect, and the integral error of the gas chromatograph has a greater impact on it.

The characteristic decomposition components under the P-type defect are shown in **Figure 17(c)**. Under this defect, four characteristic decomposition components were also generated. At 96 h, the concentration of $SOF_2$ was 238.9 μL/L, the concentration of $SO_2F_2$ was 15.82 μL/L, the concentration of $CO_2$ was 16.63 μL/L, and the concentration of $CF_4$ was 32.68 μL/L. The concentration of components in ascending order is $SOF_2 > CF_4 > CO_2 > SO_2F_2$. The concentration of the four characteristic components did not increase linearly. In the first 24 h of the experiment, the components concentration increased linearly, and the increasing rate was larger; from 24

to 36 h, the concentration of components also increased, whereas the increasing rate dropped sharply; from 36 to 48 h, the increasing rate rapidly increased. After 48 h, the increasing rate decreased slowly. At the end of the experiment, all characteristics components concentration almost stopped increasing. The main reason for this is that the discharge formed by the defects of P-type defect is unstable; the free particles are moved under strong electric field force due to their small mass. Only when moved to the position conducive to discharge will the particles lead to discharge. These particles may move randomly, which will lead to unstable discharge.

The characteristic decomposition components under G-type defect are shown in **Figure 17(d)**. The concentration of the four characteristic decomposition components under the insulation defect is low. At the end of the experiment, the concentration of $SOF_2$ was 3.71 μL/L, the concentration of $SO_2F_2$ was 7.57 μL/L, the concentration of $CO_2$ was 6.37 μL/L, and the concentration of $CF_4$ was 1.01 μL/L. The concentration of components in ascending order is $SO_2F_2 > CO_2 > SOF_2 > CF_4$. There is no obvious regularity in the increasing of concentration of the four characteristic components. The time-varying increasing rate is mainly due to the unstable PD, sometimes the discharge is very intense, and sometimes discharge stops. In addition, the overall discharge repetition rate is not high, resulting in the overall concentration of decomposition products not high and growth not regular.

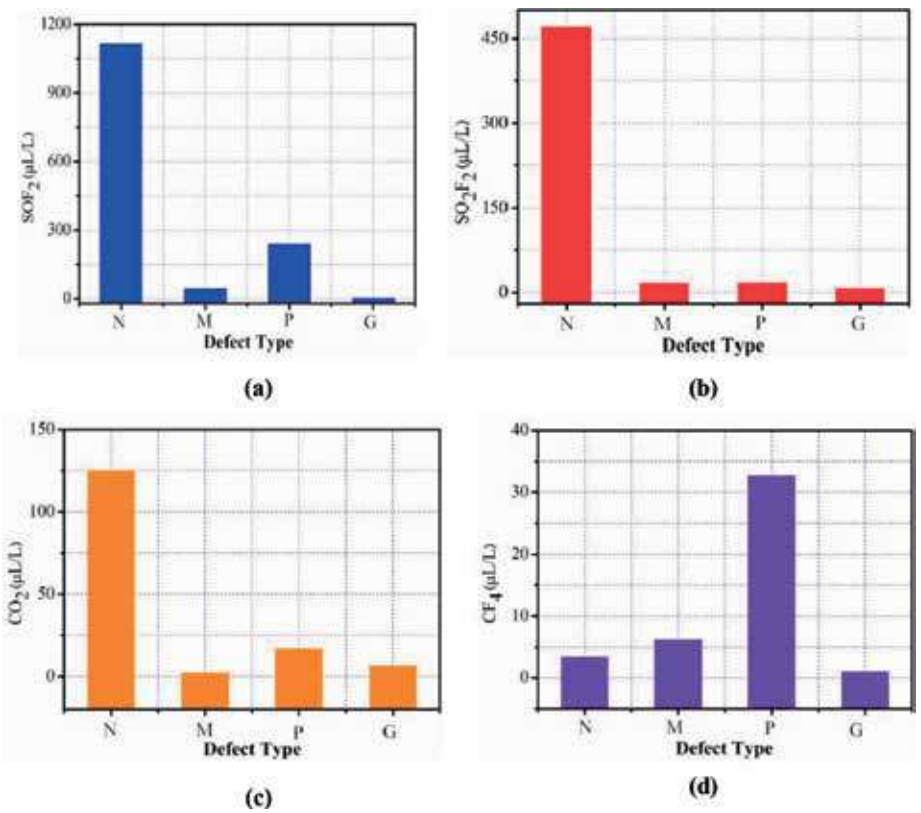


**Figure 18.** Decomposition components amount under four types of defects. (a) $SOF_2$ amount, (b) $SO_2F_2$ amount, (c) $CO_2$ amount, and (d) $CF_4$ amount.

A conclusion of $SF_6$ decomposition component under four types of insulation defects can be drawn that, amounts and ratio of decomposition components are different under different defects. Under each defect, the decomposition components under four types of defects compared with each other is as shown in **Figure 18**. For example, the amount of $SOF_2$ is higher than $SO_2F_2$ under the N-type defect, whereas the amount of $SO_2F_2$ in G-type defect is higher than $SOF_2$. The decomposition amounts of $CF_4$ and $CO_2$ also vary with different types of defects, more $CO_2$ is detected under N-type defect, and only a smaller amount of $CF_4$ is detected. Under P-type defect, the amount of $CF_4$ is larger than that of $CO_2$. Under M-type defect, only a small amount of $CO_2$ is detected; under G-type defect, both $CF_4$ and $CO_2$ are detected, but the concentration of $CO_2$ is higher than that of $CF_4$. Under N-type and M-type defects, the decomposition components increasing rate is stable, which is due to the reason that PD is stable under the two defects. In contrast, under P-type and G-type defects, PD is unstable. The reason is that particles and gap is not conducive to stable PD. The repetition rate varies with time, as well as the discharge amplitude. Especially under P-type defect, due to movement of metal particles, concentrations of decomposition components vary most intensively.

## 5. Optical characteristics of typical defects PD

In GIS, PD will ionize $SF_6$ molecules, and electrons will release and gain energy during the ionization process. When the electrons release energy, they will release photons at the same time, which are called luminescence; the positive and negative ions after ionization also recombine to release photons and become a composite light. Optical measurement uses photoelectric sensors to detect PD in the light intensity it generated to determine its strength. For optical measurement of signal generated by PD in GIS, detection system is less affected by outside interference and has higher sensitivity of measurement. It can detect PD in real time and identify the position of PD. Therefore, it can be used for on-line monitoring of PD in GIS.

At present, there are mainly two ways to detect the optical signal generated by PD in the GIS by optical measurement: one is to directly use the photoelectric sensor to detect the optical signal generated by the PD; the other is to insert the optical fiber sensor into the GIS to detect the optical signal generated by the PD. The former is more flexible to install, but the detection range is smaller, whereas the latter installation is more fixed, but the detection range is larger. Different types of insulation defects lead to different optical signals released by the PD, so the PD can be identified and diagnosed by using the optical measurement [12].

### 5.1. Experimental setup

The schematic diagram of the fluorescence optical fiber sensing system used to study the optical characteristics of the typical defects is shown in **Figure 19**. The optical fiber sensor system mainly comprises an optical sensor unit, optical transmission unit, photoelectric conversion unit, power supply module, and electrical signal transmission and acquisition unit [12].

Four types of single-defect models in this paper are respectively put into the device. After the preparation, the experimental device is applied with the experimental voltage. Slowly raise the test voltage and record the initial discharge voltage of the four single-defect models. Continue to

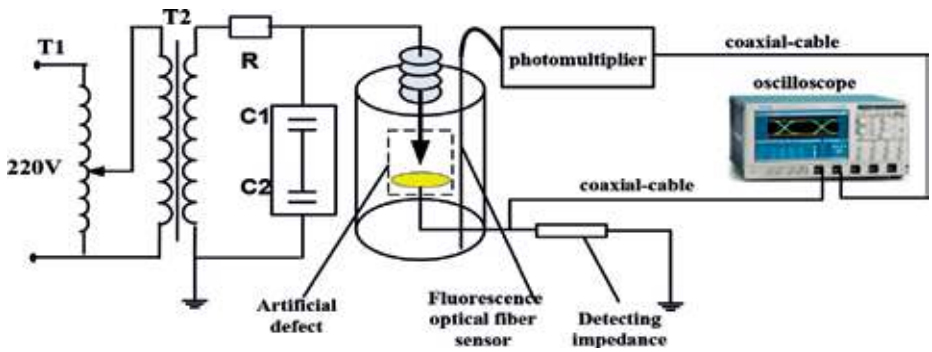


**Figure 19.** Figure of the fluorescent fiber sensor system.

slowly increase the experimental voltage and collect PD signal of different discharge intensity. Because PD signal of every power frequency cycle needs to be collected, a reference voltage signal should be introduced before the PD signal is collected to correct the phase of PD. Oscilloscope sampling frequency is set to 50 Ms/s, the total acquisition signal length 20 ms, and sampling points 1 M. In experiments, the fluorescent fiber sensing system stores signals in a time domain waveform. Therefore, PD light pulses must be extracted from the time-domain waveform that record the PD signal for each cycle. The method comprises the following steps: set a threshold firstly according to noise amplitude and extract a PD light pulse whose amplitude is greater than the threshold and record and store the amplitude and corresponding phase of the PD light pulse.

### 5.2. $\phi$-$u$-$n$ distribution characteristics of photodetector PDs with different defects

In this chapter, the $\varphi$-$u$-$n$ spectral is used to analyze PD. In $\varphi$-$u$-$n$ space, $\varphi$ represents the phase of PD power frequency, $u$ represents the amplitude of PD light pulse signal, characterizing the PD discharge level, and $n$ represents the number of discharges. The space surface is constructed by dividing the power-frequency phase $\varphi$-axis into 256 intervals from 0° to 360° and dividing the amplitude of the optical pulse signal from 0 to 0.1 V into 128 small sections so that the $\varphi$-$u$ plane is divided into 128 × 256 cells; count $\varphi$-$u$ plane discharge times within each cell, and one can get the space surface. The $\varphi$-$u$-$n$ space surface constructed in this paper is based on 200 power-frequency signals. The three-dimensional map of the different defects obtained from the collected PD data is shown in **Figure 20**. There is a significant difference between the three-dimensional spectra of the $\varphi$-$u$-$n$ obtained by detecting different internal defects in the GIS using the optical method.

For N-type defect, the repetition rate of light pulse is high, the average amplitude is large, the range of amplitude variation is small, and the light pulse distribution has obvious phase characteristics and symmetrical about 270° in phase. The reason is that the PD under N-type defect is a typical corona discharge which is relatively stable, the intensity of the single discharge is small, the light signal generated by the discharge is relatively stable, and the light intensity generated by the single discharge is relatively large. Therefore, the average amplitude of the detected light pulse is large, and the range of the amplitude is small. The initial discharge voltage of positive half cycle of corona discharge is higher than the negative half cycle of power frequency, and the

http://dx.doi.org/10.5772/intechopen.79090

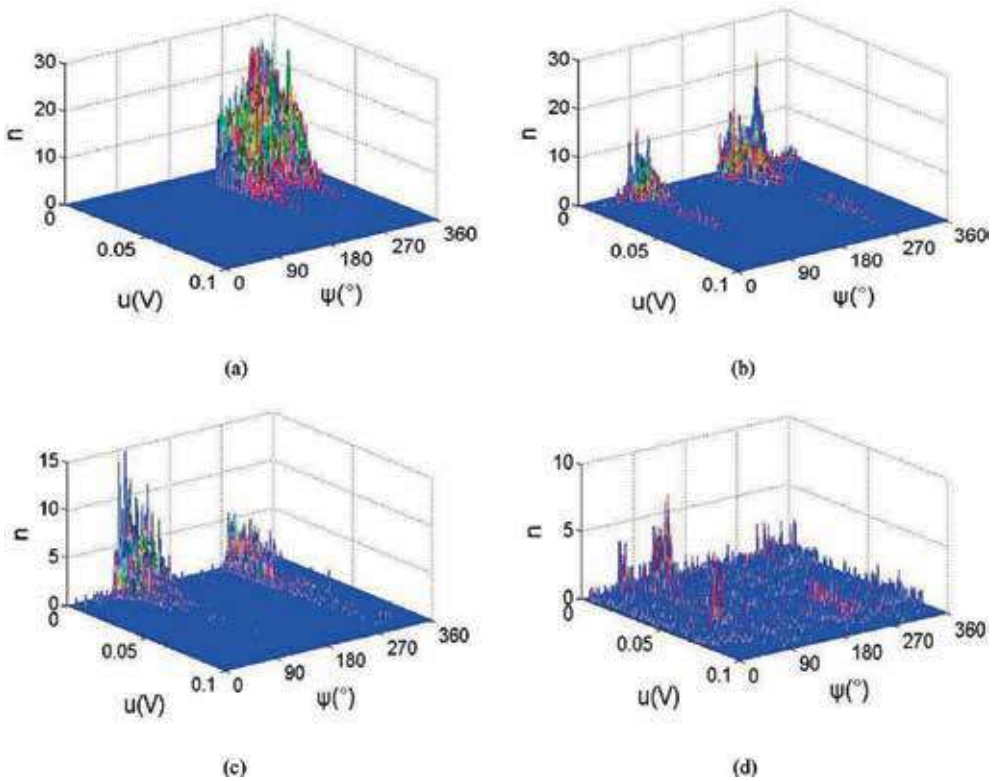


**Figure 20.** The *φ-u-n* chart of PD induced by the four types of defects in GIS. (a) N-type, (b) G-type, (c) M-type, and (d) P-type.

space charge generated by discharge diffuses rapidly in the gas. The influence of space charge on the external electric field is very small. The initial discharge voltage of corona discharge is almost equal to the extinction voltage. Therefore, the light pulses are distributed around the 270° phase of the negative half cycle of the power frequency and symmetrical about 270°.

For G-type defect, the pulse repetition rate is high, the average amplitude is small, the amplitude range is wide, and the light pulse distribution has obvious phase characteristics, which are all distributed at the phases of 90 and 270°. Phase width distributed in the 90–180° is greater than 0–90°, and 180–270° phase width greater than 270–360°. The reason is that the PD caused by the G-type defect between the insulator and the metal conductor is not very stable. The light intensity generated by a single discharge is not uniform, but the light intensity generated by the discharge is relatively small. Therefore, the average light pulse detected has small amplitude and large amplitude range. As the insulator hinders the spread of the space charge, the space charge will cause the distortion of the external electric field so that the initial discharge voltage caused by the air gap defect between the insulator and the metal conductor is higher than the extinction voltage. Therefore, the light pulse phase width distributed between 90 and 180° is greater than 0–90° and between 180–270° phase width is greater than 270–360°.

For M-type defect, the pulse repetition rate is low, the average pulse amplitude is small, the amplitude range is large, and the light pulse distribution has obvious phase characteristics

and is distributed around the phase 90 and 270°. Phase width distributed in the 90–180° is greater than 0–90° and in the 270–360° phase width is greater than 180–270°. The reason is that the PD produced by M-type defect will generate electrical branches on the surface of the insulator, which will affect the insulation of the insulator surface. As a result, the PD is not very stable, and the light intensity produced by a single discharge is different. However, the overall light intensity is relatively small, so the optical measurement method detecting average amplitude of the light pulse is small, with a wide range of amplitude.

For P-type defect, the pulse repetition rate is low, the average amplitude is large, the range of the amplitude changes is large, and the phase distribution of the light pulse is not characterized. The reason is that metal particles in the external electric field obtain the induced charge and will move under electric force. The movement intensity of the metal particles depends on the induced charges, the shape of the particles, the direction of movement of the particles, and whether the particles collide with other objects during the movement. PD generated by P-type defects is caused by the movement of the metal particles. Therefore, it is very unstable, and the phase of PD is also irregular.

## 6. Conclusion

In this chapter, typical defects in GIS are discussed and physical model is established, then different resulting PD is studied. Four typical defects and their respective PD UHF characteristics, chemical characteristics, and optical characteristics are then obtained by experiments. Different figures and data owing to different types of PD are compared with each other so that unique features could be further extracted.

As for UHF characteristics, it can be seen visually that waveforms of different defects have obvious difference. Then some parameters can be designed to measure the essential difference, which can be presented as fingerprints. In time domain, statistics parameters are selected as features. For example, these parameters include mean, variance, skewness, kurtosis, etc. While in frequency domain, these parameters also works. In addition, Shannon entropy, wavelet sub-band energy, and absolute value of peaks can also be included. Based on these features, methods such as support vector machine can be applied to classify the defects.

For chemical characteristics, it can be concluded that the $SF_6$ PD decomposition components amount under the four types of insulation defects are obviously different, and so is their ratio. So the insulation defect can be identified by detecting PD decomposition component of $SF_6$. Methods such as artificial neural network can then be set up to classify the defects. The concentration and ratio of each decomposition components are the input variables and during training process the defect is finally classified.

For optical characteristics, just as UHF characteristics, the spectrals of different defects have obvious difference. So some statistics parameters are introduced. Because the optical spectral has three dimensions, projection on two-dimension plane is firstly needed, and then parameters are extracted. The classification step is like that of UHF or chemical characteristics.

## Author details

Fuping Zeng*, Ju Tang, Xiaoxing Zhang, Siyuan Zhou and Cheng Pan

*Address all correspondence to: fuping.zeng@whu.edu.cn

School of Electrical Engineering, Wuhan University, Wuhan, China

## References

[1] Gu FC, Chang HC, Kuo CC. Gas-insulated switchgear PD signal analysis based on Hilbert-Huang transform with fractal parameters enhancement. IEEE Transactions on Dielectrics & Electrical Insulation. 2013;**20**(4):1049-1055

[2] Dai D et al. Feature extraction of GIS partial discharge signal based on S-transform and singular value decomposition. Iet Science Measurement & Technology. 2017;**11**(2):186-193

[3] Okabe S, Ueta G, Hama H, et al. New aspects of UHF PD diagnostics on gas-insulated systems. IEEE Transactions on Dielectrics and Electrical Insulation. 2014;**21**(5):2245-2258

[4] Cigre WG. 33/23-12 Insulation coordination of GIS: Return of experience, on site tests and diagnostic techniques. Electra. 1998;**176**(2):67-95

[5] Pearson JS, Hampton BE, Sellars AG. A continuous UHF monitor for gas-insulated substations. IEEE Transactions on Electrical Insulation. 1991;**26**(3):469-478

[6] Cavallini A, Montanari GC, Contin A, Pulletti F. A new approach to the diagnosis of solid insulation systems based on PD signal inference. IEEE Electrical Insulation Magazine. 2003;**19**(2):23-30

[7] Tang J, Zhou R, Wang DB, et al. Application of SA-SVM incremental algorithm in GIS PD pattern recognition. Journal of Electrical Engineering and Technology. 2016;**11**(1):192-199

[8] Koo JY et al. Identification of insulation defects in gas-insulated switchgear by chaotic analysis of partial discharge. Iet Science Measurement & Technology. 2010;**4**(3):115-124

[9] Gao W, Ding D, Liu W. Research on the typical partial discharge using the UHF detection method for GIS. IEEE Transactions on Power Delivery. 2011;**26**(4):2621-2629

[10] DEA M et al. Charge accumulation effects on time transition of partial discharge activity at GIS spacer defects. IEEE Transactions on Dielectrics & Electrical Insulation. 2010; **17**(1):247-255

[11] Zhang X et al. GIS partial discharge pattern recognition based on the chaos theory. IEEE Transactions on Dielectrics & Electrical Insulation. 2014;**21**(2):783-790

[12] Zhuo R. Feature optimization and fault diagnosis of GIS based on combined detection [PhD thesis]. Chongqing University; 2014 (in Chinese)

[13] Liu F. Decomposition characteristic of $SF_6$ under PD & recognition of PD category and calibration of impact factors [PhD thesis]. Chongqing University; 2013 (in Chinese)

[14] Wang Y. Decomposition characteristic of $SF_6$ under PD & recognition of PD category and calibration of impact factors [PhD thesis]. Chongqing University; 2013 (in Chinese)

[15] International Standard IEC 60270. High Voltage Test Techniques—Partial Discharge Measurements, 3rd ed. Geneva, Switzerland: International Electrotechnical Commission; 2000

[16] IEC-62478. High-Voltage Test Techniques—Measurement of Partial Discharges by Electromagnetic and Acoustic Methods. Proposed Horizontal Standard. 1st ed. Geneva, Switzerland: International Electrotechnical Commission (IEC); 2016

[17] Tao J. Study on partial discharge identification and harmfulness assessment for gas insulated switchgear [PhD thesis]. Chongqing University; 2013 (in Chinese)

[18] Ren M, Zhou J, Song B, Zhang C, Dong M, Albarracín R. Towards optical partial discharge detection with micro silicon photomultipliers. Sensors. 2017;**17**:2595

[19] Robles G, Albarracín R, Vázquez JL. Antennas in partial discharge sensing system. In: Chen ZN, editor. Handbook of Antenna Technologies. Singapore: Springer; 2015. pp. 1-47

[20] Álvarez Gómez F, Albarracín-Sánchez R, Garnacho Vecino F, Granizo Arrabé R. Diagnosis of insulation condition of MV switchgears by application of different partial discharge measuring methods and sensors. Sensors. 2018;**18**:720

[21] Fresno JM, Robles G, Martínez-Tarifa JM, Stewart BG. Survey on the performance of source localization algorithms. Sensors. 2017;**17**:2666

[22] Judd MD, Farish O, Hampton BF. The excitation of UHF signals by partial discharges in GIS. IEEE Transactions on Dielectrics and Electrical Insulation. 1996;**3**:213-228

[23] Tang J, Yang X, Ye G, Yao Q, Miao Y, Zeng F. Decomposition characteristics of $SF_6$ and partial discharge recognition under negative DC conditions. Energies. 2017;**10**:556

[24] Dong M, Zhang C, Ren M, Albarracín R, Ye R. Electrochemical and infrared absorption spectroscopy detection of $SF_6$ decomposition products. Sensors. 2017;**17**:2627

[25] Tang J et al. Partial discharge recognition through an analysis of $SF_6$ decomposition products part 2: Feature extraction and decision tree-based pattern recognition. IEEE Transactions on Dielectrics & Electrical Insulation. 2012;**19**(1):37-44

[26] Zhuo R et al. Study on relationship between optical signals and charge quantity of partial discharge under four typical insulation defects. Electrical Insulation and Dielectric Phenomena IEEE. 2013:1209-1212

[27] Dong Y. Research on feature extraction and severity assessment of partial discharge in GIS [master thesis]. Chongqing University; 2013 (in Chinese)

[28] Tang J et al. Study on mathematical model for VHF partial discharge of typical insulated defects in GIS. IEEE Transactions on Dielectrics & Electrical Insulation. 2007;**14**(1):30-38

Section 3

# Insulation Weaknessess Modelling for Electrical Devices Used in Smart Grids

Chapter 6

# Electrical Insulation Weaknesses in Wide Bandgap Devices

Mona Ghassemi

Additional information is available at the end of the chapter

http://dx.doi.org/10.5772/intechopen.77657

**Abstract**

The power electronics research community is balancing on the edge of a game-changing technological innovation: as traditionally silicon (Si) based power semiconductors approach their material limitations, next-generation wide bandgap (WBG) power semiconductors are poised to overtake them. Promising WBG materials are silicon carbide (SiC), gallium nitride (GaN), diamond (C), gallium oxide ($Ga_2O_3$) and aluminum nitride (AlN). They can operate at higher voltages, temperatures, and switching frequencies with greater efficiencies compared to existing Si, in power electronics. These characteristics can reduce energy consumption, which is critical for national economic, health, and security interests. However, increased voltage blocking capability and trend toward more compact packaging technology for high-power density WBG devices can enhance the local electric field that may become large enough to raise partial discharges (PDs) within the module. High activity of PDs damages the insulating silicone gel, lead to electrical insulation failure and reduce the reliability of the module. Among WBG devices, electrical insulation weaknesses in WBG-based Insulated Gate Bipolar Transistor (IGBT) have been more investigated. The chapter deals with (a) current standards for evaluation of the insulation systems of power electronics modules, (b) simulation and modeling of the electric field stress inside modules, (c) diagnostic tests on modules, and (d) PD control methods in modules.

**Keywords:** wide bandgap devices, partial discharge, electric field stress

## 1. Introduction

The growing integration of distributed generation resources, envisagement of direct current (DC) microgrids and high-voltage direct current (HVDC) networks, the continued electrification and grid-level power flow controls call for advanced power electronics with improved

efficiency, reliability and power density [1]. Undergoing dynamic evolution in power electronics is mainly due to the development of power semiconductor devices seeking simultaneous operation at a higher voltage, power, and switching frequency. Having higher blocking voltage capability, higher temperature tolerance, and higher switching frequency than Si technology, wide-bandgap (WBG) semiconductor materials such as silicon carbide (SiC) and gallium nitride (GaN) are expected to be a response to the mentioned challenge [2]. Si has a bandgap of 1.1 eV, whereas the bandgap of SiC and GaN is, respectively, 3.3 and 3.4 eV. The bandgap is the energy required to transfer an electron from the valence to the conduction band. Insulators, semiconductors, and conductors have large, small and very small bandgaps, respectively. While the highest commercial Si IGBT breakdown voltage capability is 6.5 kV, a record high blocking voltage of 15 kV was reported for the SiC IGBT produced in [3] and higher voltage capability up to 20–30 kV is expected shortly [4].

The metalized ceramic substrate shown in **Figure 1a** is well-known and established insulation technology for blocking voltages up to 3.3 kV, but it exhibits some weaknesses due to partial discharges (PDs) in silicone gel at higher voltages. In a sufficient electric stress condition localized gaseous breakdowns known as PDs can occur within an insulation system. Various measuring techniques and sensors have been developed for PD detection to perform an accurate condition monitoring and assessment of the insulation status of power equipment [5, 6]. We will discuss this topic in Section 4. The blocking voltage places across substrate solid insulating material, which is aluminum nitride (AlN) or alumina ($Al_2O_3$) ceramics where HV electrode is IGBT or diode and the ground electrode is copper or aluminum silicon carbide (AlSiC) base plate connected to the heat sink. However, both sides of the insulating ceramic are metalized by copper to evacuate better and transfer the heat generated by IGBTs or diodes to the base plate [7]. IGBTs, diodes and base plate are soldered onto the metalized ceramic substrate [7]. In this regard, solid dielectric substrates should also have appropriate thermal properties such as resistance to high temperatures and good thermal conductivity in addition to their desirable electrical insulation and mechanical properties. This is the case for AlN and $Al_2O_3$ with a thermal conductivity of typically, respectively, 180 and 27 W/mK [8]. Note that, however, the thermal resistance of the AlN substrates assembled with IGBTs is around a factor of only three less than $Al_2O_3$ substrates [8] (not 180/27 = 6.7 times for AlN and $Al_2O_3$ materials itself). Attaching the copper metallization to the ceramic substrate can be done by direct

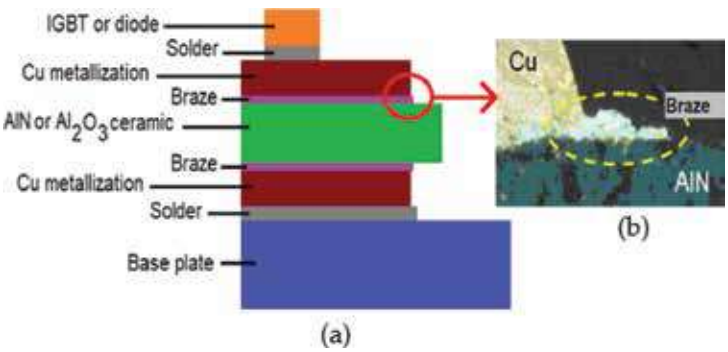


**Figure 1.** (a) A schematic of an IGBT substrate with active metal brazing (AMB) of the metallization and (b) protrusions with extremely sharp edges of some braze below the metallization.

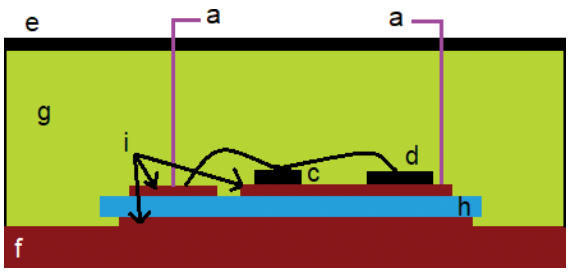


**Figure 2.** A schematic of an IGBT module with DBC, (a) connection to bus bars, (b) bond wire, (c) diode, (d) IGBT, (e) plastic case, (f) baseplate, (g) silicone gel, (h) AlN ceramic, and (i) copper metallization.

bonded copper (DBC) or active metal brazing (AMB). **Figure 1a** shows active metal brazing method [7]. No braze layers are needed for DBC as shown in **Figure 2**. Then a soft dielectric such as silicone gel is used to encapsulate the whole module to prevent electrical discharges in air as well as to protect semiconductors, substrates, and connections against humidity, dirt, and vibration. As a commercial example, "SYLGARD™ 527 Silicone Dielectric Gel" manufactured by the Dow Chemical Company has a dielectric constant of 2.85 and dielectric strength of 17 kV/mm [9].

Silicone gel also prevents thermal induced movements of bond wires attached to the semiconductor. The final encapsulation is achieved using polymer housing. The schematic layout of an IGBT with AMB is similar to that shown in **Figure 2** where brazes are also added to the structure.

As a consequence of higher blocking voltage, new packaging solutions to provide electrical insulation between the grounded heat sink and the HV terminals of the module are required. Due to the high electric fields, especially at the edges of the copper metallization, PDs can be initiated from these regions. The situation gets worse at protrusions shown in **Figure 1b** with extremely sharp edges of some braze below the metallization. High activity of PDs damages the insulating silicone gel and leads to electrical insulation failure and reduces the reliability of the module. Moreover, high-frequency PD pulses can lead to disturbance of the power electronics and cause severe shortcomings in high-power applications. The PD issue is one of the most crucial challenges to the development of HV high power density WBG power semiconductor devices. A description of current standards on PD tests on power electronics modules and relevant technical gaps is presented in Section 2. Section 3 deals with simulation and modeling of electric field stress inside power electronics modules. The various PD detection techniques employed for modules and correlation between measurements and electric field calculation is discussed in Section 4, and finally, PD control methods to relieve high field regions is explained in Section 5.

## 2. International standards on PD tests on power electronics devices

IEC 61287-1: "Railway applications-power converters installed on board rolling stock-part 1: characteristics and test methods" is the current standard commonly used for IGBT working at 1.5 kV or more [10]. The test voltage is a 50 Hz or 60 Hz alternating current (AC) root mean

square (RMS) voltage equal to $1.5\,U_m/\sqrt{2}$ or higher where $U_m$ is the maximum blocking voltage of the module in (V). For a 6.5 kV IGBT, it is $1.5 \times 6.5/\sqrt{2} \approx 6.9\text{kV}$. The voltage is ramped up to $1.5\,U_m/\sqrt{2}$ in 10 s and is maintained for $t_1$ = 1 min as shown in **Figure 3**. The rate of the ramp as shown in **Figure 3** is $(1.5\,U_m/\sqrt{2})/10\text{kV/s}$. During this time $t_1$, some PDs may be observed. After $t_1$, the voltage is decreased to $1.1\,U_m/\sqrt{2}$ in 10 s. For a 6.5 kV IGBT, it is $1.1 \times 6.5/\sqrt{2} \approx 5.1\text{kV}$. The voltage $1.1\,U_m/\sqrt{2}$ is applied for $t_2$ = 30 s. During the last 5 s of $t_2$, the peak magnitude of partial discharge in pC is measured. A typical value to pass the test for a component and a subassembly is, respectively, 10 and 50 pC.

However, IGBT modules are subjected to pulse width modulator (PWM) stress-type instead of power frequency AC voltages. To elucidate this stress-type, consider a single-phase full-bridge inverter as shown in **Figure 4a**. An inverter changes a DC input voltage to a symmetrical ac output voltage of desired magnitude and frequency. When switches (which can be IGBTs) $Q_1$ and $Q_2$ are turned on at the same time, the input voltage $U_s$ appears across the load. In this situation, the voltage on $Q_3$ and $Q_4$ which are off will be $U_s$. If switches $Q_3$ and $Q_4$ are turned on simultaneously, the voltage across the load is $-U_s$. In this situation, the voltage on $Q_1$ and $Q_2$ which are off will be $-U_s$. **Figure 4b** shows the waveform for the output voltage. Thus a unipolar square wave voltage with a magnitude of $U_s$ for $(0 - T_0/2)$ and almost zero for $(T_0/2 - T_0)$ places on $Q_3$ and $Q_4$ and a unipolar square wave voltage with an amagnitude of nearly zero for $(0 - T_0/2)$ and $-U_s$ for $(T_0/2 - T_0)$ places on $Q_1$ and $Q_2$.

In many industrial applications, it is often required to control the output voltage of inverters (1) to cope with the variations of dc input voltage, (2) for voltage regulation of inverters, and (3) for the constant volts/frequency control requirement [11]. The most efficient method of controlling the gain is to incorporate pulse-width-modulation (PWM) control with the inverters. In this regard, the commonly used techniques are:

1. Single-pulse-width modulation
2. Multiple-pulse-width modulation
3. Sinusoidal-pulse-width modulation
4. Modified sinusoidal pulse-width modulation
5. Phase-displacement control

Here we describe only sinusoidal-pulse-width modulation (SPWM) technique which is widely used. For other methods see [11]. In SPWM, the width of each gating signal can be varied in proportion to the amplitude of a sine wave. As shown in **Figure 5**, the gating signals are generated by comparing a sinusoidal reference signal with a triangular carrier wave of frequency, $f_c$, and peak, $A_c$. In this case, $Q_3$ and $Q_4$ should withstand $u_{ab}$ which is a fast-rising and fall square waveform known as PWM-stress in $(0 - \pi)$ and $Q_1$ and $Q_2$ should withstand $u_{ab}$ in $(\pi - 2\,\pi)$.

It has been known that repetitive voltage impulses generated as PWM-stress can lead to insulation premature failure of stator winding due to partial discharges in inverter-fed motors [12, 13]. About IGBTs the studies in [14, 15] show that PD behavior under 50 Hz or 60 Hz AC sinusoidal voltage is different from that for fast rise bipolar high-frequency square wave voltages. In this regard, for example for the test sample in [14] while partial discharge inception voltage (PDIV) under 50 Hz sinusoidal test voltage is 13 kV, for a bipolar square voltage with

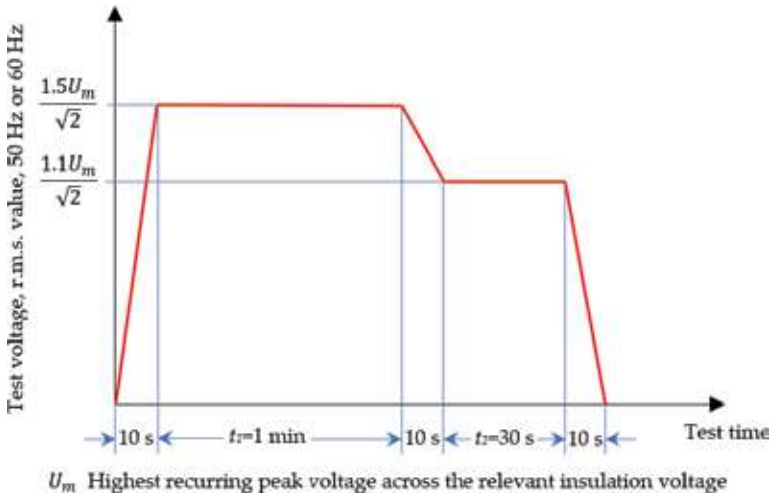


**Figure 3.** IEC 61287-1: "Railway applications-power converters installed on board rolling stock-part 1: characteristics and test methods" for partial discharge test.

rising time of about 400 μs, fast rise positive unipolar square and fast rise negative unipolar square both with rise time of about 100 ns it is 12, 9 and 7 kV, respectively. Moreover, the rate of increase in the PD magnitude concerning voltage is higher for steeper voltage rise [14].

Therefore new standards are needed to take into account actual voltages for power electronic modules. It was shown in [16] that although IGBTs could pass 50 Hz sinusoidal test under IEC 61287-1, insulation failure occurs when applying PWM input voltage with 50 Hz modulating frequency with 1 kHz carrier frequency and a rise time of 10 μs that is the stress condition more similar to the real operating conditions.

According to IEC 61287-1, the collector, emitter, and gate of a power electronics module should be connected, and PDs are measured when an alternating voltage is applied between the interconnected terminal and the metal base plate. The drawback is that it tests only the insulation

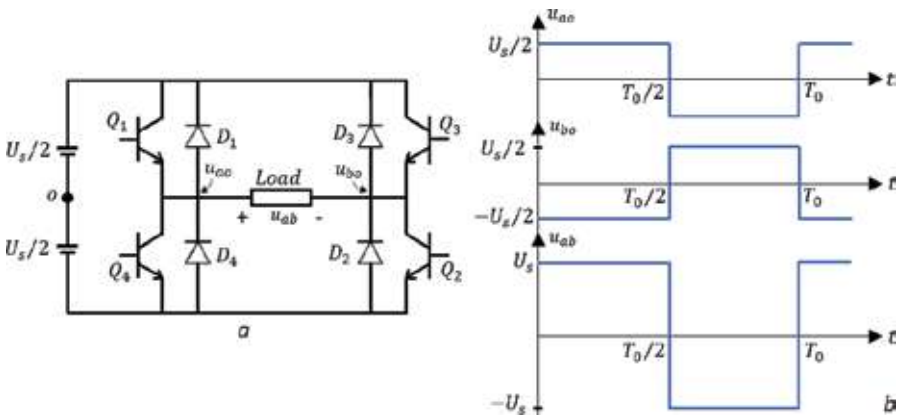


**Figure 4.** Single-phase full-bridge inverter.

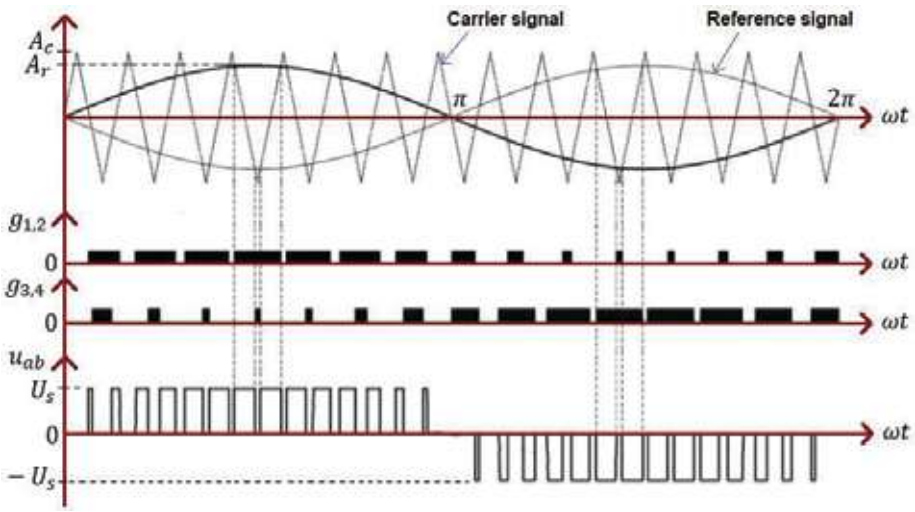


**Figure 5.** Sinusoidal pulse-width modulation.

of the substrate and the bulk of the gel is not tested. To address this issue, the test voltage is proposed as an AC voltage superimposed on a direct current (DC) one directly applied to the component turned off using a negative gate polarization [17–19]. The inverse DC offset of magnitude higher than the AC peak value as shown for an example in **Figure 6a** used as the test voltage avoids diode conduction [18]. The discharge inception voltage ($U_{DIV}$) is then defined as the peak value of the applied voltage ($U_{DC} + U_{AC}$) [17]. **Figure 6b** shows an experimental set-up generating such test voltage [17].

This method leads to detect PD for voltages lower than the one necessary to trig them during IEC 61287-1 test [17–19]. Although neither the test proposed in [17–19] nor IEC 61287-1 test can represent thoroughly the stresses endured by the power modules in inverters, the testing method proposed in [17–19] can provide more useful information on PDs during normal operation by stressing all the components involved in the packaging.

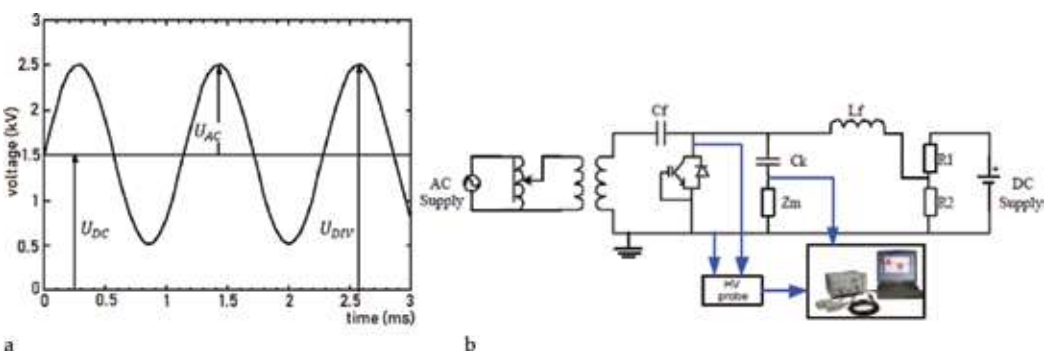


**Figure 6.** (a) New test voltage waveform and (b) set-up generating new test voltage for PD detection of an IGBT [18], License No. 4383271241884.

## 3. Simulation and modeling of electric stress inside the module

Since a combination of material defects in gel and the high electric stress due to sharp edges leads to partial discharge, PDs do not occur all along the sharp edges. However, identifying the critical spots with the maximum electric field magnitude due to only sharp edges can be useful to develop geometrical strategies to reduce the electric field magnitude peaks due to the effect of one contributing factor.

Note that the maximum electric field magnitude at perfectly sharp edges is theoretically infinite. Thus, the smaller mesh size, the higher electric stress and mathematically there is no convergence point. Assuming a rounded edge converges to a finite maximum electric field intensity with increasing resolution of the mesh grid. However, the value depends on the assumed edge radius. The smaller assumed edge radius, the higher amount of maximum electric field magnitude. To overcome this difficulty, it was shown in [20, 21] that when the distance to sharp edges becomes larger than 20 μm for the assumed geometry and dimensions, the differences between the electric field magnitudes for different meshing sizes are less than 1%. To be on the safe side, measuring points were considered at a distance of 50 μm to sharp edges in [20, 21]. In [22], both strategies containing rounded edges and considering measuring points at a distance of 20 μm from edges were benefited.

Assuming the measuring points defined above, the influence of following geometrical options are studied in [20, 22] on reducing the electric field stress values.

1. The thickness of the metallization layer,
2. The thickness of the substrate,
3. The shape of the edge,
4. Metal/conductive layer offset.

Among four parameters above, the thickness of the substrate and metal/conductive layer offset have a strong influence on the electric field magnitude. By varying the thickness of the ceramic, the electric field stress does not follow the equation of a plate capacitor: a doubling of the thickness (1–2 mm) reduces the electric field stress only by about 30% and not by 50%. However, an increased substrate thickness decreases cooling efficiency of the semiconductors, and this technique may not meet the miniaturization needs of power electronics as well.

Defining an offset of the two metallization layers as $r_{off} = r_u - r_l$ for $r_u$ (the distance from the AlN ceramic edge to the edge of the upper Cu metallization) and $r_l$ (the distance from the AlN ceramic edge to the edge of the lower Cu metallization) shown in **Figure 7a**. **Figure 8** shows the electric field stress values at measuring point located on L1 for different values of $r_{off}$ for a d = 630 μm ceramic layer [22]. For that (**Figure 7a**), a finite-element method (FEM) model was developed in the *Electrostatics* (*es*) module of COMSOL Multiphysics solving Poisson's equation.

$$\nabla^2 U = -\frac{\rho_v}{\epsilon_0 \epsilon_r} \tag{1}$$

$$E = -\nabla U \tag{2}$$

where $\rho_v$ is volume charge density which is $\rho_v = 0$ in the model considered in [22], $\epsilon_r$ is relative permittivity which for AlN and gel were considered, respectively, 8.9 and 2.7 in [22], $E$ is electric field intensity, and $U$ is electric potential.

As shown in **Figure 7b**, an extremely custom fine meshing with a maximum element size of 0.001 mm was used for Area 1 shown in **Figure 7a** to obtain precise results for electric field

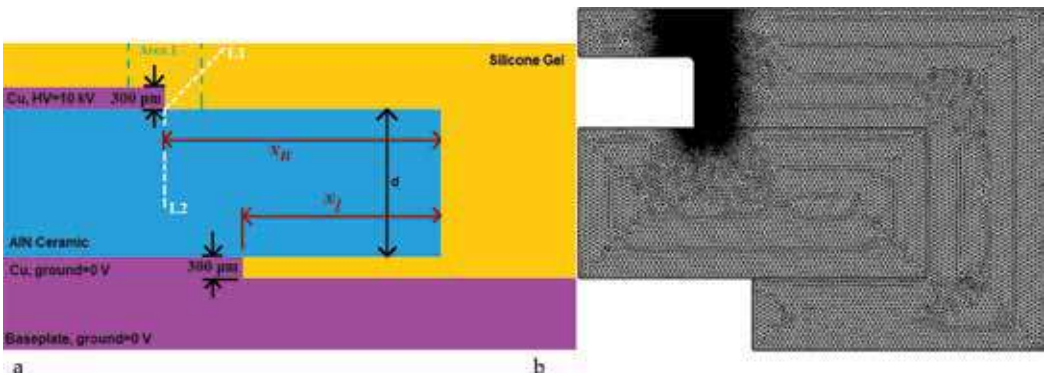


**Figure 7.** (a) The geometries considered for simulations in COMSOL Multiphysics and (b) meshing strategy.

intensity along L1 [22]. Such meshing strategy, using several levels of extremely custom fine meshing for the study area having sharp edges and a normal meshing for other areas to increase the computational efficiency was used in [23–29] as well. From **Figure 8**, it can be seen that with decreasing offset the electric field magnitude reduces. In other words, an increase in the length of the upper metal layer relieves the worst high field region. It is due to the influence of the grounded based plate, since the more extended top metal layer, the less nonuniform electric field. Changing $r_{off}$ from 0.35 to −0.5 mm reduces the electric field intensity up to 57% that presents the method as an efficient electric field control technique [22].

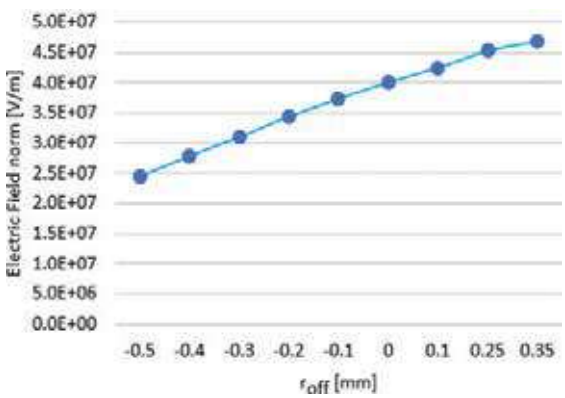


**Figure 8.** Influence of *r off* on electric field intensity.

## 4. Partial discharge measurements

Research carried out on PD detection, and localization inside an IGBT can mainly be divided into electrical and optical PD measurements. For electrical PD measurement, measured phase-resolved partial discharge (PRPD) patterns were analyzed to identify the type and location of PD. As shown in **Figure 9** [30, 31], it was observed that the PD of a metalized ceramic in an isolating liquid occurs at the maximum voltage at 90° and 270° and the amount of PD does not rise sharply with increasing voltage.

However, as shown in **Figure 10** [21, 30, 31] for the same metalized ceramic embedded in silicone gel, PD was found at a phase between zero and the maximum voltage, between 0–90° and 180–270°. Since the number and magnitude of the PDs strongly increase with rising voltage, it was argued that the origin of this discharge phenomenon is due to discharges at the interface between the silicone gel and the substrate and not due to locally restricted cavities in the gel.

In [21] the calculated electric field intensity and the measured PDIV were correlated. Combining the calculated electric field intensity in four measuring points ML1-ML4 shown in **Figure 11a**, the PDIV was plotted as shown in **Figure 11b** as a function of the geometric mean of $E$ values at ML1-ML4. A fitted equation as "PDIV (kV) = 20.4–0.25E (kV/mm)" was also reported for **Figure 11b** [21].

However, through an artificial spherical void embedded in silicone gel, it was shown in [32] that voids inside the silicone gel significantly accelerate the aging of the materials even at a normal operating electric stress. It was also found that an extremely non-uniform electric field resulted by a needle-sphere electrode with no artificial void inside the material can also lead to rapid aging at a normal operating electric stress [32]. Thus, it was concluded that the electrical treeing in front of the needle tip produces gas-filled voids inside the silicone and these week points besides conductive channels of trees lead to shortening the lifetime of the insulation [32].

In [33, 34] an optical PD localization setup benefitting from compact charge-coupled device (CCD) camera modules was used to record the small light intensities emitted by electroluminescence effects as well as the light caused by PD. It should be noted that before partial discharge inception, insulating polymers subjected to high electrical fields usually display electroluminescence as a result of the radiative relaxation of excited molecular states within the gel excited by high electrical field [34]. The measurement of electroluminescence allows the critical regions of high electric fields to be identified in the translucent silicone gel insulation

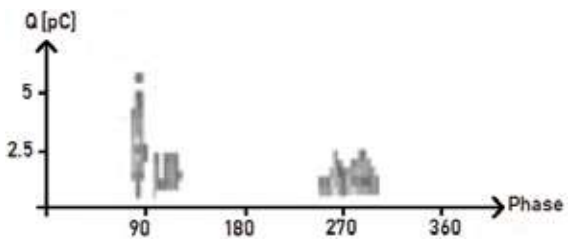


**Figure 9.** PD spectroscopy of AlN substrates in an insulating liquid [31], License No. 4383271013906.

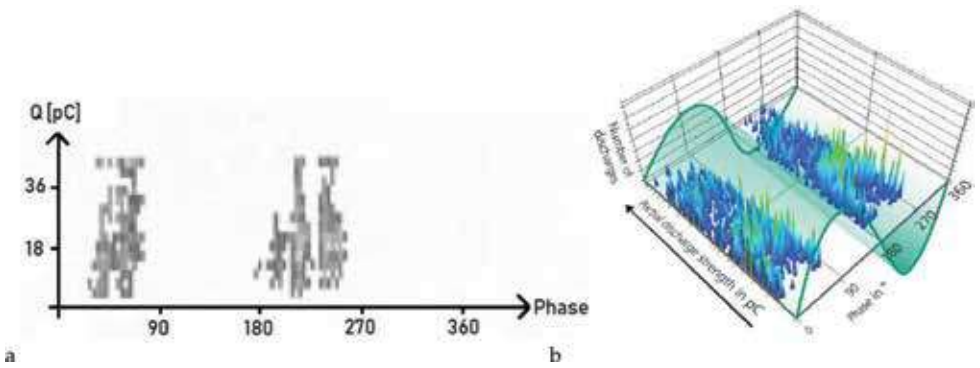


**Figure 10.** PD spectroscopy of AlN substrates in silicone gel (a) from [31], License No. 4383271013906, (b) from [21], License No. 4383270757365.

even before electrical aging begins. Increasing the voltage, PD starts at distinct locations. Bright shining spots in the image as seen in **Figure 12** show the higher possibility for PD inception.

In [35] the results concerning both electrical and optical detection of PDs occurring in the silicone gel were presented. That work showed that optical measurements could be used to study PDs in transparent gels, with any voltage shape and with very high sensitivity (<1 pC). In recent years, micro silicon photomultipliers (SiPM) were also examined and compared to conventional photomultiplier tubes (PMT) for optical PD detection [36].

In [37, 38], besides PRPD measurements, other diagnostic and quality control test methods to discriminate the dielectric condition between new and aged IGBT samples and reveal the influence of moisture on dielectric state of IGBT modules were used. They are time-dependent dielectric response measurements such as insulation resistance and polarization index, and frequency-dependent dielectric response measurements such as loss factor and frequency response analysis (FRA). Humidity as a result of the condensation caused by the difference in the interior and exterior temperatures may impact on the dielectric integrity of IGBT modules.

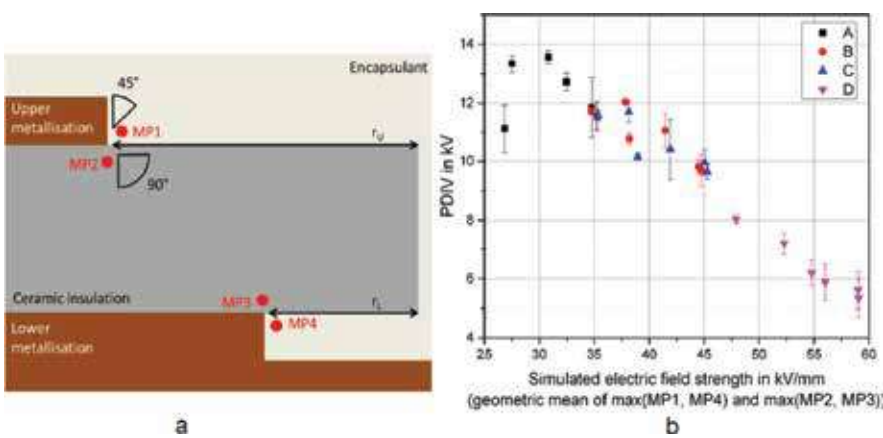


**Figure 11.** PDIV as a function of the geometric mean of MP1-4 [21], License No. 4383270757365.

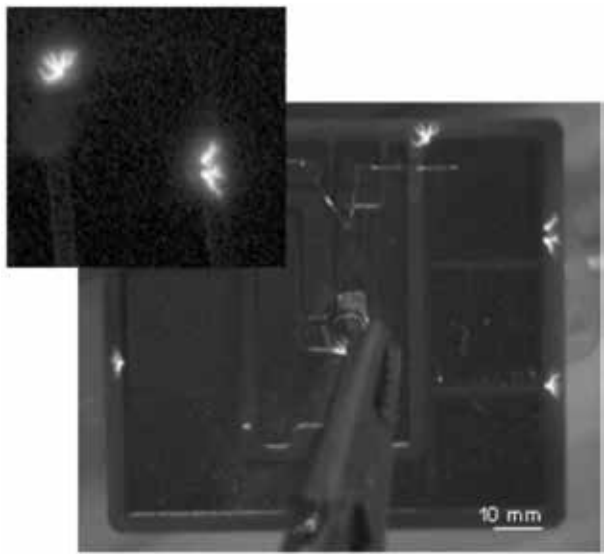


**Figure 12.** Optical localization of PD for an AIN substrate embedded in silicone gel. The discharges are located at the outer edges of the copper metallization [34], License No. 4383270494717.

Converters are often located in cubicles under atmospheric pressure, and the most widely used material for encapsulation of power electronic circuits is silicone gel [8, 15–22, 30–38, 42–45, 48, 51–54]. However, for variable-frequency drive (VFD) fed motors used in the subsea factory for oil and gas production at depths more than 3000 m, the development of pressure tolerant power electronics is envisaged where an incompressible insulating material is needed for power electronic modules. Thus, liquid embedded power electronics are investigated. In [14, 39] PDs in liquid embedded power electronics under three different waveforms as sinusoidal (50 Hz) voltage, a slow rise bipolar square voltage with a rise time of 400 μs, and a fast unipolar positive and negative rise square voltage with a rise time of 100 ns were investigated. Both electrical and optical techniques were used to study PD behavior of IGBT insulation. Regarding a good correlation found in [14, 39] between the measured electrical and optical PDs, optical PDs can also be considered for the characterization of PD phenomena. Another significant result obtained in [14, 39] is that the fast rise square voltage has the lowest PDIV while the sinusoidal voltage has the highest one. Moreover, it was reported in [14, 39] that the number and magnitude of PDs decrease when the pressure of the liquid in the test cell increases. In other words, pressure can collapse the propagation of the streamers, and that is the great merit of liquid embedded power electronics used for the subsea application.

Various liquid dielectrics such as Nytro 10XN, Midel 7131 and Galden HT230 were examined in [40, 41] for pressure tolerant liquid embedded power electronics modules for deep, and ultra-deepwater. The test object used in [40] is a printed circuit board (PCB) card shown in **Figure 13a** with a dimension of 50 × 24 × 1 $mm^3$ and a schematic shown in **Figure 13b**. The thickness of copper metallization at both sides is 420 μm. The trench located at the upper metallization layer has a width of 2 mm. The left end of the board was connected to a high voltage source and the other end of the board and the base plate (the lower metallization layer) was connected to ground. Sharp edges were rounded to ensure the set-up is PD free.

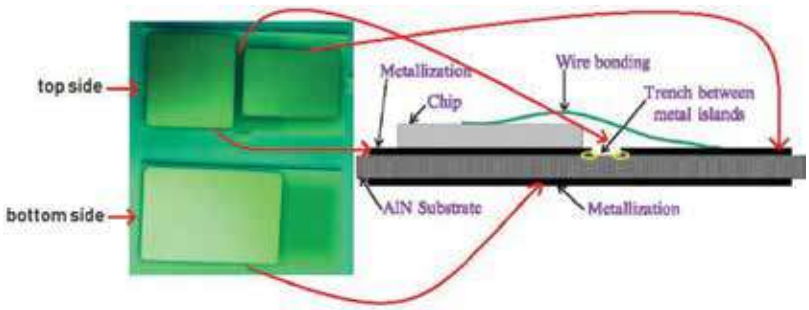


**Figure 13.** (a) PCB card test object and (b) the schematic of PCB card [40], License No. 4383270012789.

**Table 1** shows the $U_{1\%}$, $U_{50\%}$, and $U_{63\%}$ breakdown probability. For $U_{63\%}$, the cumulative Weibull function was considered given by

$$f(v) = 1 - e^{[-v/\alpha]^{\beta}} \tag{3}$$

where $v$ is voltage, $f(v)$ is the probability of failure, $\alpha$ is the characteristic breakdown voltage and $\beta$ is the range of failure voltages within the distribution. The higher the $\beta$, the lower the scatter is. Besides sinusoidal voltage (38.5 Hz), tests were carried out under a fast-rising positive square wave voltage. From **Table 1** it can be seen that Galden has a superior breakdown characteristic.

The influence of temperature on PD characteristics in silicone gel was experimentally investigated in [42]. It was found that with increasing the temperature, the PDIV and the overall shape of PD patterns remain unchanged, but both discharge amplitudes and number increase as shown in **Figure 14** for PRPD patterns in the same sample at a fixed applied voltage at 20 and 100°C [42].

**Figure 15** shows the influence of temperature on the variation of the average PD current ($I_{av}$), which is the sum of all recorded discharges per unit time, versus voltage in the same experiments [42]. It can be seen that with increasing the temperature, the PDIV remains unchanged. However, due to the increase of PD amplitudes and number the increase of $I_{av}$ is faster at high temperature [42].

| Voltage type | Samples | $U_{1\%}$ (kV) | $U_{50\%}$ (kV) | $\alpha$ (kV) | $\beta$ |
|---|---|---|---|---|---|
| Sinusoidal voltage | Nytro | 20.01 | 40.89 | 43.89 | 5.92 |
| | Midel | 25.94 | 39.76 | 41.26 | 9.92 |
| | Galden | 27.56 | 41.98 | 43.54 | 10.06 |
| Positive square voltage | Nytro | 19.19 | 22.5 | 22.86 | 26.29 |
| | Midel | 15.28 | 22.98 | 23.75 | 10.43 |
| | Galden | 20.80 | 32.17 | 33.41 | 9.7 |

**Table 1.** $U_{1\%}$, $U_{50\%}$, and $U_{63\%}$ breakdown probability for PCB card test object [40].

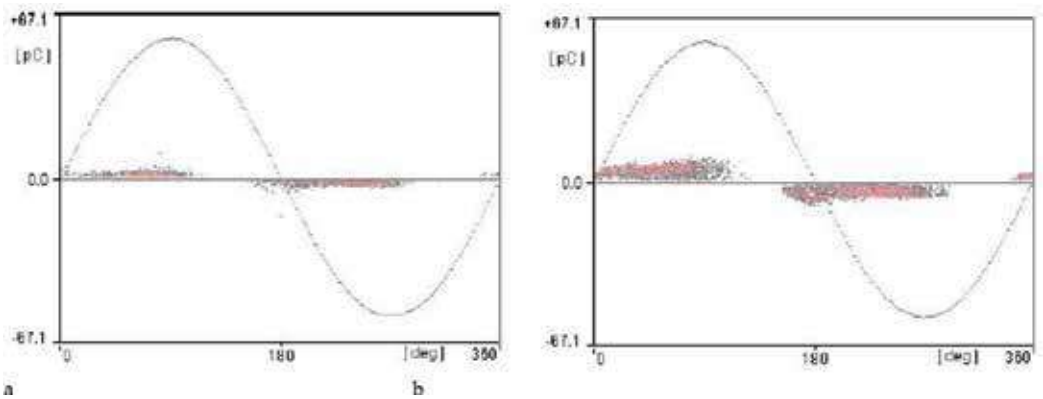


**Figure 14.** PRPD patterns at two temperatures (a: 20°C, b: 100°C) with a point-plane sample embedded in silicone gel (ac 50 Hz, the tip radius of curvature for the point of $r_0$ = 1.4 μm, gap distance of d = 4 mm, V = 8 kV) [42], License No. 4383261112180.

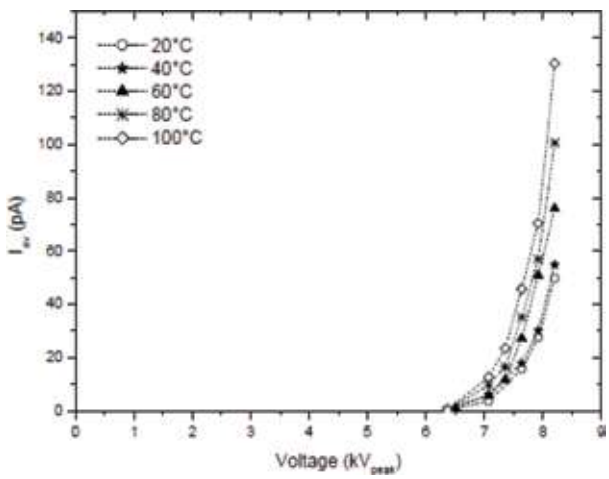


**Figure 15.** Influence of temperature on average PD current versus voltage (ac 50 Hz, $r_0$ = 1.4 μm, d = 4 mm) [42], License No. 4383261112180.

## 5. Partial discharge control

### 5.1. Linear resistive electric field control

Applying functional materials on the highly stressed region can reduce the electric field. Two types of stress relieving composite dielectrics are as follows. (1) The conductivity of the material varies with the electric field, field-dependent conductivity (FDC) [43, 48], (2) the permittivity of the material changes with the electric field, field dependent permittivity (FDP) [50].

In FDC stress relieving control, also called resistive field control, a conductive layer is applied at the metallization edge. The field distribution is modified by flowing the conduction current

through the layer. Materials used for resistive field control can be linear or nonlinear. The conductivity of linear resistive field control materials is not field dependent. Therefore, the conductivity of the layer made of linear materials must be carefully selected. For too low conductivity, the layer has no role in electric stress control [48]. On the other hand, if the conductivity of the layer is too high and for the case of a non-bridging layer, the layer behaves as a prolongation of the metallization and the high field problem is merely transferred to the end of the layer [48]. For the case of a layer bridging HV and ground potential, the layer leads to massive leakage current [48].

In [43], a 300-nm high impedance layer having an electrical conductivity of 105 Ω cm made of semiconducting amorphous silicon, a-Si: H, was applied by plasma-enhanced chemical vapor deposition (PECVD) process to the edge of the substrate connecting the top copper metallization with the bottom. The mentioned conductivity was adjusted to homogenize the electric field by having the magnitude of the conduction current higher than the capacitive current. By electric field simulations, the same value of the electric conductivity of the layer was reported in [44, 45]. Two sample modules with and without a-Si:H coating built under manufacturing conditions were tested in [43]. While the partial discharge increases sharply at low voltages of 3–4 kV without an a-Si:H coating, it does not exceed 10 pC up to a voltage of 10 kV with an a-Si:H coating layer satisfying the partial discharge requirements based on IEC 61287-1. Note that the linear resistive field control depends on the frequency and its advantage reduces with increasing frequency.

The intrinsic semi-conductive nature of the particles and their connectivity lead to non-linear behavior of nonlinear resistive electric field control composites. In this regard, the particle to particle contact is possible if the filler concentration is above a prescribed limit. The electrical field magnitude must also be high enough to allow conduction through the semi-conductive particles and barriers between particles.

A theory-based evaluation of the behavior of field grading materials with strongly field-dependent conductivities is presented in [46] with a survey of ZnO microvaristors in various applications in [47]. ZnO microvaristor layer was studied to relieve high field regions in an IGBT [48]. An advantage of nonlinear materials compared to linear materials is that losses are not permanent. They occur only when the electrical field magnitude passes a threshold known as switching filed where the material switches to a conductive behavior.

An electrostatic FEM model developed in ACE TripleC was used for electric field calculations in [48]. **Figure 16a** shows electric field distribution for without a coating layer on the protrusion considered in the model. In this case, the maximum electric stress, $E_{max}$, obtained 2.6 × 108 V/m at the gel adjacent to the protrusion [48]. To relieve this high field stress region, a layer for coating the metallization edges was considered in three cases with polyimide layer ($\varepsilon_r$ = 3.5), a high permittivity ($\varepsilon_r$ = 40) layer of a polymer/ceramic composite and ZnO microvaristor layer described above. A comprehensive study of the general structure of polymers, their properties and applications can be found in [49]. For polyimide layer, $E_{max}$ in the layer (adjacent to the protrusion) and gel will be 2.3 × 108 and 0.18 × 108 V/m, respectively [48]. In this regard, although polymer/ceramic composite with $\varepsilon_r$ = 40 can reduce the maximum electric field in the layer adjacent to the protrusion to 0.3 × 108 V/m, the electric field in the gel reaches higher values (0.2 × 108 V/m) than with polyimide coating. Employing a ZnO microvaristor layer, $E_{max}$ in both the layer (0.066 × 108 V/m as shown in **Figure 16b**) and gel (0.06 × 108 V/m) dramatically decreases.

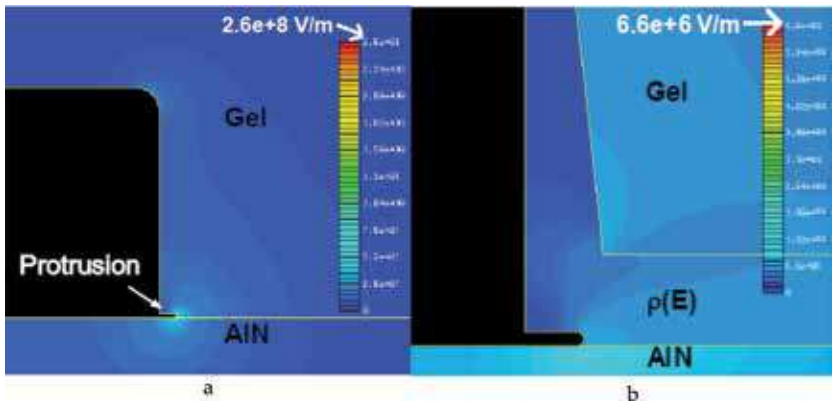


**Figure 16.** The influence of nonlinear FDC coating layer on reducing the electric field in the module [48], License No. 4383260855923.

### 5.2. FDP stress relieving control

As mentioned in Section 5.1 although a high permittivity coating layer relieves high electric field stress adjacent to the copper metallization, it leads to higher electric field stress in the gel and in particular the weak interface between the layer and the gel encapsulation. This means a high permittivity material as a coating layer may not be efficient. Thus in [50] employing it as a filler was examined. The filler studied in [50] was a ferroelectric filler, barium titanate, in the base silicone gel to form an FDP stress relieving dielectric material having a $\epsilon_r(E)$ as $\epsilon_r(E) = 6.4 + 1.3E$. By enhancing polarization mechanisms, the ferroelectric filler particles can reduce high electrical stresses. However, it should be noted that this electric field control method works only under ac fields and at the temperatures higher than Curie temperature which is 130°C for pure barium titanate [51] this advantage will disappear [50].

It is shown in [50] that applying a high permittivity non-dependent field filler can reduce electric stress by around 10% while with a dependent-field one a reduction of 29% can be achieved.

### 5.3. The quality and type of substrates

Despite all publications, which have concluded that PDs occur in the silicone gel or at the interface between the substrate and the gel, a different conclusion about the origin of PDs was reported in [52]. To explore the actual origin of PDs, six insulating liquids including Silicon oil #1 (Sil20), Silicon oil #1 (Sil350), Transformer oil (Toil), Synthetic capacitor liquid (Scl), Synthetic transformer liquid (Stl) and Ester liquid (Est), which have different PD properties were used instead of gel, and three substrate materials including AlN, $Al_2O_3$, and glass/epoxy composite were also examined.

A rather large variation in PDIV was observed for six mentioned liquids used in a point-plane electrode geometry under 50 Hz AC voltage at room temperature (20°C). However, a substrate test geometry similar to an IGBT shows almost no changes in PDIV for the mentioned different liquids. Moreover, for the IGBT test geometry, PDs appear in both polarities and provides somewhat symmetrical patterns with good stability. However, asymmetrical PRPD

patterns for the point-plane electrode geometry were obtained. Using the gel in the mentioned experiments produces no change. Thus, it was concluded that PDs recorded with the substrate indeed do not occur within the liquid or the gel. The only remaining possibility is that PDs originate from the porous nature of the AlN or $Al_2O_3$ substrates. This is a hypothesis opposed to the ideas commonly accepted. The experiments carried out with another sintered porous material, and with a non-porous material (epoxy resin) confirm this hypothesis where with epoxy, no stable PD regime can be achieved.

In the almost same direction, it was experimentally shown in [53, 54] that surface discharges initiated at the triple junction and propagated at the gel-AlN substrate interface creates cavities composed of tree-like structure and spherical sub-cavities leading to the degradation of AlN substrate [53] as well as give rise to the growth of cavities in the gel [54]. Regarding the first issue, other substrates such as $Al_2O_3$ and glass were compared with AlN. The cavities usually start from the triple junction with high voltage and being pushed away from the high voltage conductor through a conductive channel on the power module substrate. Focusing on the conductive channel, it was found that during repetitive surface discharges, desorption of nitrogen from AlN substrate results in the formation of Al and this leads to a decrease in the resistance of cavity path that was measured around 5 kΩ/100 μm for AlN compared to above 1 MΩ/100 μm for glass and $Al_2O_3$. Thus, it was justified that the high electric field at the tip of surface conductive paths is the reason for elongation the cavity stopping length for AlN to more than twice than that on other substrates. To address the second issue, the dynamic potential distribution of surface discharges in gel was measured by a two-dimensional sensing technique with a Pockels crystal [54].

Another survey of the topics discussed in this book chapter can be found in [55] where other papers, as well as other aspects of the documents reviewed in this book chapter, are evaluated. These two publications, [55] and this book chapter, cover together almost all electrical insulation issues in power electronics modules.

## 6. Conclusion

The book chapter reviews some technical issues raised for electrical insulation weaknesses in high power IGBTs. FEM modeling of electric stress inside modules, which have perfectly sharp edges, is a challenge where using rounded edges or assuming measuring points at a distance from edges are used to address this issue. Although PRPD patterns can be used to identify the origin and location of PDs, the hypotheses proposed based on the measured patterns have not reached an agreement. Further investigation is also needed to determine permissible levels for time and frequency dependent diagnostic methods for modules. The optical technique is a promising technique to localize PDs in a power electronics module. Using linear and nonlinear resistive electric field control as a coating layer or using field dependent permittivity materials as a filler in the silicone gel can be used to control PD in modules. However, these mitigation solutions are not mature and need further research.

## Author details

Mona Ghassemi

Address all correspondence to: monag@vt.edu

Virginia Polytechnic Institute and State University, ECE Department, USA

## References

[1] Kassakian JG, Jahns TM. Evolving and emerging applications of power electronics in systems. IEEE Emerging and Selected Topics in Power Electronics. 2013;**1**(2):47-58. DOI: 10.1109/JESTPE.2013.2271111

[2] Millan J, Godignon P, Perpina X, Perez-Tomas A, Rebollo J. A survey of wide bandgap power semiconductor devices. IEEE Transactions on Power Electronics. 2014;**29**(5): 2155-2163. DOI: 10.1109/TPEL.2013.2268900

[3] Ryu SH, Capell C, Jonas C, Cheng L, O'Loughlin M, Burk A, Agarwal A, Palmour J, Hefner A. Ultra high voltage (>12 kV), high-performance 4H-SiC IGBTs. In: Proceedings of the International Symposium Power Semiconductor Devices and ICs; 3-7 June 2012; Belgium. p. 257-260

[4] Marckx DA. Breakthrough in Power Electronics from SiC. USA: Nat. Renewable Energy Lab.; 2006. NREL/SR-500-38515(in press)

[5] Kreuger F. Partial Discharge Detection in High-Voltage Equipment. London, England: Butterworths; 1989

[6] Álvarez-Gómez F, Albarracín-Sánchez R, Garnacho-Vecino F, Granizo-Arrabé R. Diagnosis of insulation condition of MV switchgears by application of different partial discharge measuring methods and sensors. Sensors. 2018;**18**:720. DOI: 10.3390/s18030720

[7] Sheng WW, Colino RP. Power Electronic Modules: Design and Manufacture. Boca Raton, Florida, USA: CRC Press; 2005

[8] Mitic G, Sommer KH, Dieci D, Lefranc G. The thermal impedance of new power semiconductor modules using AlN substrates. In: Proceedings of the IEEE 33th Industry Applications Society (IAS) Meeting; 12-15 Oct. 1998; USA. p. 1026-1030

[9] Dow. SYLGARD™ 527 Silicone Dielectric Gel Technical Data Sheet. Available from: https://consumer.dow.com/en-us/document-viewer.html?ramdomVar=3447338133693297098&docPath=/content/dam/dcc/documents/en-us/productdatasheet/11/11-31/11-3136-sylgard-527-dielectric-gel.pdf

[10] IEC 61287-1: Railway applications—Power converters installed on board rolling stock-part 1: Characteristics and test methods. 3rd ed. 2014

[11] Rashid MH. Power Electronics Circuits, Devices, and Applications. 3rd ed. Englewood Cliffs, New Jersey, USA: Prentice Hall; 2003

[12] Wang P, Cavallini A, Montanari GC, Wu G. Effect of rise time on PD pulse features under repetitive square wave voltages. IEEE Transactions on Dielectrics and Electrical Insulation. 2013;**20**(1):245-254. DOI: 10.1109/TDEI.2013.6451364

[13] Wang P, Montanari GC, Cavallini A. Partial discharge phenomenology and induced aging behavior in rotating machines controlled by power electronics. IEEE Transactions on Industrial Electronics. 2014;**61**(121):7105-7112. DOI: 10.1109/TIE.2014.2320226

[14] Abdelmalik AA, Nysveen A, Lundgaard L. Influence of fast rise voltage and pressure on partial discharges in liquid embedded power electronics. IEEE Transactions on Dielectrics and Electrical Insulation. 2015;**22**(5):2770-2779. DOI: 10.1109/TDEI.2015.005411

[15] Romano P, Viola F, Miceli R, Spataro C, D'Agostino B, Imburgia A, La Cascia D, Pinto M. Partial discharges on IGBT modules: Are sinusoidal waveforms sufficient to evaluate behavior?. In: Proceedings of the IEEE Conference on Electrical Insulation and Dielectric Phenomena; 19-22 Oct. 2014; USA. p. 224-227

[16] Madonia A, Romano P, Hammarstrom T, Gubanski SM, Viola F, Imburgia A. Partial discharge of gel insulated high voltage power modules subjected to unconventional voltage waveforms. In: Proceedings of the IEEE Conference on Electrical Insulation and Dielectric Phenomena; 16-19 Oct. 2016; Canada. P. 715-718

[17] Breit F, Dutarde E, Saiz J, Lebey T, Malec D, Dinculescu S. Partial discharge detection in power modules. In: Proceedings of the IEEE 33rd Annual Power Electronics Specialists Conference; 23-27 June 2002; Australia. p. 748-752

[18] Th L, Malec D, Dinculescu S, Costan V, Breit F, Dutarde E. Partial discharges phenomenon in high voltage power modules. IEEE Transactions on Dielectrics and Electrical Insulation. 2006;**13**(4):810-819. DOI: 10.1109/TDEI.2006.1667740

[19] Breit F, Dinculescu S, Dutarde E, Lebey Th, Saiz J. Method and device for testing a power module. US Patent 6836125B2. 2004

[20] Bayer CF, Baer E, Waltrich U, Malipaard D, Schletz A. Simulation of the electric field strength in the vicinity of metallization edges on dielectric substrates. IEEE Transactions on Dielectrics and Electrical Insulation. 2015;**22**(1):257-265. DOI: 10.1109/TDEI.2014.004285

[21] Bayer CF, Waltrich U, Soueidan A, Baer E, Schletz A. Partial discharges in ceramic substrates-correlation of electric field strength simulations with phase resolved partial discharge measurements. In: Proceedings of the International Conference on Electronics Packaging; 20-22 Aug. 2016; Japan. p. 530-535

[22] Ghassemi M. Geometrical techniques for electric field control in (ultra) wide bandgap power electronics modules. In: Proceedings of the 36th Electrical Insulation Conference; 17-20 June 2018; USA

[23] Ghassemi M, Cao Y, Chen Q. A thermo-electrodynamic electric field dependent molecular ionization model to design electrical insulation system of HVDC wet-mate

connectors under transient conditions. IEEE Transactions on Dielectrics and Electrical Insulation. 2018;**25**(2):476-485. DOI: 10.1109/TDEI.2018.006691

[24] Ghassemi M, Chen Q, Cao Y. The influence magnitude and rise time of applied voltage and the type of oil on streamer growth in a wet-mate DC connector. IEEE Transactions on Dielectrics and Electrical Insulation. 2017;**24**(3):1646-1656. DOI: 10.1109/TDEI.2017.006448

[25] Ghassemi M, Tefferi MB, Chen Q, Cao Y. A thermo-electrodynamic electric field dependent molecular ionization model to realize positive streamer propagation in a wet-mate DC connector. IEEE Transactions on Dielectrics and Electrical Insulation. 2017;**24**(2):901-914. DOI: 10.1109/TDEI.2017.006323

[26] Ghassemi M, Farzaneh M. Effects of tower, phase conductors and shield wires on electrical field around FRP hot stick during live-line work. IEEE Transactions on Dielectrics and Electrical Insulation. 2015;**22**(6):3413-3420. DOI: 10.1109/TDEI.2015.004886

[27] Ghassemi M, Farzaneh M. Coupled computational fluid dynamics and heat transfer modeling of the effects of wind speed and direction on temperature increase of an ice-covered FRP live-line tool. IEEE Transactions on Power Delivery. 2015;**30**(5):2268-2275. DOI: 10.1109/TPWRD.2015.2403267

[28] Ghassemi M, Farzaneh M, Chisholm WA. A coupled computational fluid dynamics and heat transfer model for accurate estimation of temperature increase of an ice-covered FRP live-line tool. IEEE Transactions on Dielectrics and Electrical Insulation. 2014; **21**(6):2628-2633. DOI: 10.1109/TDEI.2014.004586

[29] Ghassemi M, Farzaneh M, Chisholm WA. Three-dimensional FEM electrical field calculation for FRP hot stick during EHV live-line work. IEEE Transactions on Dielectrics and Electrical Insulation. 2014;**21**(6):2531-2540. DOI: 10.1109/TDEI.2014.004580

[30] Mitic G, Lefranc G. Localization of electrical-insulation and partial-discharge failures of IGBT modules. In: Proceedings of the IEEE 36th Industry Applications Society (IAS) Meeting; 3-7 Oct. 1999; USA. p. 1453-1458

[31] Mitic G, Lefranc G. Localization of electrical-insulation and partial-discharge failures of IGBT modules. IEEE Transactions on Industry Applications. 2002;**38**(1):175-180. DOI: 10.1109/28.980373

[32] Ebke T, Khaddour A, Peier D. Degradation of silicone gel by partial discharges due to different defects. In: Proceedings of the IEE International Conference on Dielectric Materials, Measurement and Applications; 17-21 Sept. 2000; UK. p. 202-207

[33] Fabian JH, Hartmann S, Hamidi A. Partial discharge failure analysis of AlN substrates for IGBT modules. Microelectronics Reliability. 2004;**44**:1425-1439. DOI: 10.1016/j.microrel.2004.07.111

[34] Fabian JH, Hartmann S, Hamidi A. 'Analysis of insulation failure modes in high power IGBT modules. In: Proceedings of the 40th Industry Applications Society (IAS) meeting, 2-6 Oct. 2005; Hong Kong. p. 799-805

[35] Auge JL, Lesaint O, Frey D. Optical and electrical investigation of dielectric gel behavior under high electrical field. In: Proceedings of the IEEE International Conference on Solid Dielectrics; 5-9 July 2004; France

[36] Ren M, Zhou J, Song B, Zhang C, Dong M, Albarracín R. Towards optical partial discharge detection with micro silicon photomultipliers. Sensors. 2017;**17**:2595. DOI: 10.3390/s17112595

[37] Arumugam S. Influence of moisture on dielectric condition of high power insulated gate bipolar transistor modules. IEEE Transactions on Dielectrics and Electrical Insulation. 2016;**23**(3):1364-1374. DOI: 10.1109/TDEI.2015.005571

[38] Arumugam S, Gorchakov S, Schoenemann T. Dielectric and partial discharge investigations on high power insulated gate bipolar transistor modules. IEEE Transactions on Dielectrics and Electrical Insulation. 2015;**22**(4):1997-2007. DOI: 10.1109/TDEI.2015.005571

[39] Abdelmalik AA. Influence of sinusoidal and square voltages on partial discharge inceptionin geometries with point-like termination. High Voltage. 2018;**3**(1):31-37. DOI: 10.1049/hve.2017.0074

[40] Abdelmalik AA, Borge MD, Nysveen A, Lundgaard LE, Linhjell D. Statistical analysis of dielectric breakdown of liquid insulated printed circuit boards. IEEE Transactions on Dielectrics and Electrical Insulation. 2016;**23**(4):2303-2310. DOI: 10.1109/TDEI.2016.7556507

[41] Liland KB, Lesaint C, Lundgaard L, Hernes M, Glomm WR. Liquid insulation of IGBT modules: Long term chemical compatibility and high voltage endurance testing. In: Proceedings of the IEEE International Conference on Dielectrics; 3-7 July 2016; France. p. 384-389

[42] Do TM, Lesaint O, Auge JL. Streamers and partial discharge mechanisms in silicone gel under impulse and AC voltages. IEEE Transactions on Dielectrics and Electrical Insulation. 2008;**15**(6):1526-1534. DOI: 10.1109/TDEI.2008.4712654

[43] Mitic G, Licht T, Lefranc G. IGBT module technology with high partial discharge resistance. In: Proceedings of the IEEE 36th Industry Application Society (IAS) Meeting; 30 Sept.-4 Oct. 2001; USA. p. 1899-1904

[44] Frey D, Schanen J, Auge J, Lesaint O. Electric field investigation in high voltage power modules using finite element simulations and partial discharge measurements. In: Proceedings of the IEEE 38th Industry Application Society (IAS) Meeting; 12-16 Oct. 2003; USA. p. 1000-1005

[45] Frey D, Schanen JL, Auge JL, Lesaint O. Electric field investigation in IGBT power modules. In: Proceedings of the IEEE International Conference on Solid Dielectrics; 5-9 July 2004; France. p. 864-867

[46] Donzel L, Christen T, Greuter F. Nonlinear resistive electric field grading part 1: Theory and simulation. IEEE Electrical Insulation Magazine. 2010;**27**(6):47-59. DOI: 10.1109/MEI.2010.5599979

[47] Donzel L, Christen T, Greuter F. Nonlinear resistive electric field grading part 2: Materials and applications. IEEE Electrical Insulation Magazine. 2011;**27**(2):18-29. DOI: 10.1109/MEI.2011.5739419

[48] Donzel L, Schuderer J. Nonlinear resistive electric field control for power electronic modules. IEEE Transactions on Dielectrics and Electrical Insulation. 2012;**19**(3):955-959. DOI: 10.1109/TDEI.2012.6215099

[49] Haque SM, Rey JAA, Mas'ud AA, Umar Y, Albarracín R. Electrical properties of different polymeric materials and their applications: The influence of electric field. In: Du B, editor. Properties and Applications of Polymer Dielectrics. InTech; 2017. pp. 41-63. DOI: 10.5772/67091

[50] Wang N, Cotton I, Robertson J, Follmann S, Evans K, Newcombe D. Partial discharge control in a power electronic module using high permittivity non-linear dielectrics. IEEE Transactions on Dielectrics and Electrical Insulation. 2010;**17**(4):1319-1326. DOI: 10.1109/TDEI.2010.5539704

[51] Moulson AJ, Herbert JM. Electroceramics: Materials, Properties, Applications. 2nd ed. West Sussex: England John Wiley & Sons Ltd.; 2003. DOI: 10.1002/0470867965

[52] Auge JL, Lesaint O, Vu Thi AT. Partial discharges in ceramic substrates embedded in liquids and gels. IEEE Transactions on Dielectrics and Electrical Insulation. 2013;**20**(1):262-274. DOI: 10.1109/TDEI.2013.6451366

[53] Sato M, Kumada A, Hidaka K, Yamashiro K, Hayase Y, Takano T. Surface discharges in silicone gel on AlN substrate. IEEE Transactions on Dielectrics and Electrical Insulation. 2016;**23**(1):494-500. DOI: 10.1109/TDEI.2015.005412

[54] Sato M, Kumada A, Hidaka K, Yamashiro K, Hayase Y, Takano T. Dynamic potential distributions of surface discharge in silicone gel. IEEE Transactions on Dielectrics and Electrical Insulation. 2015;**22**(3):1733-1738. DOI: 10.1109/TDEI.2015.7116371

[55] Ghassemi M. PD measurements, failure analysis, and control in high-power IGBT modules. High Voltage. 2018. DOI: 10.1049/hve.2017.0186

Chapter 7

# Simulation and Optimization of Electrical Insulation in Power Quality Monitoring Sensors Applied in the Medium-Voltage

Sender Rocha dos Santos, Rodrigo Peres,
Wagner Francisco Rezende Cano and
Joao Batista Rosolem

Additional information is available at the end of the chapter

http://dx.doi.org/10.5772/intechopen.77187

**Abstract**

Thanks to the Smart Grid initiative, the focus for medium-voltage MV (13.8–34 kV) smart meters leveraged the development of sensors for distribution application. In order to be useful at power quality monitoring, the sensors needs to attend, at least, the International Electrotechnical Commission (IEC) 61000–4-30 and IEC 61000–4-7 standards with high-accuracy in terms of voltage (less than 0.1%), current (less than 1.0%) and measuring the waveform distortion data up to the 50th harmonic of 50 or 60 Hz alternating frequency. This kind of sensor is built with two capacitors connected in series. The first capacitor is a commercial electronic low-voltage device. One terminal of this capacitor is connected to the medium-voltage (MV) conductor. The second one, is connected to the other capacitor that is constructed using the own sensor packaging. This second capacitor has an electrode, that is connected with the first capacitor and the other terminal is connected to the ground. The voltage is measured between the terminals of the low voltage capacitor. The performance of this capacitor depends on the geometry and the materials used in the electrical insulation. This chapter describes the simulations and modeling of the capacitor electrodes using a finite-elements software, COMSOL Multiphysics, for modeling in order to optimize the performance of sensor in terms of electric field distribution.

**Keywords:** simulation, electrical insulation, sensors, power quality monitoring, medium-voltage, capacitive divider

## 1. Introduction

One of the fundaments of the Smart Grid concept is that user safety should be ensured while monitoring, updating and continuously reliably distributing electricity grid by adding smart meters and monitoring systems to the power grid is obtained. This is necessary in order to ensure electronic communication between suppliers and consumers [1]. Smart grid monitoring systems require various types of sensors and transducers to monitor the grid conditions. After the Smart Grid initiative, the focus for medium-voltage (MV) smart meters leveraged the development of energy quality sensors for distribution application [2]. In order to be useful at power quality monitoring, the sensors needs to attend at least the International Electrotechnical Commission (IEC) 61000–4-30 and IEC 61000–4-7 standards [3, 4] with high-accuracy in terms of voltage (less than 0.1%), current (less than 1.0%) and measure waveform distortion data up to the 50th harmonic. In addition, this sensor must be easy to install and remove without disconnect the distribution network and it must monitor the grid for a period that may last longer than 1 week.

In this context, two power quality-monitoring technologies are prominent: wireless sensors [5] or optical fiber sensors [6, 7]. Wireless sensors have the advantage of not needing any physical medium to transmit the data to a remote measuring unit, but need to use batteries in order to keep the electronic circuits working. On the other hand, optical fiber sensors have the advantage of no need for electrical powering, but they need a physical link to the remote measuring unit.

Independently of the technologic choice, current and voltage waves have to be measured in the medium-voltage (MV) in order to obtain the power quality parameters. Particularly, for voltage measurements, a capacitive or a resistive circuit divider [8–10] can be used to obtain a voltage sample of the MV conductor. In this work, it is analyzed the capacitive case. The low capacitance of this circuit accumulates more than 99.9% of the total voltage (e.g. 13.8 or 34 kV) and is totally constructed using the own sensor packaging. In this capacitive circuit the first capacitor is a commercial electronic low-voltage (LV) device. One terminal of this capacitor is connected to the medium-voltage conductor. The second one, is connected to the other capacitor that is constructed using the own sensor packaging. This second capacitor has an electrode, that is connected with the first capacitor and the other terminal is connected to the ground.

A rigorous design is necessary for these sensors considering the safety aspects regarding to the technician activities and to some environmental effects that can influence their performance, such as, temperature, pressure and wind. Besides, it should be taken into account that the external elements in the proximities of the sensors can alter the electrical and magnetic field acting inside of them.

The current sensor for power quality measurements was not evaluated in this work since its operation is different from the voltage sensor and in general it does not affect the insulation properties of the power quality sensor. Traditional devices used as current sensor are current transformer or Rogowski coil [11], and they are connected direct to the MV conductor without ground connection.

This chapter is organized as follows. Section 2 describes the physical structure of the sensor studied in this work. Section 3 describes the analytical modeling of the sensor. Section 4 describes the finite-element method (FEM) review mainly focused in simulation of an electrostatic field and the sensor. In addition in this section it is presented the sensor simulation validation. Finally, Section 5 presents the conclusions.

## 2. Voltage sensor for power quality applications

The proposed case study was the modeling of a current and voltage sensor for MV applications to be applied in live lines for the evaluation of energy quality.

According to **Figure 1**, a capacitive divider represented by $C_1$ and $C_2$ (F) provides the voltage measurement. The capacitor $C_1$ is a commercial capacitor used in electronic applications and is placed in an electronic board of the sensor. $C_2$ is a capacitor formed by an electrode and a grounded pipe isolated by an insulation material (such as polymer, ceramic, glass or oil-impregnated paper) where a high-intensity electric field remains concentrated. To meet accuracy of less than 0.5% in the voltage measurements, it is necessary to connect the LV terminal of the sensor to the ground. Thus, it is not possible to use the parasitic capacitance as the $C_2$

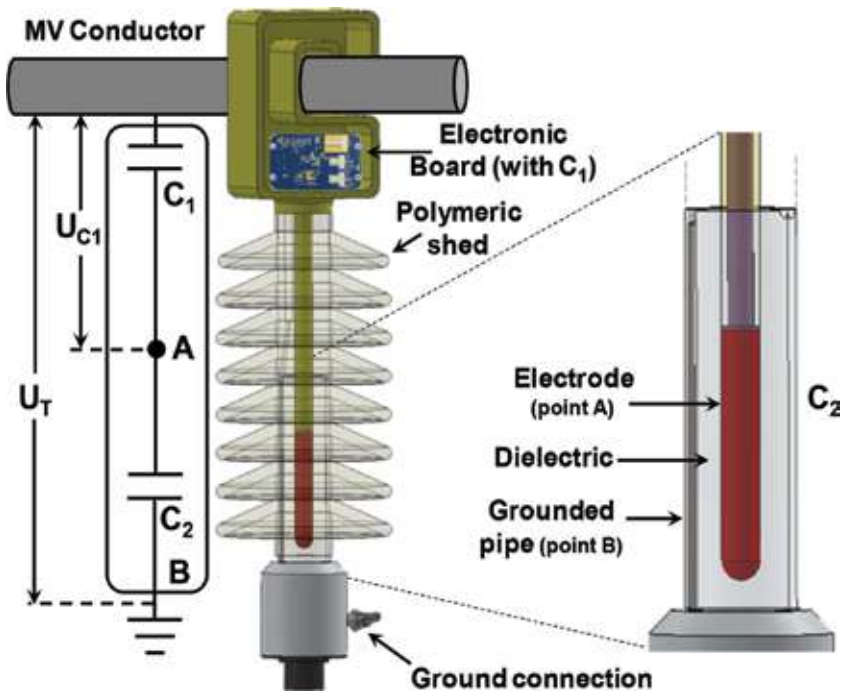


**Figure 1.** The voltage sensor for power quality applications. In the right is shown the elements that create the capacitance $C_2$.

capacitor. The capacitive divider is designed in such way that $C_2$ retains practically the totally line voltage. The voltage on $C_1$ measured by the sensor is defined by:

$$U_{C_1} = U_T \frac{C_2}{(C_1 + C_2)} \approx U_T \frac{C_2}{C_1} \tag{1}$$

where $U_T$ (V) is the total voltage. The approximation in Eq. (1) is valid when $C_1 \gg C_2$.

The maximum voltage concentrated in $C_1$ is around 5 V. The line voltage in MV can be 1 or 35 kV according [12]. Examples of voltage classifications between these values are: 4.16, 12.47, 13.2, 13.8, 24.94 and 34.5 kV.

The $C_2$ design must meet some important requirements, such as, adequate dielectric strength to support pulse voltage up to 100 kV [13], homogeneous field electric around the electrode and absence of air bubbles near the electrode interface in order to reduce the growing of partial discharges in the sensor [14]. The growing of partial discharges in the insulation due to electric field concentration in a specific place and over time causes premature aging and breakdown of insulation systems [15–19].

The dimensions of the sensor and characteristics of the insulation material will be described in Section 3.

## 3. Capacitive analytical modeling for power quality sensor

The basic reference structure adopted for the voltage sensor is composed of two coaxial cylinders terminated in hemispheres, as shown in **Figure 2**. This type of geometry simplifies the practical construction of $C_2$ and allows the creation of an analytical model. The internal electrode is at line potential ($U$) and the external electrode is in the earth potential (0 V). The internal and external electrode radii are, respectively, $a$ (mm) and $b$ (mm), the electrical permittivity of the medium is $\varepsilon$ and the cylinder length is $L$ (mm). It should be noted that there is no region of electric flux dispersion through the upper horizontal line due to the presence of a guard's electrode not shown in the figure. This figure also shows an equipotential line defined by the distance $x$ whose origin is the longitudinal axis of the cylinders. The equipotential line has a value exact in the region between the cylinders because the electric field in this region is constant and uniform while the equipotential in the hemispheres region has a value approximated because the electric field is non-uniform. As shown in [20], the equipotential surface tends toward a hemisphere and by heuristic approach this is a good approximation.

The analytical study demonstrates the optimum relation between the radii of the cylinders. The electric field is radial and is given by [21]:

$$E(x) = \frac{q}{2\pi L x \varepsilon} \tag{2}$$

where $q$ (C) is the charge on the cylindrical part of the central electrode. The integral of the electric field between the electrodes provides the voltage $U$ between them, i.e.:

http://dx.doi.org/10.5772/intechopen.77187

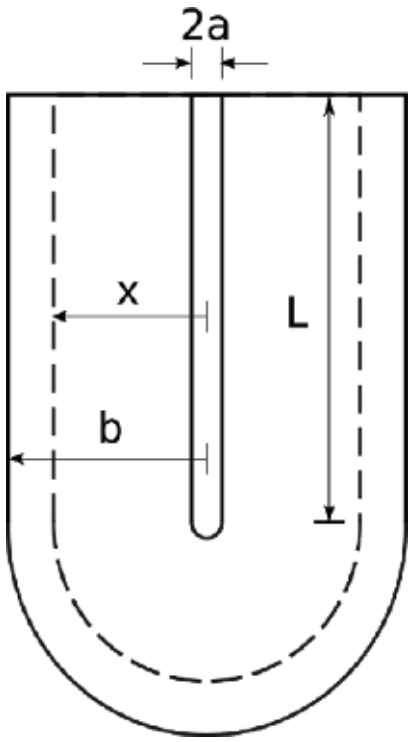


**Figure 2.** Structure of voltage sensor and equipotential surface. Dimension of geometric parameters in millimeters.

$$U = \int_a^b E(x)dx = \frac{q}{2\pi L\varepsilon}\ln\left(\frac{b}{a}\right) \tag{3}$$

Substituting $q$ from Eq. (3) into Eq. (2) leads to:

$$E(x) = \frac{U}{\ln\left(\frac{b}{a}\right)}\frac{1}{x} \tag{4}$$

where, substituting $x$ to $a$, being $a \ll b$, it is evident that the maximum value of the electric field occurs on the surface of the internal electrode. This maximum field value is given by [22]:

$$E_{max} = \frac{U}{\ln\left(\frac{b}{a}\right)}\frac{1}{a} \tag{5}$$

It is emphasized that the maximum value of the electric field is of interest in the design of the sensor, since it determines the beginning of the insulation rupture process through the dielectric. An analysis of Eq. (5) shows that this maximum field tends to infinity for the boundary conditions $a \to 0$ and $a \to b$. The first case refers to an extremely fine internal electrode, where the electric field on its surface is extremely high. The second case tends to an infinitesimal distance between the electrodes, which has to withstand voltage, . Therefore, it is clear that there is at least one minimum region between these two conditions, which is the optimal condition for

the design of the sensor. Given $b$, the minimum value of $E_{max}(a)$ can be obtained by differentiating the maximum field with respect to $a$ and making this result equal to zero:

$$\frac{dE_{max}(a)}{da} = 0 \tag{6}$$

what provides the optimal condition:

$$\frac{b}{a} = e \tag{7}$$

where $e = 2.718$ is the basis of natural logarithms. Therefore, the dimensioning of the electrodes should be such that the ratio of the radii of the internal and external electrode obeys the Eq. (7). Taking the condition of Eq. (7) into Eq. (5) it is obtained:

$$E_{max} = \frac{U}{a} \tag{8}$$

**Figure 3** shows the behavior of the maximum electric field for an external electrode of $b = 50\ mm$ of radius and different radii for the internal electrode when a voltage of 100 kV is applied between the electrodes. It is observed that the minimum region is obtained by Eq. (7), where $a = 18.4\ mm$. It is also noted in **Figure 3** that the electric field variation around the minimum value is very small, such as small variations around the optimum relation expressed in Eq. (7) do not compromise the design. It should be noted that the critical region for the rupture of the dielectric occurs in the hemispheric region, however this region can be

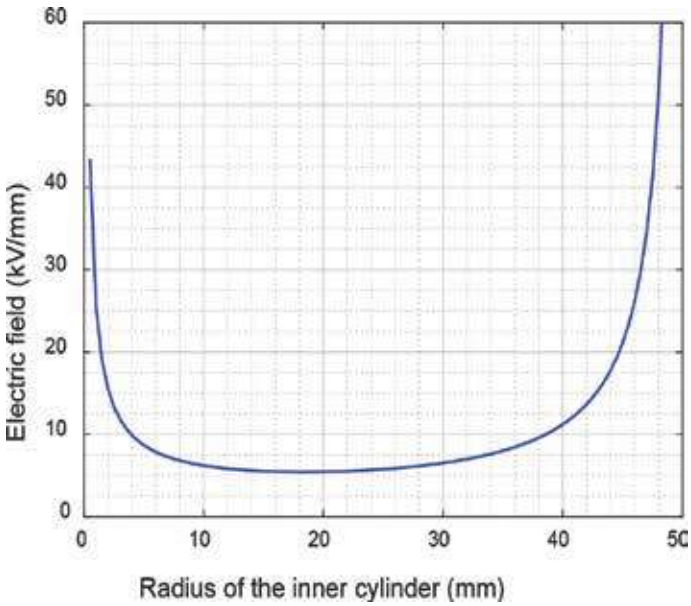


**Figure 3.** Electrical field on the surface of the internal electrode (0 < a < b), for $b = 50\ mm$ and $U_T = 100\ kV$.

elongated, increase the radius of the center electrode, tending to a revolution ellipsoid in an attempt to reduce the electric field at the electrode surface. These variations could be evaluated through COMSOL Multiphysics software.

As discussed earlier, the hemispheric region may be modified in order to attenuate the electric field at the tip surface of the central electrode. However, this makes analytical modeling difficult, and therefore the numerical calculations become necessary. For the purpose of analytical calculations, the hemispheric configuration for the electrodes (internal and external) is assumed, according to **Figure 2**. In the region between the hemispheres, the electric field is radial and could be described as follows:

$$E(x) = \frac{q_h}{2\pi x^2 \varepsilon} \tag{9}$$

where $q_h$ (C) is the charge on the hemispheric part of the central electrode. The integral of the electric field between the electrodes provides the voltage between them:

$$U = \int_a^b E(x)dx = \frac{q_h}{2\pi\varepsilon}\left(\frac{1}{a} - \frac{1}{b}\right) \tag{10}$$

Substituting $q_h$ from Eq. (10) into Eq. (9) gives:

$$E(x) = \frac{Uab}{(b-a)}\frac{1}{x^2} \tag{11}$$

In a similar way to the case of the cylinder, the maximum field occurs on the surface of the electrode:

$$E_{max} = \frac{Ub}{a(b-a)} \tag{12}$$

Differentiating Eq. (6) with respect to $a$ and making this result equal to zero, the minimum of this function occurs for the condition:

$$b = 2a \tag{13}$$

**Figure 4** shows the electric field on the surfaces of the cylinder and the hemisphere, for different values of the $a/b$ ratio. It is observed that the minimum field of the hemisphere occurs for $a/b = 0.5$ as showed by Eq. (13). The modification of the cylinder termination, passing from a flat half ellipsoid of revolution to a hemisphere and to a stretched half ellipsoid of revolution, aims to optimize the electric field on this region considering the cylindrical region as a reference. This can be done taken into account Equation 7. The dimensions of the ellipsoid could be obtained through FEM developed in the COMSOL Multiphysics software.

The capacitance between the electrodes can be easily calculated by integrating the electric flux along the spatial surface defined in **Figure 3** resulting in:

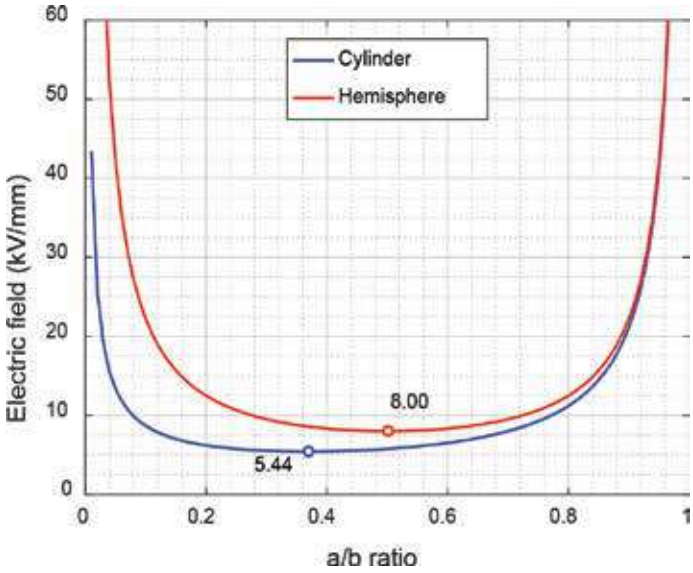


**Figure 4.** Electric field on the surface of the internal electrode, for $b = 50\ mm$ and $U = 100\ kV$. The marks indicate minimum values on the surfaces of the cylinder and the hemisphere, for different values of the a/b ratio.

$$C = 2\pi\varepsilon\left[\frac{L}{\ln\left(\frac{b}{a}\right)} + \frac{ab}{(b-a)}\right] \tag{14}$$

By inserting the condition of Eq. (7) into Eq. (14) one obtains:

$$C = 2\pi\varepsilon\left[L + \frac{ae}{(e-1)}\right] \tag{15}$$

This can also be expressed as:

$$C = 0.0556\varepsilon_r[L + 1.58a] \tag{16}$$

where $\varepsilon_r$ is the relative permittivity of the medium and the capacitance $C$ is obtained in pF for $L$ and $a$ in millimeters. For example, considering $\varepsilon_r = 3.8$ (acetal, dielectric strength >50 kV/mm, DIN 53481 [23]), $L = 50\ mm$, and $a = 18.4\ mm$ ($b = 50\ mm$), $C = 16.7\ pF$ is obtained.

It is observed that the minimum field of the hemisphere occurs for a/b = 0.5.

## 4. FEM review and simulation validation

FEM is based on the solution of a boundary value problem composed of a governing equation and boundary conditions. The main idea behind this method is the division of the domain of interest in subdomains known as elements and the adoption of shape functions for the

unknown variables, which are only solved for the nodes (element corners). Thus, instead of solving an analytical equation, these unknowns are determined by a set of algebraic equations and the results for regions other than the nodes can be obtained by interpolation. Proper domain discretization is crucial to ensure the accuracy of results since the mesh format must adequately reproduce the original geometry of the structure. An example of domain discretization can be seen in **Figure 5**.

This procedure reduces the generality of the mathematical framework, but enables the study of components of complex geometry. Many real world study cases involve the analysis of such problems, which are virtually impossible to be done by analytical methods.

A succinct overview of FEM for the simulation of an electrostatic field is presented next considering a stationary solving method since the voltage boundary condition chosen has a constant value. A more detailed explanation can be found in [24–28]. The voltage distribution in a dielectric of arbitrary geometry is described by the following differential equation:

$$\nabla\cdot(\varepsilon_0\varepsilon_r\boldsymbol{E}) = \rho_v \tag{17}$$

where $\varepsilon_0 = 8.85419 \times 10^{-12}\ F/m$, $\varepsilon_r$ is the relative permittivity, $\boldsymbol{E}$ (kV/mm) is the electric field and $\rho_v$ (C/m$^3$) is the free charge density. The relation between electric field and the voltage $U$ is defined as:

$$-\nabla U = \boldsymbol{E} \tag{18}$$

Substituting Eq. (18) into Eq. (17) and considering a homogenous dielectric with $\rho_v = 0$ results in the Laplace's equation:

$$\nabla\cdot\nabla U = 0 \tag{19}$$

Eq. (19) has to be transformed into an energy functional form that relates directly to the energy of the system in order to be used in FEM. This function can be written for an element $\alpha$ as:

$$F_\alpha = \int_\alpha \frac{1}{2}\varepsilon_0\varepsilon_r E^2 d\alpha \tag{20}$$

with units of V$^2$/m$^2$ for a one-dimensional domain, for example.

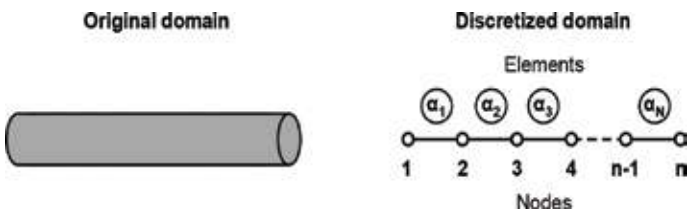


**Figure 5.** Example of one-dimensional domain discretization.

The function gives the voltage distribution that satisfies the governing partial equation when differentiated with respected to $U$ and equaled to zero. Thus, the change in the global function due to the change in the voltage of node $i$ is:

$$\frac{\partial F}{\partial U_i} = \sum_{\alpha} \frac{\partial F_\alpha}{\partial U_i} \tag{21}$$

where the summation represents the contribution from all elements associated with $U_i$ or all the elements connected to node $i$. These derivatives are equaled to zero resulting in a group of simultaneous equations arranged in matrix form as:

$$[S_t]\{U_i\} = 0 \tag{22}$$

where $[S_t]_{n\times n}$ is the stiffness matrix whose terms are defined by geometric parameters of the nodes and material properties. $\{U_i\}_{n\times 1}$ is a column matrix of voltages, which are the unknowns to be solved. Additionally, the boundary values of voltage associated to some of the nodes are applied to this matrix. After the determination of the voltage distribution, the electric field can be obtained by numerically solving Eq. (18).

As it can be noticed, the assumptions made in the original analytical problem for the FEM strongly affect the results. Thereby, the results provided by the simulation have to be validated to ensure their accuracy. To do so, these results are compared to the ones of an analytical model derived for specific conditions as previously presented. Analytical results of electric field from Eqs. (4) and (11) are taken for, respectively, the cylindrical and hemispheric regions as references for the simulation whose parameters of interest are the order of the shape functions and the mesh refinement.

It is worth to mention that the dielectric geometry has a longitudinal axis-symmetry, which implies that the unknown values do not change along the azimuthal axis and thus only a transversal plan needs to be modeled in FEM and the rest of the solution can be extrapolated. **Figure 6** shows the structure modeled around its axis of symmetry for $a = 18.4\ mm$ (inner radius) and $b = 50\ mm$ (outer radius) in both cylindrical and hemispheric regions. Additionally, voltage boundary conditions were the same as the ones used for the analytical model. Electric field values were extracted along paths $P_1$-$P_2$ and $P_3$-$P_4$, respectively, in the cylindrical and hemispheric regions.

As a default, COMSOL uses a second order shape function in order to improve the results' accuracy. This choice seems to be adequate as the analytical results showed that the radial variation of the electric field fallows a quadratic pattern. However, a mesh convergence study is still needed in order to minimize domain discretization effects on the results. In this procedure, the mesh is successively refined and the values of interest are compared to a reference. **Figure 7** shows the meshes evaluated.

**Figures 8** and **9** show the comparison of analytical results given by Eqs. (4) and (11) with numerical results for three mesh refinements using quadratic shape functions, respectively, for the cylindrical and hemispheric regions. The electric field results obtained by the simulations presented good agreement with the analytical results indicating that quadratic shape functions

http://dx.doi.org/10.5772/intechopen.77187

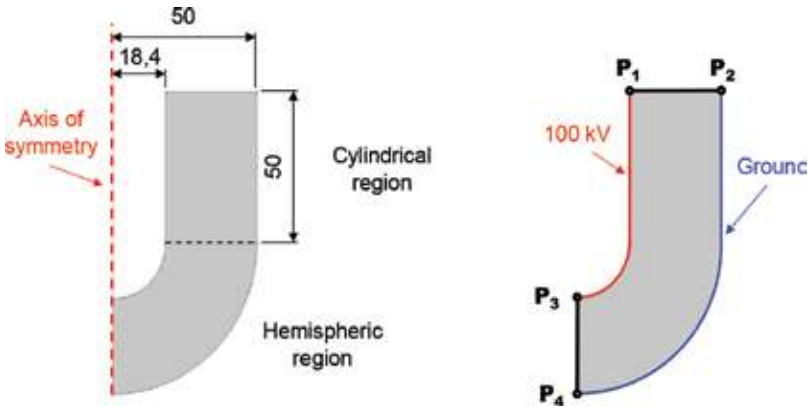


**Figure 6.** Voltage sensor modeled considering its axis of symmetry, voltage boundary conditions and paths of interest for the validation (dimensions in millimeters).

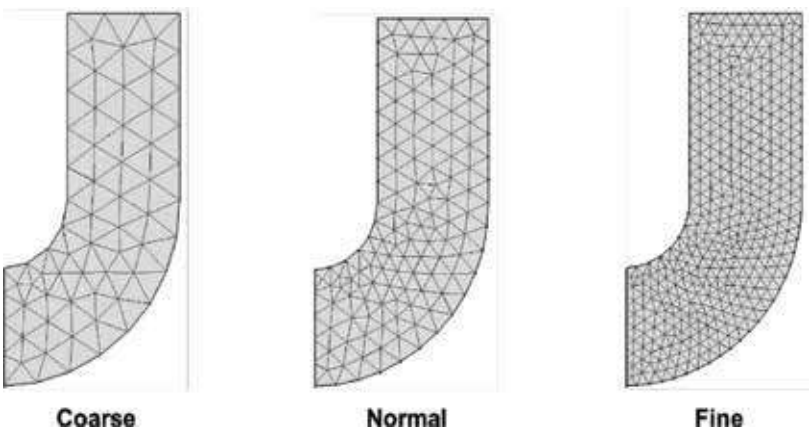


**Figure 7.** Meshes used for the mesh convergence study.

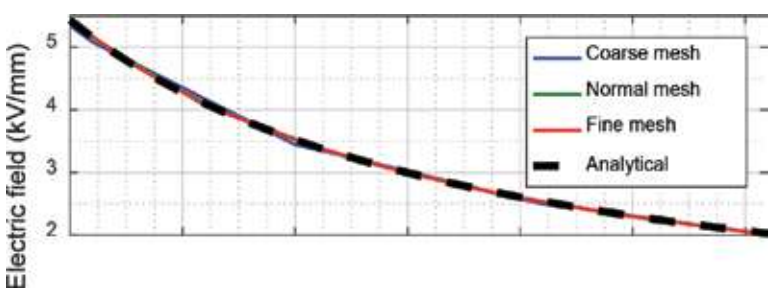


**Figure 8.** Cylindrical region—comparison of analytical and numerical electric fields for mesh selection.

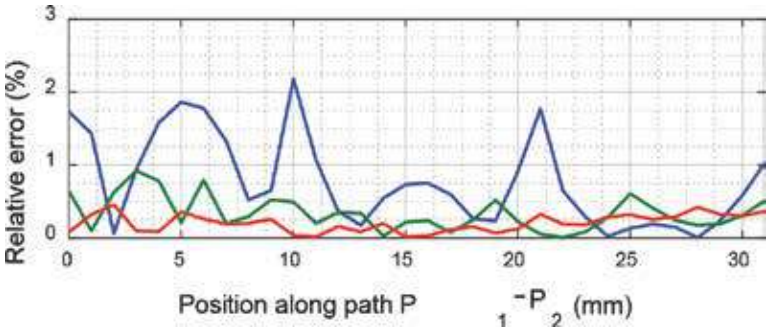


**Figure 9.** Hemispheric region—comparison of analytical and numerical electric fields for mesh selection.

| Numerical (pF) | | Analytical (pF) | Difference (%) |
|---|---|---|---|
| Coarse mesh | 16.812 | | 0.500 |
| Normal mesh | 16.810 | 16.728 | 0.488 |
| Fine mesh | 16.809 | | 0.482 |

**Table 1.** Analytical and numerical capacitance values.

are indeed a good choice. In addition, it can be seen that mesh refinement led to a better solution field as the relative error computed using the analytical values as reference decreased. Besides, the duration of the simulations for the three cases did not increase significantly with the last case taking about 1 s. The computer used was a workstation with an Intel(R) Core™ i7–4790 3.60 GHz CPU and 16 GB of RAM.

Finally, another way to validate the simulations is to compute capacitance values from the simulations by numerical integration of the electrical flux along the inner surface in which 100 kV was applied. These values are compared with the analytical one described by Eq. (14) as shown in **Table 1**.

Since the model related to the fine mesh provided electric field distributions that best agreed with the analytical results in both cylindrical and hemispheric regions of the voltage sensor, and get a capacitance value that closest matched with Eq. (14), this model was successfully validated and will be used in the case study presented below.

## 5. A case study using COMSOL

As explained in Section 3, the modification of the cylinder termination of the central electrode, passing from a flat half ellipsoid of revolution to a stretched half ellipsoid of revolution, aims to optimize the electric field on this region. Therefore, the optimum geometry of the ellipsoid could be obtained through a parametric study, as shown in **Figure 10**. Varying only the vertical semi-axis ($v$) and setting the horizontal semi-axis ($h$) constant, the geometry of the cylinder

http://dx.doi.org/10.5772/intechopen.77187

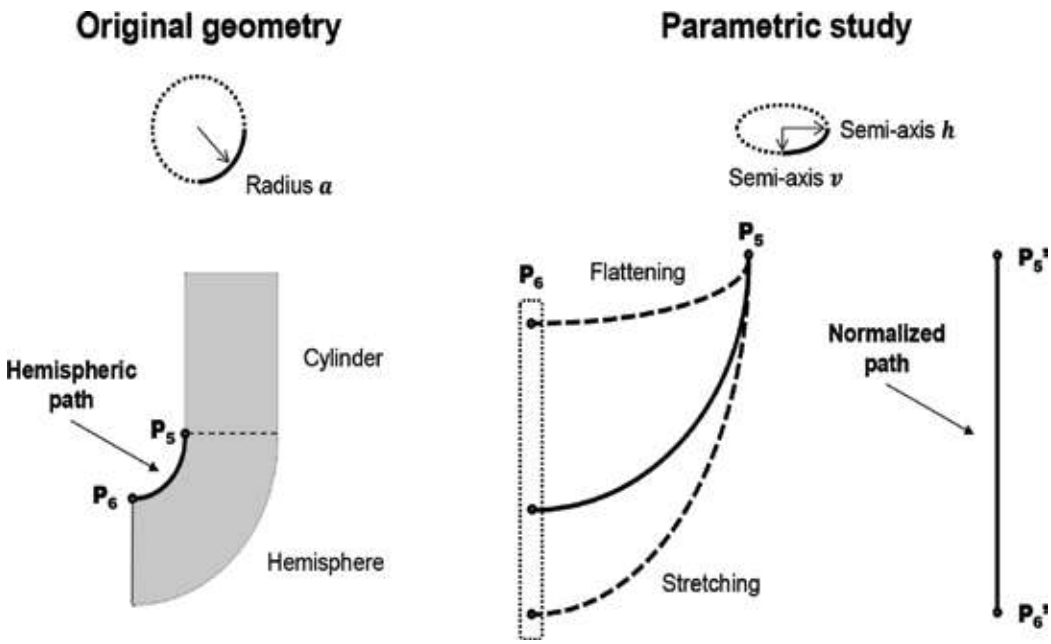


**Figure 10.** Illustration of parametric study based on the geometric modification of the hemispheric region.

termination shall change from a flat geometry up to a stretched geometry between points $P_5$ (region next to transition from cylindrical region to the elliptic region) and $P_6$ (region at the tip of centre electrode).

From the simulation of the electric field for different values of semi-axis $v$, it is verified that for small values of semi-axis $v$, the electric field is more concentrated on the edges and assumes large values in the transition region from cylinder region to elliptic region presenting irregular distribution, as shown in **Figure 11**. Similarly, an irregular distribution is observed for large values of semi-axis $v$, but with more concentration of electric field at the tip of the central electrode. On the other hand, for values of semi-axis $v$ near the hemispheric geometry of radius $a$, a better electric field distribution for the entire surface is observed with a minimum concentration. This result shows that the investigation for the optimum condition should be concentrated around the hemispheric geometry.

To do so, a normalized path between points $P_5'$ and F′ is used in order to provide a better visualization for the distribution of electric field norm for different geometries of the central electrode, as shown in **Figure 10**. As an illustration of this procedure, considering two distinct geometries having different lengths and shapes of original paths $P_5$-$P_6$, such as the flat and stretched cases of **Figure 11**, their electric filed can be directly compared thought the path normalization proposed. This is performed in **Figure 12** where the flat geometry shows an electric field concentration close to point $P_5'$ while for the stretched geometry the concentration is observed at the tip (point $P_6'$), as expected. Additionally, the hemispheric geometry produces a small electric field norm variation along the trajectory between points $P_5'$ and $P_6'$. This

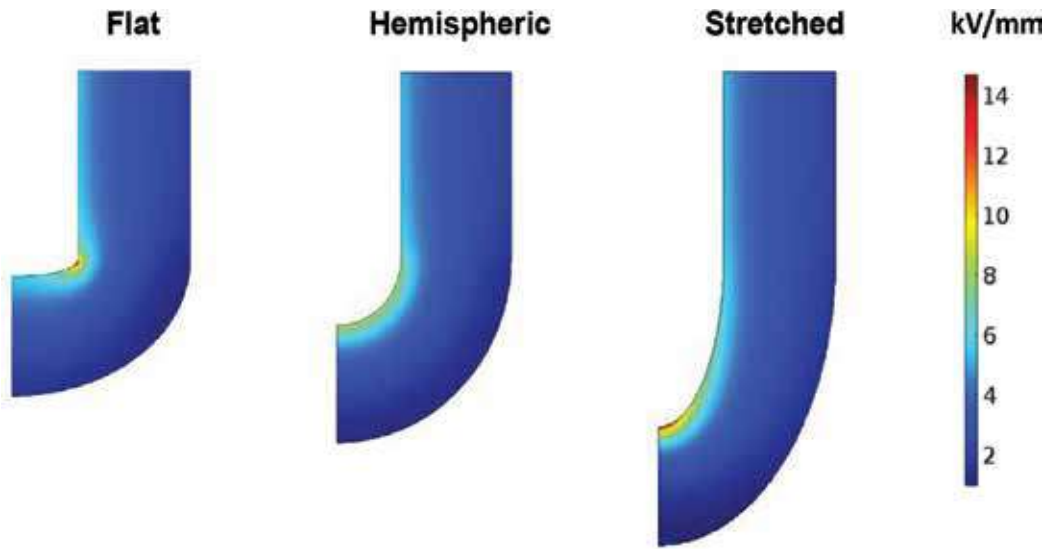


**Figure 11.** Electric field distribution for three geometries.

emphasizes that the best geometry for the central electrode in terms of electric field distribution must be close to the hemispheric geometry.

Therefore, this work has been focused on parametric studies around the hemispheric geometry with variations in the value of the semi-axis $v$ of the central electrode. Eleven cases were simulated with a step of 0.2 mm being five cases below 18.5 mm (tip flattening) and five cases above 18.5 mm (tip stretching), as shown in **Figure 13**. It is important to note the effect of geometric modification on electric field norm along normalized path $P_5'$-$P_6'$. As an example, the response curve for the flattening geometry has bigger values of electric field close to the point $P_5'$ and lower values close to the point $P_6'$. Also, these curves indicate the existence of a case whose maximum electric field value along E′-F′ path is the smaller one among the other curves, making it a candidate for the optimum condition.

**Figure 14** presents the maximum electric field norm along the normalized path $P_5'$-$P_6'$ for each case presented in **Figure 13**. The existence of an optimum condition is evidenced by the trend in the results provided by the simulated cases. The exact value of the semi-axis $v$ for this optimum condition is obtained through interpolation, leading to an optimum *value* of 17.5 mm.

A new parametric study was performed in order to confirm the best condition found. Three cases around the optimum semi-axis $v$ of 17.5 mm were simulated with a smaller step of 0.1 mm. **Figure 15** shows these results indicating that the solution for $v = 17.5\ mm$ is indeed the optimum solution since it ensures the lowest electric field norm when the whole normalized path $P_5'$-$P_6'$ is considered. Another form of analysis is to compute a relative percent difference taking the electric filed norm from the cylindrical region, which is constant for any modifications in the geometry of the hemispheric region, as a reference (5.447 kV/mm). As it

http://dx.doi.org/10.5772/intechopen.77187

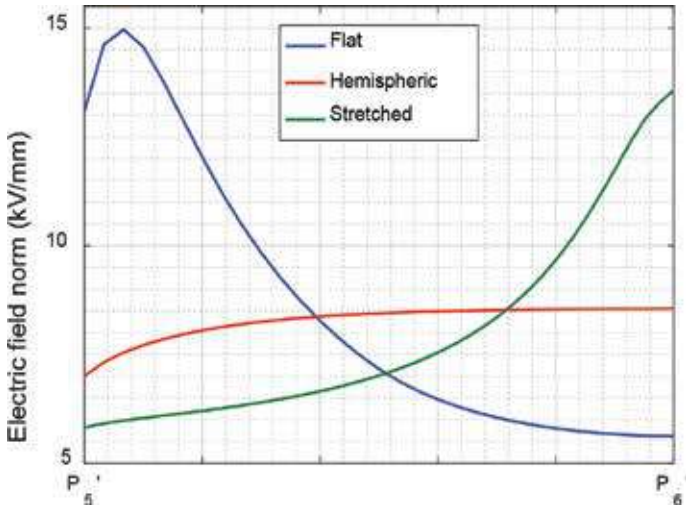


**Figure 12.** Electric field norm along normalized path $P_5'$-$P_6'$ for three geometries.

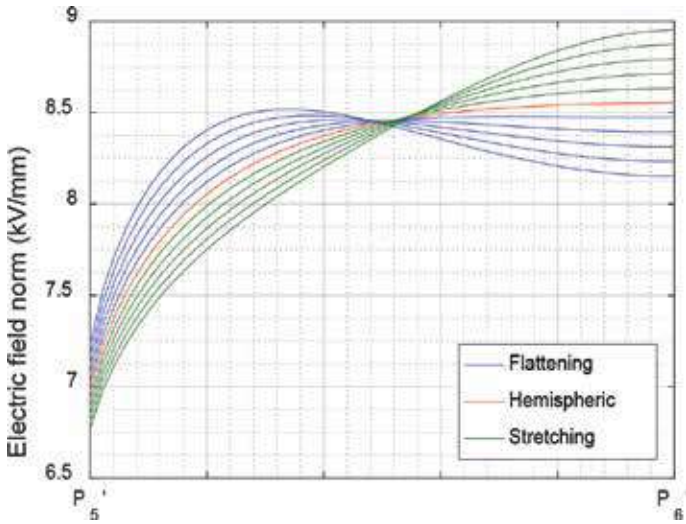


**Figure 13.** Effect of tip deformation on electric field norm along normalized path $P_5'$-$P_6'$.

can be seen, again the optimum condition curve presents smaller values than the other curves when the whole normalized path $P_5'$-$P_6'$ is considered.

This conclusion is supported by an extension of the last parametric study, as shown in the **Figure 16**, where 21 different values around 17.5 mm with a step of 0.1 mm for the semi-axis $v$ were computed. The relative difference metric was calculated for the maximum value of each electric field norm distribution evidencing the optimum condition of 17.5 mm, as expected.

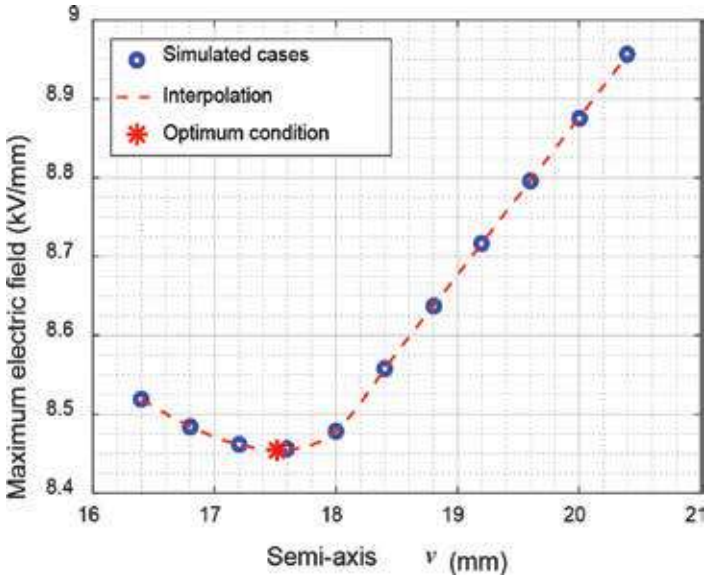


**Figure 14.** Interpolation of results for optimum condition.

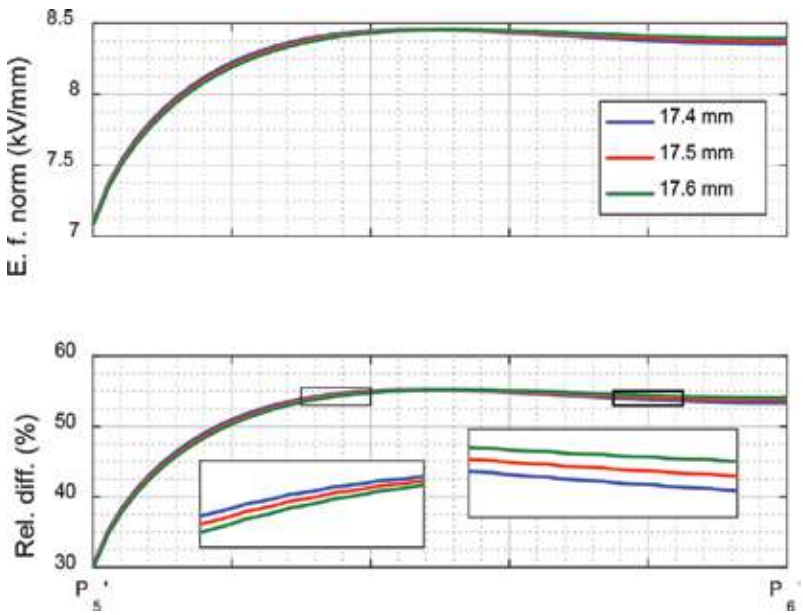


**Figure 15.** Electric field norm and relative difference metric along normalized path $P_5'$-$P_6'$ for optimum condition verification.

http://dx.doi.org/10.5772/intechopen.77187

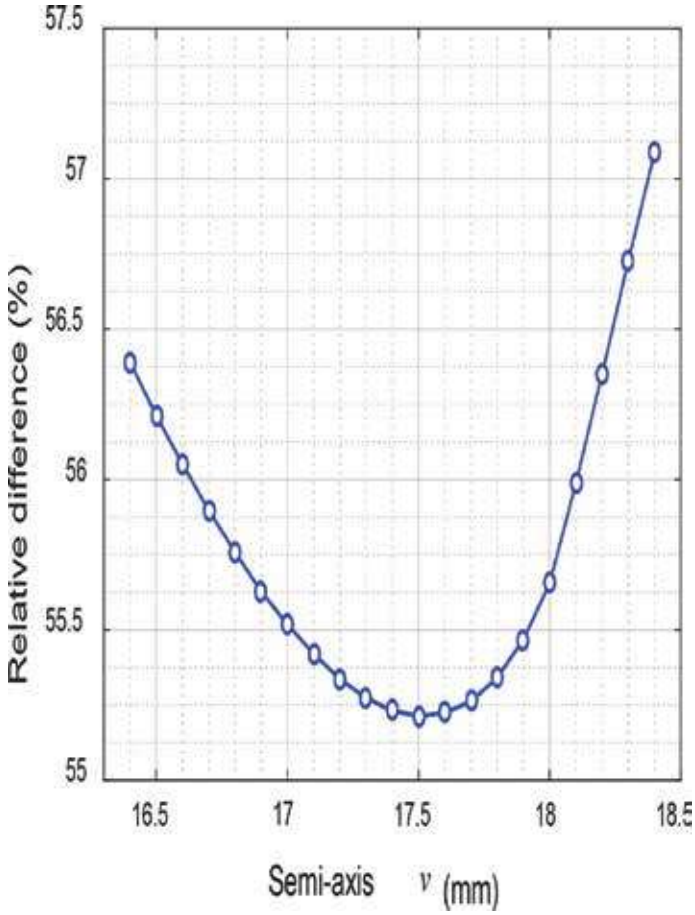


**Figure 16.** Relative difference of maximum electric field norm considering cylindrical region as reference.

Another conclusion is that, for this optimum geometry, a reduction of approximately 1.5% in the maximum electric field is achieved when compared to the hemispheric geometry. This improvement is strategic to ensure the safe operation of the sensor since partial discharge is a localized phenomenon influenced by electric field concentration. In a real scenario, because of imperfections in the dielectric due to the manufacturing process, such as air bubbles, a lightning impulse of 100 kV can lead to local discharges in points of high-electric field concentration, which will cause the failure of the sensor.

Finally, **Figure 17** shows the $C_2$ capacitance variation for a wide-range of values of semi-axis $v$ covering the geometries presented in **Figure 11**. It is possible to see that the value of $C_2$ for the optimum condition is very close to the ones shown in **Table 1** since the geometry of the optimum condition is very close to a hemisphere. In addition, the range of capacitance values obtained is compatible to the design of the capacitive divider.

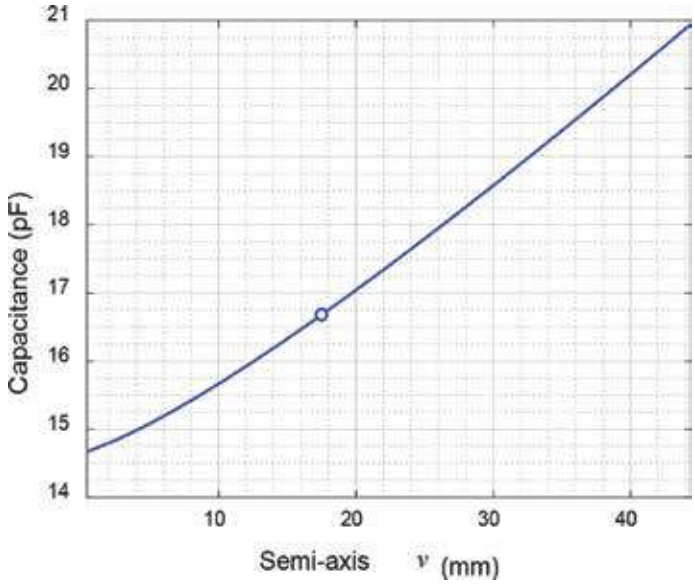


**Figure 17.** Capacitance values $C_2$ for different values of semi-axis $v$. The mark indicates optimized electric field condition.

## 6. Conclusion

A rigorous capacitor design is necessary for MV sensors when capacitive divider is used to obtain a voltage sample. This is due to safety aspects regarding to the technician activities and some environmental effects that can influence their performance, such as temperature, pressure and wind. In addition, external elements in the vicinity of the sensor can alter the electric field acting inside of it.

The basic structure adopted for the voltage sensor is composed of two-coaxial cylinders terminated in a hemisphere, which simplifies the practical construction of the capacitor. Although, this work demonstrated that the geometry of the electrode termination should be different of a hemisphere in order to minimize the electric field distribution in this region.

This conclusion was based in finite-element studies developed in COMSOL software. The first one, considered a hemispheric electrode termination of 18.4 mm of radius and was compared to an analytical model for validation purposes. Next, a parametric study was developed, in which the termination was changed from a flat to a stretched geometry, to obtain the optimum condition. The electric field distribution along the termination for this condition was compared to a reference value extracted from the cylindrical region (5.447 kV/mm). The result is that the optimum geometry is slightly flatter than a hemisphere having a semi-axis $v$ equals 17.5 mm.

Additionally, the electric field distributions of the optimum and the hemispheric geometries were compared evidencing a magnitude reduction of approximately 1.5%. This improvement is strategic to ensure the safe operation of the sensor since partial discharge is a localized phenomenon influenced by electric field concentration. In a real scenario, because of

imperfections in the dielectric due to manufacturing process imprecision, such as air bubbles, a lightning impulse of 100 kV can lead to local discharges in points of high electric field concentration, which will cause the failure of the sensor.

## Acknowledgements

The authors wish to thank their colleague Celio Fonseca Barbosa.

This work was funded by FINEP (Brazilian Innovation Agency) grant number 0115002800 0407/14.

CNPq (National Counsel of Technological and Scientific Development) sponsors the author Joao B. Rosolem under scholarship DT.

## Conflict of interest

The authors declare no conflict of interest.

## Author details

Sender Rocha dos Santos, Rodrigo Peres, Wagner Francisco Rezende Cano and Joao Batista Rosolem*

*Address all correspondence to: rosolem@cpqd.com.br

CPqD – Research and Development Center in Telecommunications, Campinas, SP, Brazil

## References

[1] Colak I. Introduction to smart grid. In: Proceedings of the International Smart Grid Workshop and Certificate Program (ISGWCP); Istanbul; 2016. pp. 1-5. DOI: 10.1109/ISGWCP.2016.7548265

[2] Parker DM, McCollough ND. Medium-voltage sensors for the smart grid: Lessons learned. In: Proceedings of the IEEE Power and Energy Society General Meeting; San Diego; 2011. pp. 1-7. DOI: 10.1109/PES.2011.6039775

[3] International Electrotechnical Commission. IEC 61000-4-30:2015 - Electromagnetic Compatibility (EMC)—Part 4-30: Testing and AQ01 25 Measurement Techniques - Power Quality Measurement Methods. Geneva, Switzerland; 2015

[4] International Electrotechnical Commission. IEC 61000-4-7:2002+AMD1:2008 CSV-Electromagnetic Compatibility (EMC)—Part 4-7: Testing and Measurement Techniques—General Guide on Harmonics and Interharmonics Measurements and Instrumentation, for Power Supply Systems and Equipment Connected Thereto. Geneva, Switzerland; 2008

[5] Lim Y, Kim H-M, Kang S. A design of wireless sensor networks for a power quality monitoring system. Sensors. 2010;**10**:9712-9725. DOI: 10.3390/s101109712

[6] Zavoda F, Yakymyshyn C. Sensors for smart grids. In: Proceedings of the Third International Conference on Smart Grids, Green Communications and IT Energy-Aware Technologies (ENERGY 2013); Lisbon; 24–29 March 2013. pp. 83-88

[7] DeMaria L, Pistoni NC. An optical approach for monitoring electrical parameters in a distribution network. In: Proceedings of the XVIII AISEM Annual Conference: Trento; 2015. pp. 1-4. DOI: 10.1109/AISEM.2015.7066792

[8] Štefanka M. Application of sensors and digitalization based on IEC 61850 in medium voltage networks and switchgears [thesis]. Brno: Brno University of Technology, Faculty of Electrical Engineering and Communication; 2016

[9] Aurilio G, Crotti G, Gallo D, Giordano D, Landi C, Luiso M. MV divider with fiber optic insulation. In: Proceedings of the IEEE International Workshop on Applied Measurements for Power Systems (AMPS); Aachen; 2013. pp. 1-6. DOI: 10.1109/AMPS.2013.6656216

[10] Sevlian R, Rajagopal R. Actively calibrated line mountable capacitive voltage transducer for power systems applications. IEEE Transactions on Smart Grid. 2016;**99**:1-1. DOI: 10.1109/TSG.2016.2643636

[11] Moreno MVR, Robles G, Albarracín R, Rey JA, Tarifa JMM. Study on the self-integration of a Rogowski coil used in the measurement of partial discharges pulses. Electrical Engineering. 2016;**99**:1-10

[12] International Electrotechnical Commission. IEC 60038:2009 – IEC Standard Voltages. Geneva, Switzerland; 2009

[13] International Electrotechnical Commission. High Voltage Test Techniques—Part I: General Definitions and Test Requirements. Geneva, Switzerland; 2010

[14] Siada AA. Power Transformer Condition Monitoring and Diagnosis. Chapter 2: Power Transformer Condition Monitoring and Diagnosis: Concepts and Challenges. Albarracín R, Robles G, Ardila-Rey JA, Cavallini A, Passaglia R. Pagination: c; 2018. 300pp. ISBN: 978-1-78561-254-1

[15] Kreuger FH. Partial Discharge Detection in High-Voltage Equipment. Oxford, UK: Butterworth-Heinemann Ltd; 1989

[16] Boggs SA. Partial discharge. III. Cavity-induced PD in solid dielectrics. Electrical Insulation Magazine IEEE. 1990;**6**(November(6)):11-16. DOI: 10.1109/57.63094 ISSN 0883-7554

[17] IEC-60270. High-Voltage Test Techniques—Partial Discharge Measurements. 3rd ed. New Delhi, India: IEC; 2000

[18] Jardine AK, Lin D, Banjevic D. A review on machinery diagnostics and prognostics implementing condition-based maintenance. Mechanical Systems and Signal Processing. 2006;**20**:1483-1510. DOI: 10.1016/j.ymssp.2005.09.012

[19] Gill P. Electrical power equipment maintenance and testing. In: Power Engineering (Willis). 2nd ed. Boca Raton, FL, USA: Taylor & Francis; 2008

[20] Barbosa CF. Horizontal electric field in the vicinity of structures hit by lightning. Atmosphere. 2016;**7**:115-130. DOI: 10.3390/atmos7090115

[21] Halliday D, Resnick R, Walker J. Fundamentals of Physics: Electromagnetism. 7th ed. Vol. 3. USA: Wiley International Edition; 2005

[22] Haque SM, Rey JAA, Masúd AA, Umar Y, Albarracín R. Electrical Properties of Different Polymeric Materials and their Applications: The Influence of Electric Field, Polymer Dielectrics Boxue Du, IntechOpen; 2017. DOI: 10.5772/67091

[23] DIN 53481. Testing of Electrical Insulating Materials; Determination of the Electrical Breakdown Voltage and Electric Strength. Berlin, Germany: German Institute for Standardization; 1974

[24] Baker AE, Preston TW, Sturgess JP. Numerical analysis of electrical fields in high voltage equipment (Energy Engineering, 2004). Advances in High Voltage Engineering, Chap. 11, pp. 511-544, IET Digital Library. DOI: 10.1049/PBPO040E_ch11

[25] Zepu W, Nelson JK, Hillborg H, Zhao S, Shadler LS. Dieletric constant and breakdown strength of polymer composites with high aspect ratio filters studied by finite element models. Composites Science and Technology. 2013;**76**:7629-7636. DOI: 10.1016/j.compscitech.2012.12.014

[26] Christen T. Nonstandard high-voltage electric insulation models. In: Proceedings of the COMSOL Conference Europe; Milan; 2012

[27] Pedersen A et al. Streamer inception and propagation models for designing air insulated power devices. In: Proceedings of the CEIDP Conference; Virginia Beach: Material; 2009. DOI: 10.1109/CEIDP.2009.5377740

[28] Christen T. Streamer inception and propagation from electric field simulations. In: Proceedings of the Scientific Computing in Electrical Engineering (SCEE); 11–14 September; Zürich; 2012

Section 4

# Insulation Aging Modelling of Power Generators

Chapter 8

# Generator Insulation-Aging On-Line Monitoring Technique Based on Fiber Optic Detecting Technology

Peter Kung

Additional information is available at the end of the chapter

http://dx.doi.org/10.5772/intechopen.78065

**Abstract**

The relationship between insulation aging and generator lifespan using fiber optic sensors (FOSs) is explored to ultimately improve asset lifespan through smart choices in running conditions and maintenance. Insulation aging is a major factor that causes generator failure. FOS provides the rare opportunity of being installed up close to the insulation, monitoring degradations that are otherwise difficult to detect. FOSs, unlike purely electrical transducers, are immune to high voltage (HV) and strong electromagnetic (EM) fields. They are small and have a proven long life by their deployment in the Telecom industry. The proposed FOS is a Fabry-Perot cavity made up of two identical fiber Bragg gratings (FBGs) using light wave interference as the working principle. Such architecture delivers simultaneous vibration (10 Hz–1 kHz) and temperature (0.1°C resolution) monitoring, both helping to spot irregular vibration patterns (signatures) and hot-spots inside the generator stator slots. The signal processing unit equipped with a gateway device can help to connect the large volume of sensor data, allowing correlation with the supervisory control and data acquisition (SCADA) system data of the plant. This chapter also elaborates on the field test jointly conducted with Calpine Corporation and Oz Optics, Ltd. (Ottawa, Ontario, Canada).

**Keywords:** hot-spot, fiber Bragg grating (FBG), Brillouin scattering, generator, vibration, Fiber optic

## 1. Introduction

Insulation aging phenomenon in air-cooled gas-fired generators is a problem confronting both original equipment manufacturers (OEMs) and owners of these competitive assets [1]. The expected life of these generators largely depends on design, manufacturing workmanship and choice of material. It also depends on the way they are used. They are used to

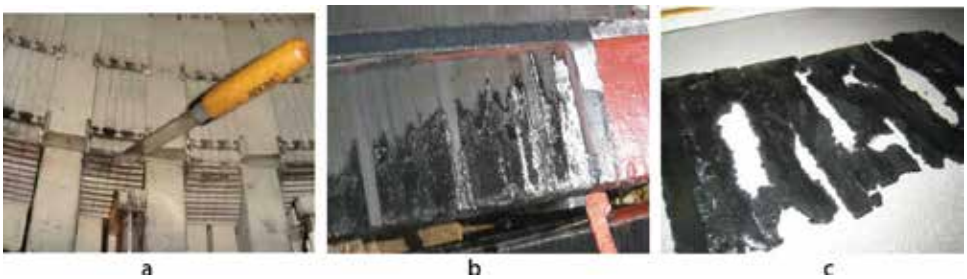


**Figure 1.** At the left, local loose core found using simple knife check. At the middle, defects start to appear as pinholes. At the right, partial discharge removes the conducting paint without affecting the underlying mica.

adapt to the intermittent nature of renewable energies, subjecting them to many start-stop cycles. Such cycles give rise to stresses and creeps from material expansion and contraction. Under constant cost reduction, pressure generators are getting less expensive and their quality also suffers. Their characteristic strong vibrations that shake the structure loose further aggravate this.

**Figure 1** (left) shows how vibration causes delamination in the core, allowing the varnish to wear out and then eddy currents to introduce hot-spots affecting the performance of the winding in the slot located close by. It becomes a downward spiral of mechanical degradation. Some of the cost reducing innovations that were previously introduced worked well in a base load operation. However, in a constant start-stop mode of operation, generators are susceptible to outage early in their life because they are air-cooled. The constant thermal cycling combined with the variable characteristics of the air contribute to early wear. They can suffer from a new failure mode called vibration sparking. This is the first time that this failure mechanism has been observed as failure in progress as shown in **Figure 1** (middle). They usually become uncovered upon a complete breakdown. A simple model that combines thermal aging and a mechanical vibration-assisted degradation process is introduced in the following sections.

Thermal aging of the insulation is often related to temperature as generators have been around for more than 100 years. The insulation material has gone through many innovative improvements [2]. A greater focus is given on the mica material and winding design that has a top layer of conductive carbon paint or conductive tape, which makes connection to the grounded stator. This is the working principle of the generator and other rotating machines such as the large industrial motors.

## 2. Insulation aging

The investigation result of generator fault event shows that the failure probability of the single generator will be increasing with the generator's capacity and applying time increasing. The investigation results show that more than 50% electrical equipment failures are caused by the insulation system [3]. How to detect generator insulation aging and degradation is of great economic and social significance. Improved reliability in power distribution affects every level of society.

### 2.1. Insulation aging reasons

For the gas-fired generator, the stator winding, which is the direct carrier that generates electricity, would sustain different kinds of combined effects in the process of operation simultaneously, such as electric, heat, mechanical and any other actions [4]. The investigation and researching results gained by many researchers, show that a series of physical and chemical changes will occur during the insulation materials operating for a long time, such as insulation medium softening, pinhole, cracking, ionization, etc. [5]. It is generally assumed that insulation aging is affected mainly by thermal cycling, heat aging, electric aging, mechanical vibration aging combined together [6].

#### *2.1.1. Heat-aging effect*

Many generator insulation materials consist of mica and epoxides. Mica and epoxides both have excellent heat resistant characteristics. The occurring rate of the aging phenomenon is slow while the generator is working under normal temperatures, and the higher the temperature of the insulating material is, the faster the heat aging. The insulation materials performance decreases with the increase of temperature. For the generator, the main reasons for the increase of insulation temperature are the resistance heat of the conductor, partial discharge, leakage current of the insulation and the heat caused by the dielectric loss. For the epoxide-mica insulation medium, there are two ways to affect the insulation performance: one is the epoxy-mica temper embrittlement and thermal degradation and another is the local defects caused by thermal expansion of the polymer [7].

#### *2.1.2. Mechanical stress effect*

The generator stator windings are nested in the mechanical supporting structure. The stator winding is generally running under mechanical stress. At the same time, there always exists vibration, which corresponds with stress. The electromagnetic force generated on the stator windings changes the rotor turning speed variation. Due to the effect of long time fluctuating mechanical force, there would produce some joint loosening and vibration. Under the action of alternating stress and vibration, the conductive carbon coating attached to insulation material would loosen and shed because of the vibration fatigue. We call it mechanical insulation aging which is caused by mechanical stress. The alternating mechanical force comes from static mechanical force, the start-stop electromagnetic force, and mechanical vibration force at running time [8]. Mechanical vibration force at running time produces as illustrated in **Figure 2**.

#### *2.1.3. Sparking effect*

The winding insulation of generators are made of epoxy & mica combined together. Due to the difference of expansion coefficient and manufacturing process, there exists some micro-gaps between materials and carbon coating, different insulation layers, under the effect of electric field, the sparking caused by partial discharge would be showing up at the micro-gap location. Due to the sparking, there are three damage types. One type is that the main insulation thickness becomes thinner because the adhesive between the coating and the insulation medium is carbonized by the high temperature in the micro-gap caused by the partial discharge. The second type is that the edges of the insulation medium and the air gap wall

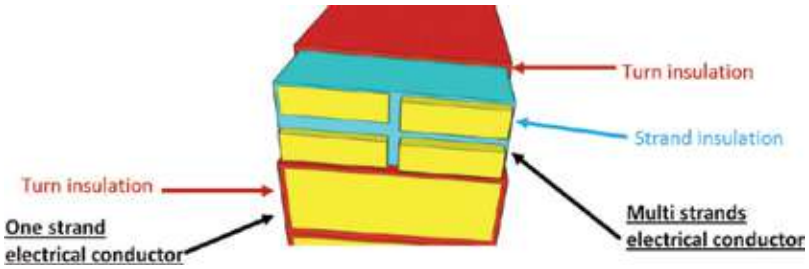


**Figure 2.** Mechanical vibration force at running time produces illustrated. Courtesy of QPS Photronics.

would appear to erode into pit and pinhole defects because of the striking by a large number of charged particles at high speed, which lead to a decline in insulation. The third type is that the discharge can produce ozone, which damages the insulation and copper conductor by combining with water, NO and $NO_2$ [9–15].

### 2.2. Gas-fired generator aging

#### *2.2.1. Insulation thermal aging*

The reliability of the insulation is dependent on the thickness of the mica layer being applied in different parts of the windings [16–18] as illustrated in **Figure 3**.

Then, a top coating of conductive layer is overlaid to complete the structure. Therefore, the full voltage will now be exercised across the insulation as depicted in **Figure 4**.

The layers are quite thick, normally free of pinholes, defects, and other imperfections. However, the material ages with time, which results in reduction of their insulation properties. Defects start to form from partial discharge (PD) occurring where the windings show traces of contamination left behind during manufacturing and handling. This phenomenon is one among other degradation processes at work.

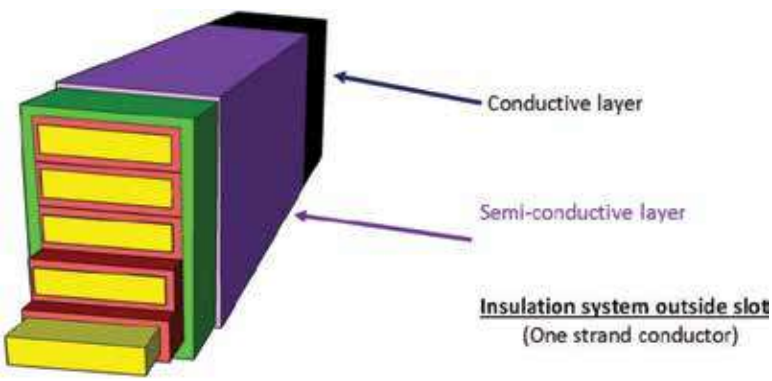


**Figure 3.** Conceptual depiction of the various insulation subdivisions. Courtesy of QPS Photronics.

http://dx.doi.org/10.5772/intechopen.78065

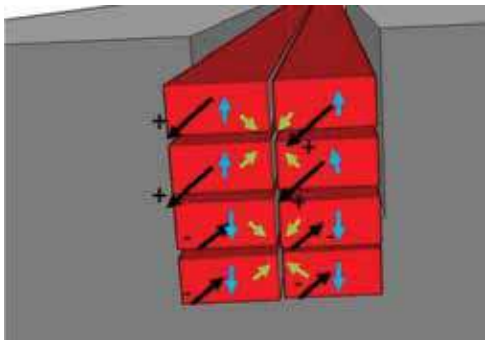

**Figure 4.** Depiction of grounded conductive outermost layer. Courtesy of QPS Photronics.

### *2.2.2. Strong vibration aging*

Vibration is an equally powerful aging mechanism. Vibration is inherent in the design structure of any rotating machine. Most generators are two-pole machines where uneven air gaps can be introduced due to misalignment, giving rise to a two-time line frequency (2xLF) nominal signature [19]. Then there is the effect of unbalancing, which gives a strong line frequency (1xLF) component. Vibration can become much stronger when the material and structure become close to a resonance mode. Excessive vibration can start rubbing the insulation, triggering shortened turns or shorts to ground. **Figure 5** shows the interactions inside a complex winding. Vibration in a generator can occur in both the radial and tangential directions.

### *2.2.3. Hot-spot vibration sparking aging*

Vibration sparking is a special process in gas-fired generators combining insulation thermal aging together with strong vibration effects [20–22]. Hot-spot measurement was performed in a random wound electric machine coil [23]. Vibration measurement was also performed

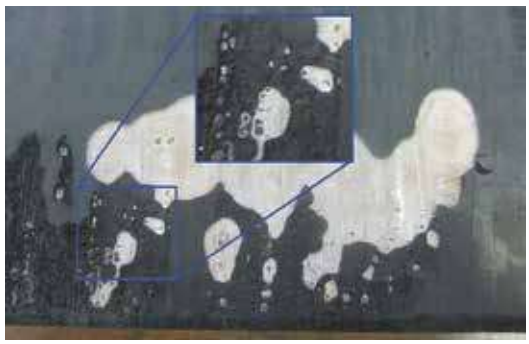

**Figure 5.** Eight strands within a stator slot interacting with each other under the effect of vibration. Courtesy of QPS Photronics.

using a wideband fiber optic vibration sensor (see [21]). For confirming the effect of vibration sparking on insulation performance, some methods were actually developed to monitor the end winding of a large power generator. For example, a simple fiber Bragg grating (FBG) have been used to measure hot-spots and they found the measured value affected by vibration of the motor (see [23]). A thin vibration sensor was developed for monitoring winding vibration inside the transformer [24] by making use of the long gauge effect, namely a length of single-mode fiber spliced onto the cavity rendered the whole fiber a distributed vibration sensor. Meanwhile, the field test was performed in cooperation with Calpine Corporation. When Calpine Corporation found signs of disturbance in the winding insulation, they realized that it was time to perform a major maintenance, leading to a rewind. Some samples of the affected windings were examined (**Figure 6**). There seems to be various stages of degradation.

All the measurement research above shows that as the revolutions per minute (RPM) are increased, various local resonances started to appear. Then, unique frequency signatures

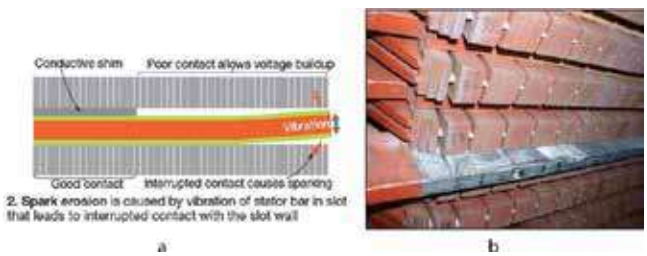


**Figure 6.** Patches of insulation damage on winding. Close-up highlights pinholes formed in the conductive carbon paint. Courtesy of QPS Photronics and Calpine Corporation.

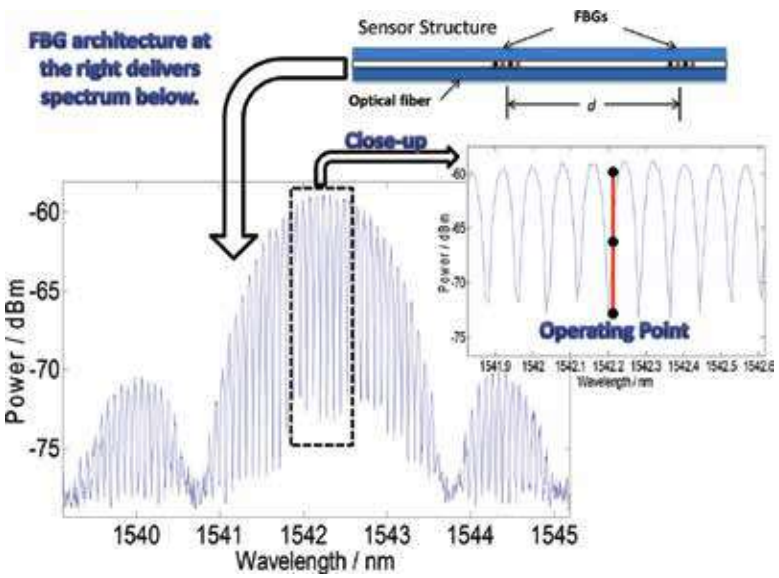


**Figure 7.** At left, conceptualization of vibration sparking. At right, complete winding insulation became destroyed at another power plant suspected of having similar problem.

appeared and were associated with different deliberately introduced faults like open-circuits, short-circuits, and bearing digs. Note that they are recoverable after the experiment. It is observed that they are very distinct from those obtained when the motor was restored to its original healthy condition (see [19]).

It is hypothesized these were related hot-spots developed in the stator, caused by eddy current loops, formed when damage occurs between the insulation and the neighboring laminated steel plate. The hot-spots reduced the performance of the insulation and PD subsequently occurred, eroding further the carbon paint. Furthermore, mica insulation also suffered from damage. PD activities would not have sufficient energy to puncture the mica and another failure mechanism might be at work, vibration sparking. Such process is defined by excessive vibration occurring in the slot so that the carbon paint, normally maintaining ground contact to the stator, failed and HV appears at some of those disturbed locations and the air breaks down to form a plasma. **Figure 7** (left) illustrates the concept. For the other side of the vibrating part, the plasma lost contact with its current source. This is a powerful source of electro-etching, an industrial process used to etch hard material like ceramics. If this process continues undetected, it destroys the mica insulation, leading to an unplanned outage as shown in **Figure 7** (right).

## 3. Insulation aging detection theory

### 3.1. Insulation aging model

In order to master the law of aging and reduce the losses due to aging, some aging models of insulation have been established based on practical experience and theoretical analysis.

*3.1.1. The aging model of single factor*

(1) Electric stress aging model

The Power Reciprocal model in low electric field and the Index model in high electric field are proposed based on a lot of electric stress affected researches. The Power Reciprocal model is as follows [25]:

$$L = kE^{-n} \tag{1}$$

where: $L$ represents failure time, $E$ represents external applied voltage, $k$ and $n$ are empirical constants.

The Index model is as follows [26]:

$$L = a\exp(-bE) \tag{2}$$

where: $L$ represents failure time, $E$ represents external applied voltage, $a$ and $b$ are empirical constants.

(2) Thermal aging model

The thermal aging model based on the equation that describing the relationship between the rate constant of the chemical reaction and the temperature as follows:

$$\ln t = \ln A + \frac{E_0}{RT} \tag{3}$$

where: $t$ represents the set testing time, $A$ is constant, $E_0$ represents the energy loss during the process of aging (unit: kJ/mol), R equals to the gas constant (8.314 J/mol·K), T represents temperature (K).

(3) Mechanical stress aging model

The mechanical stress aging model of a large motor is generally expressed by the empirical formula as follows:

$$L = K_m S^{-m} \tag{4}$$

where: $L$ represents the failure time, $S$ represents the mechanical stress, $m$ and $K$ are empirical constants related to vibration frequency [27].

*3.1.2. Electric-thermal two-factor aging model*

With the in-depth study of single factor electric and thermal aging, it is found that the reasons for the insulation aging are not isolated. The electric-thermal two-factor aging model that is widely accepted is as follows:

(1) Simoni model

Based on the function of hypothetical electric field $F(E) = \ln(E/E_0)$, Simoni proposed the two-factor aging model as follows:

$$L(T, E) = L_0 \left(\frac{E}{E_0}\right)^{-A} \exp\left[-B\Delta\left(\frac{1}{T}\right)\right] \tag{5}$$

where: $A = n - b\Delta(1/T)$, $n$ represents the index of the power reciprocal, $L_0$ represents the breakdown time at $E = E_0$, $E$ represents applied electric-field, $E_0$ represents a reference electric-field value, $b$ represents an empirical constant determined by the insulation materials, $B$ represents the constant of the single factor thermal aging model, $T$ represents the temperature (K).

(2) Ramu model

Based on the rate of Eyring physical chemistry reaction and considering the temperature function as constant, the Ramu the model is established from the Power Reciprocal aging model as follows [28]:

$$L(T, E) = c(T)\, E^{-n(T)} \exp\left[-B\Delta\left(\frac{1}{T}\right)\right] \tag{6}$$

where: parameter definitions are identical as the ones found in the Simoni model, $c$ and $n$ are empirical constants.

(3) Crine model

Crine proposed that the process of aging could be characterized by the energy barrier, and considered that the age of the insulation medium equals the time of the charged particles crossing the barrier. Based on the hypothesis that the average time of collective carriers through the potential barrier are equal to the time of a single carrier passing through the barrier, the aging model described by the relation of thermal-dynamic is obtained as follows:

$$L = \frac{h}{kT}\exp\left[\frac{\Delta G - e\lambda E}{kT}\right] \tag{7}$$

where: L represents the failure time, $h$ represents the Plank constant, $k$ represents Pohl Seidman constant, $\Delta G$ represents free energy, $\lambda$ represents the width of barrier, and $e$ represents the particle charge involved in the aging process.

The mathematical models of insulation aging above show how to theoretically predict the temperature, PD and stress in a timely fashion. It is the foundation of predicting the life of insulation materials and reducing safety accidents. In the context of the demand for electric power equipment that goes increasingly up, researchers nowadays have their full attention on predictive methods to trend the aging of insulation and therefore predict the generator's service life.

### 3.2. Fiber grating detection technology

Due to the complex environment caused by electricity, heat, machinery and chemistry, there are few sensors able to detect the insulation's aging in generators. With the increasing sophistication of fiber optic based technology, FBG based sensor has become the research focus in the field of sensors because of its inherent advantages, such as compact structure, corrosion resistance, intrinsic passivity, indifference to electromagnetic interference and its multiplexing abilities.

#### *3.2.1. Principle of optical Fiber sensing technology*

Optical fiber sensing technology senses and transmits external environment parameter variations based on the optical fiber medium. The optical fiber has the characteristic and ability to sense and transmit the information to the optical-electric field in itself directly or indirectly. When a beam of light illuminates through optical fiber, the change of the external environment parameters (e.g. vibration) could be sensed. The optical-electric fields characteristic value in the optical fiber, such as amplitude, phase, wavelength and polarization, would be affected by the signals sensed while the sensed signal propagates in the fiber. Furthermore, by using a demodulation device, the changes of the external environment physical parameters quantity could be obtained by using the signal reversing method [29]. The principle of optical fiber sensing is depicted in **Figure 8**.

#### *3.2.2. Fiber Bragg grating sensor model*

Based on the light coupling-mode theory at the scale of micro-disturbances, the effective refractive index of grating region and the central wavelength of FBG could be obtained by solving the light equation as follows [29]:

$$\delta n_{eff} = \overline{\delta n_{eff}} \left[1 + \cos\left(\frac{2\pi}{\Lambda} z\right)\right] \tag{8}$$

where: $n_{eff}$ represents the effect refractive index, $\Lambda$ represents grating period, $\overline{\delta n_{eff}}$ represents the change of the average effective refractive index.

The characteristic wavelength that interacts with the optical fiber corrugation is represented by:

$$\lambda_B = 2\, n_{eff} \Lambda \tag{9}$$

where: $\lambda_B$ represents the Bragg (central) wavelength.

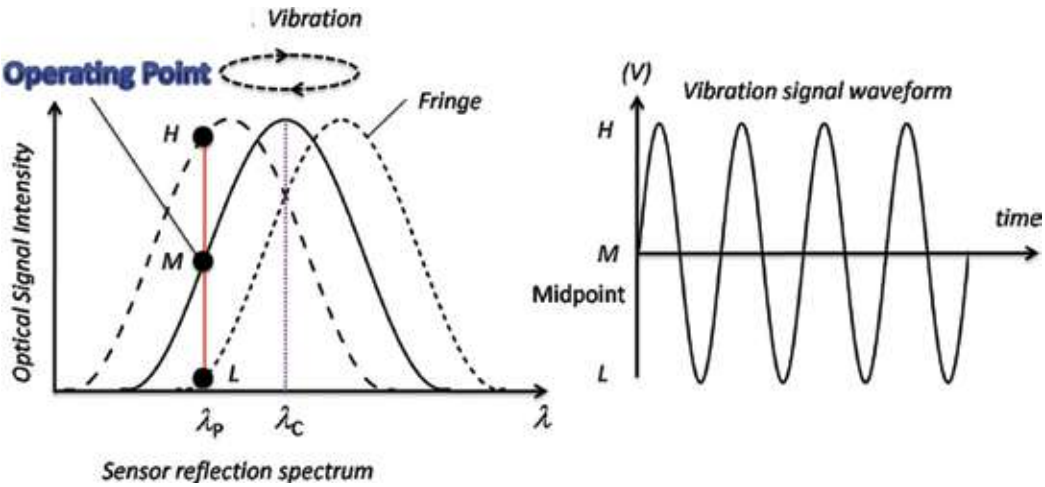


**Figure 8.** The principle of optical fiber sensing.

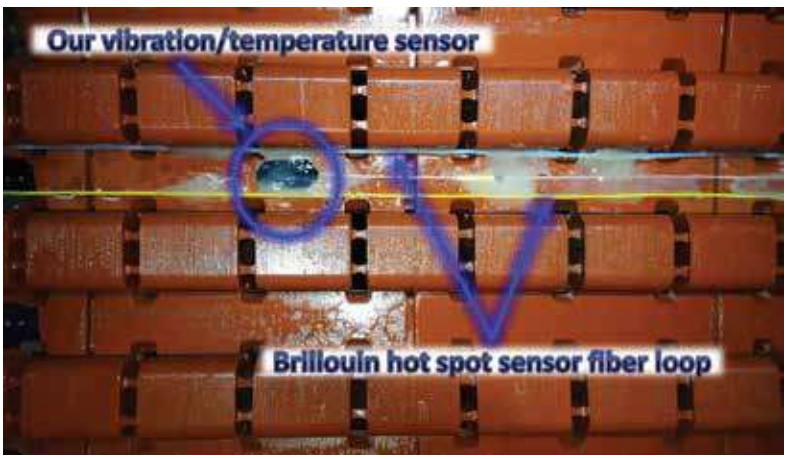


**Figure 9.** The frame of the Bragg fiber grating and its reflecting schematic diagram. Courtesy of QPS Photronics.

From the FBG central wavelength formula, we can conclude that: (A) when a beam of incident light transmits through the grating region, there always exists a fraction of the light that reflects back, and the wavelength of the reflected light must satisfy the Bragg wavelength Eq. (9); (B) The Bragg wavelength of the FBG only depends on the grating period $\Lambda$ and the refractive index $n_{eff}$.

A proper FBG will have its central wavelength solely determined by the corrugation period and effective refractive index. The FBG central wavelength, period, and effective refractive index are all fixed constants, meaning that the reflection spectrum of the FBG central wavelength is always fixed at reflecting peak on the condition that the FBG sensor is under the same environmental conditions [30, 31]. The frame of the FBG and its reflecting schematic diagram are shown in **Figure 9**.

*3.2.3. Fiber Bragg grating sensor model for temperature*

Due to the central wavelength shifted with the change of temperature, based on the formula (9) and the assumption that the fiber grating is only affected by the temperature, the central wavelength shifting value of the FBG could be obtained as follows:

$$\frac{\Delta\lambda_B}{\lambda_B} = (\alpha_s + \zeta_s)\Delta T \tag{10}$$

where: $\alpha_s = (1/\Lambda)(\Delta\Lambda/\Delta T)$ represents the fiber's thermal expansion coefficient, and is used to describe the grating pitch variation with the temperature. $\zeta_s = (1/n_{eff})(\Delta n_{eff}/\Delta T)$ represents the FBG thermo-optical coefficient, and is used to describe the variation of the material refractive index changing with the temperature.

Based on the Eq. (10), the variation of the ambient temperature could be reversed by detecting the variation of the central wavelength $\Delta\lambda_B$.

*3.2.4. Fiber Bragg grating sensor model for vibration*

Due to principle of the fiber grating pitch and refractive index that vary with the fiber undergoing strain along the axial direction, based on the central wavelength formula (9) and the assumption that the fiber grating is only affected by it, the central wavelength shifting value of the Bragg fiber grating could be obtained as follows:

$$\frac{\Delta\lambda_B}{\lambda_B} = \frac{\Delta\Lambda}{\Lambda} + \frac{\Delta n_{eff}}{n_{eff}} \tag{11}$$

where: $\Delta\lambda_B$, $\Delta\Lambda$ and $\Delta n_{eff}$ represent the changing value of FBG central wavelength, grating period and refractive index separately.

When strain is applied along the axial direction in the fiber, the refractive index variation of the FBG satisfies the following formula:

$$\frac{\Delta n_{eff}}{n_{eff}} = \frac{1}{2} n_{eff}^2 \left[(1-\mu) P_{12} - \mu P_{11}\right] \varepsilon = -P_e \varepsilon \tag{12}$$

where: $P_e$ represents the elasto-optical coefficient, and defined as $P_e = n_{eff}^2[(1-\mu)P_{12} - \mu P_{11}]/2$, $\varepsilon$ represents strain of the fiber grating along the axial direction, $\mu$ represents the Poisson's ratio of the fiber material. $P_{11}$ and $P_{12}$ represent the elastic tensor components of the fiber grating.

Based on the definition of axial strain and Eq. (11), we could obtain the strain detecting formula as follows:

$$\frac{\Delta\lambda_B}{\lambda_B} = (1 - P_e)\varepsilon$$

Based on the relationship between strain and wavelength and the detecting value of the center wavelength, the vibration could be reversed by using the relationship between stress and strain.

### 3.3. Long-gauge vibration/temperature sensor

#### *3.3.1. Introduction to QPS Photronics*

QPS is an innovator in the field of fiber optic sensors and specifically FBG's. They bring gratings from research into marketable products.

#### *3.3.2. Introduction of long-gauge vibration/temperature sensor*

Because fiber optics are made of glass with no conducting materials, fitting well in environments undergoing high-voltages and strong electromagnetic fields, based on the FBG vibration/temperature sensor model, this section introduces how the sensors were designed to satisfy the power industry requirements using FBGs.

The ability to measure both vibration and temperature is based on interference: two identical FBGs are printed on the same fiber at a small distance, which forms a cavity. When a laser beam with matching center wavelength is emitted into the cavity, it is reflected and goes through a 180° phase shift, giving rise to two interfering beams and a dense fringe spectrum as shown in **Figure 10**.

The larger the cavity length, the denser will be the fringe pack with steeper slope, playing on sensitivity. The vibration function is realized by programming an operating point at the midpoint of the rising slope of a selected fringe. This operating point stays locked using

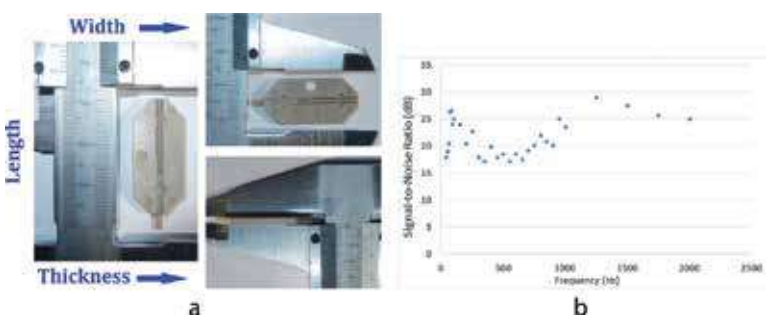


**Figure 10.** Correlation between fiber optic structure and resulting spectrum where a selected fringe will be monitored for changes due to both static/dynamic strain and temperature. Courtesy of QPS Photronics.

http://dx.doi.org/10.5772/intechopen.78065

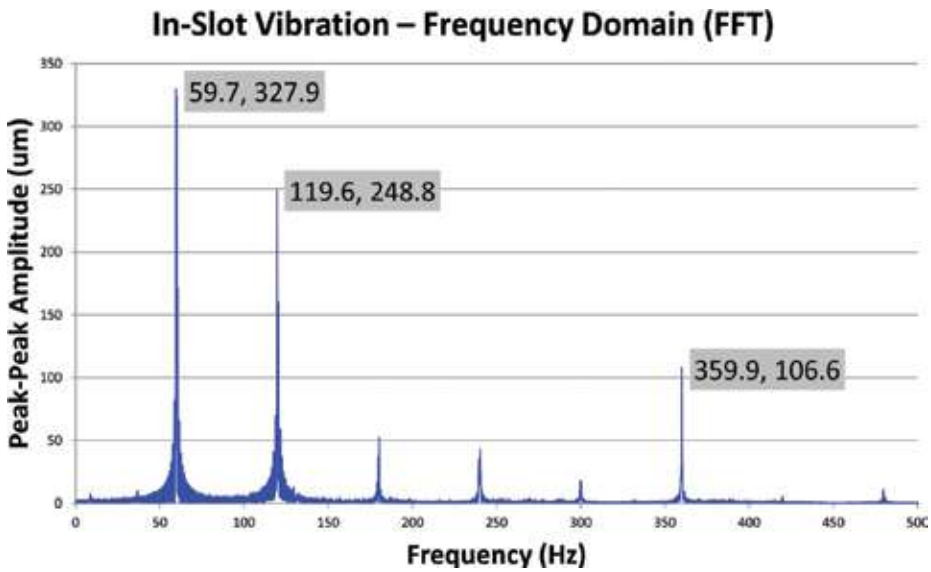


**Figure 11.** Correspondence between fringe oscillation and resulting vibration. Courtesy of QPS Photronics.

both the laser current (LC) and the thermoelectric cooler (TEC) analog controls of the laser. When vibration occurs, the fringe pattern will be moving right and left, it forces the operating point to ride up and down the slope, translated into linear intensity changes. The changes accurately reflect the actual vibration that is occurring. Since the cavity is also affected by temperature, a self-calibration algorithm was introduced to re-establish the operating point and such compensation delivers an indirect method to measure temperature (see **Figure 11**).

Another invention linked to the cavity is the long gauge technology. By splicing a length of single-mode optical fiber on to the cavity, a new cavity sprouts between the two matching FBGs cavity and the interrogation system connector. Said connector triggers a Fresnel broadband reflection, enabling a thin in-slot vibration distributed sensor to be used in a field test inside a gas-fired generator [32]. The FBG based architecture is housed within a 2 mm thin package that allows easy insertion into tight spots, whereas another supplier of the same field requires two separate large sensors that limit locations where they could be installed [33].

## 4. Sensing temperature and vibration

Based on the system for temperature and vibration monitoring shown in **Figure 12**, the generator insulation's temperature and vibration becomes possible by using different sensing units that are placed at different locations. By control and analyzing different signals received from different sensors, not only the insulation temperature and vibration can be obtained, but insulation hot-spots can be pinpointed by using the relation between wavelength and vibration.

The detecting system consists of three parts: the signal control & processing unit, signal transmission unit and sensing unit. After the output of the optical signal is converted into an electrical equivalent by the photoelectric converter, and acquired & collected by the data collecting

system, the signal can be transmitted to the computer and processed by the specific software. Then the hot-spot/temperature and vibration can be determined. The related parameters of the vibration of the measured object can be obtained after the analysis and processing of the data on the computer through the vibration monitoring software. The signal control & processing unit consists of an incident optical source, interrogator, display and computer. Incident optical source is used as the stimulating source of the incident light, computer that installed the control software was considered as the head of the detecting system and could send the information and analyze the feedback signal that come from the interrogator complete.

In order to get more information of different locations in the insulation, several fiber gratings having different center wavelength are set in different locations of the optical fiber. Many optical fibers are connected to the interrogator and form the sensing transducer array. The system of the temperature and vibration detection is shown as **Figure 12** and the sensing transducer array is shown as **Figure 13**.

### 4.1. Details of the field test

There are two types of sensors. One of them makes use of the Brillouin technology where two laser beams are fed into the same fiber optic loop and both lasers have very close center wavelengths that are made to beat against each other, generating a beat frequency. This beat frequency is sensitive to any index changes in the fiber as hot spots. Hence, it is able to report their location along the sensing fiber. The temperature sensor forms a loop inside the slot. In the middle of it a single point temperature (yet distributed for vibration) sensor is installed (see **Figure 14**). The top slightly bluish fiber together with the bottom yellow fiber are the Brillouin temperature sensing loop; the dark hexagon houses the temperature sensing cavity with vibration sensitivity for the whole length of the fiber extension. The whole length of the slot, which measures five meters long, has its vibration captured. The single point temperature measurement provides a temperature reference for the Brillouin hot spot temperature sensing measurement.

Besides the Brillouin hot spots sensor and the in-slot vibration sensor, two other cavity vibration sensors were installed. One is coupled with the end winding lead and another one with the end winding bus, all are done on the neutral phase of the generator. All sensing fibers


**Figure 12.** System diagram for temperature and vibration detection. Courtesy of QPS Photronics.

are protected by Teflon tubes where the sensor tip is housed in a molded PEEK package as shown in **Figure 15** (left). It is an open face design. The same sensor was also used to measure vibration inside the transformer. The long gauge vibration sensor is a wideband sensor, able to detect frequencies ranging from 10 Hz to 1 kHz for standard version and 5 Hz to 2 kHz for extended sensing range as depicted in **Figure 15** (right).

### 4.2. Vibration sensing

#### *4.2.1. In-slot vibration*

Gas-fired generators are known to produce strong vibration and noise [34]. The in-slot vibration sensor, which has been installed onto the wedge (see **Figure 14**), gave a very clear vibration response as illustrated in **Figure 16**.

We observed a strong line frequency (1xLF) vibration peak together with a strong two times line frequency (2xLF) component. The 1xLF component measures 15-mil peak-to-peak and the 2xLF component measured 10-mil peak-to-peak. This was very high compared with

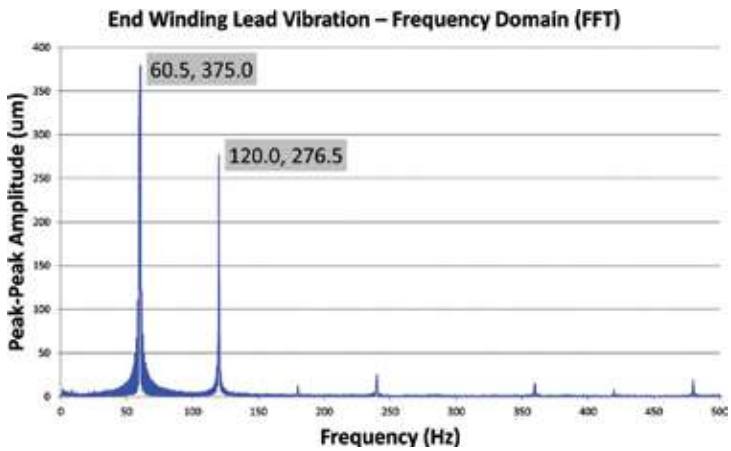


**Figure 13.** The sensing transducer array. Courtesy of QPS Photronics.

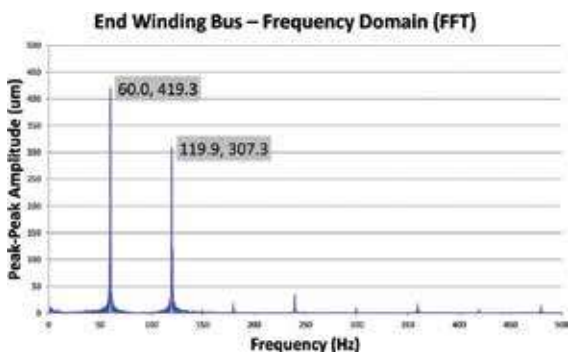


**Figure 14.** The in-slot vibration sensor installed between the Brillouin temperature sensing fiber loop (U-turn not shown). Courtesy of Calpine Corporation and QPS Photronics.

previously experienced 6-mil peak-to-peak in the end winding vibration of coal-fired generators. It is noted that there exists some harmonics, which rolled off normally but then showed a strong peak at 6xLF. In this generator design, the bearing is coupled onto the frame, which became incorporated into the slot vibration. Concern was expressed to Calpine as this seems to be slightly too high. The 1xLF vibration seems to be related to balancing while the 2xLF component to alignment. This excessive vibration appears to validate the visual inspection of the winding sample cutout from the generator before the rewind.

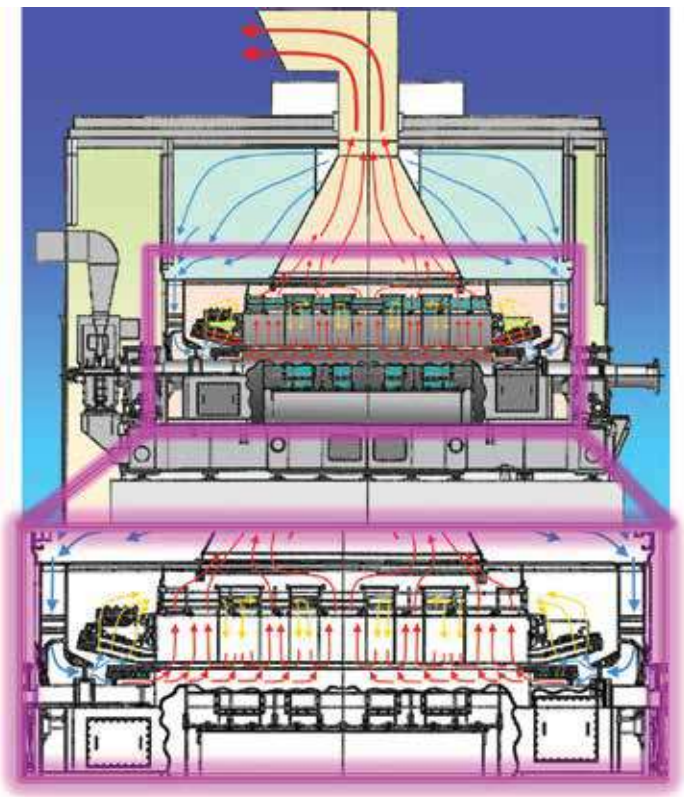

**Figure 15.** At left, the vibration sensing cavity housed inside a PEEK package. At right, the in-slot vibration sensor bandwidth can even be extended from 10 Hz~1 kHz (standard) to 5 Hz~2 kHz. Courtesy of QPS Photronics.

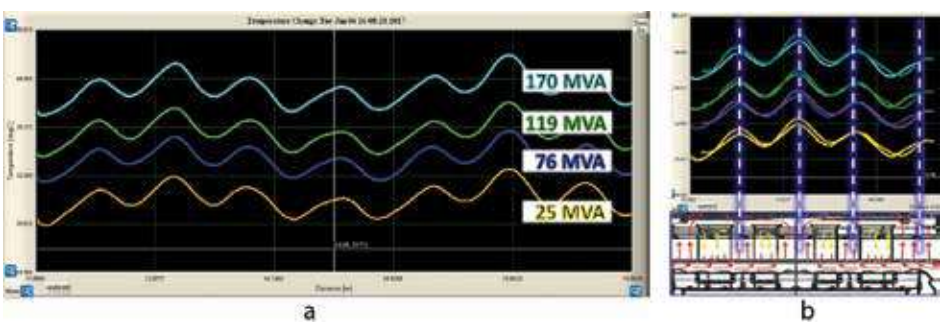


**Figure 16.** FFT shows in-slot vibration characteristics. Courtesy of QPS Photronics.

*4.2.2. End winding lead vibration*

One single point vibration sensor was installed at the end winding of the neutral lead as depicted in **Figure 17**. The photograph at the right shows the end winding conductor before installation where the colored circles pinpoint where the two additional discrete sensors would end up coupled.

The end winding lead sensor also showed strong vibration spectrum in both 1xLF and 2xLF. There were hardly any harmonics. The 1xLF component measured 15-mil peak-to-peak and the 2xLF component measured 11-mil. They are higher than what we expect but consistent to the in-slot measurement (see **Figure 18**).

*4.2.3. End winding bus vibration*

A third vibration sensor was mounted on the neutral end winding bus (see **Figure 17**). Once again, the vibration observed here is also consistent as depicted below in **Figure 19**.

Larger vibration amplitude is shown: 1xLF component measured 16.5-mil peak-to-peak and 2xLF measured 12.1-mil peak-to-peak. It seems that gas-fired generators vibrate much more than the coal-fired generators. Plant experts informed all participants of the field test that it may be related to the generator design where the bearing is coupled to the frame. Vibration was so strong in similar machines that cracks developed.

### 4.3. In-slot and end winding temperatures

The temperature distribution inside the slot was measured by the Brillouin fiber optic loop sensor. The gathered data brought up a wave-like distribution as demonstrated in **Figure 20**

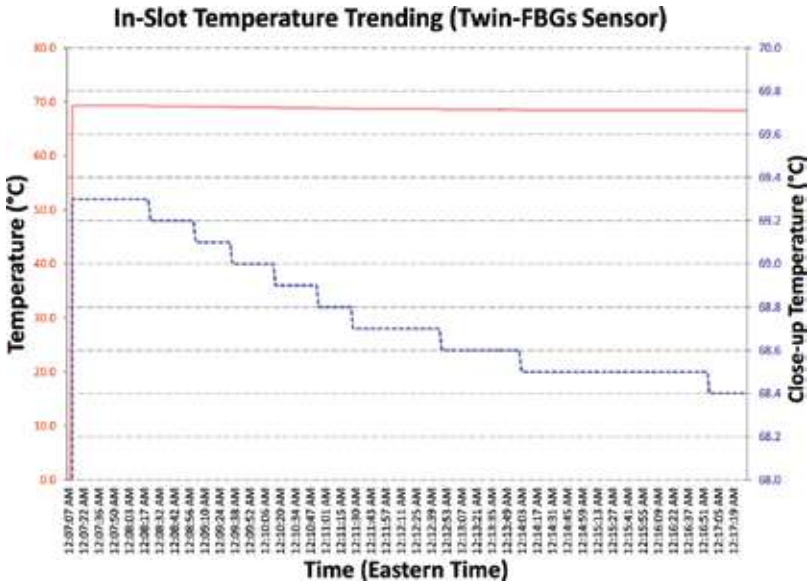


**Figure 17.** Two discrete sensors coupled at different locations of the neutral bus of the phase C conductor. Courtesy of Calpine Corporation and QPS Photronics.

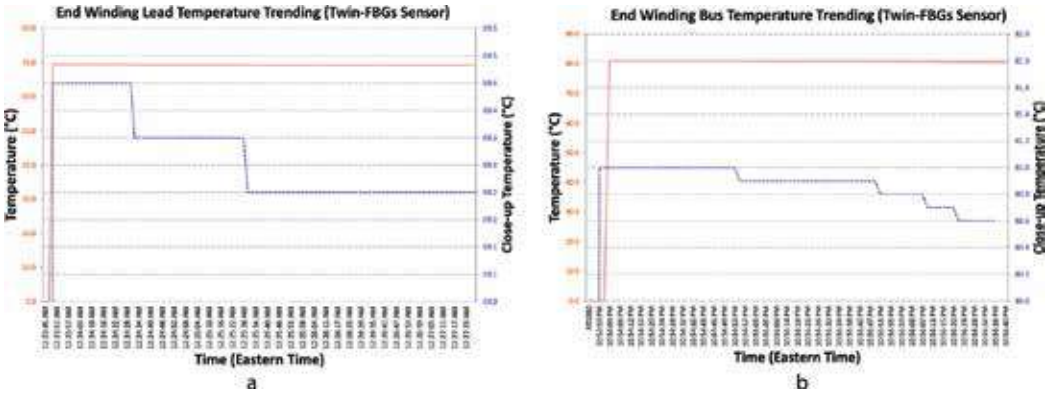


**Figure 18.** End winding lead frequency domain. Courtesy of QPS Photronics.

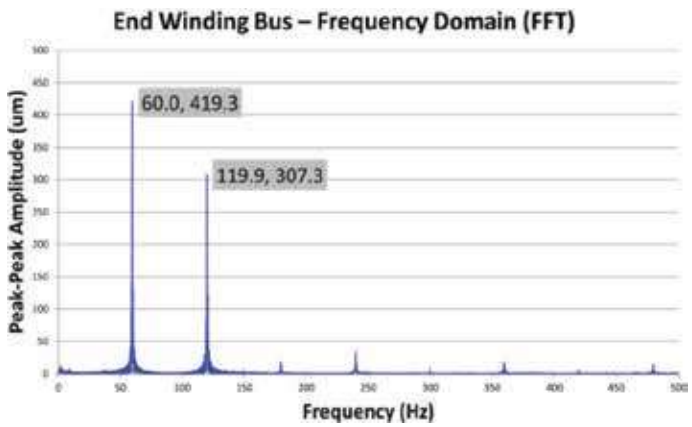


**Figure 19.** End winding bus frequency domain. Courtesy of QPS Photronics.

(left). The distribution is not flat; the cooling airflow did not form a perfect balance. The temperature extrema were less than 2°C apart, positively assuring the lack of hot spots.

We tried to line up the temperature profile with the layout of the air ducts by wrapping over at the middle. Valleys coincide very well with the air duct exhaust and the top peak always occurs in the middle between two air ducts where there is minimum cooling airflow as illustrated in **Figure 20** (right). The difference between peak and valley is consistent at different loading levels.

**Figure 21** shows the temperature measurement of the in-slot sensor. The red plot indicates the coarse temperature reading of 70°C at a loading of 170 MVA. The blue line shows the fine temperature variation over a period of 10 min. The sensor was able to detect temperature changes down to 0.1°C.

The end winding lead of **Figure 22** (left) showed a temperature consistent with the slot as well as the end winding bus plotted in **Figure 22** (right). All of them read close to each other, there does not seem to be any problem.

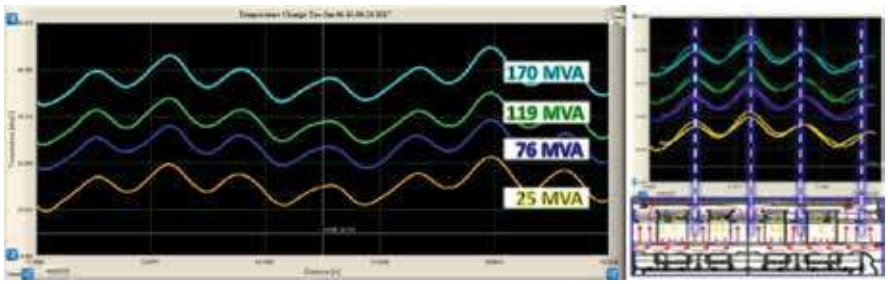


**Figure 20.** At left, temperature profiles at different loading intensities. At right, temperature profile line-ups with the air duct locations. Courtesy of Oz Optics, Ltd.

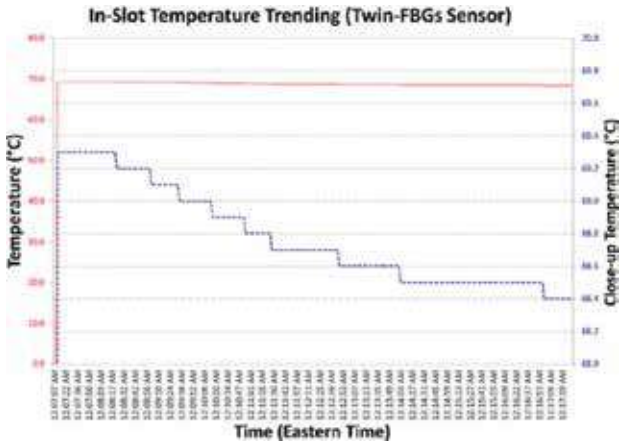


**Figure 21.** In-slot temperature measurement for 10 min. Courtesy of QPS Photronics.

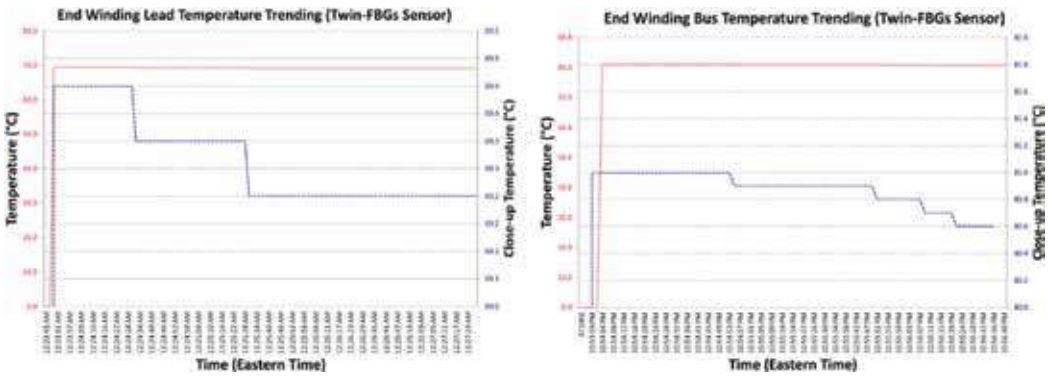


**Figure 22.** At left, end winding lead temperature measurement for about 5 min. At right, end winding bus temperature measurement for about 3 min. Courtesy of QPS Photronics.

### 4.4. Air cooling inside a gas-fired generator

The gas-fired generator involved in the field test was manufactured by Siemens [35–38]. **Figure 23** shows a conceptual diagram of the cooling air radial flow. There are resistance

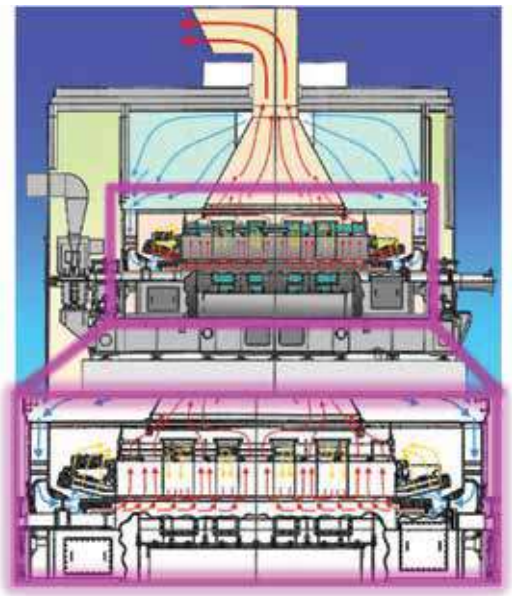

**Figure 23.** Siemens Westinghouse AeroPac I generator with emphasis on the radial airflow via colored arrows. Courtesy of Calpine Corporation.

temperature detectors (RTDs) installed at different locations along the air path. We will compare our measurement with those coming from the supervisory control and data acquisition (SCADA).

Cooling air flows through many cooling ducts placed approximately 2 inches apart from each other. Blue arrows are meant to represent cooler air entering the core. As it flows through the ducts, the air progressively relieves the stator core of its heat (yellow arrows) and it ends up evacuated (red arrows) via the main central exhaust. Since RTDs carry conducting material, they are mainly installed in the grounded core. This field test represented the first time where in-slot vibration and hot spot measurements were performed.

## 5. Analysis and discussion for temperature measurement

The field test was performed after a successful rewind. A close examination of a sample segment of the old winding showed that defects always started extremely small at the scale of few millimeters as seen in the pinholes of **Figure 6**. In the advanced stages of disturbance, there appears a single or multiple small dark depressions inside the exposed mica. These might represent two stages of degradation. If hot spots were to start as point defects, prior observations make sense. These disturbed areas in the carbon paint grew increasingly larger together with the dark spots within them. We could not confirm whether these dark spots represent complete shorts to the copper conductor. The mica insulation is usually quite thick. The dark spot certainly looks like a reduced thickness in the mica. This must be a lengthy process for the electro-etching caused by the plasma of deionized air resulting from a strong in-slot vibration

as mentioned in an earlier section of this paper. Discussion with the plant technical staff experienced with maintaining these gas-fired generators indicated that troubles seem to start typically after 5–10 years. The distributed temperature sensing Brillouin technology is usually used for oil and gas pipeline and helps to locate small leaks. Best spatial resolution is listed as three centimeters [39], which is much larger than the defects we observed, therefore, no hot spots were found despite our expectations. Given that the generator has been rewound and the insulation is new it would take several years for the defect to grow to a size large enough to be detected by the sensing fiber. We believe it is better to maintain the sensors as a continuous monitoring tool where we can see slight temperature changes down to 0.01°C increments.

### 5.1. Analysis and discussion for vibration measurement

This field test demonstrates consistent strong vibration in both 1xLF and 2xLF. A spectral analysis tool published by SKF USA Inc. [40], the strong vibration is related to misalignment (strong 2xLF amplitude) and also imbalance (strong 1xLF amplitude). Misalignment can be caused by thermal expansion; alignment could be performed when the generator is cold then heat up when it is placed in full operation. Thermal expansion might have caused the rotor to become elliptical instead of being perfectly circular. Misalignment could also be caused by shifting of the foundation or uneven support [41]. On the other hand, imbalance seems to be the cause of the strong 1xLF vibration. Their relative amplitude might indicate the extent of each problem (see [20]).

Referring to **Figure 15** of SKF USA Inc. article (see [40]), their example can be compared to the data of this field test (see **Figures 16**, **18** and **19**) and it seems that both imbalance and misalignment could be affecting the generator. These measured values were two to three times higher than typical measurements on large coal-fired generators. Those large generators do not display any 1xLF vibration signal at all because they are physically much larger in structure.

### 5.2. Proposed composite damage model for gas-fired generators

The fiber optic signal processing system equipped with a gateway device connects the large volume of sensor data with the plant data from the SCADA for parametric correlation between cause (loading, start-stop periods, etc.) and result (level of vibration and temperature). **Figure 24** displays a flowchart of damage diagnostic that would be further quantified with aforementioned correlation.

It is now possible to simplify the problem into an intuitive model that does not involve complex mathematics [42–46]. The methodology is described below and can be used to analyze the measured data from these fiber optic sensors. It has been known that gas generators are frequently subjected to many daily start-stop events: the winds are usually stronger during the night and the sun shines more strongly late morning and afternoon. When these renewable energies become abundant, gas turbines must be turned off for the total power to not overload the power grid (see **Figure 25**).

When these start-stop cycles occur [47], the inside temperature of a generator would go through significant changes. Frequent start-stop cycles together with strong vibration will potentially cause delamination of the insulation as well as voids at their interface with the conducting copper. They also have different coefficients of expansion. Severe vibration can

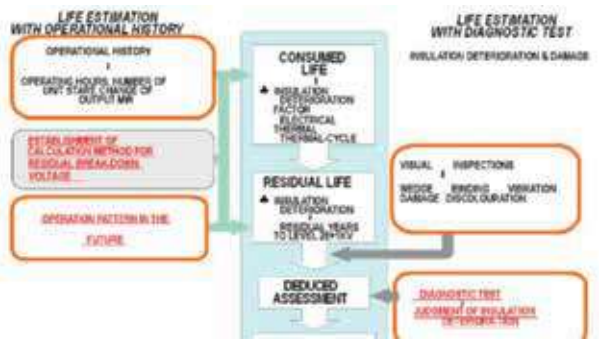


**Figure 24.** Damage model that allows residual life predictions.

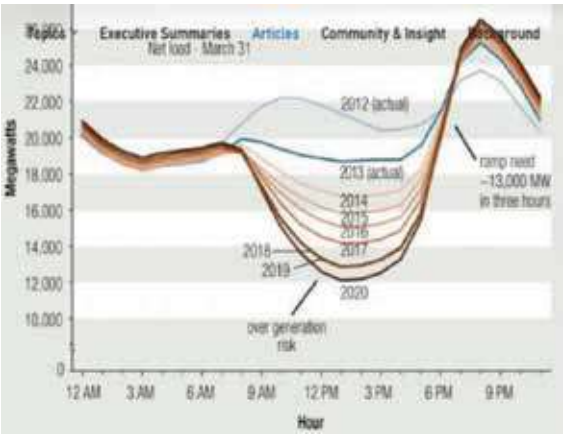


**Figure 25.** Graph showing gas generators must be turned on and off to adapt to the supply of the renewables.

introduce cracks inside the thick epoxy mica and voids inside the mica facilitating PDs [48–56]. Of course, winding temperature would depend on load which will show up in the temperature trending profile in an online monitoring configuration. Loading changes will be reflected in changes in the 2xLF vibration amplitude, which is affected by the electromagnetic forces interaction between the rotor and the stator. Simultaneously, the temperature will also see small adjustments due to additional heating caused by higher load currents. Hence, smaller temperature changes will reflect the loading conditions and correlation with the control signal from the SCADA system becomes unnecessary. Current stage of sensor development allows the freedom to take advantage of the latest technology like the internet-of-things (IofT) where signals can be analyzed by gateway devices attached to our signal processing system. Then, the partially analyzed data are transmitted to a cloud where higher level calculation is performed to form a residual life model as well as providing warnings for urgent attention and quick remedial decisions. As for the start-stop cycles, they will simply switch the vibration signals on and off. These will be very clear and easy to interpret. Since temperature change is slow, its decrease will come gradually. Again, these data can be derived without any connection to the SCADA system of the power plant (power industry is known to be very concerned about external connection to their SCADA, making it open to external hacking).

http://dx.doi.org/10.5772/intechopen.78065

The proposed model consists of a menu of degradation processes, individually selectable to form a clear picture of health of the air-cooled gas-fired generator, all based on the sensor ability to work inside high voltages, and strong electromagnetic fields. They are also small (0.5″ X 3″ X 0.08″) and can fit inside the stator slots which are approximately 1″ in width. Once installed in place, these sensors will be able to measure both thermal as well as mechanical stresses. The class of insulation material and the operating voltage of the generator have defined the limit of the electrical stress. Thermal stresses can be measured directly inside the slot as well as the end winding overhang where curvature might give rise to current crowding. These sensors are also designed to be thin; they can easily conform to any curved surface yet maintain good thermal contact. The field test described in prior sections represents the first occasion where direct measurement could be done inside the generator slot. Previous work combining the total aging effect consider vibration as related mainly to fatigue, which might not be the case here.

From the failure analysis of the extracted winding section prior to the rewind, there was clear evidence of vibration sparking. Defects first appeared as small pinholes in the carbon paint, which grew with time. Once these defects grew into sufficient size while developing local high voltage spots, they cause the air to break down into plasma, whereas the remaining half of the vibration cycle broke the current path and turns the plasma into a source for electro-etching. Vibration sparking together with frequent start-stop cycles drastically shortens the lifespan of the gas-fired generator. This hypothesis was reinforced while working with Calpine maintenance staff: gas-fired generators typically start to have trouble as early as the warranty period within 5–10 years. This information is compared to the prior field tests of coal-fired base load generators monitoring stator end winding (SEW) vibration, where rewind would only be done after 30–40 years of operation. Vibration sparking might come with a threshold related to vibration peak-to-peak amplitudes. In fact vibration amplitudes observed at Hermiston field test showed a magnitude two to three times greater than the ones collected from coal-fired power plants where they are usually less than 150 microns peak-to-peak. There is another possibility. Large coal-fired generators are hydrogen-cooled. Hydrogen does not break down easily, pinhole defects in their old winding samples were rare occurrences. The proposed second field test for Calpine Corporation will take place in their plant of Texas (Hidalgo Energy Center) where the gas-fired generator would be hydrogen-cooled. We will go through the same analysis and compare the vibration and temperature data there. Fiber optic sensor capturing PD events will be introduced, provided PD first produced the pinhole defects that facilitated the following vibration sparking destruction. Those PD sensors are based on a very long FBG cavity. Cavity length affects sensor performance: the longer the cavity, the denser would be the interference fringes. These fringes will have steeper slopes and therefore more sensitive to small surface acoustic wave perturbations. Fringes are so densely packed spectrally that maintaining the operating point will not be needed. This PD sensor will not be affected by small changes in temperature and will pick up PD events along the full length of the optical fiber cavity. However, it is a dedicated PD sensor and will not be able to measure temperature. The distributed low frequency vibration sensor will be set in the same slot as the PD sensor to collect all the data that would complement each other.

The influence of PD on the proposed aging model is that they start to register pinhole formation. As the defects grew both in magnitude and incidence, an indication is given about the size of the carbon paint disturbance. However, the PD sensor would not be able to detect the

**Figure 26.** Cracking of copper turns and also bowing of the rotor.

onset of electro etching. Arcing experiments will be conducted in laboratory environment to study and relate the signatures associated with the electro-etching process.

In summary, it is a damage model of the insulation. It is related to the accelerated aging of insulation inside the gas-fired generator and additional work will be needed to turn it into a residual life prediction model. Such a model will depend on the design, and manufacturing workmanship, which vary depending on the individual OEMs.

### 5.3. Influence of start-stop cycles

Frequent start-stop cycles can cause stresses due to coefficient of expansion differences between different materials used inside the generator (see **Figure 26**).

In the industry, the effect of start-stop cycles is introduced as a life consumption factor. Attempts to use the gas generator to compensate for the intermittent renewables like the solar and wind is one instance. It might have to be turned on and off several times per day. The number of times per day serves to cause an apparent acceleration factor. In a case where it is done three times a day, each additional day of operation in that fashion is equivalent to 3 days of operation, effectively shortening their lifespan. An increasingly accumulated number of start-stop cycles per day correspondingly shorten the life of the generator. This explains the difference between the expected onsets of problems comparing a coal-fired power plant versus the gas-fired unit. Coal-fired plants usually need to be rewound after 30 years, whereas the gas generator needs adjustments at a daily pace depending of the wind and solar, leading to a major maintenance even inside the warranty period. This aging factor ranges from three to six, depending on the frequency of start-stop cycles per day.

So the life of a gas generator depends not only on who manufactured them, but it also depends how owners use them. Using fiber optic sensors it would be possible to get a real-time picture of how the generator is doing and extend its lifespan.

In summary, a new class of fiber optic sensors is introduced and can address the following complex problems:

- Marginal design and poor choice of material to be indicated by the onset of PD activities
- Number of start-stop cycles in its mode of operation as observed in the cycle of large temperature changes

- Ongoing electrical and thermal stresses
- Degradation due to vibration sparking
- Signature analysis of the observed vibration spectrum indicating structural looseness and other mechanical problems like misalignment and unbalancing.

With the upcoming field tests, this aging model covering generators of various sizes and make will become more sophisticated, turning the monitoring solution into a service business.

## 6. Conclusion

Sensors which can survive in a hostile environment are essential to understanding the aging process of turbines. It is quite possible that the key to extending the lifespan of turbines is real time monitoring using fiber optic sensors for both vibration and temperature.

We have proven through this test that real time monitoring of vibration and temperature is both possible and economical. What needs to happen now is that these measurements need to take a part in the day to day operation of generating plants. By sensing internal vibration and temperature we can know when a particular turbine is on the edge of conditions which will lead to lasting damage and a control scheme can be implemented where other turbines will start up to alleviate those conditions before damage happens resulting in increased life span of all the turbines. At the moment these turbines have a very limited lifespan, typically 7 or 8 years. With improved controls there could be a significant improvement in that lifespan. This would have benefits in reducing asset costs, improving reliability to customers and improved safety for workers at the plant.

## Acknowledgements

The authors would like to express gratitude to Calpine Corporation for allowing and facilitating the installation of the fiber optic sensing systems at the Hermiston Power Project plant. Likewise, contribution from Oz Optics, Ltd. is highlighted for providing temperature records from their Brillouin distributed temperature technology. At last, acknowledgements are given to the senior consultant George F. Dailey for bringing all participants together and Refined Manufacturing Acceleration Process (ReMAP) network for providing a substantial financial aid.

## Author details

Peter Kung

Address all correspondence to: peter@qpscom.com

QPS Photronics Inc., Canada

## References

[1] Maughan C. Premature failure of modern generators. Proceedings of 20th International Conference on Nuclear Engineering; July 30-August 3 2012; Anaheim, California: pp. 866-870. DOI: 10.1115/ICONE20-POWER2012-54584

[2] Barré O, Napame B. The insulation for machines having a high lifespan expectancy, design, tests and acceptance criteria issues. Machines. Feb. 2017;**5**(1):7. DOI: 10.3390/machines5010007

[3] Ge J, Qiu C, Xie H. Partial Discharge Measurements[M]. Beijing: China machine press; 1984

[4] Stone GC, Wu R. Examples of Stator Winding Insulation Deterioration in New Generators. DOI: 10.1109/ICPADM.2009.5252475

[5] Morshuis PH. F partial discharge mechanisms in voids related to dielectric. Degradation IEE Proceedings–Science, Measurement and Technology. 1995;**142**(1):62-68

[6] Brutsch R, Tari M, Frohlich K, et al. Insulation failure mechanisms of power generators. IEEE Electrical Insulation Magazine. 2008;**24**(4):17-25

[7] Jiang Q. Research on UHF Detection Technology of Partial Discharge in Power Transformer [D]. Baoding: North China Electric Power University; 2006

[8] Stone GC. Deterioration of Stator Winding Insulation by Vibration Sparking. Proceedings of 2008 International Symposium on Electrical Insulating Materials, Yokkaichi, Mie, Japan, September 7-11, 2008. pp. 171-174. DOI: 10.1109/ISEIM.2008.4664445

[9] Xie H. Electrical Insulation Structure Design Principle. Beijing: Machinery Industry Press; 1993

[10] Wu S, Xie D, Chen S, Yu B. Electrical Insulation Materials and Engineering. Xi'an: Xi'an Jiaotong University Press; 1996

[11] Kako Y, Tsukui T, Mitsui H, Hirabayashi S, Kimura K, Natsume F. The process of electrical strength and insulation aging for the system of HV motor. Foreign Electrical Machinery. 1989;**3**:52-57

[12] Wang S. The formation characteristics and development of common generators insulation faults. Large Electrical Machinery Technology. 1987;**6**:25-29

[13] Lei Q. Structure and Electrical Properties of Polymer. Wuhan: Huazhong University of Science and Technology Press; 1990

[14] Iike M, Tsujimura T, Muraoka M. Life diagnosis of epoxy resin coil insulation system. Fuji Electric Journal. December 1989;**62**:12

[15] Wang S, Zhou D. Operation Characteristics and Test of Large Generator Insulation. Beijing: Machinery Industry Press; 1992

[16] Tshiloz K, Smith AC, Mohammed A, Djurović S, Feehally T. Real-time insulation lifetime monitoring for motor windings. Proceedings of International Conference on Electrical Machines, ICEM. 2016. pp. 2335-2340. DOI: 10.1109/ICELMACH.2016.7732847

[17] Hydro A. Generator Winding Insulation [Internet]. 2011. Available from: http://www.nwhydro.org/wp-content/uploads/events_committees/Docs/2011_Tech_Workshop/GeneratorWinding-Heaton.pdf [Accessed: 2018-02-07]

[18] Niikura H, Inoue S, Yamazaki M. Global vacuum pressure impregnation insulation applied to hydrogen-cooled generators. Fuji Electric Review. 2009;**55**(3):93-98

[19] Kung P, Wang L, Comanici MI. Stator end winding vibration and temperature rise monitoring. Electrical Insulation Conference (EIC). June 2011. pp. 5-8. DOI: 10.1109/EIC.2011.5996105

[20] Wan S, He Y. Investigation on stator and rotor vibration characteristics of turbo-generator under air gap eccentricity fault. Transactions of the Canadian Society for Mechanical Engineering. 2011;**35**:161-176

[21] Oliquino R, Islam S, Eren H. Effects of types of faults on generator vibration signatures. Australasian Universities Power Engineering Conference (AUPEC2003). 2003. pp. 1-6

[22] Djurović S, Vilchis-Rodriguez D, Kung P, Comanici MI, Smith AC. Investigation of induction generator wide band vibration monitoring using fibre Bragg grating accelerometers, Proceedings of International Conference on Electrical Machines, ICEM 2014. pp. 1772-1778. DOI: 10.1109/ICELMACH.2014.6960423

[23] Mohammed A, Djurovic S, Smith CA, Tshiloz K. FBG Sensing for Hot Spot Thermal Monitoring in Electric Machinery Random Wound Components. Proceedings of International Conference on Electrical Machines, ICEM 2016. DOI: 10.1109/ICELMACH.2016.7732837

[24] Kung P, Comanici MI, Li Q, Zhang Y. Development of a long-gauge vibration sensor. Proceedings of SPIE–The International Society for Optical Engineering. 2015. p. 9359. DOI: 10.1117/12.2076068

[25] Cygan P, Laghari JR. Models for insulation aging under electrical and thermal multistress. IEEE Transaction on Electrical Insulation. 1990;**25**(5):923-934

[26] Shi J, Yang Y. Study on fault characteristics of large turbo generator. Proceedings of the CSEE. 2000;**20**(7):44-47

[27] Jing S. Design of Main Insulation Aging Multi Factor Test System for Large Motor and Research on Aging Property of Stator Bar[D]. Harbin: Harbin University of Science and Technology; 2011

[28] Raman TS. Degradation of HV generator insulation mechanical, electrical and thermal stresses. IEEE International Symposium on Electrical Insulation, Toronto, Canada, June 1990. pp. 21-24. DOI: 10.1109/ELINSL.1990.109699

[29] Feng D. Research on New Fiber Bragg Grating Sensor [D]. Taiyuan: Northwest University; 2016

[30] Kersey D, Patrick HJ, LeBIanc M, et al. Fiber grating sensors. Journal of Lightwave Technology. 1997;**15**(8):1442-1463

[31] Othonos A, Kalli K. Fiber Bragg Gratings. London: Artech House, ISSN: 0342-4111,1999

[32] Griscenko M, Vitols R. Stator core vibration and temperature analysis of hydropower generation unit at 100 Hz frequency. In: proceedings of 14th International Scientific Conference. Jelgava, Latvia. May 20-22, 2015. pp. 383-388

[33] VibroSystM. On-line vibration and temperature direct measurement on high voltage devices using fiber optic sensor technology. In: CMD Conference Proceedings. 2010

[34] Srinivas MB, Ramu TS. Multifactor aging of HV generator stator insulation including mechanical vibrations. IEEE Transactions on Electrical Insulation. 1992;**27**(5):1009-1021

[35] Westinghouse Electric Corporation. Installation Operation Maintenance Instructions: Air-Cooled Turbine Generators 1000 to 7500 kW. East Pittsburgh, PA: Author; 1947 Available from: http://www.electricalpartmanuals.com/manual/air-cooled-turbine-generators-1000-to-7500-kw

[36] Energy GE. Generator In-Situ Inspections – A Critical Part of Generator Maintenance Cost Reduction. Schenectady, NY: Markman C & Zawoysky R J; 2012 Available from: https://www.gepower.com/content/dam/gepower-pgdp/global/en_US/documents/technical/ger/ger-3954c-generator-in-situ-inspections.pdf

[37] Hattori K, Takahashi K, Tohnosu S, Miyakawa K. State-of-the-art technology for large turbine generators. CIGRE SC A, 1, 2008; 2008

[38] Siemens. Generator Upgrades and Modernization. Ruhr, Germany: Michal Gawron; 2015. Available from: http://www.siemens.fi/pool/cc/events/160years-vip-seminar/gawron.pdf

[39] Oz Optics Ltd. Fiber Optic Distributed Temperature Sensors (B-DTS). 2018. Available from: https://www.ozoptics.com/ALLNEW_PDF/DTS0127.pdf

[40] SKF USA Inc. 2002. Spectrum Analysis – The Key Features of Analyzing Spectra (CM5118). Available from: http://www.skf.com/binary/tcm:12-113997/CM5118%20EN%20Spectrum%20Analysis.pdf

[41] VESKi d.o.o. CASE STUDY-07 Loose Bearing to Foundation Support/Portable Diagnostic System. Available from: http://www.veski.hr/public/brochures/Case%20study%2007%20TG%20Loose%20bearing.pdf

[42] Zhe H. Modeling and Testing of Insulation Degradation Due to Dynamic Thermal Loading of Electrical Machines [Thesis]. Lund: Division of Industrial Electrical Engineering and Automation, Faculty of Engineering, Lund University; 2017

[43] Adawi S, Rameshkumar G. Vibration diagnosis approach for industrial gas turbine and failure analysis. British Journal of Applied Science & Technology. 2016;**14**:1-9. DOI: 10.9734/BJAST/2016/23163

[44] Twiddle J, Muthuraman S, Connolly N. Condition Monitoring of the SSE Generation Fleet. Journal of Physics Conference Series (Online). May 2012;**364**(1):1-12. DOI:101088/1742-6596/364/1/012104

[45] ABB Brazil. LEAP-life expectancy analysis program. For Electrical Rotating Machines. 2006. Santiago, Chile: Marcio gennari. Available from: http://www02.abb.com/global/clabb/clabb151.nsf/0/588c647ab96ec0fdc12571f00064d269/$file/MAPLA+2006+-+ABB+Marcio+Gennari+Presentation.pdf

[46] ABB Group. Stator Winding-Condition & Lifetime Assessment. 2013. Available from: http://www02.abb.com/global/zaabb/zaabb011.nsf/bf177942f19f4a98c1257148003b7a0a/71d80922c9b6b63ac1257b7200343c9b/$file/dmmg+6+-+abb+leap+stator+winding-condition+and+lifetime+assessment.pdf

[47] Kokko V, Ahtiainen J. Ageing Due to Start-Stop Cycles and Frequent Regulation in Lifetime Estimation of Hydro Turbines and Generators. Grenoble, April. 2014: 9-11

[48] Kung P, Qin Z, Li W, Bao X. Using Distributed Sensing for Generator Condition Monitoring. 2013. Available from: http://www.hydroworld.com/articles/hr/print/volume-32/issue-7/articles/using-distributed-sensing-for-generator-condition-monitoring.html

[49] Robles E. Field Diagnostic Testing of Power Generators and Transformers Using Modern Techniques. Paper No. 12 presented at HV Testing, Monitoring and Diagnostics Workshop 2000, Alexandria, Virginia, USA, 13 & 14 September 2000. pp. 1-6

[50] Harjo S. Partial discharge in high voltage insulating materials. International Journal on Electrical Engineering and Informatics. 2016;**8**:147-163. DOI: 10.15676/ijeei.2016.8.1.11

[51] Rao B. Assessment of stator winding insulation by spectroscopic and thermo analytical techniques, PART 1-Review of deterioration mechanisms and condition monitoring techniques. The Journal of Central Power Research Institute. 2009;**5**:2. ISSN 0973-0388

[52] Li R, Pan L, Yan C, Li H, Hu B. Condition evaluation of large generator stator insulation based on partial discharge measurement. Advances in Mechanical Engineering. 2013;**5**. DOI: 10.1155/2013/765374

[53] Clemmons S. Continuous, On-Line PD Monitoring for Generators. 2017. Available from: http://www.power-eng.com/articles/print/volume-121/issue-10/features/continuous-on-line-pd-monitoring-for-generators.html

[54] Ruihua L, Pan L, Yan C, Li H, Hu B. Condition evaluation of large generator Stator insulation based on partial discharge measurement. Advances in Mechanical Engineering. 2013;**2013**. DOI: 10.1155/2013/765374

[55] ReliaSoft Corporation. Accelerated Life Testing Reference. 2015. Available from: http://www.synthesisplatform.net/references/Accelerated_Life_Testing_Reference.pdf

[56] Luo Y, Li Z, Wang H. A review of online partial discharge measurement of large generators. Energies. 2017;**10**:1694. DOI: 10.3390/en10111694

*Edited by Ricardo Albarracín Sánchez*

Around 80% of electrical consumption in an industrialised society is used by machinery and electrical drives. Therefore, it is key to have reliable grids that feed these electrical assets. Consequently, it is necessary to carry out pre-commissioning tests of their insulation systems and, in some cases, to implement an online condition monitoring and trending analysis of key variables, such as partial discharges and temperature, among others. Because the tests carried out for analysing the dielectric behaviour of insulation systems are commonly standardised, it is of interest to have tools that simulate the real behaviour of those and their weaknesses to prevent electrical breakdowns. The aim of this book is to provide the reader with models for electrical insulation systems diagnosis.

Published in London, UK


IntechOpen

ISBN 978-1-83881-685-8